University of Bath

PHD

Coupling finite element meshes for modelling movement in electromagnetic devices

Lai, Hong Cheng

Award date:
1994

Awarding institution:
University of Bath

Link to publication

Alternative formats
If you require this document in an alternative format, please contact:
openaccess@bath.ac.uk

Copyright of this thesis rests with the author. Access is subject to the above licence, if given. If no licence is specified above, original content in this thesis is licensed under the terms of the Creative Commons Attribution-NonCommercial 4.0 International (CC BY-NC-ND 4.0) Licence (https://creativecommons.org/licenses/by-nc-nd/4.0/). Any third-party copyright material present remains the property of its respective owner(s) and is licensed under its existing terms.

Take down policy
If you consider content within Bath's Research Portal to be in breach of UK law, please contact: openaccess@bath.ac.uk with the details. Your claim will be investigated and, where appropriate, the item will be removed from public view as soon as possible.

Download date: 06. May. 2023

Coupling Finite Element Meshes for Modelling Movement in Electromagnetic devices

by Hong Cheng Lai

Submitted for the Degree of Doctor of Philosophy

of the University of Bath

1994

COPYRIGHT

Attention is drawn to the fact that copyright of this thesis rests with its author. This copy of the thesis has been supplied on condition that anyone who consults it is understood to recognise that its copyright rests with its author and that no quotation from the thesis and no information derived from it may be published without the prior written consent of the author.

This thesis may be made available for consultation within the University Library and may be photocopied or lent to other libraries for the purpose of consultation.

UMI Number: U058694

All rights reserved

INFORMATION TO ALL USERS
The quality of this reproduction is dependent upon the quality of the copy submitted.

In the unlikely event that the author did not send a complete manuscript
and there are missing pages, these will be noted. Also, if material had to be removed,
a note will indicate the deletion.

UMI U058694
Published by ProQuest LLC 2013. Copyright in the Dissertation held by the Author.
Microform Edition © ProQuest LLC.
All rights reserved. This work is protected against
unauthorized copying under Title 17, United States Code.

ProQuest LLC
789 East Eisenhower Parkway
P.O. Box 1346
Ann Arbor, MI 48106-1346

33 15 AUG 1994
PHD
504-903

Summary

A new scheme for use in Finite Element modelling of electromagnetic devices with moving parts has been implemented. This type of device is troublesome to analyse using standard Finite Element techniques because of the need to model the moving parts at different relative positions.

The new scheme is based on the use of the Lagrange multipliers method to link the potential variables of separate meshes together by imposing extra continuity constraints at the common interface of the meshes. The implementation of the method using both two and three dimensional Finite Elements is described.

Tests have shown that the method performs well and is able to handle cases in which the meshes have significantly different number of nodes on the common interface. A few other alternative implementations have also been investigated but were found to be less effective than the Lagrange multipliers method. The method was also verified by comparison with measurements on a test rig.

Practical applications of this new method are demonstrated and results compared favourably with experimental measurements. The new scheme is convenient for use in modelling devices with moving parts. As meshes are free to move relative to each other on their interface, a new position can be analysed by simply placing the meshes of the moving members into the required position and the coupling terms recalculated. The need to remesh at a new position is eliminated. In order to implement this method the shape of the common interface is required to be consistent with the type of movement, for instance, a rotating machine model would require a cylindrical interface in the air gap between rotor and stator meshes.

Acknowledgements

Thanks must first go to my parents for their love, support and guidance over all these years.

I would like to thank Prof. J.F. Eastham and Prof. D. Rodger, my supervisor, for providing the opportunities to me to expand my horizon. I am also much indebted to Prof. D. Rodger for his patience, guidance and generous assistance throughout the whole of this project. Working under his unique style of leadership has been an invaluable experience.

I have also learned a great deal from the critical yet enlightening comments of Dr. P.J. Leonard on this project. For that, I must thank.

I would also like to express my gratitude to Ms N. Allen for designing the experiment described in Section 3.8 and for the supply of the test data. Thanks also go to Dr. P. Sangha and LUCAS Advanced Engineering Centre for their permission to use some of their results.

Last, but not the least, I would like to thank Ms R. Lau for her encouragement, forbearance and unwavering support over this past few years.

List of Symbols

$\mathbf{A}$	Magnetic vector potential (Wb/m)
A_z	Z-component of $\mathbf{A}$
$\delta\mathrm{A}$	Small change in A
$\mathbf{B}$	Magnetic flux density (T)
$\mathbf{E}$	Electric field strength (V/m)
$\mathbf{f}$	The load vector
$\mathbf{H}$	Magnetic field strength (Ampere-turn/meter)
I	Current (A)
$\mathbf{J}$	Current density (A/m^{-2})
J_z	Z-component of $\mathbf{J}$
$\mathbf{K}$	The stiffness matrix
$\mathbf{K}^e$	Elemental stiffness matrix
K_{ij}	The ij'th element of $\mathbf{K}$
$\mathcal{J}$	The Jacobian matrix
$\mathbf{L}$	Lower triangular Cholesky matrix
$\mathbf{L}^T$	Transpose of $\mathbf{L}$
$\mathbf{L}'$	Incomplete Cholesky triangular matrix
N	The shape function
N^e	Elemental shape function
$\hat{N}$	Shape function of the Master element
t	time (s)
V	Voltage (V)

w	Weighting function
α	Penalty number
Γ	The interface between two regions
Γ_λ	The Lagrange interface
δ	Delta Dirac function
$\boldsymbol{\lambda}, \lambda$	Lagrange multipliers
μ	Permeability (H/m)
ν	Reluctivity
ξ, η, ζ	Local coordinate system of Master element
Π	An equivalent functional
Π'	Lagrange multipliers functional
$\delta\Pi$	First variation of Π
Π^h	Re-substituted Lagrange multipliers functional
Π^p	Penalty functional
Π^a	Augmented Lagrange multipliers functional
σ	Conductivity
ϕ	Reduced-scalar potential/magnetic flux
ψ	Magnetic scalar potential
$\boldsymbol{\psi}$	Flux linkage (Wb)
Ω	The problem domain/ Resistance $(Ohms)$

Contents

Chapter 1

Introduction

Ever since the discovery of magnetism, engineers and scientists alike have struggled continuously to devise models and techniques to aid in the understanding and prediction of the electromagnetic field in different situations. Along the way, many useful methods have been developed and refined, for example the method of images, the circuit approach, the use of conformal transformations and the Finite Difference method. Many have produced effective and accurate answers in their time.

As society and technology progresses, specifications on electromagnetic devices have become more and more stringent. Increased power, higher efficiency, better reliability, tighter safety regulations and more economical manufacturing processes are all called for at the same time. As a result, it is becoming even more important now than ever before to be able to analysis and accurately predict the electromagnetic fields in and around devices so that designs can be improved and mistakes can be recognised as soon as possible

Many of the early methods are failing to deliver accurate enough answers to keep up with these requirements. With the advent of the computer technology in the 60's, attention has shifted to numerical methods, among them is the Finite Element method. The method was not new at the time and had already been popularly used by the structural and civil engineering communities. It is widely acknowledged that Winslow [1] was the first to introduce the Finite Element method to the electrical engineering community. Active research and development on the method following

its introduction has led to early 2D applications on electrical machines [2]. Today, three decades since the first introduction of the method, the range of electromagnetic problems which the Finite Element method can solve is impressive, [3] [4] [5] and [6] are just some examples.

Although the Finite Element method in electrical engineering has advanced and matured a lot, it is surprising to see that it is still ill-equipped to handle possibly one of the most commonly encountered type of problems in the field; that of modelling the movement of different parts of a device. This type of problem is most frequently found in the analysis of electrical machines. The Finite Element method is able to solve this type of problem in its static form, that is with the rotor and stator of the machine holding a fixed position with respect to each other. However, difficulties arise when it is required to model the rotor at different positions relative to the stator. This may be for a static study of the machine in which variations of certain machine characteristics with respect to rotor position are required or, more critically, a dynamic analysis in which the rotor assumes different positions with time. In both cases, the ability to be able to move the rotor arbitrarily is called for.

1.1 Difficulties of modelling devices with moving parts

While it is conceptually easy to move part of a Finite Element mesh relative to the rest, the practical realization of such mesh movements is unfortunately not as straightforward as one would like. The difficulties arise mainly because of the requirement that adjacent elements in a Finite Element mesh have to be geometrically compatible with each other. By geometrically compatible, we mean that adjacent

elements must share common corner nodes, that is, corner nodes of one element cannot appear on the edge of an adjacent element as shown in Fig.(1.1).

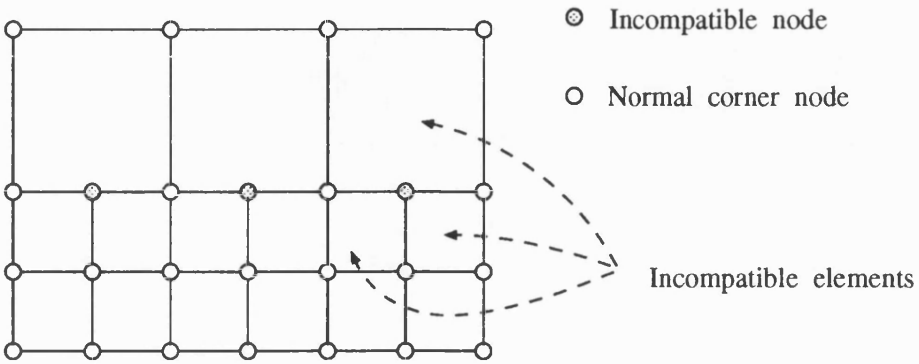

Figure 1.1: Incompatible elements

This, together with the requirement that surrounding air has to be discretized as well, will result in elements in the air gap being distorted when one part of a Finite Element mesh moves. This is illustrated in Fig.(1.2). The presence of distorted elements is undesirable since it impairs the accuracy of the solution. Further movement of the mesh will eventually destroy the elements in the air gap, resulting in the latter having to be remeshed.

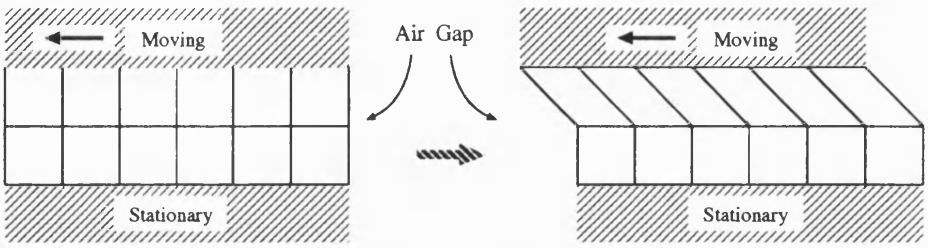

Figure 1.2: Distortion of elements in the air gap

Several methods have been put forward by researchers to tackle the problem in 2D. There is the so called Moving Band method [7] in which a layer of elements in the air gap is allowed to become distorted during a displacement. Remeshing of this band of elements is postponed as long as possible. The decision to remesh is based on certain criteria which measure the 'badness' of the distorted elements, a typically example of which is the size of the interior angles of the elements.

With 2D quadrilateral elements the most direct way of remeshing is probably to join up nearest nodes on opposite sides as shown in Fig.(1.3). For triangular elements the Delaunay triangularisation [8] technique would most likely be used to optimize the shape of the new elements generated.

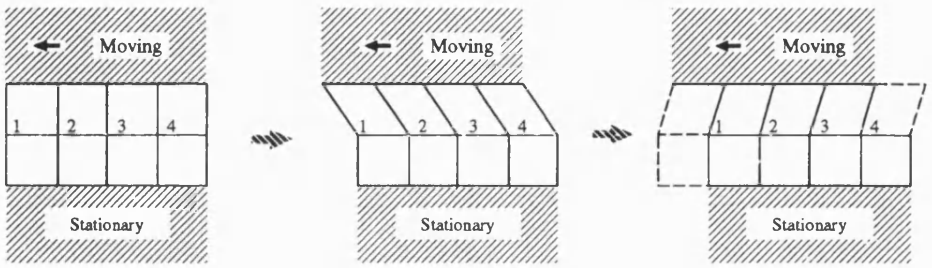

Figure 1.3: Remeshing in the Moving Band Method

This Moving Band method, though simple in concept, introduces extra complexities in the post-processing stages as the connectivity of the nodes in the moving band and the total number of nodes/elements in the problem may change from position to position. Moreover, it does not resolve the question of distorted elements.

Another possible way of dealing with mesh movements is to mesh the moving and stationary parts as two disconnected meshes and then use a 'slip' surface [9] to

interface them in the air gap. By ensuring the nodes of the two meshes coincide at equal intervals on the the 'slip' surface, the moving part of the model can be allowed to move at such steps which are an integer multiple of the node interval. This arrangement requires only a relatively simple algorithm to identify coinciding nodes on the surface which are then assigned equal potentials. This method is simple to implement; however, it suffers from the disadvantage that the smallest possible movement is limited by the size of the node interval on the surface. Care thus has to be taken at the initial meshing phase to cater for small movements.

It is also possible to solve the air gap vector potential distribution analytically and represent the result by a Fourier Series which is then used to couple nodes on either side of the air gap together [10]. This method has been used on machines under unbalanced and non-sinusoidal conditions. Although it does not require the air gap to be meshed up, its use results in a dense matrix which is more difficult to solve. Furthermore, its generalization to 3D will not be as straightforward as in 2D.

There is, of course, always the possibility of using an automatic mesh generator to create a new mesh for each position. It must be pointed out that the subject of automatic mesh generation is still under active research. Most of the algorithms published so far have concentrated on producing 2D triangular meshes. By comparison, very few 3D mesh generation schemes have been published. It should also be realized that the brute force approach of generating a new mesh for each position manually is impractical as that requires too much human effort in the pre-processing stages.

Though all of the above approaches have been shown to be able to handle 2D cases, their generalization to 3D has not been shown. With the Finite Element method

being used more and more on the analysis of electrical machines, it seems that developing a general method which allows easy modelling of this kind of problem with moving parts , both in 2 and 3D, will be beneficial.

1.2 Outline of this thesis

The purpose of this thesis is to develop a new scheme based on the Lagrange multipliers method which will solve this multiple position problem in both 2 and 3D. The method allows the moving and the stationary parts of a model to be meshed up independently so that each is free to move relative to the other. The meshes are not physically connected with each other, coupling between them is done at a later stage with Lagrange multipliers. As they are free to move independent to each other, a new position can be solved simply by placing the moving member at the desired position and the coupling terms recalculated. The need to remesh at different positions is eliminated.

Chapter 2 gives a brief review of the Finite Element method as used in electromagnetic field computation. Attention will be concentrated on magnetostatic formulations.

Chapter 3 introduces the concept of the Lagrange multipliers. Its implementation in 2D Finite Elements will be described. The various characteristics of the method will also be investigated and experimental results will be presented to verify the method.

Chapter 4 examines a few alternative implementations of the Lagrange multipliers

method. Their performance will be compared, their relative merits and drawbacks will be accessed.

Chapter 5 extends the Lagrange multipliers method to three dimensional Finite Elements. Numerical implementation of the method will be described and experimental verifications will be shown. Some computational aspects of the method will also be investigated.

Chapter 6 illustrates two practical applications of the method.

Chapter 7 concludes the work on this thesis.

Chapter 2

The Finite Element Method

2.1 Introduction

Electromagnetic field problems, like field problems in many other engineering disciplines, are governed by sets of partial differential equations. The solution to these field problems can sometimes be obtained in closed form by analytical means if both the given equations and the given domains are simple. But as the configurations and the domains of the problem in question becomes more complicated, obtaining a solution by analytical means has proved to be rather difficult. Various methods of finding approximate numerical solutions to these types of problems can be used. Examples of these are the Finite Element method, Finite Difference method and Integral method. Among them, the Finite Element method has gained considerable popularity in various science and engineering communities mainly because of its flexibility in handling complex shapes and boundary conditions.

The Finite Element method is basically a variational procedure for solving boundary value problems. Unlike the Finite Difference method which attempts a direct discretization of the equations, the Finite Element method tackles the problem by seeking an approximate solution to a sometimes energy related equivalent functional of the governing partial differential equations over a collection of simple subdomains which replaces the original problem domain.

The basic steps involved in finding the solution usually begins with the subdivision

of the problem domain into well defined simple subdomains, the finite elements. Over each of these finite elements, a local approximate function is constructed by interpolating the unknown function in terms of its nodal values. Using this approximate function and the functional, a set of algebraic equations can be derived among the nodal values of an element.

The final set of algebraic equations are formed by combining equations of all the elements in the mesh. This can then be solved after the boundary conditions are specified.

This chapter presents a brief review of the two and three dimensional formulations used in the BATH Finite Element package *MEGA* . Attentions will be focussed particularly on magnetostatic formulations.

2.2 Basic Assumptions and Equations

The electromagnetic fields at low frequencies with displacement current ignored are described by a subset of Maxwell Equations [11] :

$$\nabla \times \mathbf{H} = \mathbf{J} \tag{2.1}$$

$$\nabla \times \mathbf{E} = -\frac{\partial \mathbf{B}}{\partial t} \tag{2.2}$$

$$\nabla \cdot \mathbf{B} = 0 \tag{2.3}$$

$$\nabla \cdot \mathbf{J} = 0 \tag{2.4}$$

The equations that describe the material properties are

$$\mathbf{B} = \mu \mathbf{H} \tag{2.5}$$

and

$$\mathbf{J} = \sigma \mathbf{E}. \tag{2.6}$$

It is also assumed that all materials considered are isotropic and that their **BH** characteristic are monotonic and single-valued.

2.3 Two Dimensional Finite Elements

In 2D Finite Elements [12], fields can conveniently be modelled using one component of the magnetic vector potential, $\mathbf{A}$, defined as

$$\nabla \times \mathbf{A} = \mathbf{B}. \tag{2.7}$$

This automatically satisfies the non-divergence condition (2.3) of $\mathbf{B}$. From equations (2.7), (2.1) and (2.5), the governing partial differential equation to be solved is

$$\nabla \times \nu \nabla \times \mathbf{A} + \sigma \frac{\partial \mathbf{A}}{\partial t} = \mathbf{J}, \tag{2.8}$$

where ν is the reluctivity, $\mathbf{J}$ is the source current density and $\sigma \frac{\partial \mathbf{A}}{\partial t}$ is the induced eddy current density.

In magnetostatic problems where eddy currents are ignored, the above equation reduces to

$$\nabla \times \nu \nabla \times \mathbf{A} = \mathbf{J}. \tag{2.9}$$

When the fields are modelled using one component of $\mathbf{A}$, the above equation can further be reduced to

$$-\nabla \cdot \nu \nabla \mathrm{A}_z = \mathrm{J}_z. \tag{2.10}$$

This assumes that fields only vary in a two dimensional manner on the plane of the Finite Element mesh. Currents in the problem are also assumed to flow entirely in the direction orthogonal to this plane.

The Finite Element method does not attempt to solve the equation (2.10) directly.

Instead, it first puts the equation into an integral form which is then minimised. This integral form allows the approximation to be obtained on an element by element basis.

The two most commonly used procedures for obtaining the approximation in such integral forms are the Variational method and the Weighted Residual method. In the Variational method [13], an equivalent functional whose Euler equation is the governing equation of the problem is first obtained. The functional is equivalent to the original system equation in the sense that the solution function which minimises it also satisfies the system equation. Such functionals are usually related to the energy of the system and hence provide some physical meaning to the minimisation process.

On the other hand, the Weighted Residual method [13] forms a residual by substituting a trial function in the partial differential equation. The residual is then multiplied by a weighting function and the product is integrated over the problem domain. The solution to the problem is found by equating this integral of the product to zero. There are various methods for choosing the weighting function, examples are the Point Collocation method, Sub-domain Collocation method and the Galerkin method (Appendix C), but the Galerkin method in which the trial function is chosen to be the same as the weighting function is the most popular.

In general, the range of problems to which the Weighted Residual method can be applied is much bigger than that of the variational approach since it is not always possible to find an equivalent functional for all kinds of problems with well defined partial differential equations. However, when a variational principle can be found, the resulting matrix will always be symmetric. Matrix symmetry is important when

it comes to solving the set of equations.

2.3.1 The Galerkin Weighted Residual Method

In the Weighted Residual method, we look for an approximate solution A_z which minimises the weighted integral of the residual. We therefore solve the following equation :

$$\int_{\Omega} w_i \left(-\nabla \cdot \nu \nabla \mathrm{A}_z - \mathrm{J}_z\right) \mathrm{d}S = 0, \tag{2.11}$$

where Ω is the problem domain and w_i is a suitable set of weighting functions.

To write the above integral into a set of equations, the problem domain is first subdivided into a collection of simple subdomains called finite elements [13]. We now approximate A_z over this collection of finite elements with the following :

$$\mathrm{A}_z = \sum_{i=1}^{k} N_i A_{z_i}, \tag{2.12}$$

where N_i are called the shape functions and A_{z_i} are the nodal values of A_z. Fig.(2.1) illustrates this approximation idea.

To avoid the requirement of second order derivatives on the shape functions, the above equation can be transformed using Green's Theorem. Yielding

$$\int_{\Omega} \left(\nabla w_i \cdot \nu \nabla \mathrm{A}_z\right) - \left(w_i \mathrm{J}_z\right) \mathrm{d}S - \oint_{\Gamma} w_i \nu \frac{\partial \mathrm{A}_z}{\partial n} \, \mathrm{dl} = 0. \tag{2.13}$$

Different choices of the weighting function leads to different methods. In the Galerkin method, it is conveniently chosen to be the same as the nodal shape functions. The

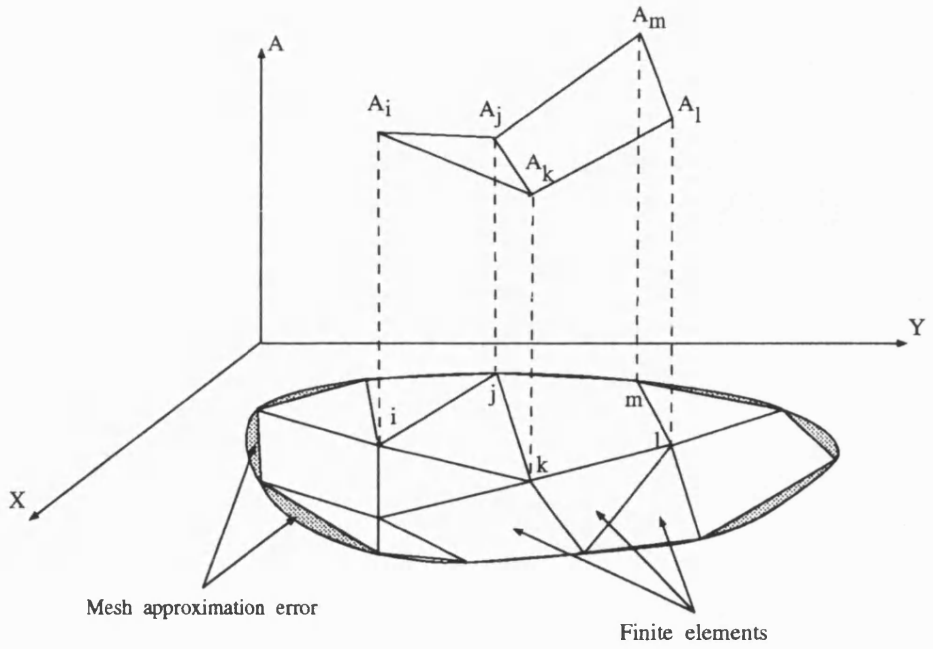

Figure 2.1: Approximation by Finite Elements

above equation can now be written as a set of equations using the Finite Element technique. Within each of the finite elements, the vector potential A_z^e is described by a relation similar to equation (2.12) :

$$A_z^e = \sum_{j=1}^{k^e} N_j^e A_{zj}^e, \tag{2.14}$$

where k^e is the number of nodes of the element concerned. N_j^e is the shape function of node j of the element and A_{zj}^e is the nodal A_z^e at node j. The same technique can also be used to approximate the prescribed current density, J_z, within an element. At the element level, equation (2.13) can therefore be rewritten as

$$\int_{\Omega_e} (\nabla N^e \cdot \nu_e \nabla A_z^e) - (N^e J_z^e)\, dS - \oint_{\Gamma_e} N^e \nu_e \frac{\partial A_z^e}{\partial n}\, dl = 0. \tag{2.15}$$

The term J_z^e only applies to elements with prescribed current density. The line integral cancels between adjoining elements and can be ignored. This also enforces weakly the continuity of $\mathbf{H} \times \mathbf{n}$ across elements. Similarly, ignoring the integral at the problem boundary enforces the condition $\mathbf{H} \times \mathbf{n} = 0$ weakly. The above equation can be expressed in matrix form after substituting with equation (2.14) as

$$[\mathbf{K}^e]\{\mathbf{A}^e\} = \{\mathbf{f}^e\}, \tag{2.16}$$

where

$$K_{ij}^e = \nu_e \int_{\Omega_e} \left(\frac{\partial N_i^e}{\partial x} \frac{\partial N_j^e}{\partial x} + \frac{\partial N_i^e}{\partial y} \frac{\partial N_j^e}{\partial y} \right) \mathrm{d}S \tag{2.17}$$

and

$$f_i^e = \int_{\Omega_e} N_i^e J_i^e \, \mathrm{d}S. \tag{2.18}$$

Using the isoparametric element concept outlined in Appendix A.1, both integrations can be performed over the master element by using the following transformations :

$$K_{ij}^e = \int_{-1}^{1} \int_{-1}^{1} \nu_e \left(\frac{\partial N_i^e}{\partial x} \frac{\partial N_j^e}{\partial x} + \frac{\partial N_i^e}{\partial y} \frac{\partial N_j^e}{\partial y} \right) |\mathcal{J}| \, \mathrm{d}\xi \mathrm{d}\eta$$

and

$$f_i^e = \int_{-1}^{1} \int_{-1}^{1} N_i^e J_i^e |\mathcal{J}| \, \mathrm{d}\xi \mathrm{d}\eta.$$

$\mathcal{J}$ is the Jacobian matrix of the transformation from the $\xi\eta$ to the XY coordinate

system. The derivative terms are given by

$$\begin{bmatrix} \frac{\partial N_i^e}{\partial x} \\ \frac{\partial N_i^e}{\partial x} \end{bmatrix} = \mathcal{J}^{-1} \begin{bmatrix} \frac{\partial \hat{N}_i}{\partial \xi} \\ \frac{\partial \hat{N}_i}{\partial \eta} \end{bmatrix}, \tag{2.19}$$

where $\hat{N}$ is the shape function of the master element (Appendix A.1).

The global $\mathbf{K}$ matrix and $\mathbf{f}$ vector, which are often called the stiffness matrix and the force vector, are obtained by summing $\mathbf{K}^e$ and $\mathbf{f}^e$ of all elements together :

$$[\mathbf{K}]\{\mathbf{A}\} = \{\mathbf{f}\}. \tag{2.20}$$

The $\mathbf{K}$ matrix resulting from this formulation is symmetric and sparse. Solution to the above equation can be obtained by various matrix techniques, Gaussian elimination, Gauss-Seidel etc. More recently, however, the Preconditioned Conjugate Gradient method has proved to be efficient in handling large sparse systems and is now popularly used.

2.4 Three Dimensional Finite Elements

The vector potential is very attractive for use in 2D Finite Elements since it involves only one unknown per node. Unfortunately, the simple extension of this approach to 3D magnetostatic problems is not so economical. There are at least 3 unknowns per node and the resulting stiffness matrix will become much denser and difficult to solve. To circumvent these difficulties and also reduce the problem size to a more manageable one, an alternative formulation which uses a combination of magnetic scalar potential, ψ, and reduced magnetic scalar potential, ϕ, is often used [14].

In this scheme, the problem is partitioned into two regions as illustrated in Fig.(2.2). Region 1 in Fig.(2.2) is assumed to contain all the source currents and has constant low permeability. The rest of the problem is grouped under region 2 which may contain non-linear materials.

With such partitioning, the field in region 1, $\mathbf{H}_1$, can be split up into 2 parts as

$$\mathbf{H}_1 = \mathbf{H}_s + \mathbf{H}_m, \tag{2.21}$$

where $\mathbf{H}_s$ is the field produced by the source alone and $\mathbf{H}_m$ is the rest of the field. Since

$$\nabla \times \mathbf{H}_s = \mathbf{J}, \tag{2.22}$$

therefore

$$\nabla \times \mathbf{H}_m = 0. \tag{2.23}$$

Thus, $\mathbf{H}_m$ can be defined as the negative gradient of a scalar potential, the reduced

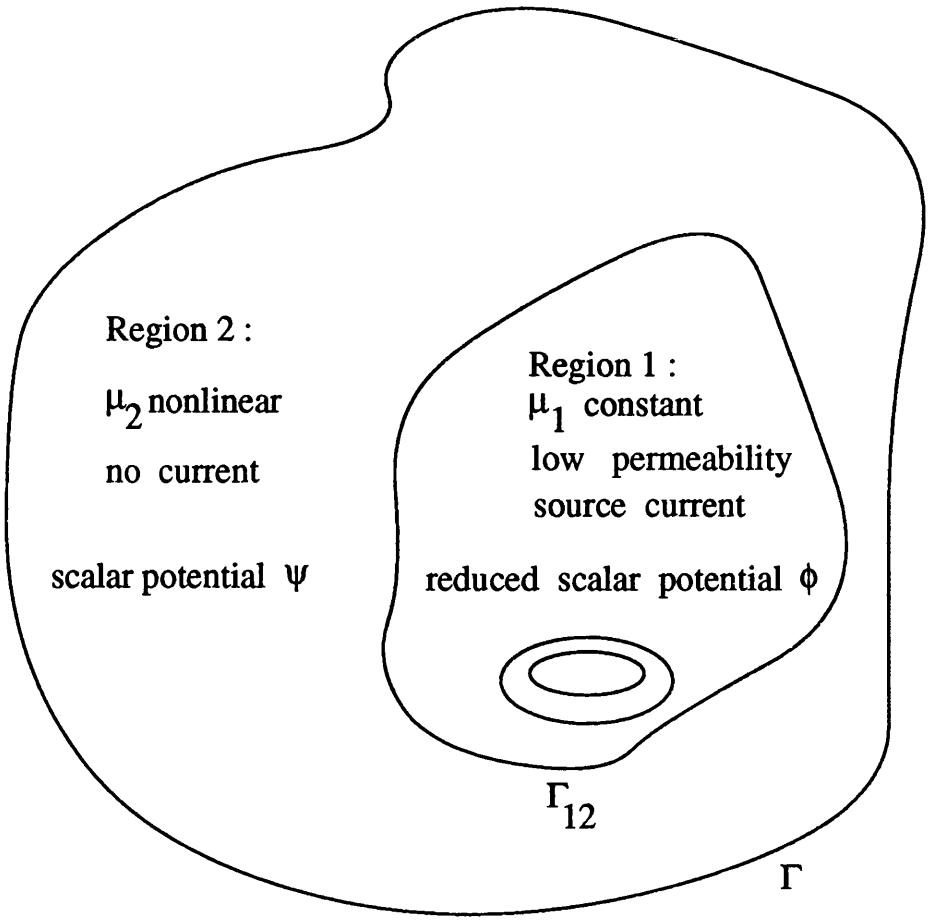

Figure 2.2: Partitioning of a 3D magnetostatic problem

scalar potential ϕ, and therefore we have

$$\mathbf{H}_m = -\nabla\phi. \tag{2.24}$$

Substituting the above equation into equation (2.3), we obtain

$$\nabla \cdot \mu_1 \mathbf{H}_s - \nabla \cdot \mu_1 \nabla\phi = 0. \tag{2.25}$$

$\mathbf{H}_s$ can be calculated using Biot-Savart's Law. Although it is theoretically possible to model the field in region 2 with the same approach, it is rarely done in practice because of cancellation of $\mathbf{H}_s$ and $\mathbf{H}_m$ inside materials with high permeability [14]. For the same reason, only materials with low constant permeabilities are allowed in region 1; usually it contains only air. Therefore in this region, the following equation is solved for :

$$-\nabla \cdot \mu_1 \nabla\phi = 0. \tag{2.26}$$

Non-linear and highly permeable materials are contained in region 2. The field in this region is modelled using the total scalar potential, ψ, which is defined as

$$\mathbf{H}_2 = -\nabla\psi. \tag{2.27}$$

We therefore have

$$-\nabla \cdot \mu_2 \nabla\psi = 0. \tag{2.28}$$

At the interface between these two regions, Γ_{12}, the continuity of normal components

of **B** and the tangential components of **H** apply. Hence,

$$-\mu_1(\frac{\partial\phi}{\partial n} + \mathrm{H}_{sn}) = -\mu_2\frac{\partial\psi}{\partial n} \tag{2.29}$$

and

$$-\frac{\partial\phi}{\partial t} + \mathrm{H}_{st} = -\frac{\partial\psi}{\partial t}, \tag{2.30}$$

where H_{sn} and H_{st} are the normal and tangential direction of the interface Γ_{12} respectively. Equation(2.30) can be integrated along the interface to give

$$\psi = \phi - \int_{\Gamma_{12}} \mathrm{H}_{st}\,\mathrm{dl}, \tag{2.31}$$

which can be used later to eliminate either ψ or ϕ on the interface.

2.4.1 Numerical Implementation

Applying the Galerkin procedure to both regions results in

$$\int_{\Omega_1} \mu_1(\nabla N_i \cdot \nabla\phi)\,\mathrm{d}V - \oint_{\Gamma_1} N_i\mu_1\frac{\partial\phi}{\partial n}\,\mathrm{d}S = 0 \tag{2.32}$$

and

$$\int_{\Omega_2} \mu_2(\nabla N_i \cdot \nabla\psi)\,\mathrm{d}V - \oint_{\Gamma_2} N_i\mu_2\frac{\partial\psi}{\partial n}\,\mathrm{d}S = 0. \tag{2.33}$$

Following the Finite Elements procedure outlined earlier, the problem region is subdivided into finite elements. Typically, these are 8-noded bricks, 6-noded triangular prisms or 4-noded tetrahedra. Though the two latter types of element may provide more flexibility in the subdivision process, the brick element has a better accuracy

in approximating the potential function. Appendix A.2 shows a brick element and its shape functions. Similar to the 2D case, the potentials are approximated with

$$\begin{aligned} \psi &= \sum_{i=1}^{k} N_i \psi_i \\ \phi &= \sum_{i=1}^{l} N_i \phi_i \end{aligned} \tag{2.34}$$

Evaluation of equation (2.32) and equation (2.33) are now performed and summed in an element by element manner in exactly the same way as that outlined in the previous section. Ignoring the surface term in the summation will automatically satisfy the continuity of $\mathbf{B}\cdot\mathbf{n}$ across element interface interior to the region; at the outer boundary, this will satisfy the Neumann condition. At the interface between the two regions, however, this surface term must be calculated and is used to link the normal components of $\mathbf{B}$ together. Adding the above two equations together, we have

$$\int_{\Omega_1} \mu_1(\nabla N_i \cdot \nabla\psi)\,\mathrm{d}V + \int_{\Omega_2} \mu_2(\nabla N_i \cdot \nabla\phi)\,\mathrm{d}V = \int_{\Gamma_{12}} N_i(\mu_1 \frac{\partial\phi}{\partial n_1} + \mu_2 \frac{\partial\psi}{\partial n_2})\,\mathrm{d}S. \tag{2.35}$$

Substituting equation (2.29) yields

$$\int_{\Omega_1} \mu_1(\nabla N_i \cdot \nabla\psi)\,\mathrm{d}V + \int_{\Omega_2} \mu_2(\nabla N_i \cdot \nabla\phi)\,\mathrm{d}V = \int_{\Gamma_{12}} \mu_1 N_i \mathrm{H}_{sn}\,\mathrm{d}S. \tag{2.36}$$

The surface term now appears as the right hand side of the set of equations. Thus $\mathbf{H}_s$ is only required to be calculated on Γ_{12}. Furthermore, by first choosing a reference node at which ψ and ϕ are made equal, one of them can be eliminated on Γ_{12} by using equation (2.30). The stiffness matrix resulting from this formulation is also

sparse and symmetric.

The use of scalar potentials to model the fields leads to a substantial reduction of system unknowns since there is only one variable per node instead of three as in the vector potential case. Consequently, the same problem can be solved with a much lighter demand on computer resources which is still an important factor to take into consideration despite the latest advent in computer technology.

2.5 Newton-Raphson

In practical applications, most materials encountered are nonlinear in nature with their permeability being a function of the magnetic field. Their presence in problems modelled using Finite Elements will result in a set of nonlinear equations. Various iterative techniques can be used to solve this set of equations, among them Newton-Raphson is a popular choice. We begin by considering again equation (2.20) for the 2D A formulation and re-writing as :

$$F(\mathbf{A}) = \mathbf{K}\mathbf{A} - \mathbf{f} = 0 \tag{2.37}$$

where

$$K_{ij} = \int_{\Omega} (\nabla N_i \cdot \nu \nabla N_j)\, \mathrm{d}S$$

Assuming that an approximate solution $\mathbf{A}^k$ to $F(\mathbf{A})$ is reached, then the increment, $\delta\mathbf{A}^k$, to a better estimate to the solution satisfies

$$F(\mathbf{A}^k + \delta\mathbf{A}^k) \approx F(\mathbf{A}^k) + \left.\frac{\partial F(\mathbf{A})}{\partial \mathbf{A}}\right|_{\mathbf{A}^k} \delta\mathbf{A}^k = 0. \tag{2.38}$$

The first term in the above equation is simply the residual of $F(\mathbf{A})$ after $\mathbf{A}^k$ has been substituted. On differentiating $F(\mathbf{A})$ with respect to A_j, we obtain the following for a typical i'th equation for the second term :

$$\frac{\partial F(\mathbf{A})}{\partial A_j} = \int_{\Omega} (\nabla N_i \cdot \nu \nabla N_j)\, \mathrm{d}S + \int_{\Omega} \frac{\partial \nu}{\partial A_j} (\nabla N_i \cdot \nabla \sum NA)\, \mathrm{d}S \tag{2.39}$$

Expressing the reluctivity ν as a function of $\mathbf{B}^2$, we can write the following :

$$\frac{\partial \nu}{\partial A_j} = \frac{\partial \nu}{\partial \mathbf{B}^2} \frac{\partial \mathbf{B}^2}{\partial A_j}. \tag{2.40}$$

The values of $\partial\nu/\partial\mathbf{B}^2$ are obtained from a ν vs $\mathbf{B}^2$ curve which can in turn be derived from the **BH** data. In 2D,

$$\mathbf{B}^2 = (\nabla \sum NA) \cdot (\nabla \sum NA)$$

and the term $\frac{\partial \mathbf{B}^2}{\partial A_j}$ becomes

$$\frac{\partial \mathbf{B}^2}{\partial A_j} = 2\,(\nabla N_j) \cdot (\nabla \sum NA)\,.$$

Equation(2.39) can now be expanded to :

$$\frac{\partial F(\mathbf{A})}{\partial A_j} = \int_{\Omega} (\nabla N_i \cdot \nu \nabla N_j)\,\mathrm{d}S + 2\frac{\partial \nu}{\partial \mathbf{B}^2} \int_{\Omega} (\nabla N_j \cdot \nabla \sum NA)(\nabla N_i \cdot \nabla \sum NA)\,\mathrm{d}S. \tag{2.41}$$

The above equation will also result in a symmetric and sparse square matrix after A^k is substituted. A typical ij term in this matrix is :

$$\mathbf{K'^k}_{ij} = \int_{\Omega} (\nabla N_i \cdot \nu \nabla N_j)\,\mathrm{d}S + 2\frac{\partial \nu}{\partial \mathbf{B}^2} \int_{\Omega} \left(\nabla N_j \cdot \nabla \sum NA^k\right)\left(\nabla N_i \cdot \nabla \sum NA^k\right)\mathrm{d}S. \tag{2.42}$$

Equation(2.38) can now be written in matrix form :

$$\{\mathbf{F}(\mathbf{A}^k)\} + [\mathbf{K'^k}]\{\delta \mathbf{A}^k\} = 0. \tag{2.43}$$

After solving for $\delta \mathbf{A}^k$, the new estimate is obtained by

$$\mathbf{A}^{k+1} = \mathbf{A}^k + \delta \mathbf{A}^k. \tag{2.44}$$

The procedure is repeated until some chosen convergence criteria are met. At the end of each iteration, the reluctivity ν and its derivative with respect to $\mathbf{B}^2$ have to be calculated from the **BH** data. In order to reduce the overhead incurred in such calculations, these two quantities are usually pre-calculated and stored as two separate curves. Various types of curve fitting methods such as piecewise linear approximation, spline fit, least square fit etc. can be used. The linear curve fit is not satisfactory since at places along the curves the derivative term changes abruptly, producing inconsistent information about the reluctivity and its derivative which can cause difficulties in the Newton-Raphson iterations. The cubic spline type of curve fitting methods, for example [15], are commonly used because of their modest demand on computing cost and their ability to ensure function as well as slope continuity. It is also necessary sometimes to smooth experimentally obtained **BH** data to remove unwanted errors before they are curve fitted.

2.6 Matrix Solution

The formulations described in the previous sections result in a system of equations whose coefficient matrix, $\mathbf{K}$, is sparse and symmetric. When the number of unknowns is small, direct methods like Gaussian elimination are most reliable and effective in obtaining the solutions. But as the number of unknowns in the system increases, most likely due to a refinement of the mesh or a 3D analysis, the methods begin to lose their appeal as efficient solvers. This is mainly due to the enormous increase in demand of computational time and memory storage as a result of extra 'fill-in' during the elimination process. Here, we define 'fill-in' as zero entries in the matrix which become non-zero as the algorithm progresses.

Iterative methods such as Gauss-Seidel, Successive-Over relaxation etc. offer an alternative way of solving the equations with much reduced demand in storage requirements. If rapid convergence is achieved, a sufficiently accurate solution can be obtained in a much shorter time than a direct method. However, the convergence rate of these methods is very much affected by the condition of the equations and could be quite slow in some problems and in others, indeed, may never happen.

In recent years, the Conjugate Gradient method [16] has been rediscovered and proved to be efficient when used with a suitable preconditioner. The method is said to be a direct method in principle since it converges to the true solution in N steps if exact arithmetic is used. In practice, however, it behaves more like an iterative method and produces an accurate enough solution in a much smaller number of steps. Similar to other iterative methods, the convergence of the Conjugate Gradient method is closely linked to the condition of the matrix [17]. As such, the use of the

method in its basic form to solve matrices resulting from Finite Elements usually results in very slow convergence.

The technique of preconditioning [18] is introduced to improve the rate of convergence. The idea basically involved the multiplication of the matrix $\mathbf{K}$ by a preconditioning matrix $\mathbf{P}$ so that the condition of $\mathbf{KP}$ is much improved over the original one. This leads to a better rate of convergence when the transformed matrix is solved using the Conjugate Gradient method. The best preconditioning matrix is the inverse of $\mathbf{K}$, $\mathbf{K}^{-1}$; then the solution will converge in 1 iteration. The construction of an exact $\mathbf{K}^{-1}$, however, brings us back to all the problems suffered by the direct methods. Moreover, there is no need to perform any C-G iteration if $\mathbf{K}^{-1}$ is obtained since the equations are practically solved.

A reasonable compromise in practice is to construct a matrix which is only an approximate inverse to $\mathbf{K}$ and is relatively cheap to compute. The Incomplete Cholesky Decomposition technique [19] is a convenient way of obtaining such approximate inverse. The Cholesky Decomposition method constructs a triangular matrix such that

$$\mathbf{K} = \mathbf{L}\mathbf{L}^T,$$

where $\mathbf{L}$ is a lower triangular matrix. An incomplete Cholesky decomposition of $\mathbf{K}$, on the other hand, constructs a triangular matrix $\mathbf{L}'$ which is only an approximate to $\mathbf{L}$:

$$\mathbf{K} \approx \mathbf{L}'\mathbf{L}'^T. \tag{2.45}$$

$\mathbf{L}'$ is incomplete in that some terms are missing. This is permissible since we are only looking for an approximate decomposition. Hence the name ICCG which stands

for "Incomplete Cholesky-Conjugate Gradient". Various strategies can be used to decide which terms are to be kept, the one by Kershaw [20] which retains the sparsity structure of the original matrix by ignoring entries in $\mathbf{L}$ which fall outside the sparsity pattern of $\mathbf{K}$ is an example.

The preconditioned system of equations of equation (2.20) now can be written as :

$$[\mathbf{L}'^{-1}\mathbf{K}(\mathbf{L}'^{T})^{-1}](\mathbf{L}'^{T}\mathbf{A}) = (\mathbf{L}'^{-1}f) \tag{2.46}$$

$$[\mathbf{K}']\{\mathbf{A}'\} = \{f'\} \tag{2.47}$$

Conjugate Gradient iteration is then performed on equation (2.47) instead of equation (2.20). Solution to the original problem can be recovered once equation (2.47) is solved.

Chapter 3

Lagrange Multipliers in 2D Finite Elements

3.1 Introduction

The Finite Element method has proved to be extremely useful in solving a wide range of electromagnetic field problems, among these is the modelling of electrical machines. The difficulties in modelling these types of devices, as mentioned in Chapter 1, is because in addition to varying the excitation/load parameters, the movement of the rotor have to be taken into consideration. This latter requirement means that instead of solving one fixed position, a whole series of rotor positions has to be solved in order that the relationship between certain device characteristics and the rotor position can be studied. This knowledge is essential in understanding the devices and also later in the optimisation process.

The problems associated with this multiple positions problem have been discussed in Chapter 1 and a brief review of the techniques proposed before has been given. The chapter has concluded that there is a lack of methods general enough to be applied to both 2 and 3D problems. The objective of this chapter is thus to develop a scheme for solving this multiple position problem in 2D. Its extension to 3D will be presented in Chapter 5. The scheme is based on the use of the Lagrange multipliers method.

3.2 The Variational Approach to the 2D A Formulation

In Chapter 2, it was shown how the Galerkin Weighted Residual method can be used to transform the governing equation of the vector potential formulation into a set of linear equations. It was also mentioned that the same set of equations can alternatively be obtained by formulating the governing equation in variational terms by means of an energy related functional. The latter approach is sometimes preferred since it provides a physical meaning to the minimisation process. A similar benefit can be enjoyed if it is used to introduce the Lagrange multipliers into the system. This section reviews briefly the variational approach to the 2D formulation. The same approach will also be used in subsequent sections to introduce the Lagrange multipliers.

Using the magnetic vector potential, $\mathbf{A}$, we have to solve for

$$\nabla \times \nu \nabla \times \mathbf{A} = \mathbf{J}. \tag{3.1}$$

The variational formulation of the above equation centres on the establishment of an equivalent functional. Subsequent minimisation of this functional leads to a set of linear equations. It is shown in Appendix B that a suitable equivalent functional for the above equation is

$$\Pi = \int_{\Omega} \mathbf{A}(\nabla \times \nu \nabla \times \mathbf{A}) - 2(\mathbf{A} \cdot \mathbf{J})\, \mathrm{d}V. \tag{3.2}$$

According to variational principles [13], the solution function that minimises Π is

also the solution of equation (3.1). As shown in Appendix B, equation (3.2) can be rewritten in the following form :

$$\Pi = \int_{\Omega} \frac{1}{2}\nu(\nabla \times \mathbf{A})(\nabla \times \mathbf{A}) - (\mathbf{A} \cdot \mathbf{J})\,dV. \tag{3.3}$$

Which in 2D reduces to

$$\Pi = \int_{\Omega} \frac{1}{2}\nu \left[\left(\frac{\partial A_z}{\partial x}\right)^2 + \left(\frac{\partial A_z}{\partial y}\right)^2\right] - (A_z J_z)\,dxdy. \tag{3.4}$$

The governing equation (3.1) can easily be shown to be the Euler equation of this functional by performing a variation on it. For convenience, A_z and J_z will be written as A and J for the rest of this chapter. Approximating the vector potential in the usual way as

$$A = \sum_{i=1}^{k} N_i A_i,$$

and substituting it into equation (3.4), the following is obtained.

$$\Pi = \int_{\Omega} \frac{1}{2}\nu \left[\left(\sum \frac{\partial N_i}{\partial x} A_i\right)^2 + \left(\sum \frac{\partial N_i}{\partial y} A_i\right)^2\right] - \left(\sum N_i A_i J\right)\,dxdy \tag{3.5}$$

Minimisation of Π requires that the variation with respect to each nodal A be zero. For a typical variable A_j, we have

$$\frac{\partial \Pi}{\partial A_j} = \int_{\Omega} \nu \left[\left(\sum \frac{\partial N_i}{\partial x} A_i\right)\frac{\partial N_j}{\partial x} + \left(\sum \frac{\partial N_i}{\partial y} A_i\right)\frac{\partial N_j}{\partial y}\right] - (N_j J)\,dxdy = 0. \tag{3.6}$$

Differentiating Π with respect to all nodal A results in an set of equations which can be seen to be identical to that obtained with the Galerkin method in Section 2.3.1. The global stiffness matrix and load vector can be calculated by summing all elemental stiffness matrices and load vectors following standard Finite Element techniques.

3.3 Lagrange Multipliers

Instead of pursuing the remeshing path for a solution to the multiple position problem, the method developed in this chapter approaches the problem in a different way, using the Lagrange multipliers method. The Lagrange multipliers method is closely associated with the study of optimisation of functions under subsidiary conditions.

Consider the minimisation of a two-dimensional function $f(x, y)$ subject to the constraint

$$c(x, y) = 0.$$

Using the Lagrange multipliers method, the solution to this constrained problem is obtained by minimising a new function $F(x, y, \lambda)$ constructed from $f(x, y)$ and $c(x, y)$:

$$F(x, y, \lambda) = f(x, y) + \lambda\, c(x, y) \tag{3.7}$$

where λ is the Lagrange multiplier. The equations to be solved are obtained by differentiating $F(x, y, \lambda)$ with respect to x, y and λ and are therefore :

$$\frac{\partial F(x, y, \lambda)}{\partial x} = \frac{\partial f(x, y)}{\partial x} + \lambda \frac{\partial c(x, y)}{\partial x} = 0 \tag{3.8}$$

$$\frac{\partial F(x, y, \lambda)}{\partial y} = \frac{\partial f(x, y)}{\partial y} + \lambda \frac{\partial c(x, y)}{\partial y} = 0 \tag{3.9}$$

$$\frac{\partial F(x, y, \lambda)}{\partial \lambda} = c(x, y) = 0 \tag{3.10}$$

These are also the necessary conditions for a local minimum to occur at a point (x^*, y^*) according to the theory of optimisation [21]. The first two conditions are the same as saying that at (x^*, y^*) the normal vectors of $f(x, y)$ and $c(x, y)$ are

related by

$$\nabla f(x^*, y^*) = \bar{\lambda} \nabla c(x^*, y^*).$$

Any small variation along the constraint curve $c(x, y)$ from this point will be orthogonal to $\nabla f(x^*, y^*)$. The last condition requires that (x^*, y^*) must also satisfy the specified constraint. These conditions are illustrated in Fig.(3.1). At the point (x', y') at which $\nabla f(x', y') \neq \bar{\lambda} \nabla c(x', y')$, it is possible to move in a direction orthogonal to $\nabla c(x', y')$ and at the same time reduce $f(x, y)$. Such a direction does not exist at the local minimum point (x^*, y^*). Generalization of the Lagrange multipliers method to multi-dimensional functions with multiple constraints can be found, for example, in [21].

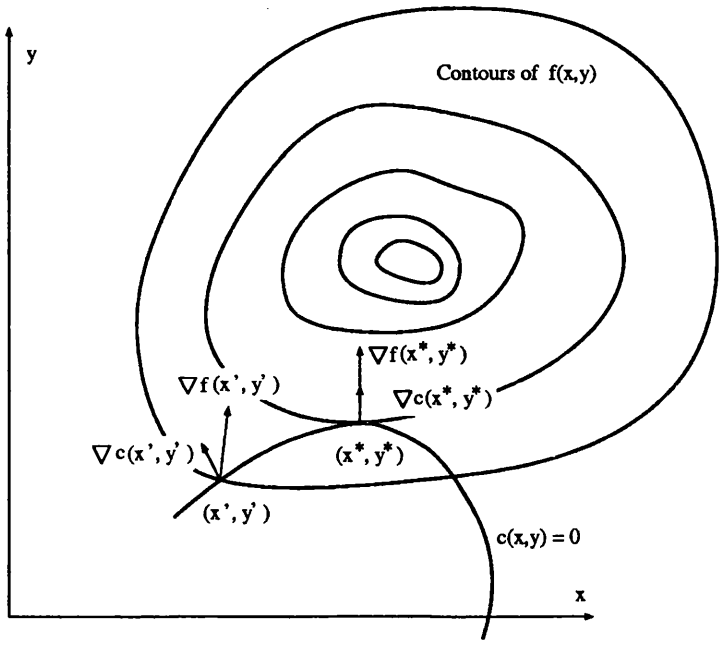

Figure 3.1: Example constrained problem in two-dimension

3.4 Using the Lagrange Multipliers

To see how the Lagrange multipliers method can be used for our purpose, consider the schematic diagrams in Fig.(3.2) which show the two most common type of movement found in electrical machine problems: linear translation and circular rotation. We will first set out a few assumptions which define the scope of the discussion that follows.

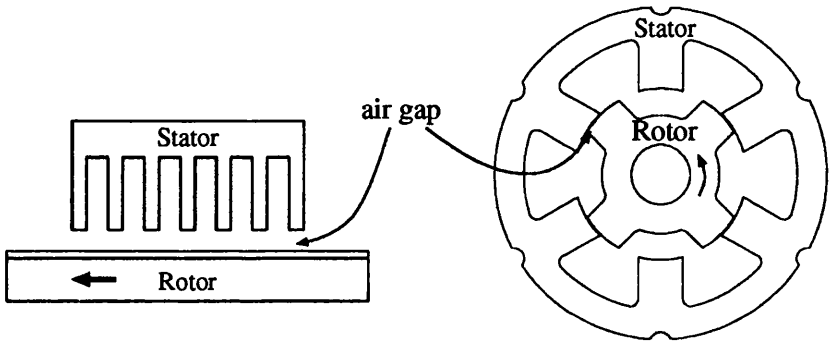

Figure 3.2: Translational and rotational movements

To begin with, it is assumed that the problem we are going to consider consists of only one moving and one stationary part. It is also assumed that the movement does not cause the parts to collide with each other. As happens in most practical cases, the presence of an air gap between the moving and the stationary part is assumed. This last assumption allows us to concentrate the discussion on coupling regions which carry no eddy currents.

The two members of the model are first meshed up as two independent meshes following the normal Finite Element procedure. A special sliding interface, the

shape of which is consistent with the type of movement, is introduced into the air gap. The two meshes are then brought together to meet on this sliding interface; they are also allowed to move freely on this interface relative to each other. This sliding interface is different from the 'slip' surface mentioned in Section 1.1 in that nodes from the two meshes do not need to be matched on the interface.

Consider the case shown in Fig.(3.3) which consists of an upper moving mesh, and a lower stationary mesh touching each other at the sliding interface, Γ_λ.

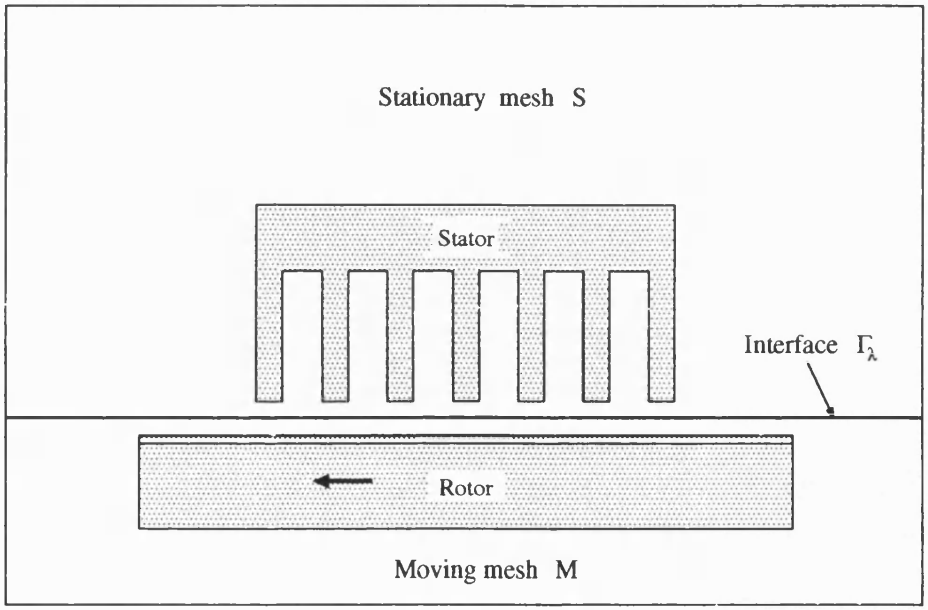

Figure 3.3: A typical problem with moving parts

Following the variational approach outlined in Section 3.2, functionals of the form of equation (3.4) can be written for the two meshes separately. Using a subscript M to indicate quantities belonging to the moving region and a subscript S for the

stationary region, we have

$$\Pi_M = \int_{\Omega_M} \frac{1}{2}\nu_M \left[\left(\frac{\partial A_M}{\partial x} \right)^2 + \left(\frac{\partial A_M}{\partial y} \right)^2 \right] - (A_M J_M)\, dxdy \tag{3.11}$$

and

$$\Pi_S = \int_{\Omega_S} \frac{1}{2}\nu_S \left[\left(\frac{\partial A_S}{\partial x} \right)^2 + \left(\frac{\partial A_S}{\partial y} \right)^2 \right] - (A_S J_S)\, dxdy. \tag{3.12}$$

The functional for the whole system now becomes

$$\Pi = \Pi_M + \Pi_S. \tag{3.13}$$

Minimising Π will result in a system of equations which can be represented in matrix form as

$$\begin{bmatrix} \mathbf{K}_M & 0 \\ 0 & \mathbf{K}_S \end{bmatrix} \begin{bmatrix} \mathbf{A}_M \\ \mathbf{A}_S \end{bmatrix} = \begin{bmatrix} \mathbf{f}_M \\ \mathbf{f}_S \end{bmatrix} \tag{3.14}$$

In the above equation $\mathbf{K}_M$, $\mathbf{A}_M$ and $\mathbf{f}_M$ are the stiffness matrix, potential vector and the force vector of the moving mesh respectively. The corresponding matrix and vectors of the stationary mesh are denoted with a subscript S . The above equation as it stands still represents two unconnected problems. There is no coupling between the potentials of the two meshes. In order to link them together, extra conditions specifying certain relationships between the potentials have to be imposed. For the present configuration, it would appear that the most obvious constraint to be placed upon the potentials is to require them to be continuous across the sliding interface. That is, we impose

$$A_M - A_S = 0 \qquad \text{on } \Gamma_\lambda. \tag{3.15}$$

In 2D Finite Element modelling using vector potential, this is equivalent to imposing the continuity of $\mathbf{B} \cdot \mathbf{n}$ across the interface. The Lagrange multipliers method mentioned earlier can be used to enforce this constraint. Following the procedure outlined in Section 3.3, a new functional Π' is formed such that

$$\Pi' = \Pi + \int_{\Gamma_\lambda} \lambda(\mathrm{A}_M - \mathrm{A}_S)\,\mathrm{d}l. \tag{3.16}$$

Notice that the line integral above is performed on the interface Γ_λ as this is where the potentials of the two meshes are required to be made continuous. The Lagrange multiplier λ is now a new function of the independent coordinates defined only on Γ_λ, instead of a scalar number as indicated before. A solution to the coupled problem is obtained by minimising Π' with respect to A_M, A_S and λ.

3.5 A Physical Interpretation of the Lagrange Multipliers

The Lagrange multipliers technique has so far been viewed solely as a mathematical device for enforcing the potential continuity constraints on the interface. It is, however, possible to show that in our case the Lagrange multiplier has a physical significance with respect to the original problem. Such physical identification of the Lagrange multipliers will help to explain in the next chapter why the method works better than some of the other similar implementations.

To obtain first of all a physical meaning of the Lagrange multipliers in the 2D **A** case, consider again the equivalent energy functional :

$$\Pi = \int_{\Omega} \frac{1}{2}\nu(\nabla^2 \mathrm{A}) - (\mathrm{AJ})\,\mathrm{d}S.$$

The first variation of Π is

$$\delta\Pi = \int_{\Omega} \nu(\nabla \mathrm{A})\delta(\nabla \mathrm{A}) - \delta\mathrm{AJ}\,\mathrm{d}S. \tag{3.17}$$

Integrating by parts, we obtain

$$\delta\Pi = \int_{\Omega} \left[-\delta\mathrm{A}(\nu\nabla^2 \mathrm{A}) - \delta\mathrm{AJ}\right] \mathrm{d}S + \oint \delta\mathrm{A}(\nu\nabla \mathrm{A}) \cdot \mathrm{dl}, \tag{3.18}$$

which can be written as

$$\delta\Pi = -\int_{\Omega} \delta\mathrm{A}(\nu\nabla^2 \mathrm{A} + \mathrm{J})\,\mathrm{d}S + \oint \delta\mathrm{A}\left(\nu\frac{\partial \mathrm{A}}{\partial n}\right) \mathrm{dl}. \tag{3.19}$$

Similar expressions can be written for the moving and stationary side so that we have

$$\begin{aligned}\delta\Pi &= \delta\Pi_M + \delta\Pi_S \\ &= \int_{\Omega_M} -[\delta A_M(\nu_M \nabla^2 A_M)] - [\delta A_M J_M]\,dS + \oint \delta A_M \left(\nu_M \frac{\partial A_M}{\partial n_M}\right) dl + \\ &\quad \int_{\Omega_S} -[\delta A_S(\nu_S \nabla^2 A_S)] - [\delta A_S J_S]\,dS + \oint \delta A_S \left(\nu_S \frac{\partial A_S}{\partial n_S}\right) dl. \qquad (3.20)\end{aligned}$$

Restating the Lagrange multipliers functional, equation (3.16).

$$\Pi' = \Pi + \int_{\Gamma_\lambda} \lambda(A_M - A_S)\,dl$$

The first variation of the this functional is required to be zero so that

$$\begin{aligned}\delta\Pi' &= \delta(\Pi + \int_{\Gamma_\lambda} \lambda(A_M - A_S)\,dl) \\ &= \delta\Pi + \int_{\Gamma_\lambda} \delta\lambda(A_M - A_S)\,dl + \int_{\Gamma_\lambda} \delta A_M \lambda\,dl - \int_{\Gamma_\lambda} \delta A_S \lambda\,dl. \qquad (3.21)\end{aligned}$$

which can be expanded to give

$$\begin{aligned}\delta\Pi' &= \int_{\Omega_M} \delta A_M(-\nu_M \nabla^2 A_M - J_M)\,dS + \int_{\Omega_S} \delta A_S(-\nu_S \nabla^2 A_S - J_S)\,dS + \\ &\quad \oint_{\Gamma_\lambda} \delta A_M(\nu_M \frac{\partial A_M}{\partial n_M} + \lambda)\,dl + \oint_{\Gamma_\lambda} \delta A_S(\nu_S \frac{\partial A_S}{\partial n_S} - \lambda)\,dl + \\ &\quad \oint_{\Gamma_\lambda} \delta\lambda(A_M - A_S)\,dl. \qquad (3.22)\end{aligned}$$

$\delta\Pi'$ is required to be zero with respect to any variations δA_M, δA_S and $\delta\lambda$. The

first two surface integrals are those of the originally disconnected M and S meshes. The last line integral of $\delta\Pi'$ simply restates the constraint itself while the first and second line integral provide a physical meaning to the Lagrange multipliers. It can be seen that :

$$\lambda = -\left(\nu_M \frac{\partial \mathrm{A}_M}{\partial n_M}\right) \tag{3.23}$$

$$\lambda = +\left(\nu_S \frac{\partial \mathrm{A}_S}{\partial n_S}\right) \tag{3.24}$$

Thus the Lagrange multipliers can be interpreted as the tangential component of H at the interface Γ_λ.

3.6 Numerical Implementation

On the interface Γ_λ, the Lagrange multipliers can be approximated in a way similar to the vector potential using the idea of shape functions.

$$\lambda = \sum_{i=1}^{k} N_{L_i} \lambda_i \tag{3.25}$$

In the above there are k nodal values of λ and N_{L_i} is the i'th shape function for the multipliers. It is possible to create new line elements in 2D to implement the above equation. A more convenient scheme, however, is to use the surface discretization of either one of the two meshes to approximate λ. This is achieved by conceptually placing the multipliers at the interface nodes of the selected mesh. We will call this mesh the master mesh and the other one the slave mesh. Using this approach avoids the extra complexities arising from the creation of new surface elements. Each node of the master mesh which is on Γ_λ now has two variables attached; the vector potential and the Lagrange multiplier.

Equation(3.16) is again minimised, this time with respect to both A and λ, to yield a system of linear equations. Substituting the shape function approximations of A and λ into equation (3.16), we obtain

$$\Pi' = \Pi + \int_{\Gamma_\lambda} \sum N_L \lambda \left(\sum N_M A_M - \sum N_S A_S \right) \mathrm{dl}. \tag{3.26}$$

Differentiating with respect to typical variables A_{M_j}, A_{S_k} and λ_l results in the

following equations :

$$\frac{\partial \Pi'}{\partial A_{M_j}} = \frac{\partial \Pi}{\partial A_{M_j}} + \int_{\Gamma_\lambda} N_{M_j}(\sum N_L \lambda)\,\mathrm{dl} = 0 \tag{3.27}$$

$$\frac{\partial \Pi'}{\partial A_{S_k}} = \frac{\partial \Pi}{\partial A_{S_k}} + \int_{\Gamma_\lambda} N_{S_k}(\sum N_L \lambda)\,\mathrm{dl} = 0 \tag{3.28}$$

$$\frac{\partial \Pi'}{\partial \lambda_l} = \int_{\Gamma_\lambda} N_{L_l}(\sum N_M A_M - \sum N_S A_S)\,\mathrm{dl} = 0. \tag{3.29}$$

This can be written in matrix form as

$$\begin{bmatrix} \mathbf{K}_\Pi & \mathbf{K}_\lambda \\ \mathbf{K}_\lambda^T & 0 \end{bmatrix} \begin{Bmatrix} \mathbf{A}_\Pi \\ \lambda \end{Bmatrix} = \begin{Bmatrix} \mathbf{f}_\Pi \\ 0 \end{Bmatrix}, \tag{3.30}$$

where $\mathbf{K}_\Pi$ and $\mathbf{f}_\Pi$ is the stiffness matrix and force vector of equation (3.14) respectively and

$$\mathbf{K}^T_{\lambda\, ij} = \int_{\Gamma_\lambda} N_{L_i}(\sum N_M A_M - \sum N_S A_S)\,\mathrm{dl}.$$

The final stiffness matrix is still symmetric though now with zeros on the diagonals of the λ rows.

3.6.1 Numerical Integration

The line integrals are evaluated in a similar element by element manner on Γ_λ as would be done in a conventional Finite Element scheme although the details are more complex. The interface edge of each master element on Γ is considered in turn. Since the nodes on Γ_λ do not need to be matched, each master edge may

overlap with more than one slave edge at any time, thus making it impossible to perform the integration over it in one single step. Instead, the integration has to be carried out over the few overlap edge-segments which the master edge makes with the slave edges. This extra step is a direct result of the presence of the cross-interface shape function product term in the line integrals of equations (3.27) to (3.29).

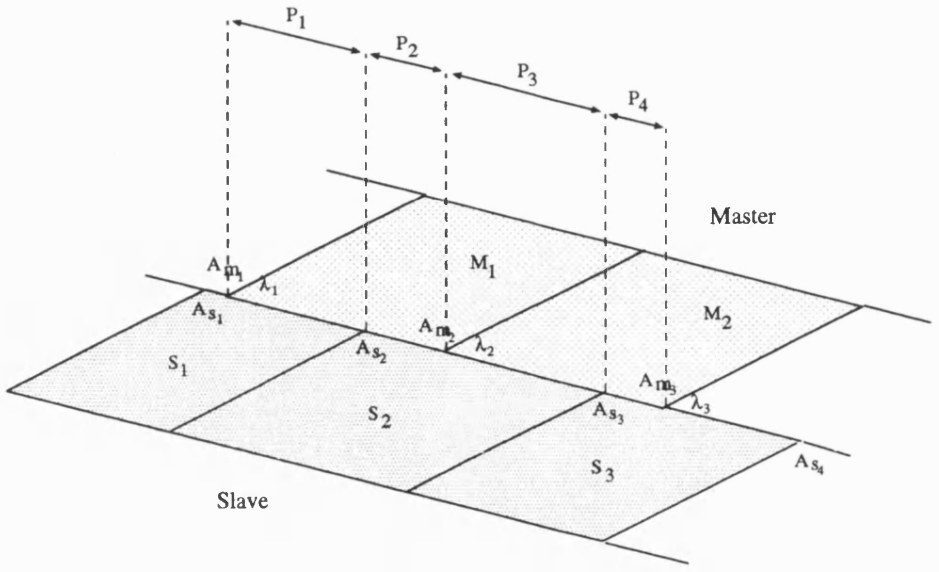

Figure 3.4: Integration over overlapping segments

Referring to Fig.(3.4) which illustrates a representative overlap pattern on the interface, the contributions of the integral over the interface edge of element M_1 to row λ_1 and λ_2 are

$$\int_{P_1} N_{L_1}(N_{M_1}A_{M_1} + N_{M_2}A_{M_2} - N_{S_1}A_{S_1} - N_{S_2}A_{S_2})\,\mathrm{dl} \quad +$$
$$\int_{P_2} N_{L_1}(N_{M_1}A_{M_1} + N_{M_2}A_{M_2} - N_{S_2}A_{S_2} - N_{S_3}A_{S_3})\,\mathrm{dl}$$

and

$$\int_{P_1} N_{L_2}(N_{M_1}A_{M_1} + N_{M_2}A_{M_2} - N_{S_1}A_{S_1} - N_{S_2}A_{S_2})\,\mathrm{dl} \quad +$$
$$\int_{P_2} N_{L_2}(N_{M_1}A_{M_1} + N_{M_2}A_{M_2} - N_{S_2}A_{S_2} - N_{S_3}A_{S_3})\,\mathrm{dl}$$

respectively. With λ defined at the nodal points of the master elements, the shape functions of the λ's , N_L, can conveniently be replaced by N_M. The local matrix of the above then becomes

$$\begin{bmatrix} & & & & & K_{M_1M_1} & K_{M_2M_1} \\ & & & & & K_{M_1M_2} & K_{M_2M_2} \\ & & & 0 & & K_{M_1S_1} & K_{M_2S_1} \\ & & & & & K_{M_1S_2} & K_{M_2S_2} \\ & & & & & K_{M_1S_3} & K_{M_2S_3} \\ K_{M_1M_1} & K_{M_1M_2} & K_{M_1S_1} & K_{M_1S_2} & K_{M_1S_3} & & \\ & & & & & 0 & \\ K_{M_2M_1} & K_{M_2M_2} & K_{M_2S_1} & K_{M_2S_2} & K_{M_2S_3} & & \end{bmatrix} \begin{bmatrix} A_{M_1} \\ A_{M_1} \\ A_{S_1} \\ A_{S_2} \\ A_{S_3} \\ \lambda_1 \\ \lambda_2 \end{bmatrix} \tag{3.31}$$

where

$$K_{M_1M_1} = \int_{P_1+P_2} N_{M_1} N_{M_1}\,\mathrm{dl} \qquad K_{M_2M_1} = \int_{P_1+P_2} N_{M_2} N_{M_1}\,\mathrm{dl}$$

$$K_{M_1M_2} = \int_{P_1+P_2} N_{M_1} N_{M_2}\,\mathrm{dl} \qquad K_{M_2M_2} = \int_{P_1+P_2} N_{M_2} N_{M_1}\,\mathrm{dl}$$

$$K_{M_1S_1} = -\int_{P_1} N_{M_1} N_{S_1}\,\mathrm{dl} \qquad K_{M_2S_1} = -\int_{P_1} N_{M_2} N_{S_1}\,\mathrm{dl}$$

$$K_{M_1S_2} = -\int_{P_1+P_2} N_{M_1} N_{S_2}\,\mathrm{dl} \qquad K_{M_2S_2} = -\int_{P_1+P_2} N_{M_2} N_{S_2}\,\mathrm{dl}$$

$$K_{M_1S_3} = -\int_{P_2} N_{M_1} N_{S_3}\,\mathrm{dl} \qquad K_{M_2S_3} = -\int_{P_2} N_{M_2} N_{S_3}\,\mathrm{dl}$$

Integration over an overlapping segment such as P_1 in Fig.(3.4) can be done numerically using Gaussian Quadrature. The integration limits, however, will not be the standard $(-1, 1)$ anymore. Nevertheless, standard quadrature sampling points and weights can still be used, provided the limits are first transformed to the standard one by [22]

$$z = \frac{(2x - (a+b))}{(b-a)}. \tag{3.32}$$

Thus, an integral with limits $a \leq x \leq b$ is transformed as

$$\int_a^b f(x)\,\mathrm{d}x = \left(\frac{b-a}{2}\right) \int_{-1}^{1} f\left(\frac{z(b-a)+(b+a)}{2}\right) \mathrm{d}z. \tag{3.33}$$

With Gaussian Quadrature, this is equivalent to transforming the sampling point with equation (3.32) and the weighting factor modified by the constant $(b-a)/2$. The local matrix in equation (3.31) can easily be incorporated into the global stiffness matrix following standard Finite Element procedures.

Periodic conditions specified can be handled without much difficulties. On the other hand, the case in which the two meshes do not fully overlap will require extra computational steps. This is illustrated in Fig.(3.5). In this particular case, rotor edges which are found 'outside' the limits of the stator mesh have to be conceptually rotated clockwise by 180 degree to the other side of the mesh to look for overlapping edges. The shape functions of the nodes and the Lagrange multipliers also have to be transformed to the correct frame of reference before the line integral is evaluated. Fig.(3.6) on next page outlines the implementation of the method described in this section.

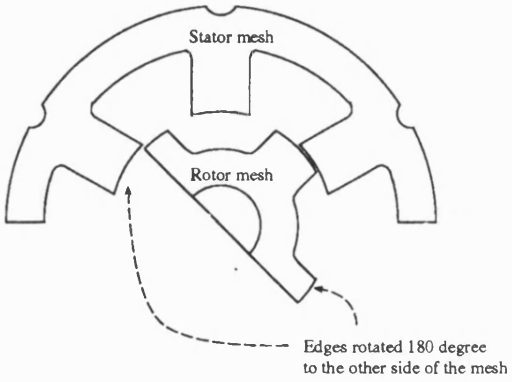

Figure 3.5: Handling of edges found outside the overlap

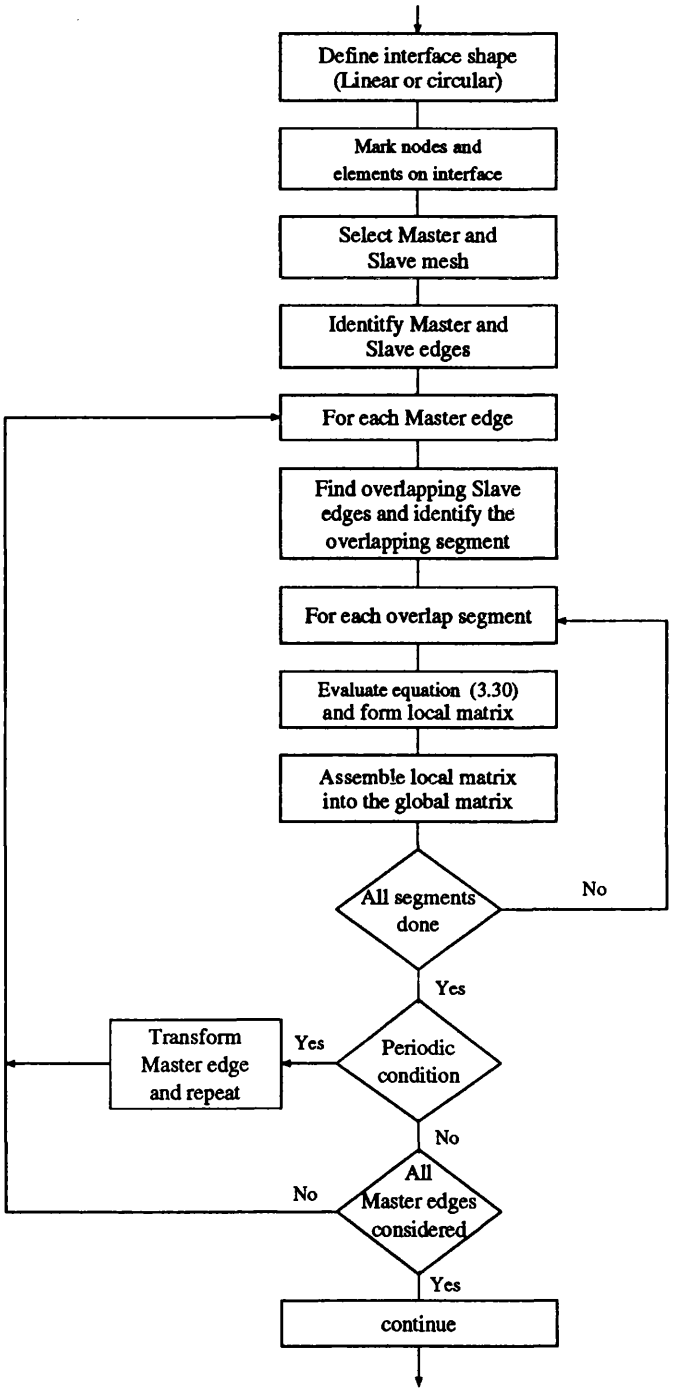

Figure 3.6: Flow Chart outlining 2D implementation of Lagrange Multipliers

3.7 Numerical Tests

The Lagrange multipliers method described in the previous sections has been implemented. This section examines the various properties of the method when applied to a typical Finite Element problem. The answers obtained were also compared with that from a standard Finite Element mesh. The test configuration used consists of an iron C-core placed above an iron plate as shown in Fig.(3.7). The material properties and dimensions of the individual parts are also indicated on the figure. The materials were assumed linear and the problem was modelled using the 2D Cartesian magnetic vector potential formulation.

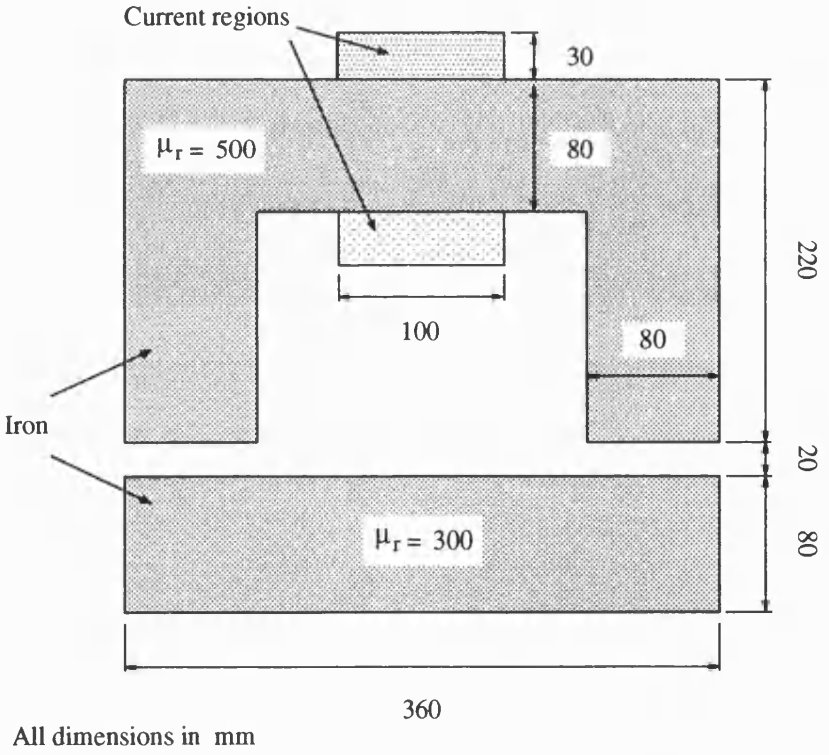

Figure 3.7: Dimensions of the test problem

To gain initial confidence in the method, the test problem was first solved using standard Finite Element techniques. The mesh used is shown in Fig.(3.8). Only half of the problem had to be modelled due to the symmetry. The same mesh was then split up along the middle of the air gap, forming two separate meshes. These were coupled together and solved using the Lagrange multipliers formulation. The answers obtained from the two runs were compared. The normal finite element mesh has 2268 unknowns. This number was increased to 2340 with the Lagrange multipliers formulation. Half of the increase was due to the extra normal nodes on the interface, the other half was the Lagrange multipliers. The difference in the time taken to solve them was negligible on an HP 720 workstation. The resulting contour plots of the vector potential are shown in Fig.(3.9) and Fig.(3.10).

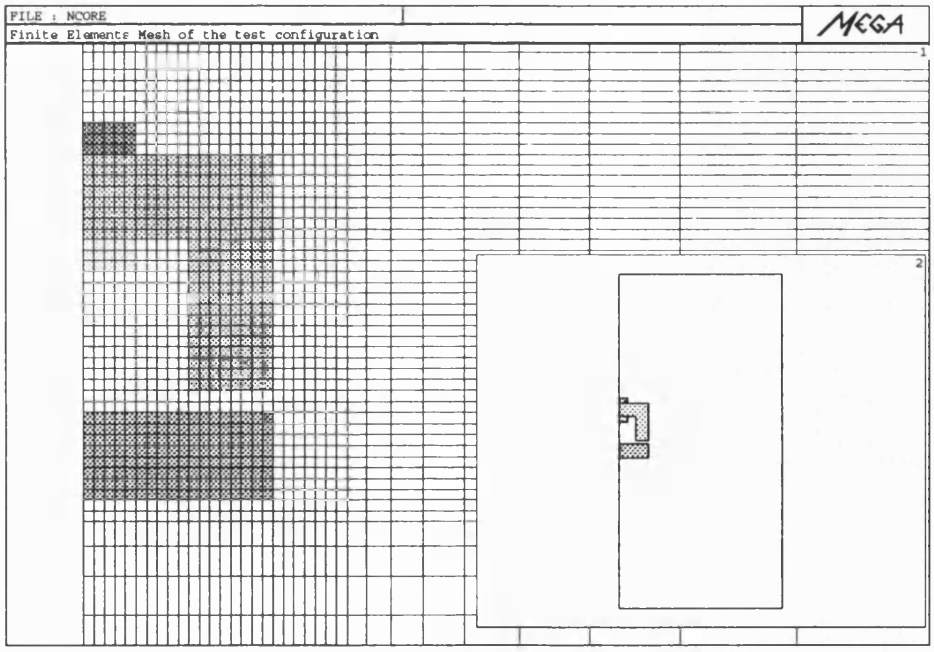

Figure 3.8: Finite Elements mesh of the test problem

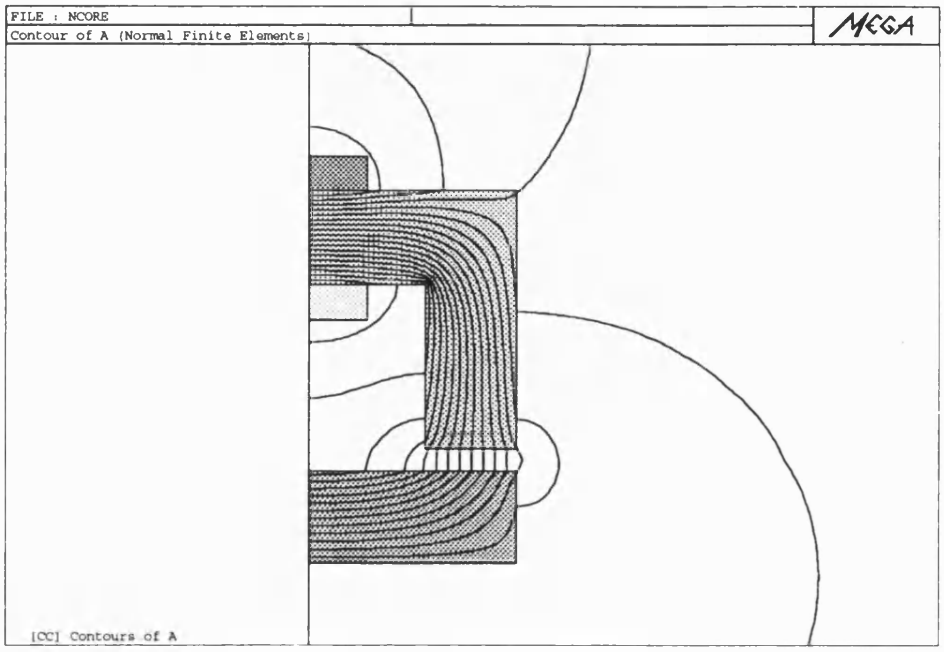

Figure 3.9: Contours of A using normal Finite Elements

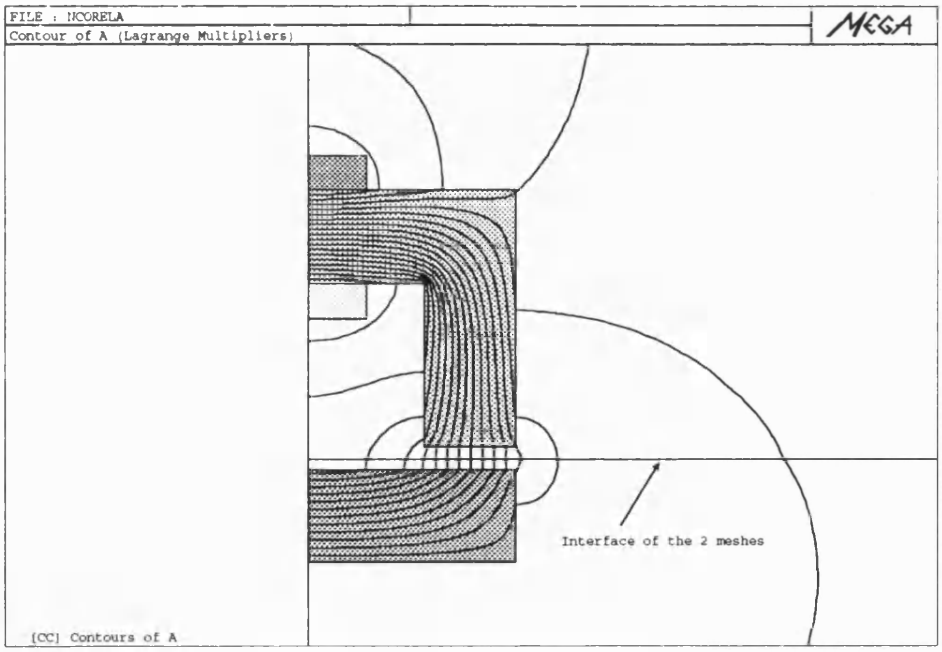

Figure 3.10: Contours of A using Lagrange Multipliers Method

The same contour levels were used in both plots and there are no visible discrepancies observed between the two plots. To examine the effect, if any, the Lagrange multipliers has on the answers both locally and globally, the stored energy and the force on the lower iron-bar were calculated and compared. This is shown in Table (3.1) on page 59. The Y-component of the **B** field in the air gap is also compared in Fig.(3.11). Good agreement between the answers can be observed from these results.

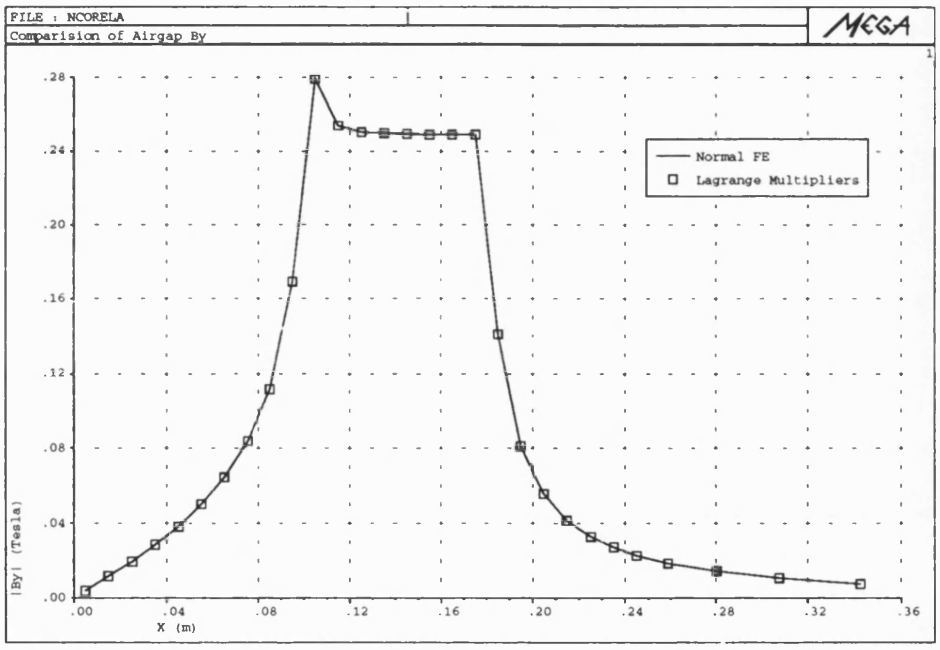

Figure 3.11: Comparison of $\mathbf{B}_y$ in the air gap

A more interesting comparison, however, is to compare the actual potential values at the centre of the air gap, where the Lagrange interface is situated. This is shown in Fig.(3.12) and again shows a good degree of agreement between the two methods. In fact, discrepancy between the answers only began to occur at the 6th decimal

place.

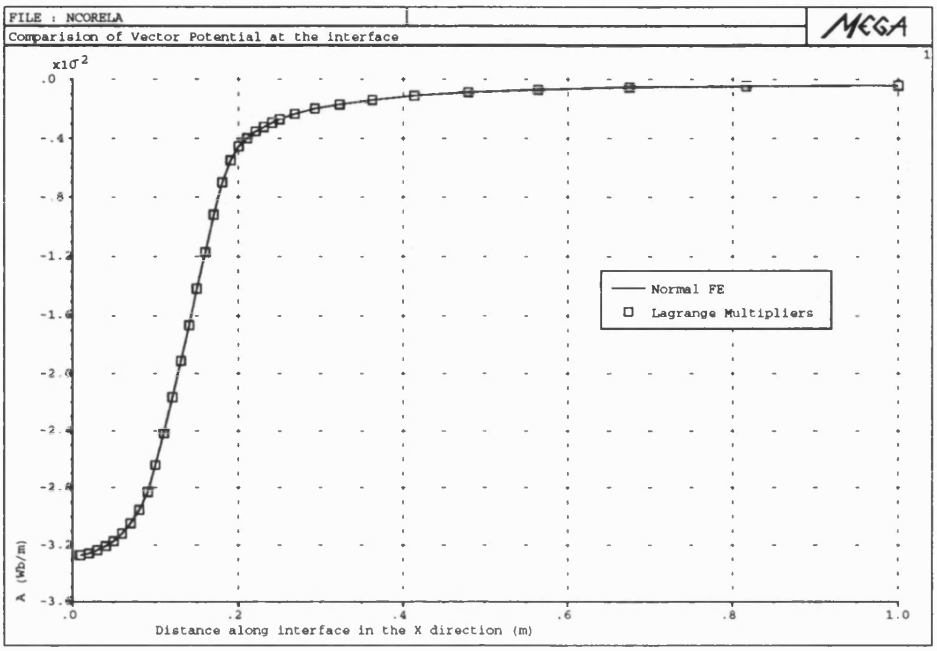

Figure 3.12: Comparison of **A** in the air gap

3.7.1 Non-coincident Nodes

As mentioned, one of the advantages of using the Lagrange multipliers method is that it permits the presence of non-coincident nodes on the interface. Further tests were therefore carried out to examine the ability of the method to handle non-coincident interface nodes. To this end, the lower mesh in Fig.(3.8) that contains the iron bar was modified to introduce such nodes into the system. The modified mesh is shown in Fig.(3.13).

The model was solved and Fig.(3.14) shows a contour plot of the answer. It was

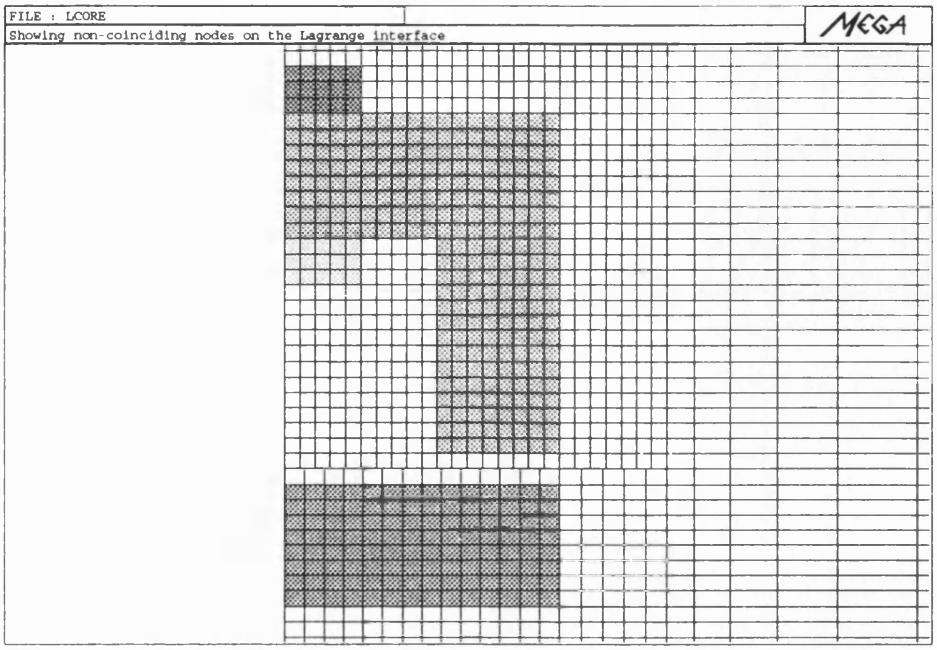

Figure 3.13: Modified mesh with non-coincident nodes

encouraging to see that the contours are still remarkably continuous across the interface. Nonetheless, the fact that nodes were appearing in the middle of an adjacent edge made it more important to examine how the potentials of the 2 meshes are matched at the interface here compared with the previous 'matched' case. For this, the graph of the nodal potentials of the 2 meshes on the interface was obtained and is shown in Fig.(3.15). A good match between the potential values can be observed, reinforcing the previous findings.

3.7.2 Unbalanced Node Distribution

The number of nodes of the two meshes on the interface and their distribution along it are so far closely matched. This represents a somewhat idealised situation which is

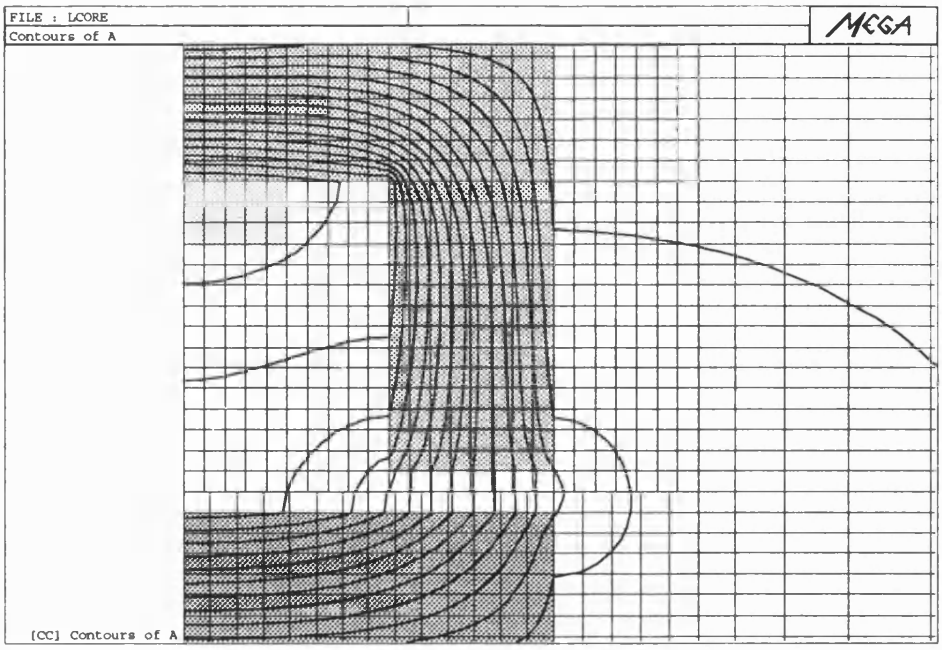

Figure 3.14: Contour plot of **A**

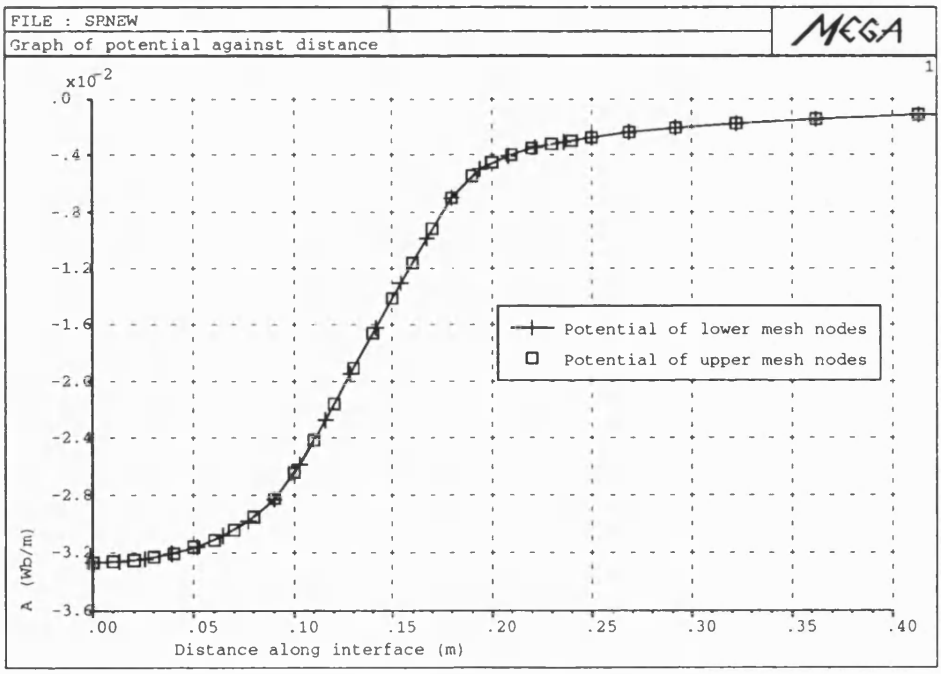

Figure 3.15: Graphs showing how interface potentials are matched

often difficult to achieve in practice. Usually, these would vary from place to place along the interface in a more acute manner. It is, therefore, of practical interest to examine how the method performs in these conditions. The problem mesh of Fig.(3.13) was modified with its top mesh refined as shown in Fig.(3.16).

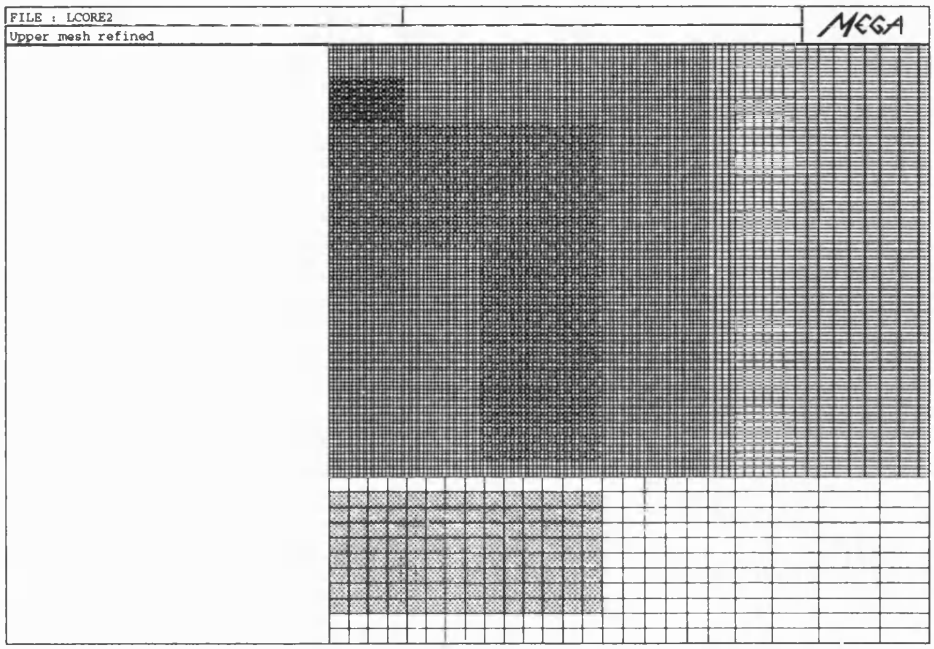

Figure 3.16: Mesh with upper part refined

There are on average about 5 nodes of the the top mesh adjoining each edge of the lower mesh. Also of interest is the question of whether it is better to define the Lagrange multipliers on the finer mesh or not. Both possibilities were tried. The resulting contour plot of the answer with the Lagrange multipliers defined on the finer top mesh of Fig.(3.13) is shown in Fig.(3.17). The continuity of the contour across the interface is clearly displayed. With the Lagrange multipliers defined at the coarser bottom mesh, a similar contour plot was also obtained.

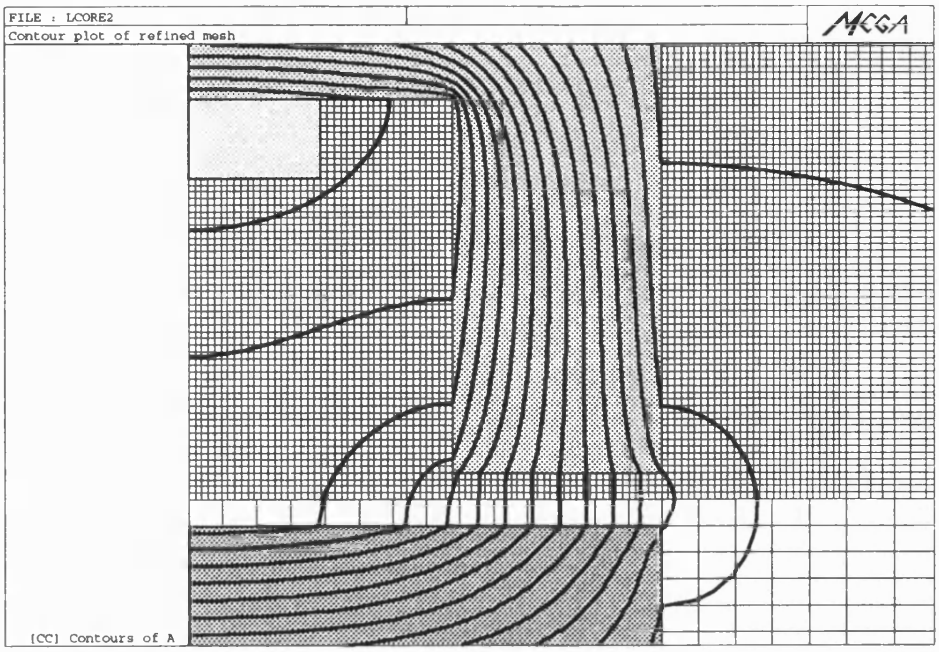

Figure 3.17: Contour plot of the refined mesh

The graphs of the potential along the interface in both cases are shown in Fig.(3.18) and Fig.(3.19). As can be seen, the potentials are well coupled together in both cases. Closer examination of the graphs revealed evidence which indicates that defining the Lagrange multipliers at the finer mesh enforces the constraints more vigorously at local level than the other case. This though may seem to suggest that with a denser Lagrange function, a better answer could be achieved. Such a conclusion, however, does not necessary follow as we must bear in mind that the coarser mesh is the ultimate barrier to a more accurate answer.

It must also be pointed out that despite all these doubts about the Lagrange multipliers not being able to pin down the potentials together absolutely at the local level, the constraint was found to be satisfied extremely well in an average sense in both cases. This is in fact what the constraint in equation (3.16) has originally

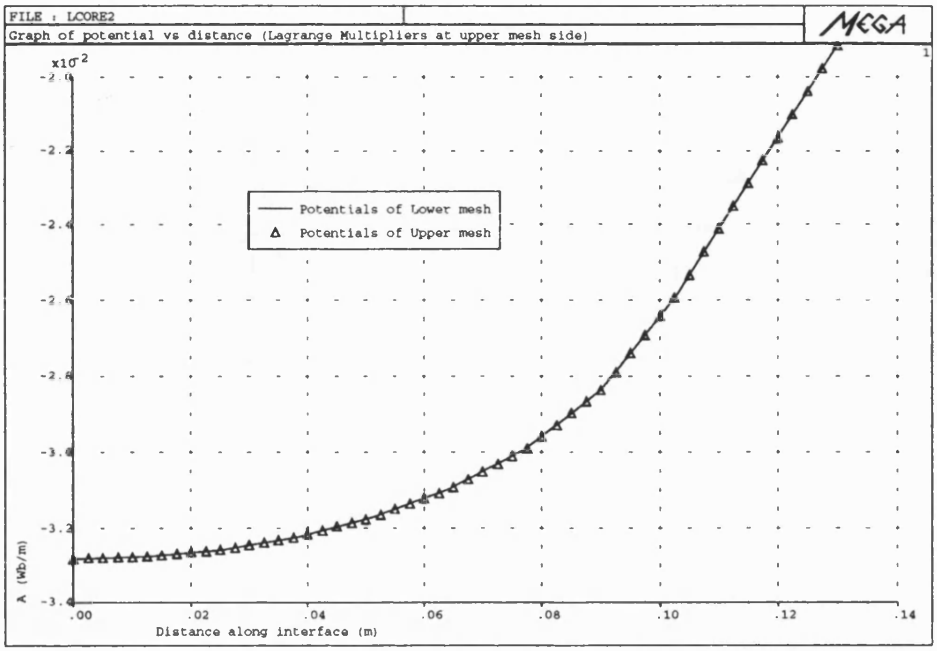

Figure 3.18: Showing Potential along interface with Lagrange Multipliers defined at the finer top mesh

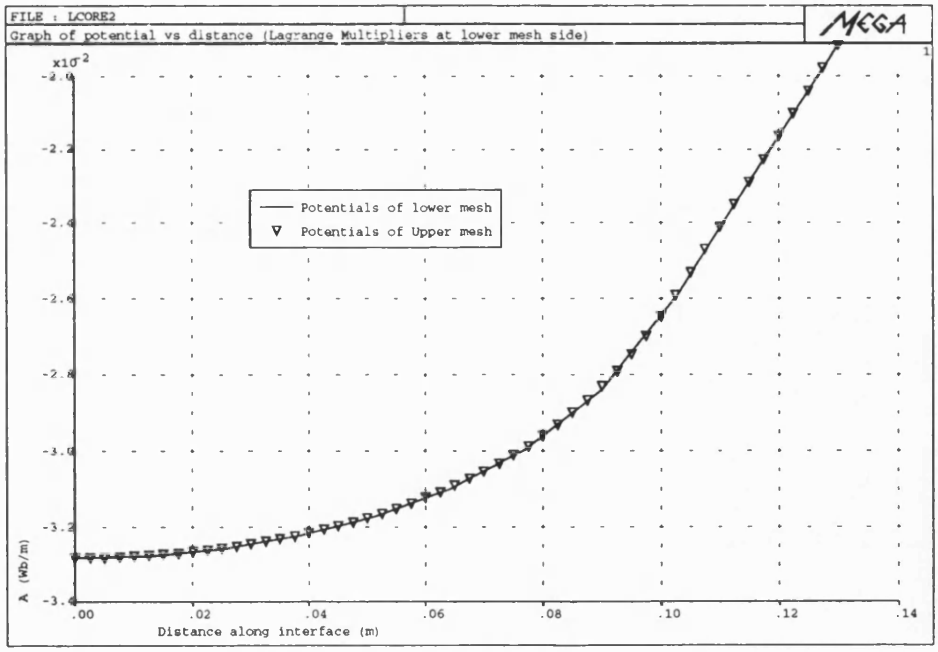

Figure 3.19: Showing Potential along interface with Lagrange Multipliers defined at the coarser bottom mesh

asked for. It only demands the potential to be continuous in a weighted average sense on the interface. In this respect, it can be seen that the Lagrange multipliers has achieved a good degree of success in both cases.

Table (3.1) summaries the results of the stored energy and force calculations on the various models. The last row of results was obtained from a very fine mesh of the problem solved using a normal Finite Element mesh and is intended to serve as a reference for the calculations.

#	Model	Number of unknowns	Stored energy per metre (J)	Force on bar per metre (N)
1	Normal mesh Fig.(3.8)	2234	100.664	2311.5
2	(1) with Lagrange	2340	100.671	2311.8
3	(2) with upper mesh refined Lagrange at upper mesh Fig.(3.13)	24066	101.298	2328.5
4	(3) with Lagrange at bottom mesh	23955	101.325	2332.2
5	Very fine normal mesh	74813	101.597	2344.9

Table 3.1: Table of 2D results

3.8 Experimental Verification

To verify the method experimentally, the test rig of Fig.(3.27) was used. It was originally designed for verification of non-linear modelling of transient 3D eddy currents formulations but was found suitable for our test purposes since it allows the method to be easily tested at a broad range of saturation. The rig is physically similar to a two pole switched reluctance motor but with both the rotor and stator built with solid steel. The rotor is mounted on a non–magnetic stainless steel shaft with provision for easy adjustment to different positions. The stator is fitted with two 350 turns coils and is securely fastened to an outer cage which can swing relative to the rotor.

The experiment involved the measurement of the steady state torque produced at different rotor positions. This was done by attaching the stator cage to a Kistler load cell which measures transient torques. The rotor was first adjusted to the desired angle and then securely locked. A constant magnitude step current of 7.515A was applied to the two coils. The transient torque waveforms were recorded and then the steady state results were deduced. This was repeated at several other rotor positions to simulate different saturation conditions. The rig was demagnetized between each measurement.

Experience has indicated that the accuracy of a non-linear FE analysis depends critically on the accuracy of the BH curves used. To ensure that the BH characteristics used in the model accurately represent that of the test rig, the steel was annealed after machining to homogenise the magnetic characteristics. The initial magnetisation curve of a cylindrical sample was measured using a *Magnet Physic*

REMAGRAPH BH tester. This curve is shown in Fig.(3.20). The dimensions of the magnetic parts of the rig and the coils are shown in Fig.(3.21) and Fig.(3.22).

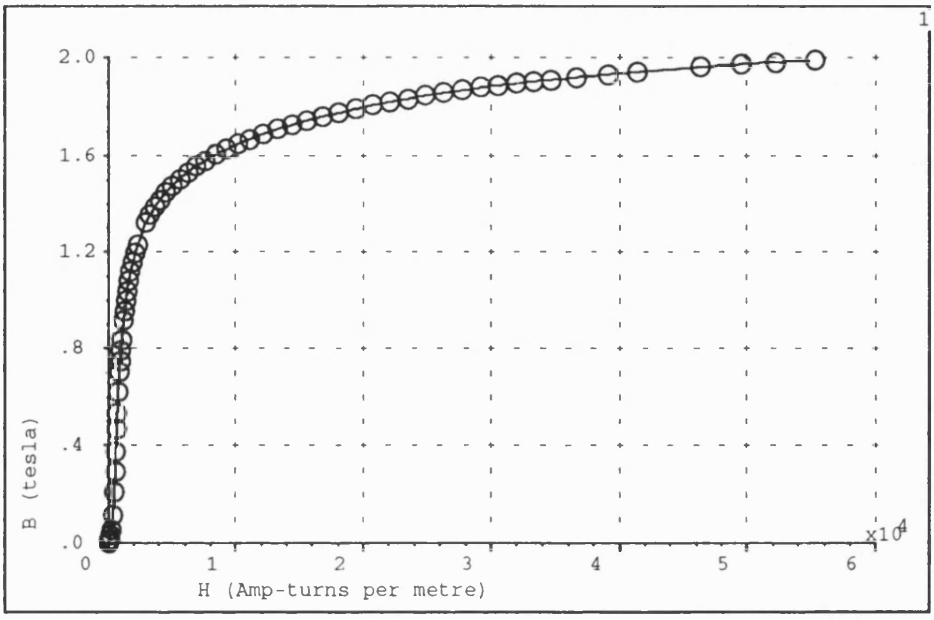

Figure 3.20: BH characteristic used

3.8.1 2D Finite Elements Model

The rotor and stator were meshed up as two separate meshes, touching each other at the centre of the air gap. Fig.(3.23) shows a general view of the 2D mesh used, the inset illustrates how the meshes do not match at the interface. The bottom half of the two meshes are symmetric with the top half. As can be seen, the use of the Lagrange multipliers method allows meshes with an unequal degree of mesh

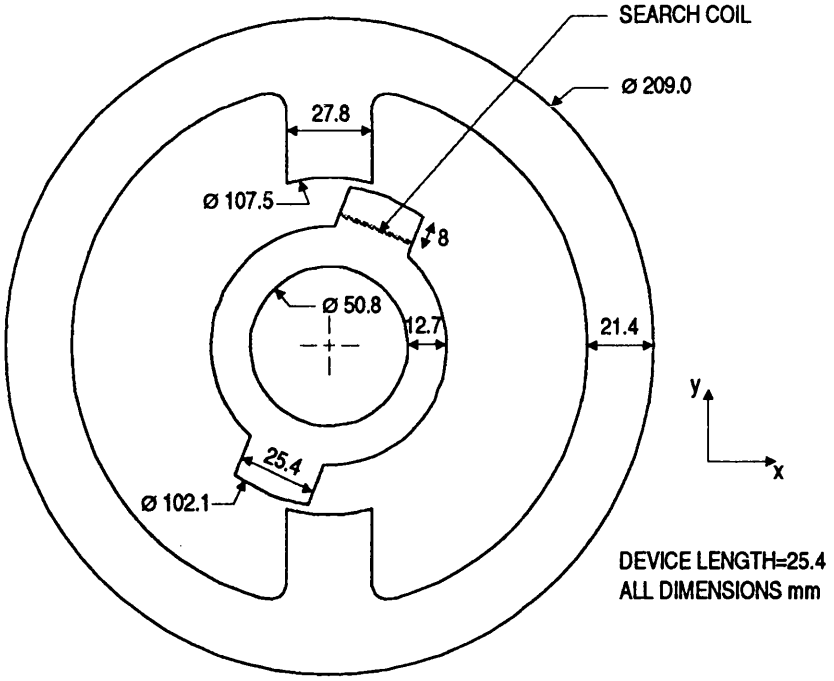

Figure 3.21: Dimensions of rotor and stator

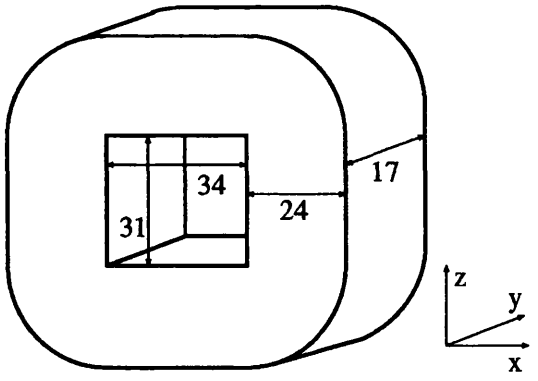

Figure 3.22: Dimensions of the stator coil

refinement to be coupled together easily. This is particularly useful in such cases where features of two adjacent parts are so different that it is difficult to represent the intermediate air with a sensible mesh.

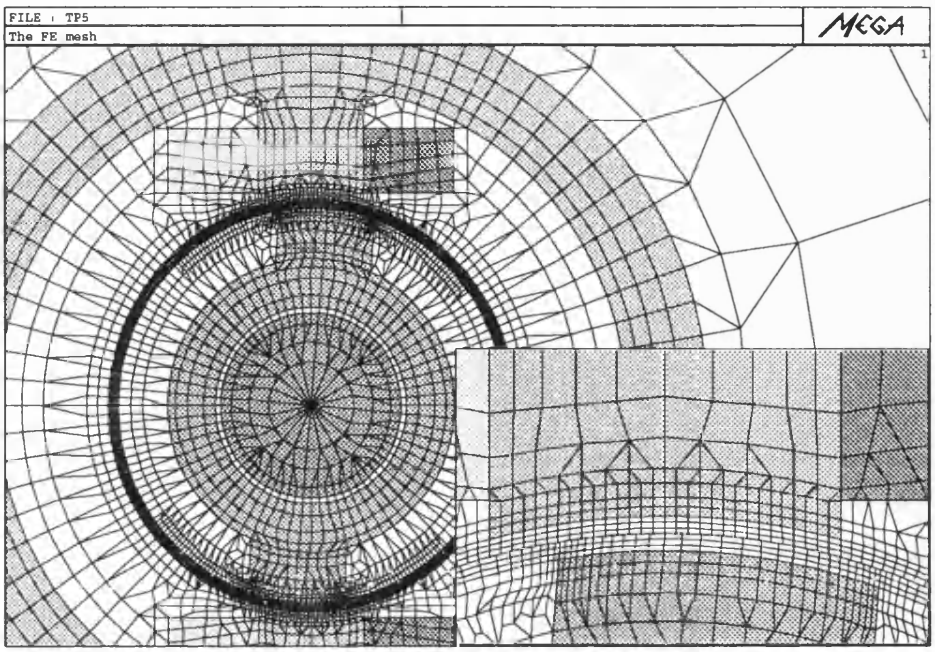

Figure 3.23: A general view of the 2D mesh

The mesh of Fig.(3.23) represents the rotor 5° away from the position where the two poles are completely aligned. The 2D model was set up to have a series of rotor positions solved successively starting from the aligned position. All together, 26 positions were solved and it took about 23 minutes on an HP720 workstation.

Fig.(3.24) compares the 2D calculated torques and the experimental measurements. The results compare reasonably well considering the amount of approximation that 2D Finite Elements has intrinsically made on the model. The 2D formulation made the assumptions that the model is infinitely long in the third, Z, direction and that

fields vary only in the XY direction. Though this is a reasonable assumption for devices which are relatively long in length, the rig, unfortunately, does not fit too well into this category. Its length is short compared with the radius. There are strong 3D effects at the end of the device: flux leaking in the axial direction, extra MMF being injected into the stator pole by the end turns and so on, all interact in a complex manner. It is no surprise that omitting these effects will affect the solution. As will be seen later, the correspondence between measured and calculated torques improves with the use of 3D FE. Fig.(3.25) and Fig.(3.26) shows the contours of A and the saturation at four different rotor positions. The trend of saturation is very similar to that found in a switched reluctance motor; severe local saturation occurred near the tip of the pole when they began to overlap while everywhere else remained relatively unsaturated. As the overlap increased, this gave way to global saturation.

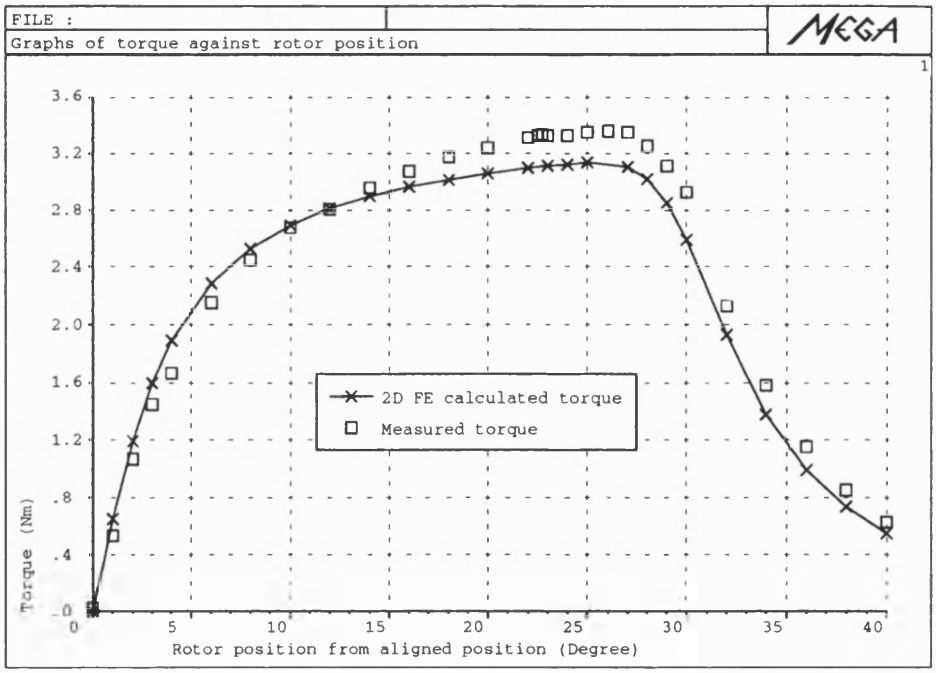

Figure 3.24: Graph comparing measured and 2D FE calculated torque

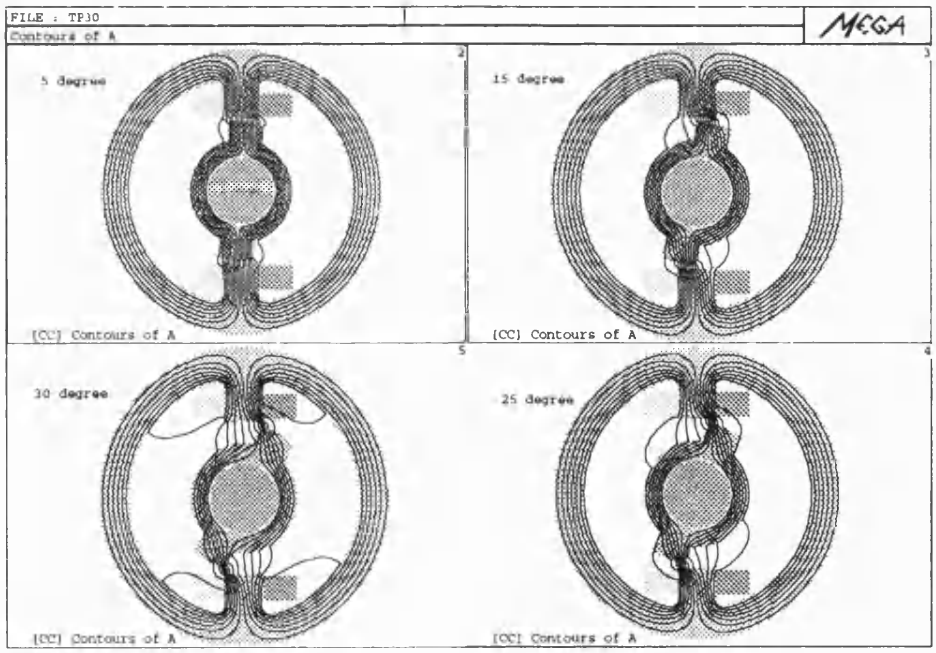

Figure 3.25: Showing flux patterns at different rotor positions

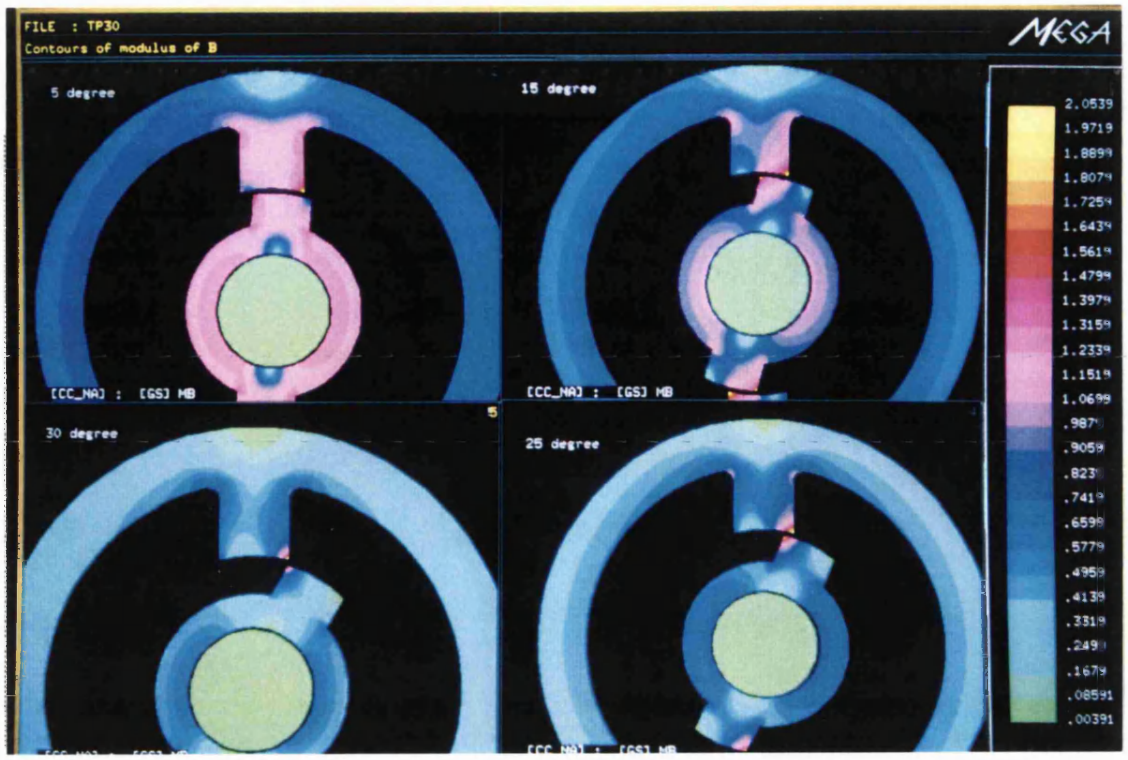

Figure 3.26: Showing saturation patterns at different rotor positions

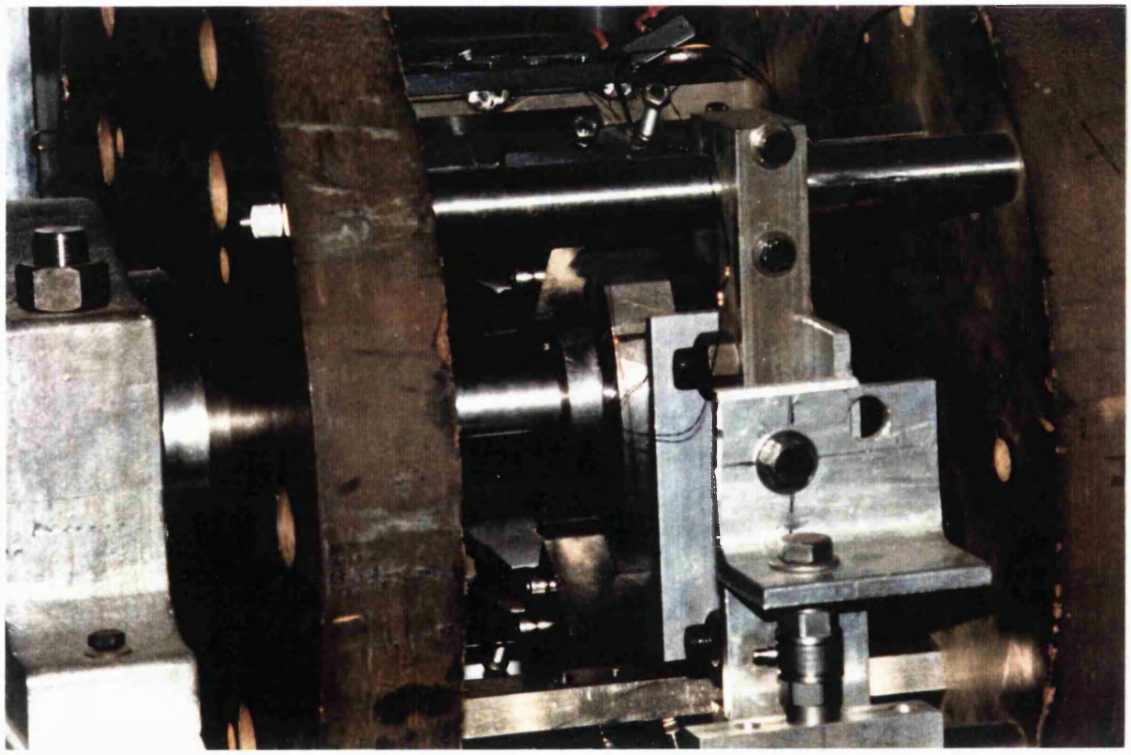

Figure 3.27: The test rig

3.9 Conclusions

This chapter has introduced the use of the Lagrange multipliers method in 2D Finite Elements for coupling disconnected meshes together. Extra equations constraining the continuity of potential across mesh interfaces were introduced into the original system by Lagrange multipliers, resulting in a new modified functional. Solution to the constrained problem was obtained by finding the stationary point of this modified functional.

Numerical implementation of the method has been described. Although extra steps have to be taken to handle segmented integration paths as a result of adjacent meshes not totally matched at their interface, the method in general is readily incorporated into existing FE packages.

Investigations into the various operational aspects of the method have also been carried out. Results have shown that solutions produced by the method are comparable to that obtained from a similar mesh using normal Finite Element techniques. A valuable feature of the Lagrange multipliers method is its ability to couple meshes with different numbers of nodes together. A node ratio of 1:5 happening locally between two adjoining meshes does not seem to pose any serious difficulties. Nevertheless, it must be pointed out again that the accuracy of the solution in such an unbalanced case will most likely be limited by the coarser member of the meshes. Similarly, using more Lagrange multipliers than it is needed does not necessarily lead to improvement on the accuracy of the solution.

Experiments have been performed to verify the method. These involved the measurement of the rotor torque of a switched reluctance motor like test rig under

different levels of saturation. Results were satisfactory considering the type of assumptions made by the 2D formulation.

Chapter 4

Alternative Implementations of the Lagrange Multipliers Method

4.1 Introduction

In the previous chapter, a way of implementing the Lagrange multipliers method in Finite Elements has been described. The various aspects of that implementation have also been investigated and have proved favourable. The implementation of the method followed a path which is both natural to the standard Finite Element technique and compatible with the form of the constraint equation introduced. This involved approximating the Lagrange multipliers function with existing mesh discretizations, hence nodal shape functions, and integrating the product of the Lagrange multipliers and the vector potential along the interface.

This, as expected, is just one possible way of implementing the method. Other possibilities exist. To be able to use this approach with confidence in the long term, it is essential that its performance be studied and compared with that of the other approaches.

This forms the objective of this chapter. In particular, the following three alternative schemes will be considered. These will be referred to as :

1. Point Collocation Lagrange method,

2. Re-substituted Lagrange method and

3. Penalty method.

The Point Collocation Lagrange method uses the point collocation idea (Appendix C) to approximate the Lagrange multiplier function. This makes the implementation of the method easier to carry out and the method was in fact the first one implemented. The Re-substituted Lagrange method substitutes the Lagrange multipliers with its physical interpretation as described in Section 3.5 and is attractive because it does not increase the number of unknown in the problem. The Penalty method is a popular method used to impose constraints onto the original problem and has been used successfully in Finite Elements in other contexts [23]. Similar to the Re-substituted Lagrange method, the Penalty method does not introduction extra unknowns into the system. A hybrid of the Lagrange multipliers method and the Penalty method, the Augmented Lagrange multipliers method will also be briefly discussed.

4.2 Point Collocation Lagrange Method

In the previous chapter, the Lagrange multipliers function in the modified functional

$$\Pi' = \Pi + \int_{\Gamma_\lambda} \lambda(\mathrm{A}_M - \mathrm{A}_S)\,\mathrm{dl} \tag{4.1}$$

was approximated following the usual Finite Element approach. Hence, we have

$$\lambda = \sum_{i=1}^{k} N_{L_i}\lambda_i. \tag{4.2}$$

The shape function was chosen to be the same as that of the nodal potential of one of the two meshes concerned. In so doing, the line integral of equation (3.16) has to be evaluated and special arrangements have be made to handle partially overlapped edges. Although this approach has been demonstrated to produce very good results, it is nevertheless constructive to investigate a similar implementation of the method using the point collocation idea. The most attractive feature of this latter approach is undoubtedly the ease of its implementation.

In this point collation scheme, the shape function N_L above is replaced by the Delta Dirac function. That is,

$$N_{L_i} = \delta_i = \delta(x - x_i).$$

Equation(4.1) is now written as

$$\Pi' = \Pi + \sum \delta_i\lambda_i(\mathrm{A}_M - \mathrm{A}_S).$$

Using the properties of the Delta Dirac function and differentiating with respect to λ_i, we have

$$\frac{\partial \Pi'}{\partial \lambda_i} = [\mathrm{N}_M \mathrm{A}_M]_i - [\mathrm{N}_S \mathrm{A}_S]_i \,, \tag{4.3}$$

in which $[]_i$ means evaluate the contents of the brackets at point i.

The form of $\partial \Pi'/\partial \mathrm{A}_M$ and $\partial \Pi'/\partial \mathrm{A}_S$ are modified in a similar fashion. Thus we now require that the constraints be satisfied at 'N' discrete collocation points. Only the value of the relationship at these points are needed to be evaluated. This results in a significant simplification on the algorithm required.

4.2.1 Selection of Collocation Points

The implementation of the method is very similar to that of the integration method. Instead of integrating along the interface, a series of points where the equations are evaluated is now selected. The simplest choice is perhaps to sample the constraint at the nodal points of one of the two meshes on the interface. This choice of sampling point is possible as we are dealing with the actual unknown function, the vector potential, which is continuous across elements.

For problems with nodes evenly spaced along the interface such as the one shown in Fig.(3.8), it was observed that the Point Collocation method produced comparable results to the integration method. A more interesting test is, as before, to apply the method to a problem with widely varying node distribution along the interface. The mesh shown in Fig.(3.13) was used for this purpose. The resulting contour of **A** with the sampling points chosen to be at the interface nodes of the lower (coarser) mesh is shown in Fig.(4.1). Distinct discontinuities in the contours can easily be seen.

The corresponding contour plot obtained using the integration method is shown in Fig.(4.2). Fig.(4.3) shows how the potential at the interface are tied together by both methods. It confirms the better coupling power of the integration method.

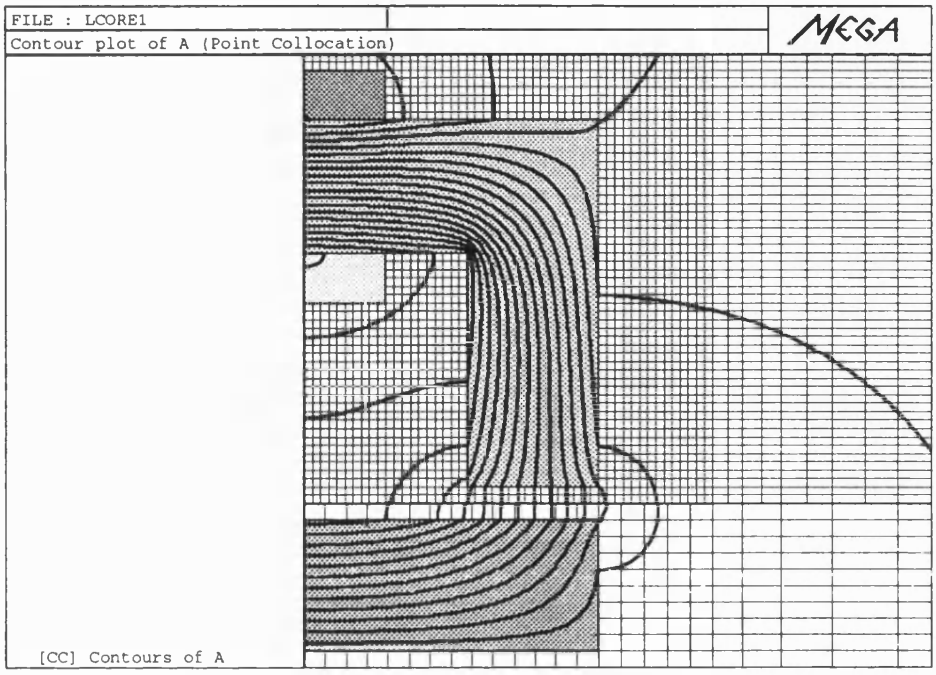

Figure 4.1: Contour plot of **A** with Point Collocation

This poor coupling power of the Point Collocation method is directly due to the fact that each Lagrange multiplier only links the potential of the nodes at which it is located to that of the two end nodes of the edge which it is touching. Fig.(4.4) depicts this situation. Potential at M_1 is only linked to that at S_1 and S_2 in the figure. Similarly, M_2 is linked to S_4 and S_5, leaving S_3 somewhat free floating. This lack of constraint on S_3 causes it to drop out of alignment, thus resulting in a graph similar to Fig.(4.3). The accuracy of the answer is bound to suffer if more nodes like S_3 exist.

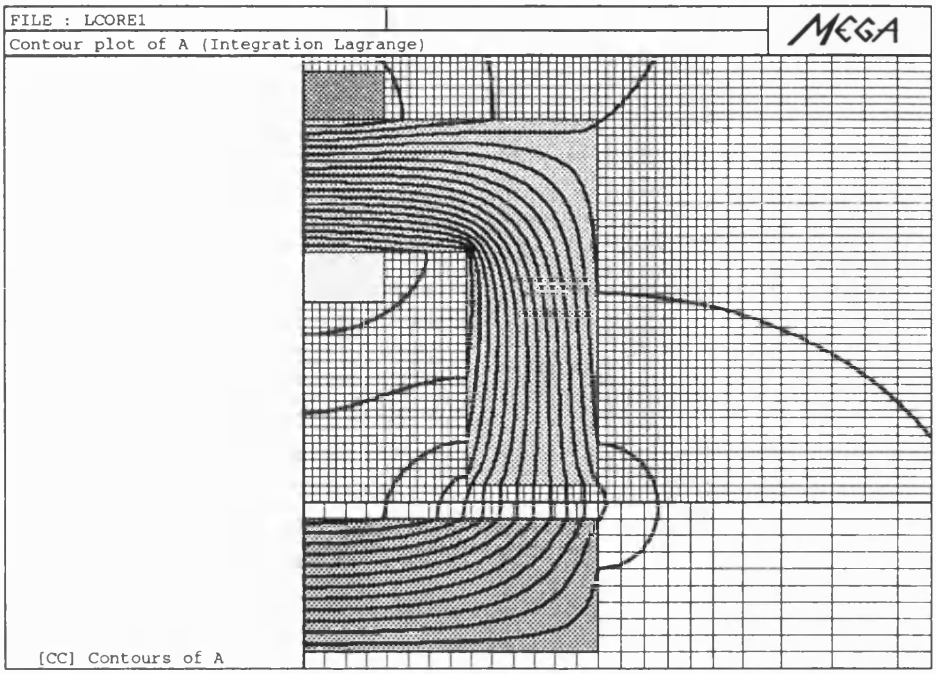

Figure 4.2: Contour plot of **A** with integration Lagrange

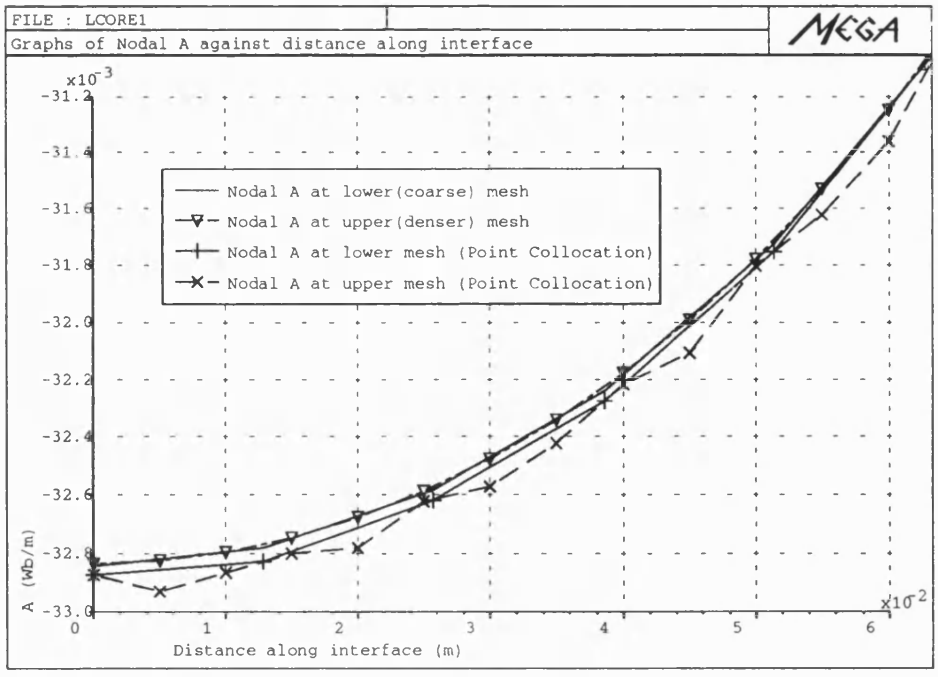

Figure 4.3: Graph showing how potential are coupled at the interface

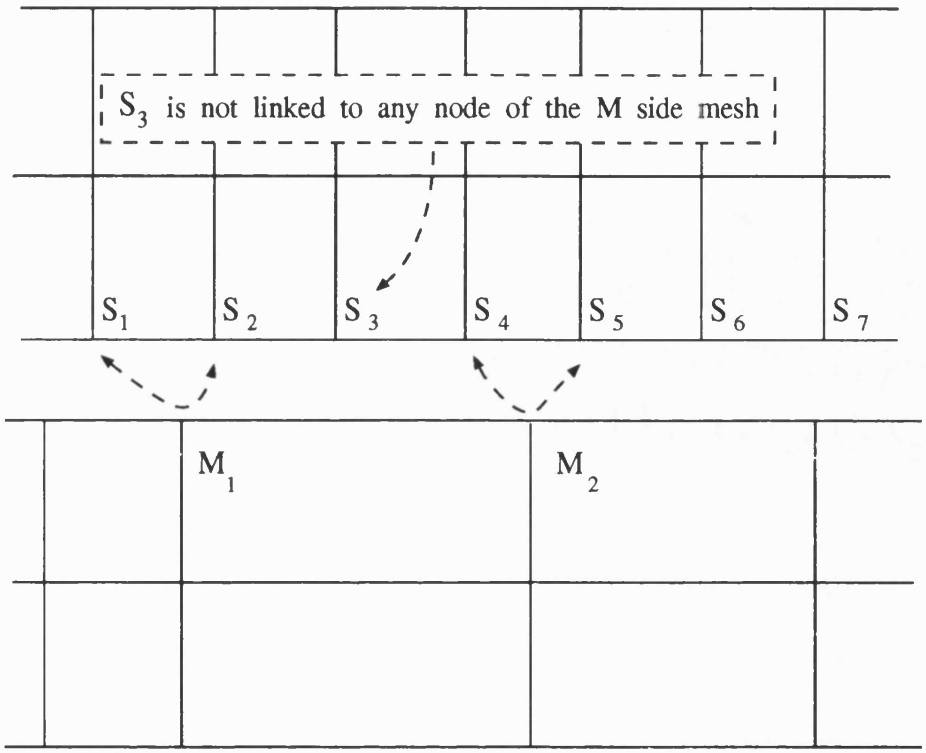

Figure 4.4: Linking of potential in Point Collocation method

In contrast, each Lagrange multiplier in the integration method provides linkage support to a greater number of interface nodes. Taking Fig.(4.4) as an example again, potentials at M_2 would be linked to S_1 through S_7. S_3 is not free floating anymore in this case. As a result, the constraints are satisfied more successfully in a global sense.

It was also observed that the potentials at the region directly underneath the core leg are much better tied together than elsewhere along the interface. This is also true in the Point Collocation case. The core leg and the iron bar both have a high relative permeability. Flux in this region, to a large extent, is running normal to the interface. Normal flux is precisely the natural boundary condition in the Vector Potential formulation. Potentials in this region, therefore, do not require great effort to be tied together.

This suggests that the Point Collocation method will have difficulties in cases where the flux is tangential to the interface. This situation can easily be simulated by simply reducing the relative permeability of the iron bar. Fig.(4.5) shows the vector of $\mathbf{B}$ with μ_r of the bar reduced to 1×10^{-3} using Point Collocation Lagrange. The Lagrange multipliers are located at the bottom coarse mesh. The vectors in regions further away from the core leg can be seen to oscillate up and down. The corresponding vector plot using the integration method is shown in Fig.(4.6). The vectors of $\mathbf{B}$ can be seen to be following a consistent path.

Fig.(4.7) compares the nodal potential on the interface returned by the two methods. As predicated, the interface potentials of the upper mesh in the Point Collocation case oscillate widely. Notice also that the potentials in the region underneath the core leg are quite well coupled in both cases. The disadvantage of using the Point

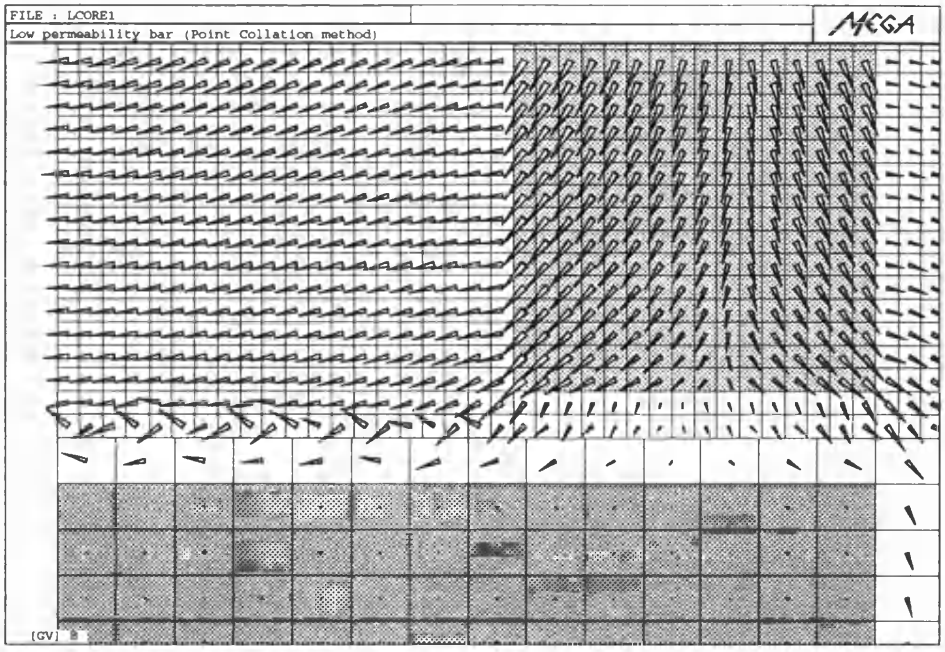

Figure 4.5: Vector of **B** with Point Collocation method

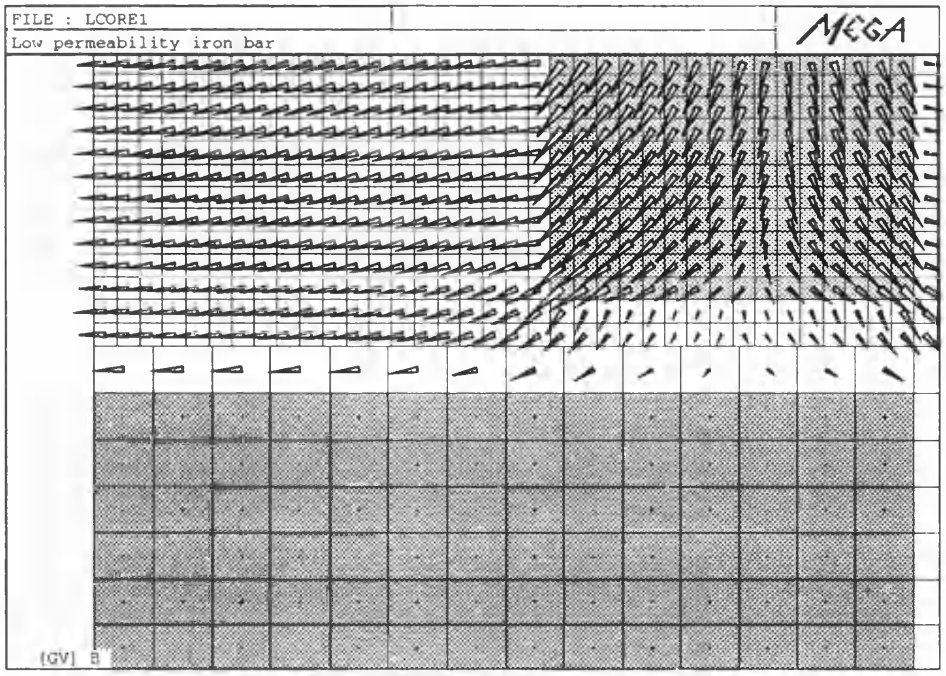

Figure 4.6: Vector of **B** with integration Lagrange

Collocation method is clearly highlighted by these results.

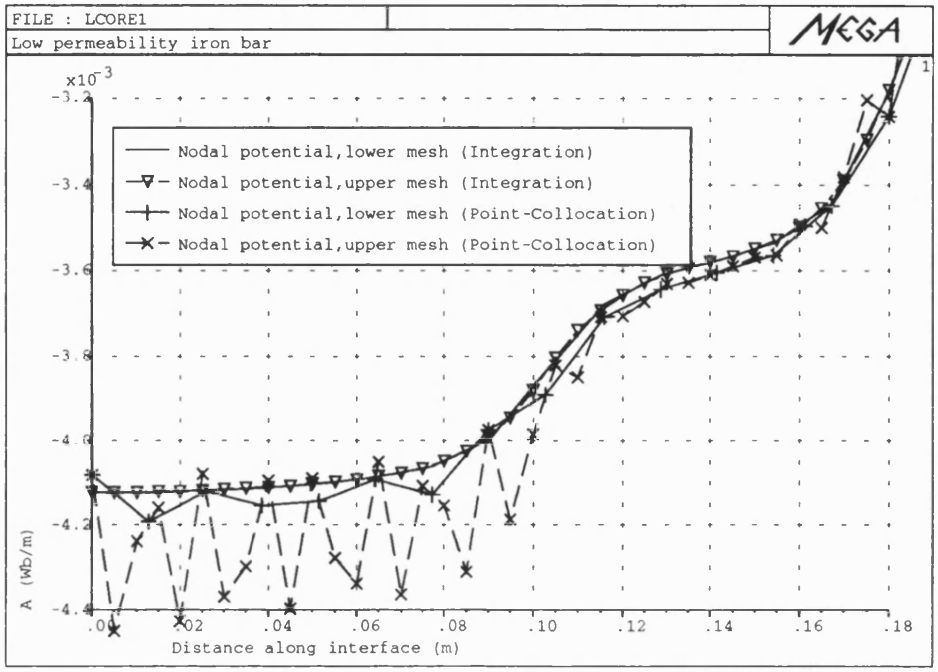

Figure 4.7: Oscillation of potential in Point Collocation method

The alternative scheme of placing the Lagrange Multipliers at the upper denser mesh has also been tried. Although the vector plot and the coupling of the potential at the interface has much improved over the earlier results, they were still not as good as that of the integration method. A natural extension of this idea is to put a Lagrange Multiplier at every node on the interface. This strategy is not pursued further as it will introduce a lot more unknowns into the system which would most likely make the solution more difficult to obtain.

There is also the 'Orthogonal collation' scheme [24] which basically places the sampling points at the Gauss-point of the element. This was also not attempted as we

did not think it will have significant advantages over the integration method. Furthermore, it would also suffer from the same oscillation problem as above in region where mesh discretizations are widely different.

4.3 Re-substituted Lagrange Method

It has been shown in Section 3.5 that a physical meaning can be attached to the Lagrange multipliers. In particular, the Lagrange multiplier as used in the vector potential formulation is identified as the tangential component of **H** on the mesh interface. The implication of this identification is that it is possible to create a new modified variational functional of equation (3.16) based on this new interpretation of the Lagrange multipliers. Since the Lagrange multipliers and their new physical meaning are theoretically equivalent, so are the two variational principles.

4.3.1 Modifying the Lagrange Functional

The identification of the Lagrange multipliers enables a new modified variational principle, in which λ is replaced by $\mathbf{H}\times\mathbf{n}$ at the interface, to be established. Using equations (3.16) and (3.23), this new functional can be written as

$$\Pi^h = \Pi + \int_{\Gamma_\lambda} -\left(\nu_M \frac{\partial \mathrm{A}_M}{\partial n_M}\right)(\mathrm{A}_M - \mathrm{A}_S)\,\mathrm{dl}. \tag{4.4}$$

Since the $(\nu\frac{\partial \mathrm{A}_M}{\partial n_M})$ term can be evaluated at the interface using existing nodal vector potential variables, this modified approach does not require the introduction of new unknowns to model the Lagrange multipliers. This is an attractive advantage over the original implementation. Numerically Π^h can be written as

$$\Pi^h = \Pi + \int_{\Gamma_\lambda} -\nu_M \frac{\partial(\sum N_M A_M)}{\partial n_M}\left(\sum N_M A_M - \sum N_S A_S\right)\mathrm{dl} \tag{4.5}$$

and the typical contributions to the system are,

$$\frac{\partial \Pi^h}{\partial A_{M_i}} = \frac{\partial \Pi}{\partial A_{M_i}} + \int_{\Gamma_\lambda} -\nu_M \frac{\partial N_{M_i}}{\partial n_M} \left(\sum N_M A_M - \sum N_S A_S \right) \mathrm{dl} \tag{4.6}$$

$$\frac{\partial \Pi^h}{\partial A_{S_j}} = \frac{\partial \Pi}{\partial A_{S_j}} + \int_{\Gamma_\lambda} \left(\nu_M \frac{\partial}{\partial n_M} \sum N_M A_M \right) N_{S_j} \mathrm{dl} \tag{4.7}$$

Alternatively, equation (3.24) can be used in place of equation (3.23) in equation (4.4) since theoretically both refer to the same $\mathbf{H}\times\mathbf{n}$ at the interface. The implementation of this method follows closely that described earlier. Modifications are only needed to be made when evaluating the above two equations.

4.3.2 Test on the Re-substituted Lagrange

The C-core model was again used to test the performance of this scheme. Fig.(4.8) to Fig.(4.10) are some results obtained from the test. Fig.(4.8) is the resulting contours of the vector potentials. Discontinuity in the contours across the interface can easily be seen. This is also reflected in the vector plot of **B** in Fig.(4.9) in which the vectors are seen to be pointing inconsistently with respect to each other near the interface. These are due to the poor enforcement of the constraints on the interface as shown in Fig.(4.9). The two graphs of the nodal potentials along the interface can be seen to oscillate around each other throughout the whole region of significance.

These results clearly indicate that this approach does not work satisfactorily in practice. The reason for this poor result originates from the very concept which the scheme is based on, that is, the evaluation of the tangential **H** on the interface by nodal potentials. With the Finite Element method based either on the Magnetic

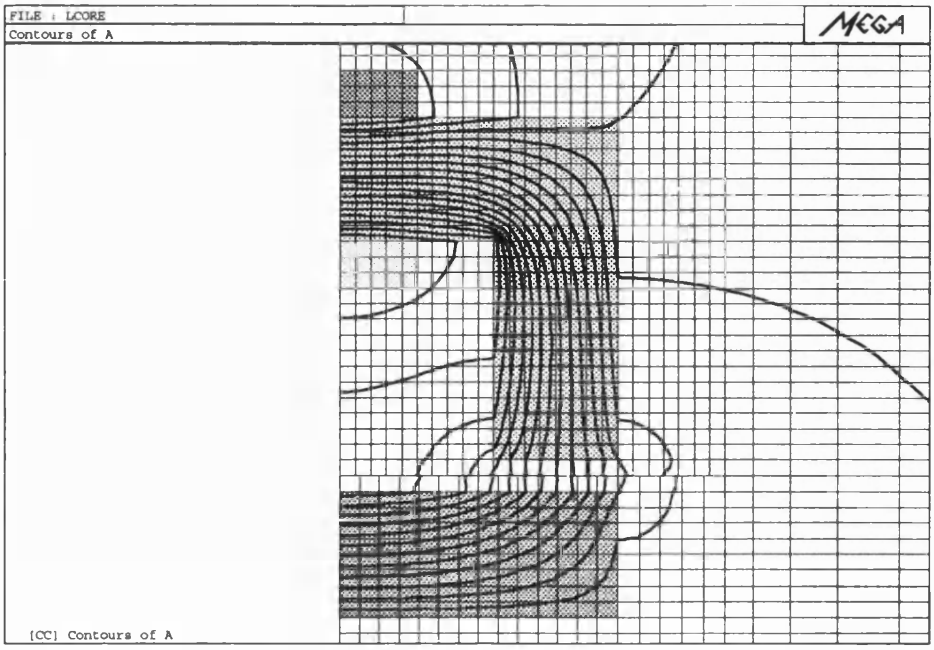

Figure 4.8: Contours of vector potentials

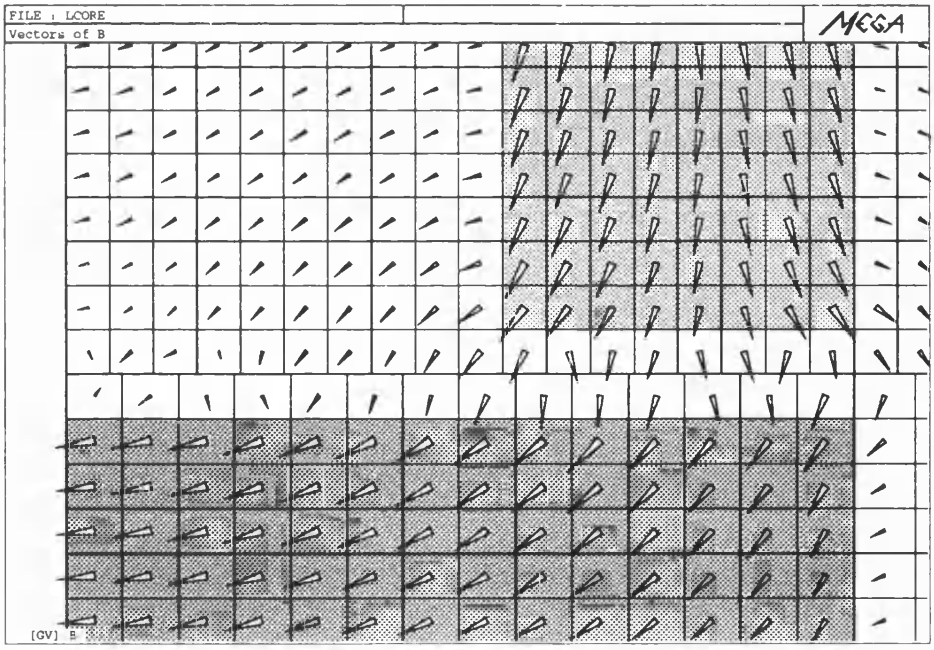

Figure 4.9: Vector plots of **B**

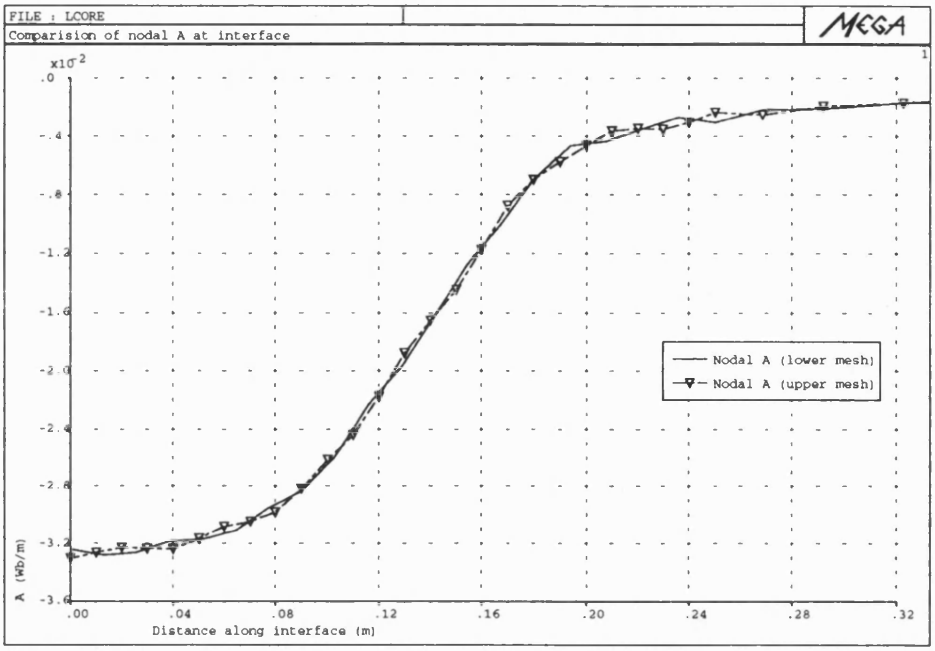

Figure 4.10: Graphs of nodal potential along the interface

Vector or Scalar potential, the continuity of the normal component of **B** and the tangential component of H across element interface in general can not both be satisfied simultaneously. In the case of the vector potential, the continuity of $\mathbf{B}_n$ across element is guaranteed while that of $\mathbf{H} \times \mathbf{n}$ is not. The latter is so because $\nu_1 \frac{\partial A_1}{\partial n} \neq \nu_2 \frac{\partial A_2}{\partial n}$. In general, a jump in the value of the $\mathbf{H} \times \mathbf{n}$ occurs when crossing from one element to the other. This can be illustrated by the simple case shown in Fig.(4.11). The potential is assumed to vary only in the X direction. Fig.(4.11.b) and Fig.(4.11.c) show how the potential and the corresponding H_y values are being approximated across the elements.

The jump in $\mathbf{H} \times \mathbf{n}$ means that the value derived at the element interface may not, and usually is not the correct one and that its value is also dependent on which element is used in the calculation. Hence in practice, the use of such derived values

to substitute λ in equation (4.4) will usually lead to erroneous results. Although the discrepancy between the derived and the correct $\mathbf{H} \times \mathbf{n}$ value will be reduced somewhat in regions where the flux is crossing the interface at near right angles, it is only in cases in which the field is uniform across the interface or the elements adjacent to it are infinitesimally thin that the derived $\mathbf{H} \times \mathbf{n}$ value be correct.

These observations suggest that this modified approach would perform worst in situations where the flux is running parallel to the interface. This can be easily simulated by reducing the μ_r of the lower iron bar in the test model. The resulting vector plot of $\mathbf{B}$ and the comparison between the nodal potentials on the interface are given in Fig.(4.12) and Fig.(4.13). The μ_r of the iron bar used was 1×10^{-3}.

The ripply occurances of the vectors of $\mathbf{B}$ and the oscillatory nature of the nodal potential graphs are clearly visible, confirming the prediction. Although it has been claimed that the oscillation of the interface potential can be reduced by putting equal emphasis on elements on both side of the interface when calculating the $\mathbf{H} \times \mathbf{n}$ value [25], such an improvement was not observed in our test case. It was felt that further pursuit of improvement to the approach would be futile.

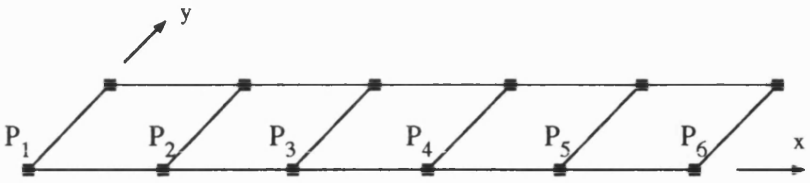

(a)

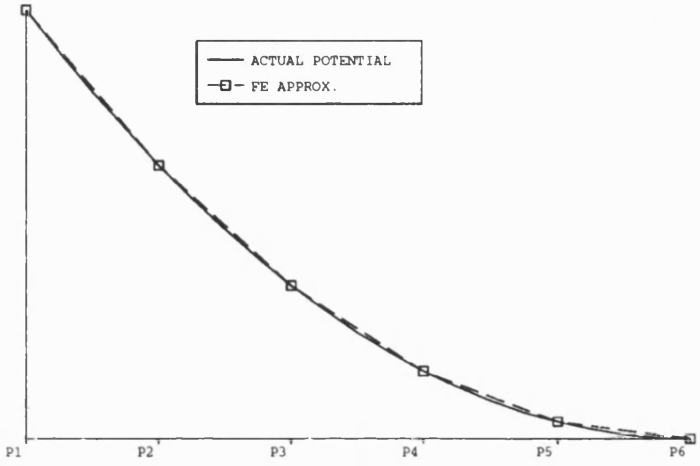

(b)

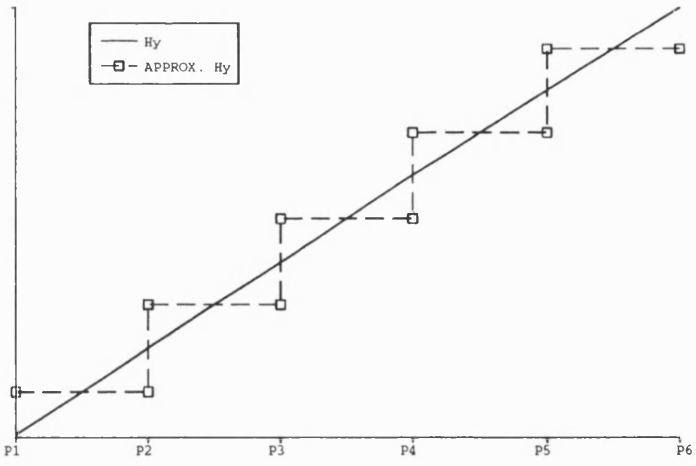

(c)

Figure 4.11: Discontinuous of H

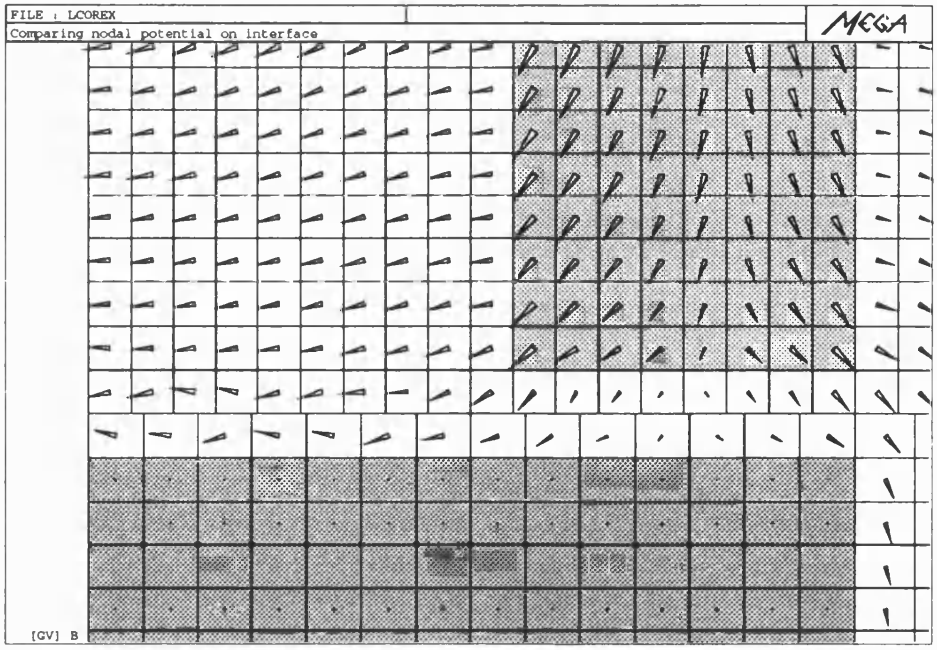

Figure 4.12: Vector Plot of **B** showing inconsistency

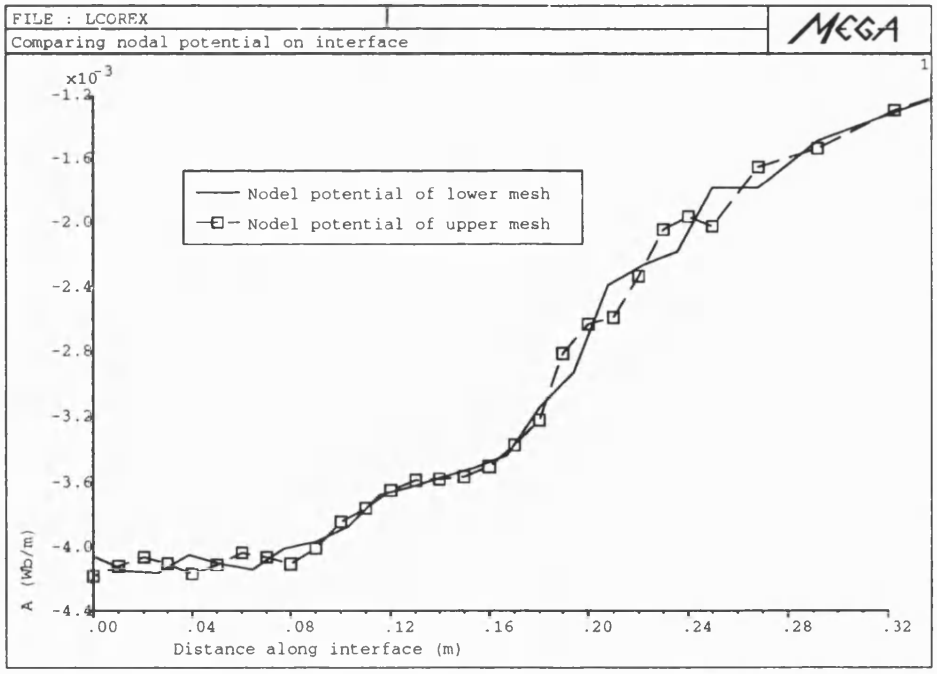

Figure 4.13: Comparison of nodal potentials on the interface .

4.4 The Penalty Method

An alternative approach to the use of the Lagrange multipliers method for constrained problems is the Penalty method. It originates from the theory of optimisation for handling constrained optimisation problems but is also popularly used in Finite Elements to enable additional constraints to be imposed on the system, most noticeably the gauging of the vector potential in 3D eddy current problems [23].The method is based on the minimisation of a penalty functional which is some combination of the original functional and the constraints. This enables the original function to be minimised while controlling the violation of the constraints in the solution by penalising them.

In our case, the most commonly used form of the penalty functional can be written as

$$\Pi^p = \Pi + \alpha \int_{\Gamma_\lambda} (A_M - A_S)^2 \, dl, \tag{4.8}$$

where Π^p is the new penalty functional,

Π is the original functional and

α is a penalty number which controls the violation of the constraints.

Other forms of the penalty functional can also be used provided they satisfy certain criteria [26]. By minimising Π^p, the solution which minimises Π and at the same time violates the constraints least can be found and can be regarded as the best solution to the problem. This solution is only an approximation, so is the fulfillment of the constraints. Theoretically, however, as α gets larger and larger, the constraints will be satisfied more and more, hence the solution will approximate closer to the true

solution. However, the penalty number in the final matrix can become so large that they 'swamp out' the information which describes the original problem. Hence, there is a practical limit to the size of α.

4.4.1 The Penalty Functional

With Π^p written in the form given in equation (4.8) and the vector potentials of the two meshes, A_M and A_S, approximated in the usual way :

$$\begin{aligned} A_M &= \sum N_M A_M \\ A_S &= \sum N_S A_S \end{aligned} \tag{4.9}$$

The penalty functional can be expanded as

$$\Pi^p = \Pi + \alpha \int_{\Gamma_\lambda} \left(\sum N_M A_M - \sum N_S A_S \right)^2 \mathrm{dl}, \tag{4.10}$$

and after differentiating with respect to typically A_M and A_S, we obtain the following :

$$\frac{\partial \Pi^p}{\partial A_{M_i}} = \frac{\partial \Pi}{\partial A_{M_i}} + \alpha' \int_{\Gamma_\lambda} \left(\sum N_M A_M - \sum N_S A_S \right) N_{M_i} \, \mathrm{dl} \tag{4.11}$$

and

$$\frac{\partial \Pi^p}{\partial A_{S_j}} = \frac{\partial \Pi}{\partial A_{S_j}} + \alpha' \int_{\Gamma_\lambda} \left(\sum N_M A_S - \sum N_S A_S \right) N_{S_j} \, \mathrm{dl}. \tag{4.12}$$

α' above equals to 2α.

A potential advantage of this penalty method over the Lagrange multipliers method is that it does not introduce new unknowns to the system. Extra contributions are

added to the diagonal terms and the cross interface terms on the rows of interface potential. In this respect, the penalty method is more attractive than the Lagrange multipliers method.

The penalty method, however, does have a serious drawback relating to the size of the penalty number α in practice. As the size of α is increased to ensure a closer satisfaction of the constraints, it causes the penalty terms to assume a more and more dominant role over the original functional when calculating the matrix terms using equation (4.11) and equation (4.12). If α is kept on being increased further , the penalty term will eventually outweigh the original functional completely, resulting in a solution which will be irrelevant to the problem.

4.4.2 Test on the Penalty Method

The penalty method was applied to the C-core test problem. Figures(4.14) to (4.17) show how the size of α affects the answer. With small α, Fig.(4.14) with $\alpha = 100$, no significant coupling between the two meshes can be seen and the contours of the upper mesh leave the interface perpendicularly, the Neumann boundary condition for vector potential formulation. As α increases, the degree of coupling between the meshes can be seen to have improved, Fig.(4.15) and Fig.(4.16), though the results are still much inferior to that of the Lagrange multipliers method. At large α, the penalty terms dominate the whole system, driving the potentials on the interface towards zero, the trivial solution for the constraints.

The above observations can also be made by examining Fig.(4.18) which shows how the penalty number affects the calculated stored energy. The stored energy

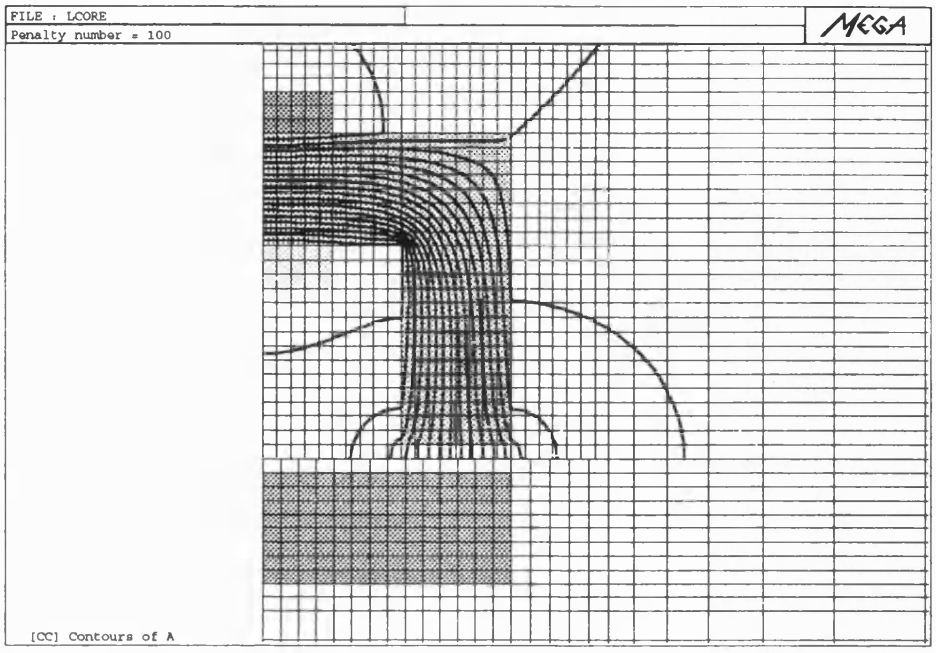

Figure 4.14: Contours of A with $\alpha = 100$

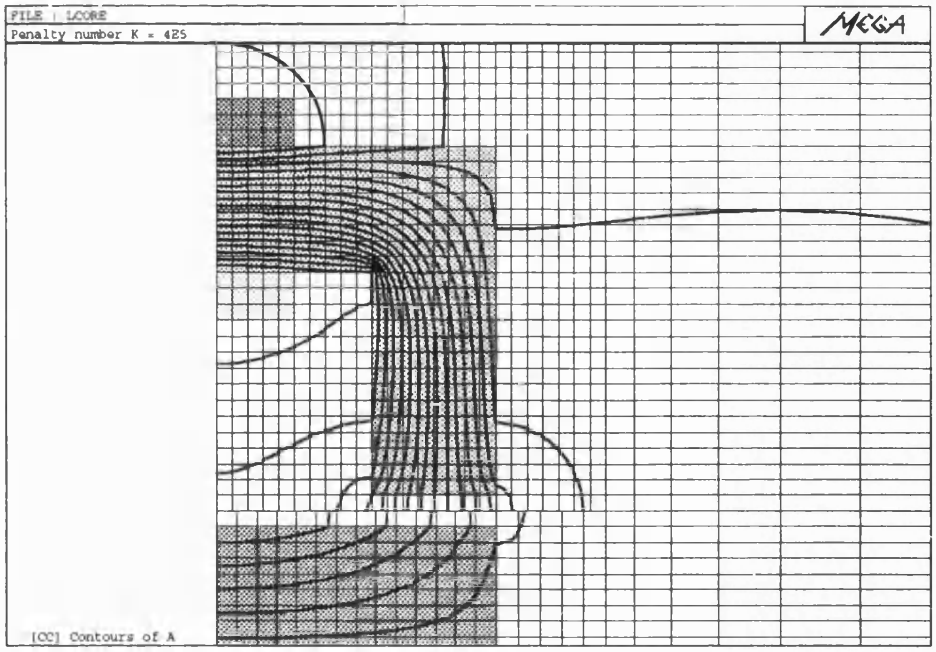

Figure 4.15: Contours of A with $\alpha = 4 \times 10^5$

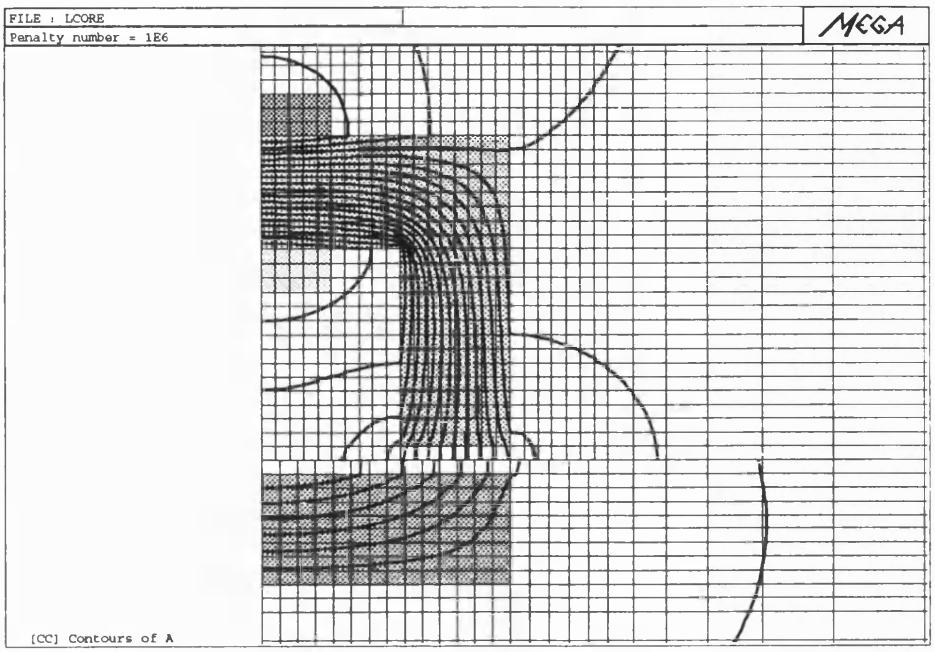

Figure 4.16: Contours of A with $\alpha = 1 \times 10^6$

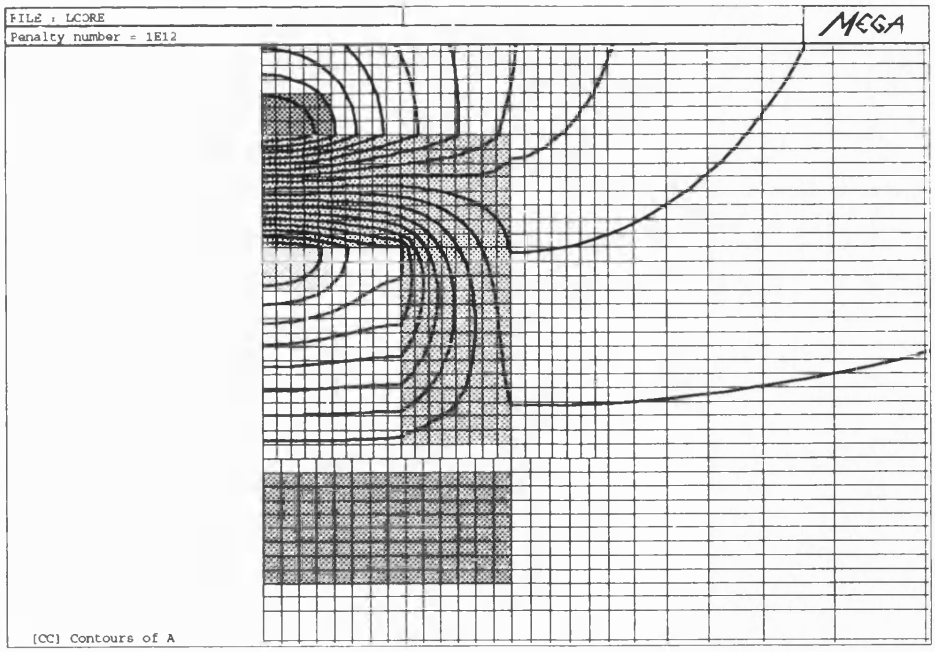

Figure 4.17: Contours of A with $\alpha = 1 \times 10^{12}$

is normalised against the value obtained with a very fine normal Finite Element mesh. This reference value was 101.597 and is shown in Table (3.1) on page 59. The normalised stored energy is plotted against the log of the penalty number. The best result attained by the method was with a penalty number , α, close to 4×10^5. But even at this region, the answer was still not satisfactory compared to that of the standard Lagrange multipliers. The contours of the potentials with $\alpha = 4 \times 10^5$ is shown in Fig.(4.15).

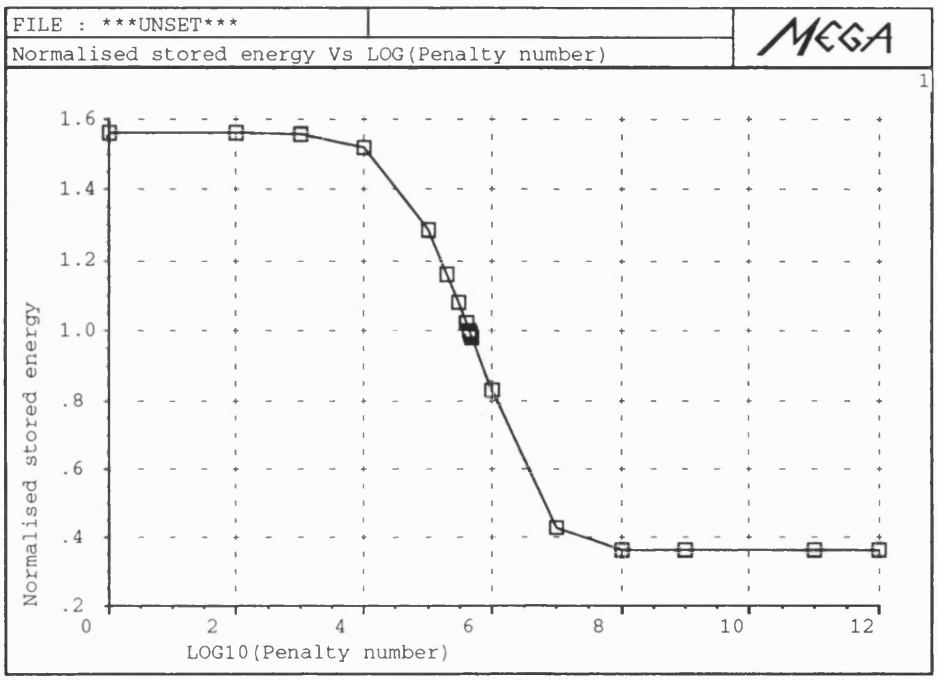

Figure 4.18: Showing how penalty number affects the calculated stored energy

It is surprising to find that the penalty method failed to achieve a respectable degree of success. The reason of this is most probably due to the failure of the formulation to impose the continuity of the tangential component of $\mathbf{H}$ across the interface. In order to link two separate meshes together, the continuity of the normal component of $\mathbf{B}$, $\mathbf{B}_n$, and the tangential component of H, $\mathbf{H}\times\mathbf{n}$, has to be satisfied. While the former condition is achieved by imposing the continuity of the vector potential, the latter is not mentioned in the penalty formulation. With such incomplete specification, it is not difficult to explain the poor performance of the method.

These difficulties do not exist in the Lagrange Multipliers formulation. The continuity of $\mathbf{H}\times\mathbf{n}$ condition is specified by the extra $\mathrm{A}-\lambda$ terms on the λ columns in a normal A row. The $\mathbf{B}_n$ constraint is specified by the extra λ rows. This is so since the Lagrange multipliers is physically identified with $\mathbf{H}\times\mathbf{n}$ on the interface, as shown earlier in Section 3.5. These terms now act as the line integrals of $\mathbf{H}\times\mathbf{n}$ on element interface which are ignored in the normal Finite Element formulation since adjacent elements always share a common edge and are therefore cancelled out. In our case, however, they provide the missing continuity specification.

4.5 The Augmented Lagrange Multipliers Method

There is yet another variation of the Lagrange multipliers method which is popularly used in solving optimisation problems with additional constraints. It is called the Augmented Lagrange multipliers method [21]. The method solves the constrained problem by transforming it into an unconstrained one, this time based on a combination of the Penalty method and the Lagrange multipliers method, hence the name. Using this idea, the original functional of our problem can be modified to

$$\Pi^a = \Pi + \int_{\Gamma_\lambda} \lambda(A_M - A_S)\,dl + \alpha \int_{\Gamma_\lambda} (A_M - A_S)^2\,dl. \tag{4.13}$$

This method is an improvement over the Penalty method since it avoids the ill-conditioning situation with large α by simply allowing a much smaller α to be used. This is possible since the solution is independent of the penalty number by virtue of the presence of the Lagrange multipliers.

This scheme has also been implemented and tested on the C-core problem. Fig.(4.19) shows how the magnitude of the penalty number affects the calculated stored energy.

The stored energy is normalised against the same reference stored energy used in the last section and the normalised value is plotted against the log of the penalty number in Fig.(4.19). From this graph, it can be seen that the solution obtained at small α ($\alpha < 1000$) was very close to that of the standard Lagrange multipliers method ($\alpha = 0$). It began to diverge rapidly from this value once α had exceeded 1×10^4. Further increase in K resulted in too much emphasis being put on the constraint, causing it to dominate over the original functional and as a result brought back the ill-conditioning problem of the Penalty method. As no significant computational

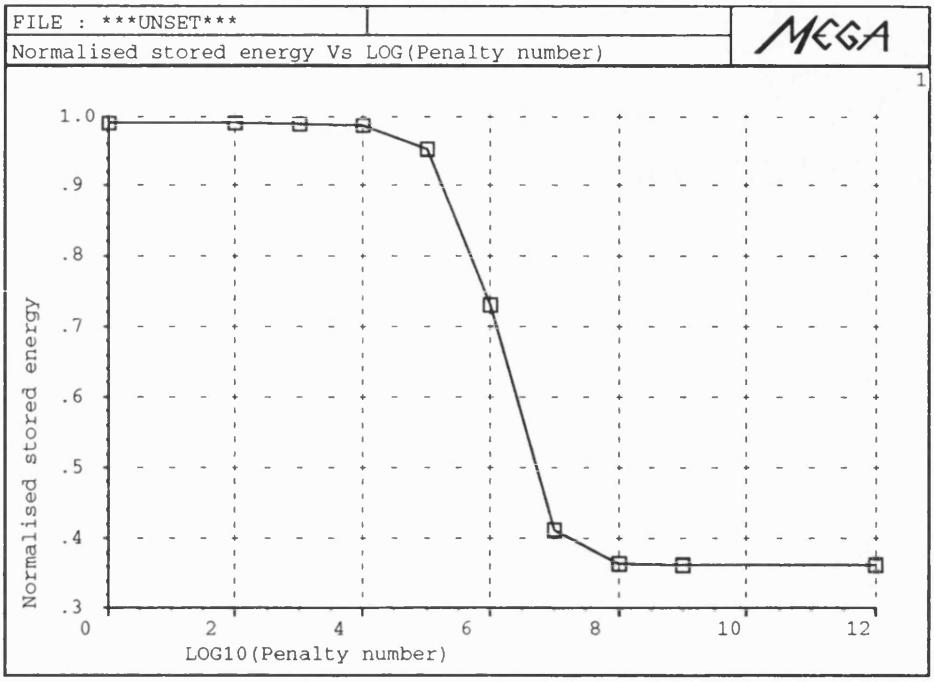

Figure 4.19: Showing how Penalty number affects the solution

advantages over the original Lagrange multipliers method could be observed, this method was not pursued further.

4.6 Conclusion

This chapter has examined four alternative schemes to impose the potential continuity constraint on the system. Two of these, the Point Collocation Lagrange and the Re-substituted Lagrange, are direct variations of the standard Lagrange multipliers Method. The third scheme considered was the Penalty method, and the so called Augmented Lagrange Multipliers Method was examined last.

The Point Collocation Lagrange method is basically the standard Lagrange multipliers method with the Delta Dirac function used as the approximating shape functions for the new Lagrange multipliers function. The method produces answers comparable to the standard Lagrange method when the discretization patterns of the two meshes to be coupled do not differ wildly on the interface. Once this condition is not met, the accuracy of the answers depends heavily on where the constraint is sampled. Simply increasing the number of sampling points is not attractive as it will further increase the number of unknowns being added to the system of equations and could make it more difficult to obtain the solution.

The Re-substituted Lagrange method is based on replacing the Lagrange multipliers with its physical identification. In 2D Finite Elements using vector potential, the Lagrange multipliers can be identified as the tangential component of $\mathbf{H}$ at the interface. The results obtained using this scheme were, however, less than satisfactory. This was explained by the inability of the Finite Elements to model accurately $\mathbf{H}\times\mathbf{n}$ at element edges. Since $\mathbf{H}$ is calculated by differentiation, this is most accurate at the internal Gauss points of the element. Substituting the Lagrange multipliers with this derived $\mathbf{H}\times\mathbf{n}$ would introduce inconsistent information into the system of

equations, and lead to a less accurate solution. Moreover, the fact that the $\mathbf{H} \times \mathbf{n}$ is discontinuous across element interface causes the results returned by this scheme to be heavily dependent on which elements are used to estimate the $\mathbf{H} \times \mathbf{n}$ value.

The Penalty method was also examined and the performance was found to be less than satisfactory. This was due to the failure of the method to enforce the continuity of $\mathbf{H} \times \mathbf{n}$ condition. A hybrid form of the Penalty method and the Lagrange multipliers method, the Augmented Lagrange multipliers method, was then considered and used to overcome the problem of the Penalty method. The results were satisfactory although with a large penalty number, the problem of the constraints dominating the original functional returned.

Chapter 5

Three Dimensional Lagrange Multipliers

5.1 Introduction

While it is possible to model with good confidence certain devices using 2D Finite Elements, there are many other situations in which the reduction of the problem to 2D would not be entirely justifiable. This could occur either because the geometry, the field variation, or a combination of both is highly three dimensional or because field variation around the third dimension ends are too significant to be safely ignored. In such cases, a full 3D Finite Element analysis of the device has to be carried out. The amount of time and effort required to be spent in the pre-processing — solving — post-processing phase increases disproportionally.

As mentioned in Chapter 3, obtaining the positional characteristic of devices with moving parts using Finite Elements usually requires a series of solutions at different positions. This kind of exercise is expensive even in 2D using standard Finite Element techniques. The cost and amount of effort involved in carrying out a similar exercise using normal 3D Finite Elements escalates prohibitively.

In view of the success that the Lagrange multipliers method has enjoyed in tackling this problem in 2D Finite Elements, it is logical to extend the method to 3D Finite Elements. This forms the objective of the current chapter.

As in Chapter 3, we shall consider only devices which consist of a moving and a

stationary part separated by an air gap. This allows us to concentrate on coupling together regions in which no current flows.

5.2 The Lagrange Multipliers Functional

The development of the Lagrange multipliers method in 3D Finite Elements follows closely that described in the 2D case, though the implementation details differ significantly. The type of example which we are going to consider is shown schematically in Fig.(5.1). It consists of a moving and a stationary region separated by an air gap. The two regions are discretized into two separate meshes, touching at the interface Γ_λ. The mesh which contains the moving part will be referred to as mesh M and the mesh that contains the stationary part mesh S.

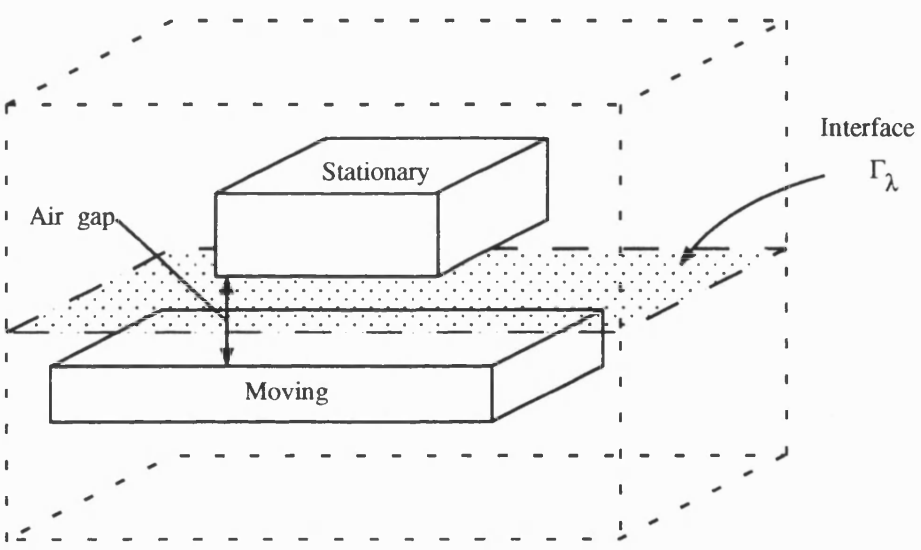

Figure 5.1: A schematic diagram of a typical 3D problem with moving parts

In 3D Finite Elements, fields in non-conducting regions such as air can be economically modelled using the magnetic scalar potential defined as

$$\mathrm{H} = -\nabla\psi. \tag{5.1}$$

Hence we must solve for :

$$\nabla \cdot \mu \nabla \psi = 0 \tag{5.2}$$

Following a path similar to that shown in Appendix B for the vector potential case, it can be shown that an equivalent functional for equation (5.2) is

$$\Pi = \frac{1}{2} \int_{\Omega} \nabla \psi \cdot \mu \nabla \psi \, \mathrm{d}V. \tag{5.3}$$

As before, the solution to equation (5.2) can be obtained by minimising Π.

With our example being made up of two separate meshes as described above, the functional of the whole problem can be written as

$$\Pi = \Pi_M + \Pi_S. \tag{5.4}$$

where Π_M and Π_S are functionals of the form of equation (5.3) for mesh M and mesh S respectively. The two meshes are still not connected. To link them together, we need to enforce the continuity of normal $\mathbf{B}$ and tangential $\mathbf{H}$ across the interface. This can be done by imposing the following potential continuity constraint using the Lagrange multipliers method :

$$\psi_M - \psi_S = 0 \qquad \text{on } \Gamma_\lambda, \tag{5.5}$$

where ψ_M and ψ_S are the scalar potential of mesh M and mesh S on Γ_λ respectively.

Using the Lagrange multipliers method, the above constraint can be incorporated

into the system by modifying the functional to

$$\Pi' = \Pi + \int_{\Gamma_\lambda} \lambda(\psi_M - \psi_S)\,\mathrm{d}S, \tag{5.6}$$

where λ is again a new set of Lagrange multipliers which exist only on the interface Γ_λ.

With the scalar potentials and λ approximated in the usual way by :

$$\begin{aligned} \psi_M &= \sum_{i=1}^{m} N_{M_i}\psi_{M_i} \\ \psi_M &= \sum_{j=1}^{s} N_{S_j}\psi_{S_j} \\ \lambda &= \sum_{k=1}^{l} N_{L_k}\lambda_k \end{aligned} \tag{5.7}$$

The solution to the connected problem can be obtained by minimising Π' with respect to ψ_M, ψ_S and λ. Typically this yields the following :

$$\begin{aligned} \frac{\partial \Pi'}{\partial \psi_{M_i}} &= \frac{\partial \Pi}{\partial \psi_{M_i}} + \int_\Gamma N_{M_i}\left(\sum N_L\lambda\right)\mathrm{d}S \\ \frac{\partial \Pi'}{\partial \psi_{S_j}} &= \frac{\partial \Pi}{\partial \psi_{S_j}} + \int_\Gamma N_{S_j}\left(\sum N_L\lambda\right)\mathrm{d}S \\ \frac{\partial \Pi'}{\partial \lambda_k} &= \frac{\partial \Pi}{\partial \lambda_k} + \int_\Gamma N_{L_k}\left(\sum N_M\psi_M - \sum \mathrm{N}_S\psi_S\right)\mathrm{d}S \end{aligned} \tag{5.8}$$

This would result in a matrix of equations of the form

$$\begin{bmatrix} \mathbf{K}_\Pi & \mathbf{K}_\lambda \\ \mathbf{K}_\lambda^T & 0 \end{bmatrix} \begin{bmatrix} \psi_\Pi \\ \lambda \end{bmatrix} = \begin{bmatrix} \mathbf{f}_\Pi \\ 0 \end{bmatrix}, \tag{5.9}$$

where $\mathbf{K}_\Pi$ is the stiffness of the original Π and

$$\mathbf{K}_\lambda^T = \int_{\Gamma_\lambda} \mathrm{N}_L \left(\sum \mathrm{N}_M \psi_M - \sum \mathrm{N}_S \psi_S \right) \mathrm{d}S \ .$$

The Lagrange multipliers enter the original system of equations as new columns which are symmetrical to the extra rows which specify the constraints. Together, they enforce the continuity conditions across the interface.

5.3 Lagrange Multipliers as Normal B

In Chapter 4, it has been shown that the Lagrange multipliers used in 2D Finite Elements can be identified as the tangential component of **H** at the interface. This identification, apart from giving some physical meaning to the multipliers, also helps explain the superior performance of the method over some other similar schemes.

It is possible to attach a physical meaning to the 3D Lagrange multipliers by following a similar procedure. The equivalent functional for 3D Finite Elements using magnetic scalar potential is

$$\Pi = \frac{1}{2}\int_{\Omega} \nabla\psi \cdot \mu\nabla\psi \, \mathrm{d}V.$$

For our problem with 2 unconnected meshes, the functional for the whole system is

$$\begin{aligned} \Pi &= \Pi_M + \Pi_S \\ &= \frac{1}{2}\int_{\Omega_M} \nabla\psi_M \cdot \mu_M\nabla\psi_M \, \mathrm{d}V + \frac{1}{2}\int_{\Omega_S} \nabla\psi_S \cdot \mu_S\nabla\psi_S \, \mathrm{d}V. \end{aligned} \tag{5.10}$$

The first variation of Π is now

$$\delta\Pi = \int_{\Omega_M} \nabla\psi_M \cdot \mu_M\nabla(\delta\psi_M) \, \mathrm{d}V + \int_{\Omega_S} \nabla\psi_S \cdot \mu_S\nabla(\delta\psi_S) \, \mathrm{d}V. \tag{5.11}$$

Using Green's theorem, the above can be re-written as

$$\delta\Pi = -\int_{\Omega_M} \delta\psi_M(\mu_M\nabla^2\psi_M) \, \mathrm{d}V - \int_{\Omega_S} \delta\psi_S(\mu_S\nabla^2\psi_S) \, \mathrm{d}V +$$

$$\oint_{\Gamma_\lambda} \delta\psi_M(\mu_M \nabla\psi_M) \cdot \mathrm{dS} + \oint_{\Gamma_\lambda} \delta\psi_S(\mu_S \nabla\psi_S) \cdot \mathrm{dS}. \tag{5.12}$$

When the Lagrange multipliers Method is used to enforce the continuity constraint, the functional Π is modified to

$$\Pi' = \Pi + \int_{\Gamma_\lambda} \lambda(\psi_M - \psi_S)\,\mathrm{d}S. \tag{5.13}$$

The first variation of Π' is

$$\delta\Pi' = \delta\Pi + \int_{\Gamma_\lambda} \delta\lambda(\psi_M - \psi_S)\,\mathrm{d}S + \int_{\Gamma_\lambda} \lambda(\delta\psi_M)\,\mathrm{d}S - \int_{\Gamma_\lambda} \lambda(\delta\psi_S)\,\mathrm{d}S. \tag{5.14}$$

Substituting $\delta\Pi$ yields the following :

$$\begin{aligned} \delta\Pi' \;=\; & -\int_{\Omega_M} (\text{ terms of mesh M })\,\mathrm{d}V - \int_{\Omega_S} (\text{ terms of mesh S })\,\mathrm{d}V \\ & \int_{\Gamma_\lambda} \delta\psi_M(\lambda + \mu_M \frac{\partial\psi_M}{\partial n_M})\,\mathrm{d}S + \int_{\Gamma_\lambda} \delta\psi_S(\lambda - \mu_S \frac{\partial\psi_S}{\partial n_s})\,\mathrm{d}S + \\ & \int_{\Gamma_\lambda} \delta\lambda(\psi_M - \psi_S)\,\mathrm{d}S. \end{aligned} \tag{5.15}$$

As we require the first variation of Π' to be zero, we therefore have :

$$\begin{aligned} \lambda + \mu_M \frac{\partial\psi_M}{\partial n_M} &= 0 \\ \lambda - \mu_S \frac{\partial\psi_S}{\partial n_S} &= 0 \end{aligned} \tag{5.16}$$

Thus, the 3D Lagrange multipliers can be seen to be associated with the normal component of **B** on the interface of the two meshes.

5.4 Numerical Implementation

The numerical implementation of the method again centres on the incorporation of the extra surface terms in equation (5.8) into the system matrix. Since each element facet usually overlaps with more than one facet of the opposite mesh on the interface, these surface terms cannot normally be evaluated in the familiar one element to one element manner as in usual Finite Elements. Instead, the overlapping areas of the facets have to be first identified and the terms evaluated over them.

To facilitate the identification of the overlapping facets, coordinate transformations may sometimes be required to transform the meshes so that the interface is orientated in a more convenient direction. For example, for an interface which is of a linear surface type as shown in Fig.(5.2.a), positioning it in the X–Y plane orientation would help the identification process considerably. This is so because one needs to consider only the new X′–Y′ coordinates when finding out overlapping facets, effectively reducing the process to a 2D operation. For a cylindrical type of interface, it is more appropriate to align the main axis of the surface with the Z axis as shown in Fig.(5.2.b). Then the new θ'–Z′ coordinates could be used conveniently. The use of these newly transformed coordinates allows a more uniform approach to be taken in calculating the overlaps in both type of interface, since both X′–Y′ and θ'–Z′ are proper two dimensional coordinate systems.

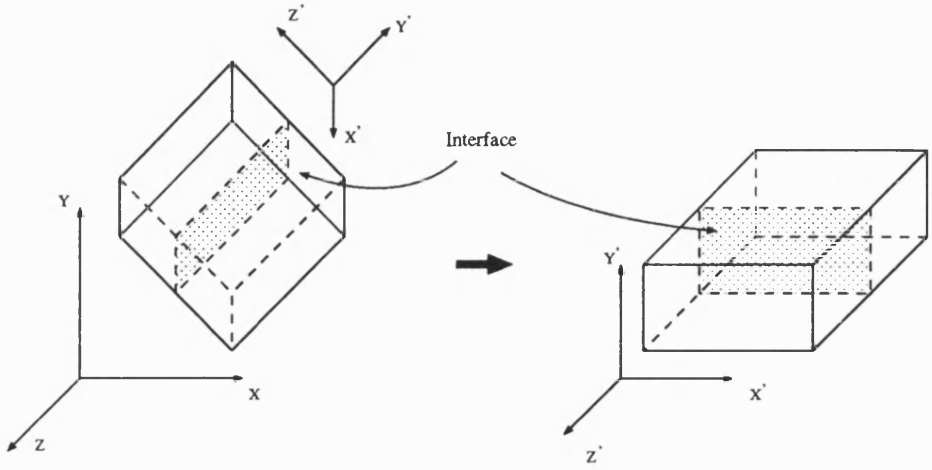

(a) Linear type interface

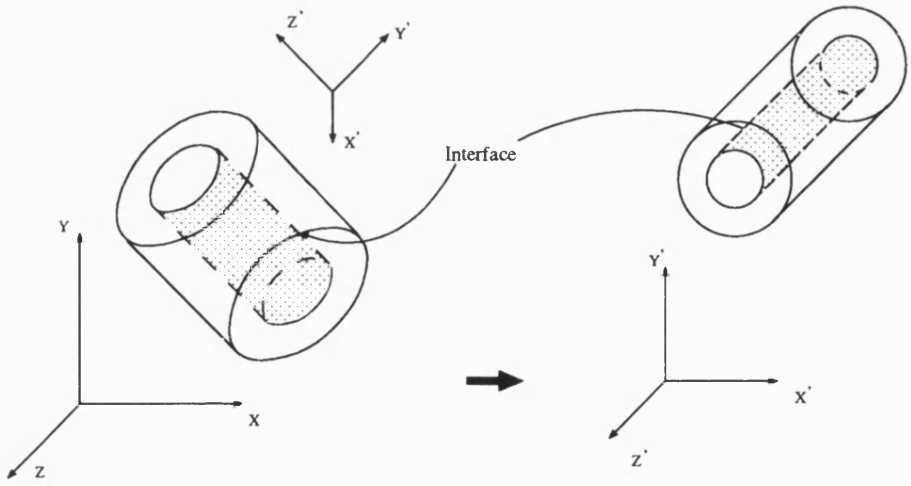

(b) Cylindrical type surface

Figure 5.2: Showing schematically a typical 3D problem with moving parts

5.4.1 The Surface Integration

Blanket Sampling

Once the group of element facet from the opposite mesh has been identified, the next step is to integrate the surface terms numerically. Gaussian Quadrature is again used to evaluated these surface integral terms. As in Chapter 3, either one of the two meshes can be used to accommodate the new Lagrange multipliers.

To see how the integration can be done, consider Fig.(5.3) which shows a representative facets overlapping pattern. The shaded facet has overlapped with 10 other facets from the other mesh. One possible way of integrating the surface terms over the shaded facet is to increase the order of integration used in Gaussian Quadrature. This effectively places a much larger number of sampling points over the facet than is necessary under normal circumstances in the hope that an adequate number of them will land on each overlapping regions so that the surface terms can be integrated accurately enough there.

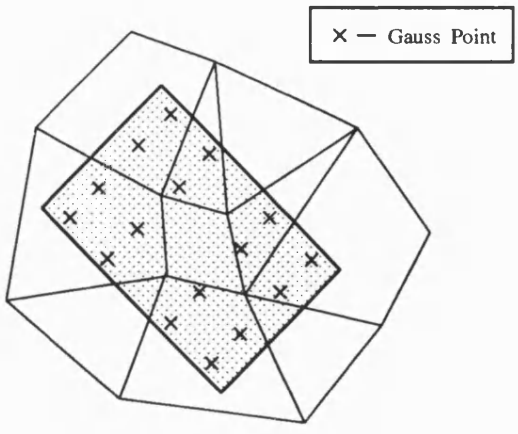

Figure 5.3: Overlapping facets

This approach, although easier to implement, suffers from the uncertainty that enough Gauss points have been used. Fig.(5.3) illustrates this point. The small crosses on the shaded facet indicate the location of the 16 Gauss points if 4×4 Quadrature rules were used. It can be seen that 4 out of the 10 overlapping regions do not have any Gauss points in them. These four regions together cover a moderate amount of the total surface area of the shaded facet, and so missing out the contributions to the surface integral from them can introduce significant errors into the solution. A less dramatic but equally disastrous case is one in which an overlapping region does not have enough Gauss points landed in it to allow the integral to be calculated accurately. In practice, these two sources of error can often happen, especially when a large facet overlaps with a group of small facets and the former is used to derive the location of the Gauss points.

It is difficult to conclude how high an order of integration must be used in order that most cases of these two types can be taken care of. It depends very much on how the facets are overlapped. Though it is conceivable that certain checking procedures can be put in to monitor the occurances of these two types of cases and increase the integration order should they arise.

Target sampling

A second integration scheme which is more accurate and effective, works by targeting the sampling points to where they are needed. This is, to certain extent, an extension of the method used in the 2D Lagrange multipliers method described in Chapter 3. Referring to Fig.(5.4), each of the 10 overlapping regions are considered in turn. An auxiliary finite element with nodes coinciding with the corners of the region

under consideration is created. The integration is now performed over this auxiliary element. The advantage of this scheme is that the order of integration required is not affected by how fragmented the overlapping regions are, and can be chosen to be just high enough for the integral concerned, thus avoiding wasting computer time on too many sampling points. Furthermore, as each overlapping region is considered in turn, it can be certain that none, no matter how small they are, are left out.

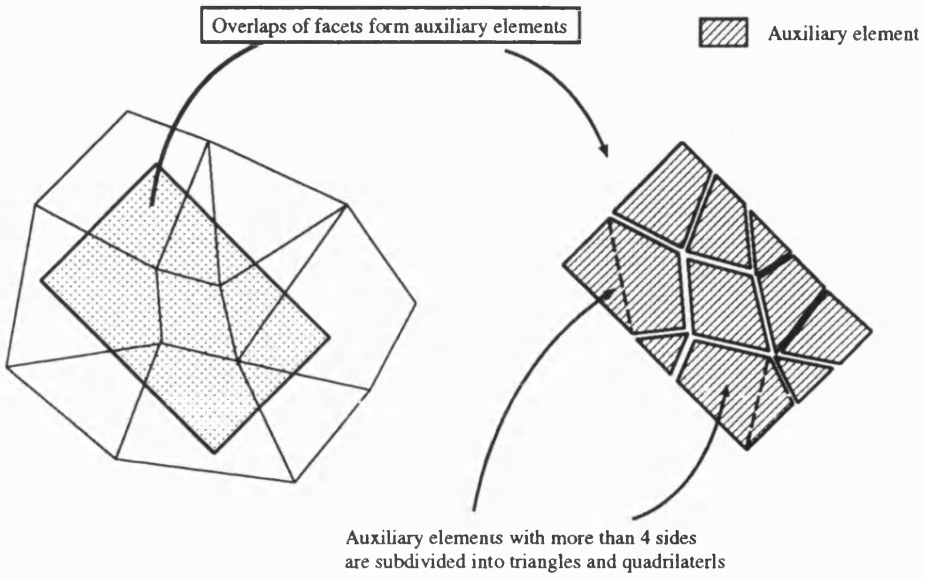

Figure 5.4: Creating auxiliary elements for integration

By ensuring that the auxiliary elements are created in the same way as ordinary finite elements, existing routines can be used to return the location of the Gauss points within the element. Overlapping facets with five or more sides can be handled by first splitting them into triangles and quadrilaterals. The location of a Gauss point within the auxiliary element is usually expressed in its local coordinate system. This has to be translated back into the local coordinate system of the two overlapping elements

for sampling the potentials properly. The process involves firstly transforming the Gauss point from the local coordinate of the auxiliary element back to the global XYZ coordinate system in which the meshes are defined. From there, it is once again translated into the local coordinates of the overlapping elements concerned.

The first transformation is quite straightforward, it is done by using

$$x_g = \sum_{i=1}^{m^a} N_i x_i^a,$$
$$y_g = \sum_{i=1}^{m^a} N_i y_i^a,$$
$$z_g = \sum_{i=1}^{m^a} N_i z_i^a,$$

where m^a is the number of nodes of the auxiliary element and (x_i^a, y_i^a, z_i^a) is the coordinates of node i of the element.

The second transformation, however, requires the use of Newton Raphson to solve the set of equations which transform the coordinates from the global to the local coordinate system of the overlapping elements. This is not as expensive as it might seem, only 3 to 4 iterations are usually enough to achieve convergence.

The assembling of these surface terms into the system matrix follows the usual pattern and poses no serious difficulties.

5.5 Experimental Verification

The results of the experiment described in Chapter 3 were again used. Fig.(5.5) shows a symmetry view of the 3D model. Only the front half of the model shown was actually solved due to symmetry. The 3D mesh was created by extruding a 2D base plane into levels. The base plane was the mesh used in Chapter 3 with some minor modifications. Each model has 52380 nodes, 47916 elements and 54910 degrees of freedom.

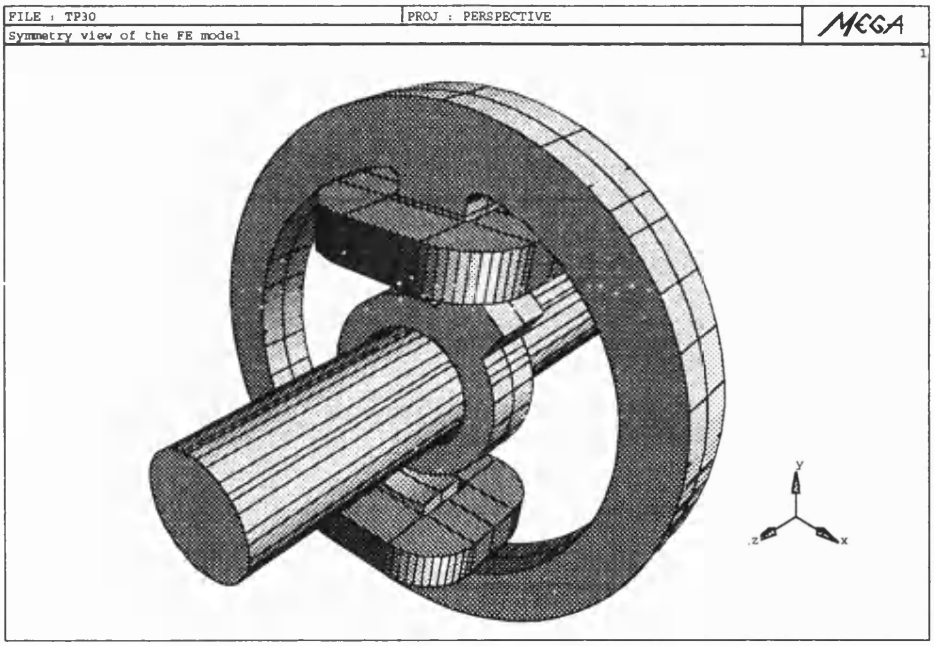

Figure 5.5: A 3D view of the computer model

Fig.(5.6) shows how the torques calculated from the 3D models compare with that measured experimentally. The graph of the calculated 2D torques is also shown. It can be seen that the 3D FE torques correspond to the measurements much better

than the 2D FE calculations. This indicates the significance of the the 3D effecs which the 2D models have ignored. The variation of flux in the axial direction is illustrated in Fig.(5.7) which shows a colour contours plot of the modulus of **B** in the poles with the rotor 6° away from the aligned position. The assumption of field invariance in the axial direction made in the 2D models is inaccurate. The field fringing from the 3D ends can be seen in Fig.(5.8), which shows the vectors of **B** on a plane cutting through the model in the axial direction. The figure also explains the saturation near the front edge in Fig.(5.7). Fig.(5.9), Fig.(5.10) and Fig.(5.11) give general views on the field pattern at different rotor positions. The shaft and the reduced scalar regions are not displayed.

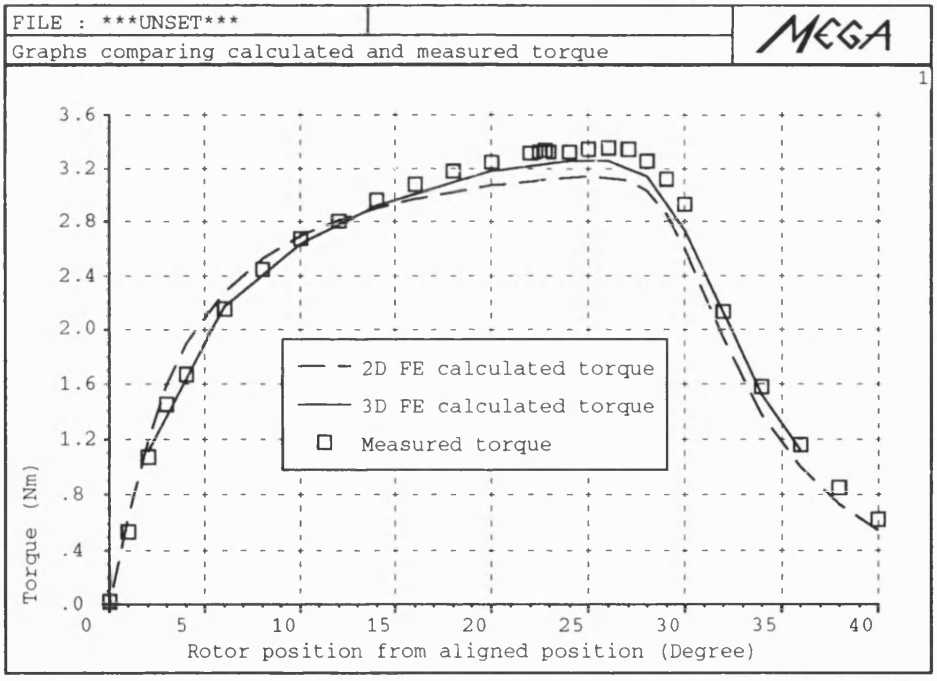

Figure 5.6: Graph comparing measured and calculated torque

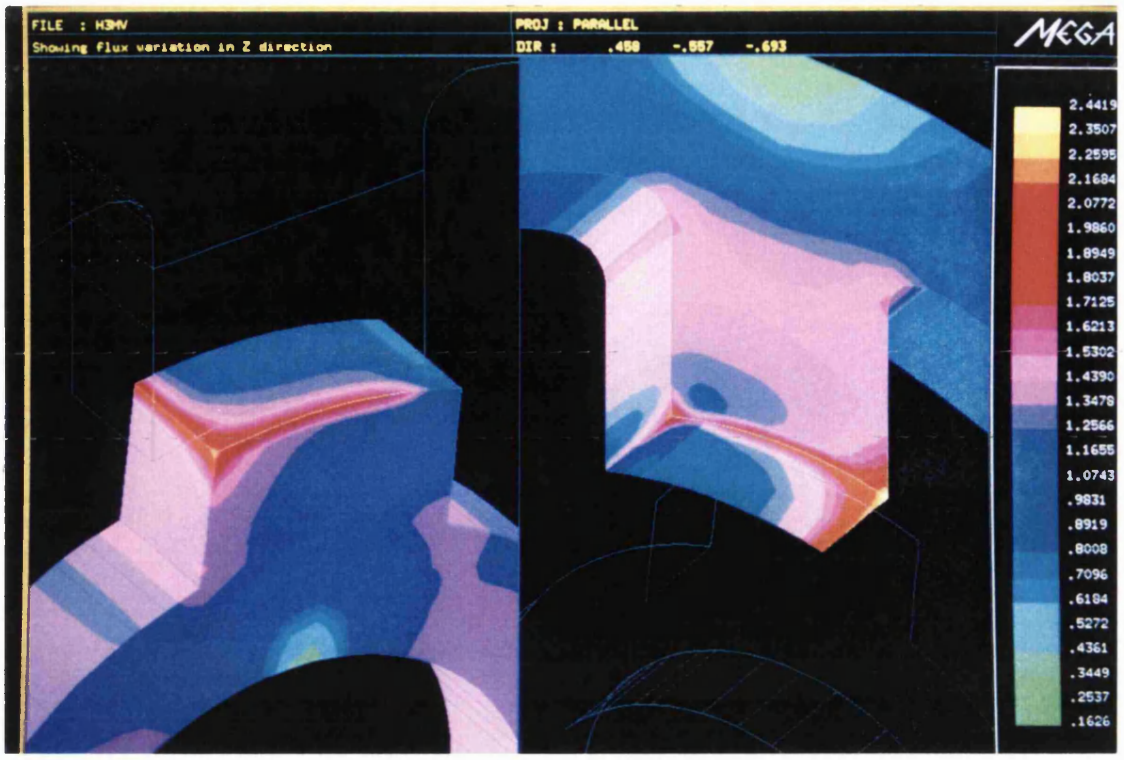

Figure 5.7: Showing the variation of the **B** field in axial direction

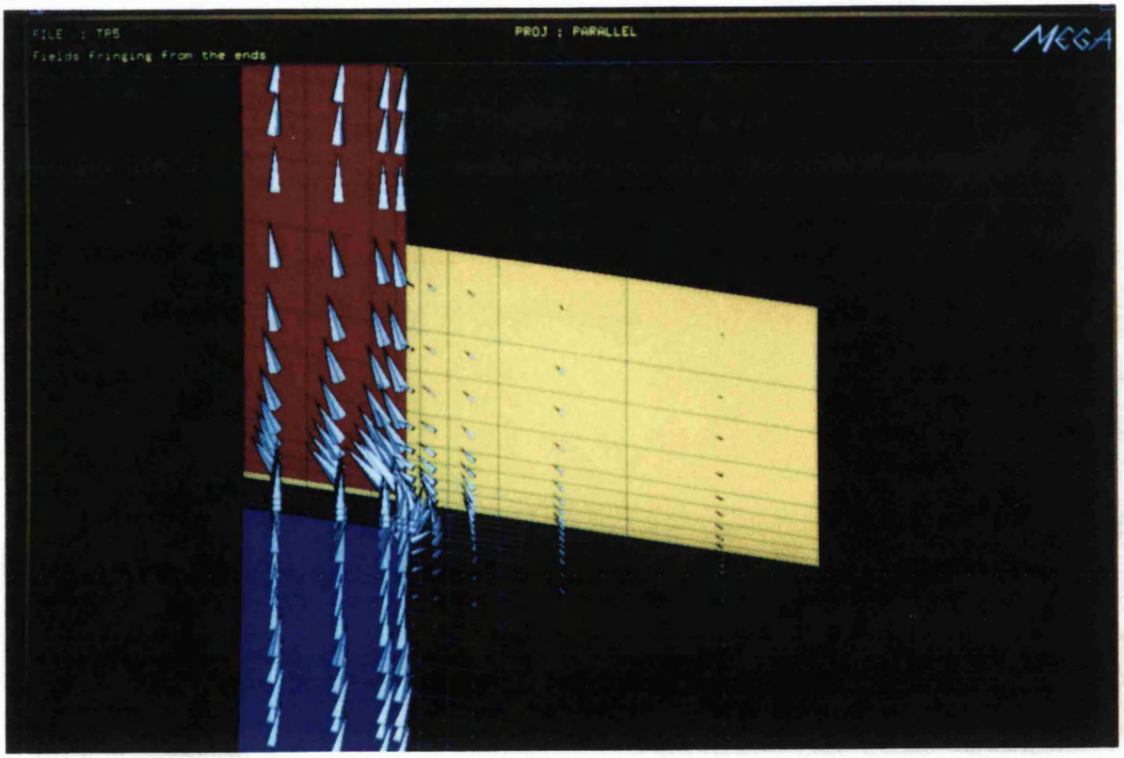

Figure 5.8: Vectors of **B** on an axial cut

Figure 5.9: Field pattern with rotor 6° from aligned position

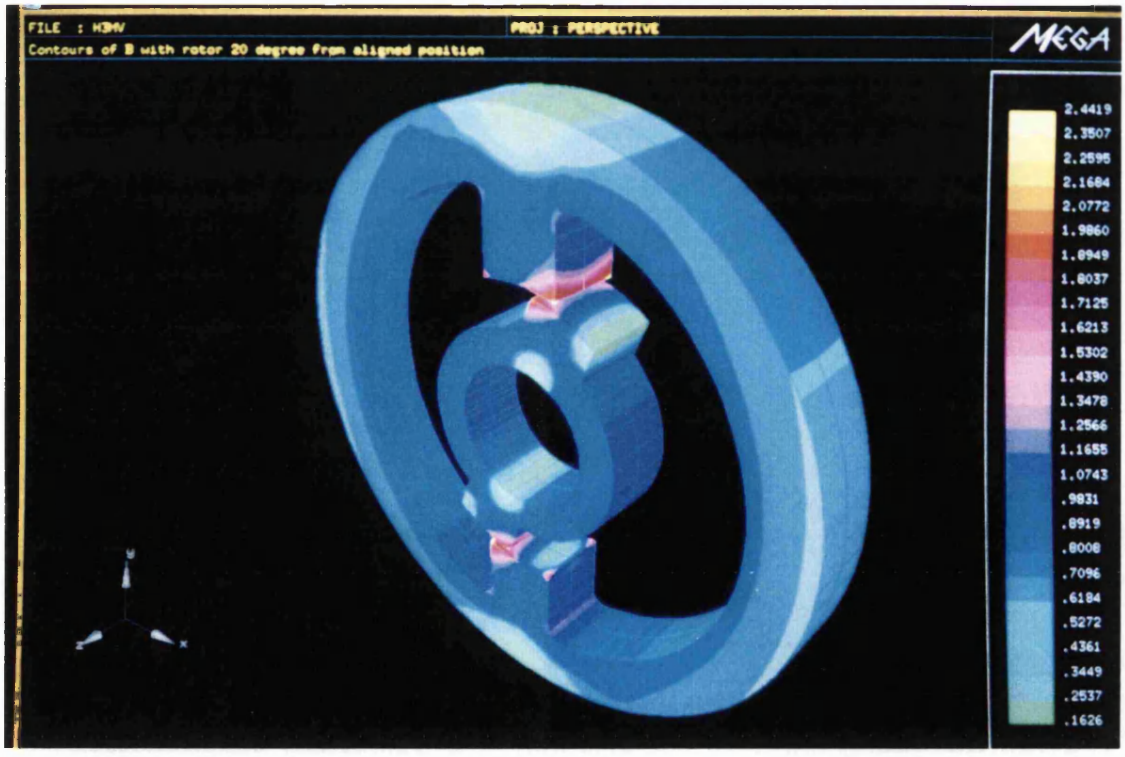

Figure 5.10: Field pattern with rotor 20° from aligned position

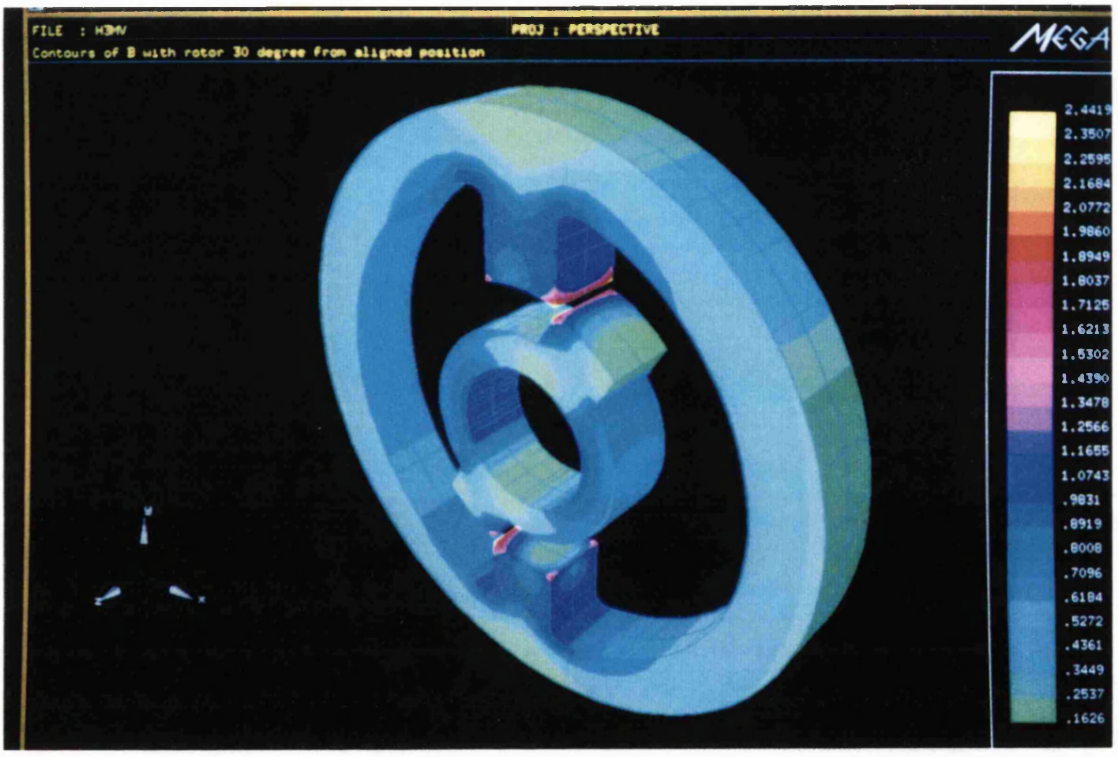

Figure 5.11: Field pattern with rotor 30° from aligned position

5.6 Computational Time Penalty

Although the Lagrange multipliers method offers considerable flexibility in meshing difficult geometry and in the modelling of moving parts, it has, at the same time, introduced some potential drawbacks into the solution solving phase. The most notable ones are :

1. Increased number of unknowns,
2. zeros on the diagonal of the Lagrange rows and
3. saddle point nature of the modified functional.

The extra unknowns are the Lagrange multipliers. This number depends on the number of interface nodes of the mesh which accommodates the Lagrange Multipliers. As the Lagrange Multipliers only exist on the interface, this number is usually reasonably small compared with the total number of unknowns in the system. Typically, it is about 5% of the total number of ordinary nodes.

As pointed out earlier, the system matrix resulting from the use of the Lagrange Multipliers Method possess zeros in the diagonal of the Lagrange rows. A direct consequence of this is the indeterminate nature of the sign second derivatives of the Lagrange functional. By analogy with the calculus of ordinary functions, the Lagrange functional has the saddle point property. The diagonal zeros may cause difficulties in the pre-conditioning phase of an ICCG technique if care is not being taken. As it turned out, by ensuring that each Lagrange multiplier row comes after all of the ordinary variables which it couples together, the presence of these zeros does not seem to cause any difficulties.

To obtain some measure of how much computationsl time penalty the Lagrange multipliers method has put onto the solution phase, six rotor positions were modelled individually using both normal Finite Element meshes and the Lagrange multipliers method. The time taken to solve the models were compared. Each mesh used in the normal Finite Elements solve was created by remeshing the air gap of the corresponding Lagrange multipliers mesh so as to minimise extra complications due to different mesh patterns. Care was taken to minimise the presence of distorted elements in the air gap. However, as both the stator and rotor mesh near the air gap have different number of nodes and distribution patterns, their presence is sometimes difficult to avoid. The number of unknowns of each model was also made to be roughly equal to that of the corresponding Lagrange multipliers mesh. On average, each has about 1000 less unknowns than the corresponding Lagrange multipliers mesh.

Table (5.1) shows the time comparison. The time is the total cpu time taken on a DEC α 3000 workstation. Each Lagrange multipliers model took about 25% more time to solve than the corresponding normal model solved using normal Finite Elements techniques. Only a small portion of the extra time was spent on the evaluation of the extra surface integral of equation (5.8) and its assemblage into the system matrix. The majority of which, however, was expended on the ICCG stages.

However, a convenient feature resulting from the use of the Lagrange Multipliers method is that this six positions can be made to solve in succession. At the end of each position, the solver automatically rotates the rotor to the next position and repeat the solve again. By using the answer of the last position as the starting vector, the solution converges very rapidly. In fact, the total solution time for the

six positions was reduced to 208 minutes using this approach which is 20% less than the total for the normal Finite Elements method.

Degree from aligned position	Normal FE (minute)	Lagrange multiplier	
		(minute)	% increase
20	39.8	49.6	24.6
22	40.2	49.0	21.9
24	39.3	48.2	22.6
26	40.6	50.7	24.9
28	43.2	54.2	25.5
30	43.1	55.4	28.5
Total time	246.2	307	24.7

Table 5.1: Computation time comparison

5.7 Conclusions

This chapter has extended the idea of the Lagrange multipliers method to three dimensional Finite Elements. The development of the method has concentrated on magnetostatic problem modelled using magnetic scalar potentials. A numerical implementation of the method has been described.

Verification with experimental data has been carried out and results were good. The superiority of the 3D results over that of the 2D FE only serves to highlight the inherent limitations of the latter in modelling short structures like the test rig which produce magnetic fields that exhibit a considerable amount of variation in all three directions.

There were initial concerns on the possible computational difficulties/penalty imposed on the solution stage by the method. The presence of zero diagonals was particularly disquieting. Tests, however, have shown that the pre-conditioned BICCG solver used is well capable of handling the resulting matrix. Nevertheless, individual models solved using the Lagrange multipliers method on average take about 25% more time than a comparable normal finite elements mesh. This is acceptable considering the amount of time saved on the pre-processing stage. On the other hand, problems which require multiple positions to be solved will benefit from the method.

Chapter 6

Some Practical Applications

6.1 Introduction

The previous chapters have shown how the Lagrange multipliers method can be implemented in 2 and 3D Finite Elements. The various operational aspects of the method have been studied. The method has also been verified experimentally and the results were found to be favourable.

One of the aims of studying the method in the context of Finite Elements is to develop a convenient and reliable scheme whereby situations which pose considerable difficulties to current Finite Element techniques can be handled more readily. These include problems in which complex 3D shape objects are modelled and, as mentioned in Chapter 1, cases in which a series of solutions are required in order to obtain certain positional dependent characteristics of a device.

The method has been implemented into the Finite Element package *MEGA* and in this chapter, the effectiveness of the Lagrange multipliers method in tackling these types of problems will be examined. In particular, the method will be applied in modelling magnetostatically the following two devices.

1. A Claw-Pole car alternator and
2. A Switched Reluctance motor.

The car alternator has a stator and rotor which are complex in shape. It is troublesome to model because the features of these two parts are so different both circumferentially and axially that it is almost certainly guaranteed that their discretization patterns along these 2 directions will be totally incompatible with each other. As a result, the meshing of the intermediate air will become even more difficult.

In contrast, the difficulties in modelling the Switched Reluctance motor lie not in its discretization into finite elements but in the fact that many rotor positions have to be modelled. This is so because the variations of many of its electromagnetic characteristics are usually sought after by researchers and designers in the analysis and optimisation process of the device. The problems of modelling moving parts have been discussed in Chapter 1.

6.2 Car Alternator

Within the framework of modern vehicles there is an elaborate network of electrical equipment ranging from simple license-plate lamps to complex fuel management systems. At the heart of this network lie the battery and the alternator which are responsible for the supplying the electrical power.

The car alternator is basically a small three phase A.C. generator. Fig.(6.1) shows the basic construction of a typical claw-pole type car alternator. This type of alternator offers compact construction with favourable power characteristics and low weight. The stator is made up of insulated laminations which are pressed together to form a laminated core. It carries a three-phase winding in the slots, the output of which is taken directly from the terminals of the winding. The field winding is a simple toroidal shaped coil enclosed between the two rotor pole. Their claw-shaped pole fingers, hence the name claw-pole alternator, intermesh to form the north and south poles. Current is supplied to the field winding via carbon brushes pressed against the ends of two slip-rings to which the winding is connected.

Rectification of alternator output is achieved by means of six silicon diodes in a full-wave three-phase bridge connection. The diodes are often built into the bracket at the slip-rings end of the machine. At normal operating speeds, the alternator is self-excited by currents rectified by three field diodes. The level of field excitation is controlled by the voltage regulator. Fig.(6.2) shows a typical alternator circuit.

With more and more electrically operated components being installed in today's vehicles, the efficiency and reliability of the alternator have become more and more critical. At the same time, there is also the constant drive from companies to drive

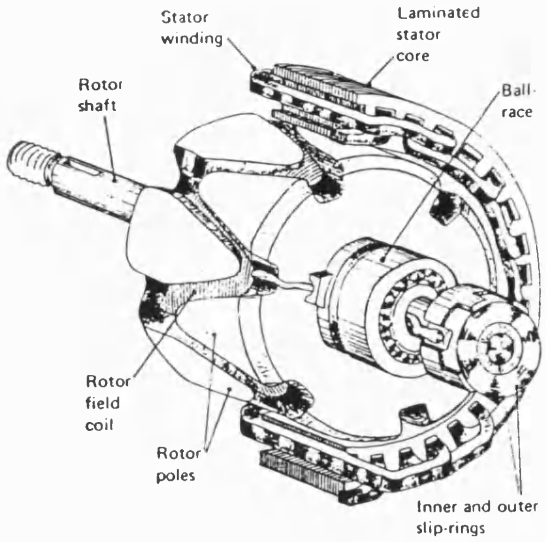

Figure 6.1: Car Alternator

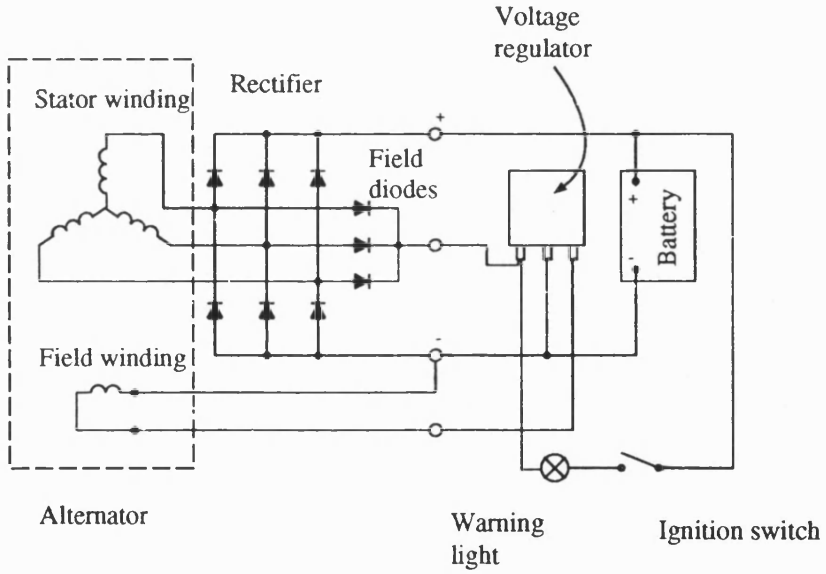

Figure 6.2: Typical self-excited alternator circuit

the material and manufacturing cost down in order to stay competitive. Traditionally, the design process of the alternator relied heavily on the testing of prototypes.

The process is quite time consuming and it is difficult to obtain from it a clear picture of how the flux is distributed or where saturation is occurring to aid the design process. The Finite Element method is well capable of producing this missing information.

Although there are no conceptual difficulties for the Finite Element method to handle the complex shape of the parts of the alternator, the creation of a finite element mesh to describe the geometry of the device usually is not as straightforward as one would like. In the following sections, it will be shown how the Lagrange multipliers method developed earlier can be used to help to analysis one such alternator.

6.2.1 No Load Test

The alternator used is a prototype machine by Lucas-TVS. Fig.(6.3) shows a photograph of the machine. It is a claw-pole type alternator with 12 rotor poles. The field winding has 434 turns and is housed between the two claw-pole halves. The stator is laminated and has 36 slots. Each stator phase is wound as a single layer wave winding, joining with the other two phase windings at one end to form a star connection. There are 8 turns per coil.

No load tests on the alternator were carried out at Lucas. The rotor speed was set at 1000rpm and the field current was controlled externally. The test was performed over a range of field current, from 0.5A to 4.5A. The open circuit line to line voltage waveform was measured at the desired field current values. Table(6.1) gives the results obtained. Since the line to line voltage waveforms of the 3 phases were found to be reasonably sinusoidal and also balanced with each other at all levels of field

current used, only the voltage of one of the 3 phases is therefore given in Table (6.1) as a representative result. The sinusoidal nature of the output voltage will also be taken up again later in the estimation of its value using the Finite Element results.

Field Current I_f (A)	Rms Line to line voltage V_l (V)
0.5	2.52
1.0	4.55
1.5	6.55
2.0	7.98
2.5	8.93
3.0	9.38
3.5	9.66
4.0	9.98
4.5	10.28

Table 6.1: Table of open circuit test results

6.2.2 Finite Element model

The Lucas alternator was modelled with 3D Finite Elements using *MEGA* [27]. A 3D mesh in *MEGA* was created by extruding a 2D base plane into levels along the Z axis. These levels can be thought of as 2D slices throughout the model. Elements are defined between levels and their material properties are appropriately modified to reflect the shape of the object. Although it is not difficult to create a 3D mesh for

the rotor and stator part of the Lucas alternator individually, joining them together has proved to be rather troublesome. This is because the features of the two parts near the air gap differ so significantly that it is very difficult to join them together without creating many distorted elements in the air gap.

Using the Lagrange multipliers method approach, the rotor and the stator can be meshed up separately as before, typically each includes half the air gap. There is no need to join them together topologically. The only requirement on the two meshes is that they touch at a common interface. In the present case, this will be a cylindrical surface spanning around the air gap. Fig.(6.5) and Fig.(6.6) show what the mesh looks like at two different levels, Fig.(6.5) near the tip of one of the rotor pole halves and Fig.(6.6) towards the other end of the same pole half.

Fig.(6.7) shows a 3D view of the model. Due to symmetry, only one-twelveth of the whole alternator was modelled. The yellow region between the two claw poles is the reduced scalar region which encloses the field coil. The field coil is easily defined by selecting from an extensive library of coils provided in the package. The air region is not shown in the figure. A view of the full machine can easily be generated by *MEGA* and is shown in Fig.(6.8). The 3D model has 55775 nodes, 35325 elements and a total of 58040 unknowns. Eight models, each with the field current corresponding to one of the levels used in the experiment, were created and solved as non-linear problems using the **BH** curve of Fig.(6.4) shown below for both the rotor and stator.

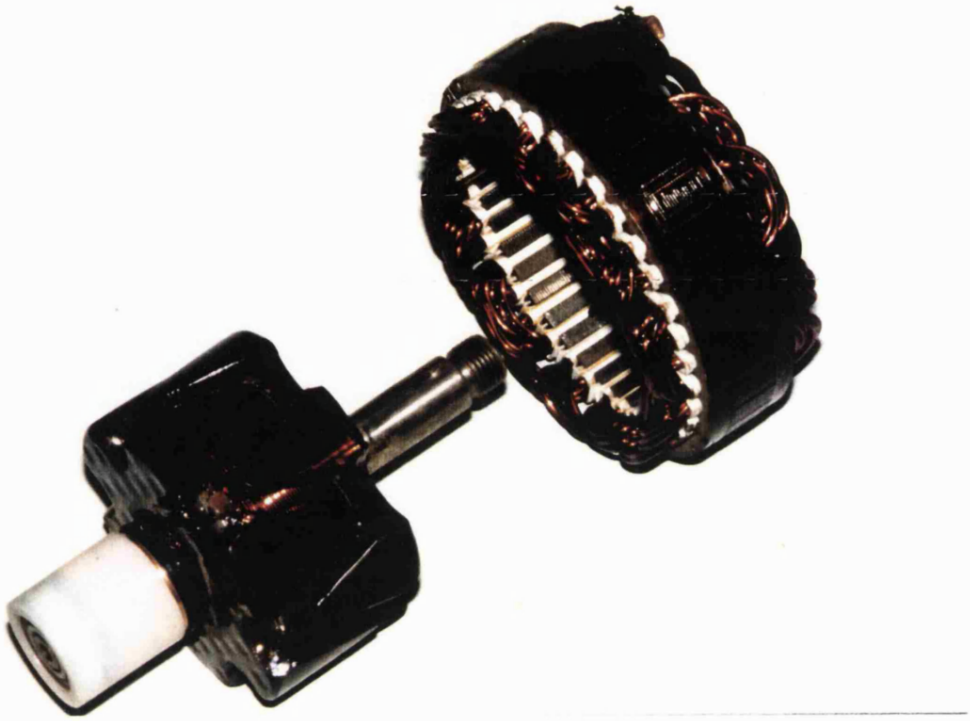

Figure 6.3: The prototype alternator used

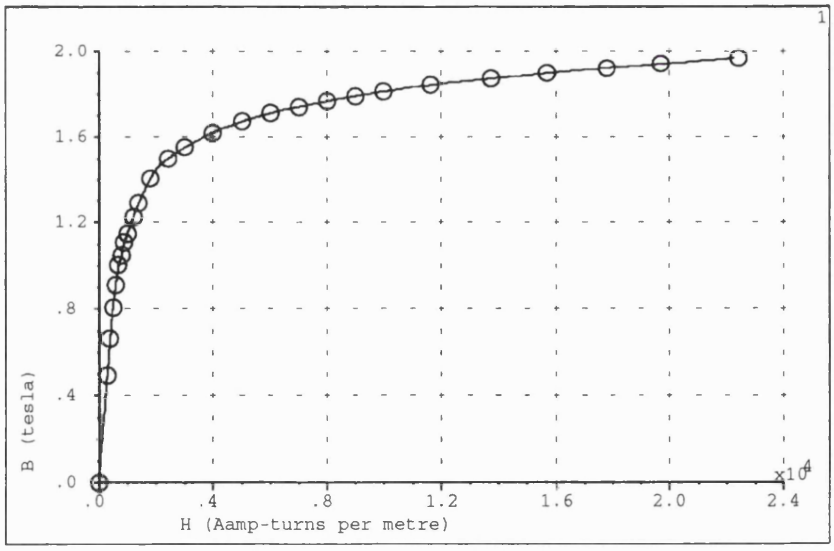

Figure 6.4: Low Carbon Steel **BH** Characteristic

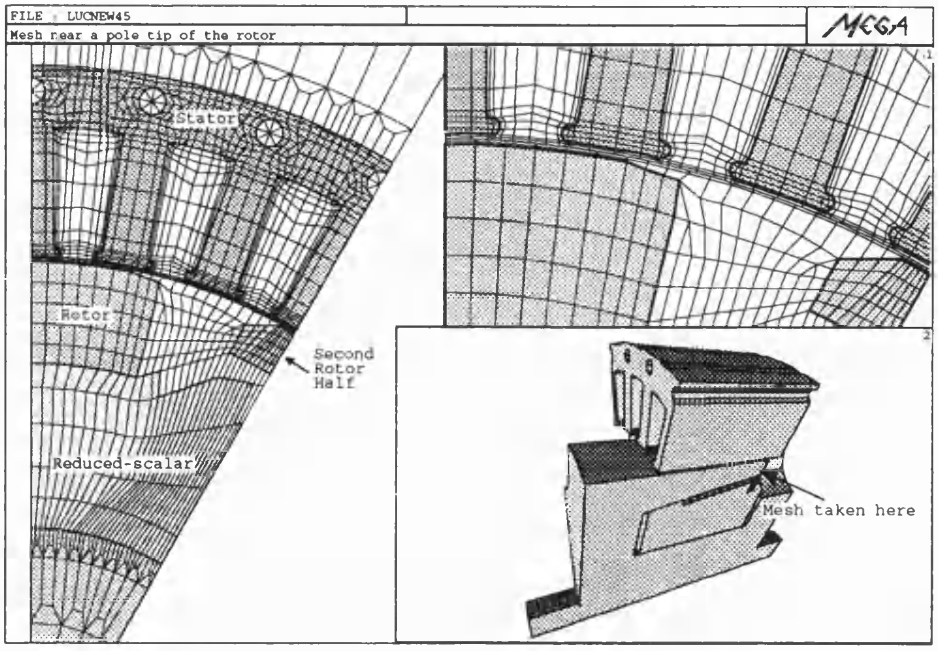

Figure 6.5: Mesh near one rotor pole tip

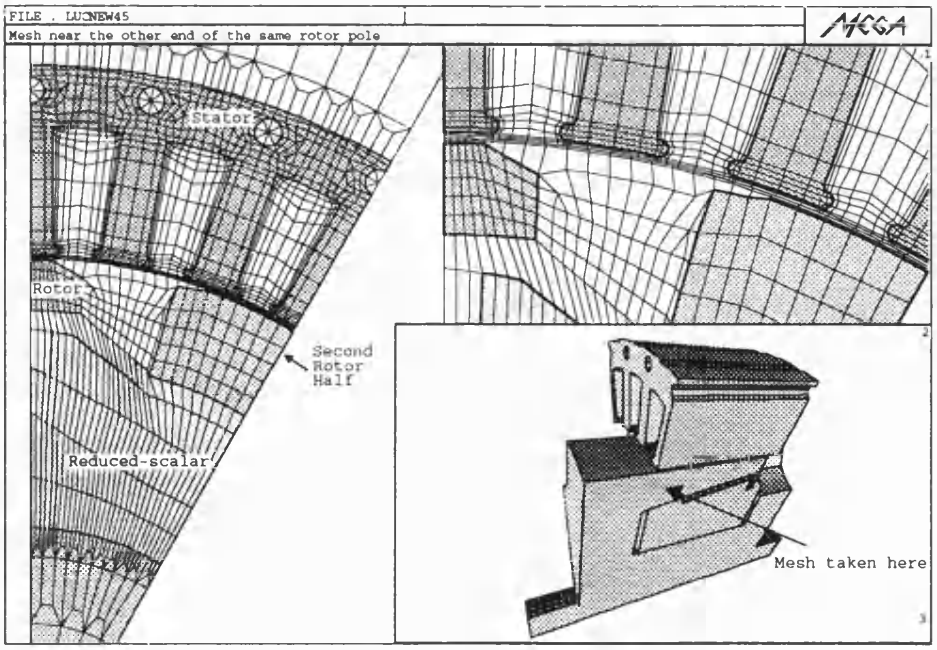

Figure 6.6: Mesh near the base of the same rotor pole

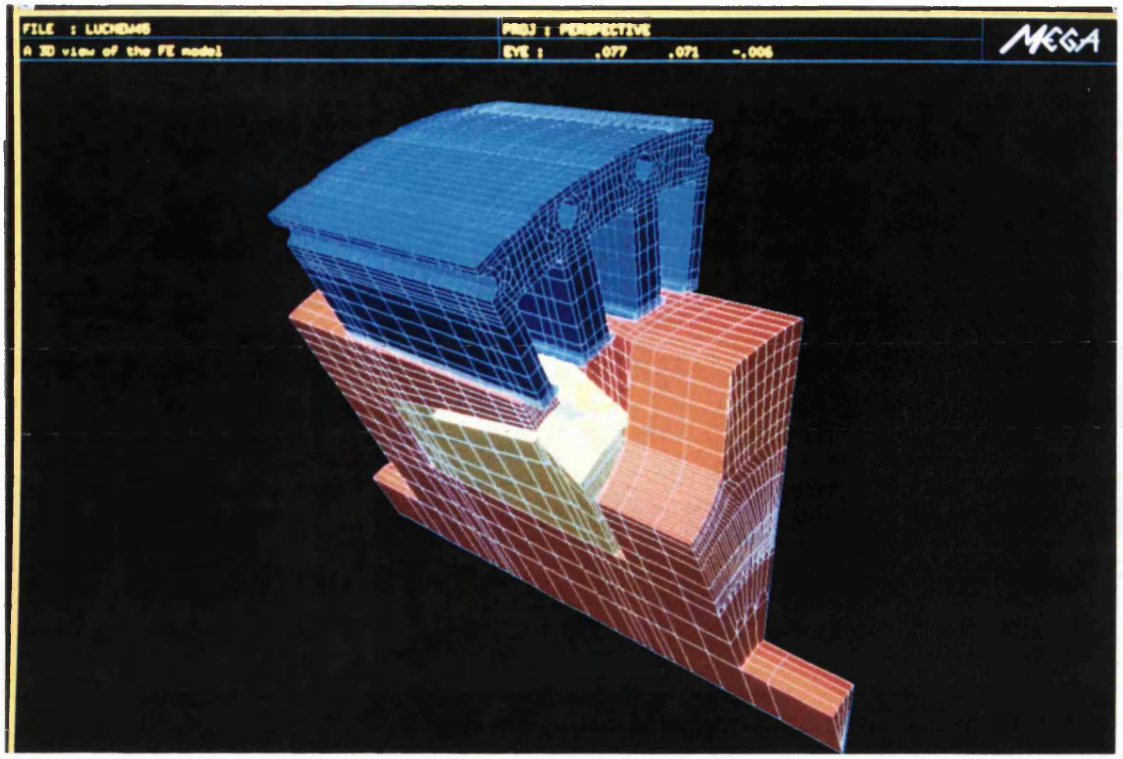

Figure 6.7: A 3D view of the alternator mesh

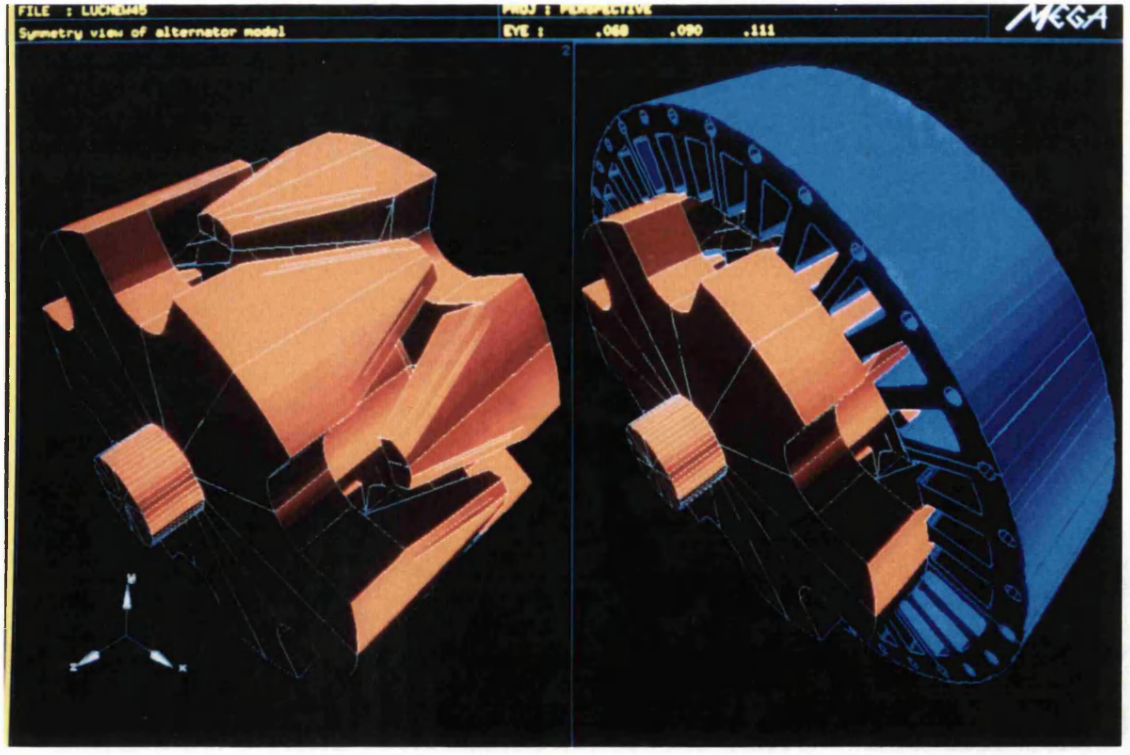

Figure 6.8: Symmetry view of the model

6.2.3 Results

Table (6.2) compares the measured stator line to line voltage to values estimated from the Finite Element results. This comparison is also shown in Fig.(6.9) as graphs. The stator voltage was calculated using Faraday's Law. The flux linking a single stator coil was obtained by integrating **B** over a surface which spanned the coil's space. The flux was also assumed to vary sinusoidally in time in view of the measured output waveforms. With the rotational speed, the number of poles and the number of turns of each coil known, the phase voltage and hence the line to line voltage can easily be calculated.

The voltages calculated from *MEGA* 's results are typically about 5% higher then the corresponding measured value. This is probably because the rotor was modelled with a **BH** characteristic which allows better saturation than the material's actual curve does. This points out the importance of specifying an accurate **BH** curve in non-linear Finite Element analysis. Furthermore, the magnetostatic model does not include the iron and eddy current losses in the stator laminations. It is also informative to see how the **B** field looks in general inside the machine. Fig.(6.10) shows the vectors of **B** near the tip of one of the rotor pole while Fig.(6.11) shows the same kind of vector plot near the stator centre plane. Both showing that there is a noticeable field leaking between the two rotor poles. Fig.(6.12) shows a representative picture of how the **B** field flows in the axial direction. Flux can also be seen leaking out from the tip of the rotor pole.

It is also interesting to estimate the percentage of flux that has leaked away and failed to reach the stator. A rough indicator of this can be obtained by comparing the flux at the centre plane of the the rotor shaft to that linking the stator coil.

Field Current I_f (A)	Calculated voltage V_l (V)	Measured Rms voltage V_l (V)
0.5	2.56	2.52
1.0	5.07	4.55
1.5	7.14	6.55
2.0	8.60	7.98
2.5	9.39	8.93
3.0	9.83	9.38
3.5	10.12	9.66
4.0	10.33	9.98
4.5	10.49	10.28

Table 6.2: Comparing calculated with measured line to line voltages

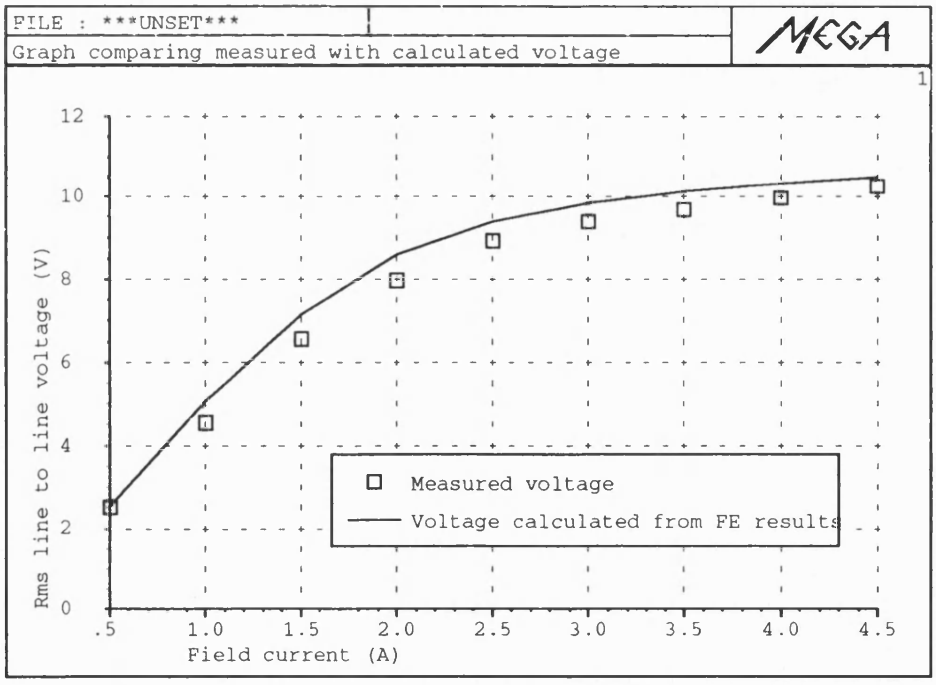

Figure 6.9: Graphs comparing calculated with measured line to line voltages

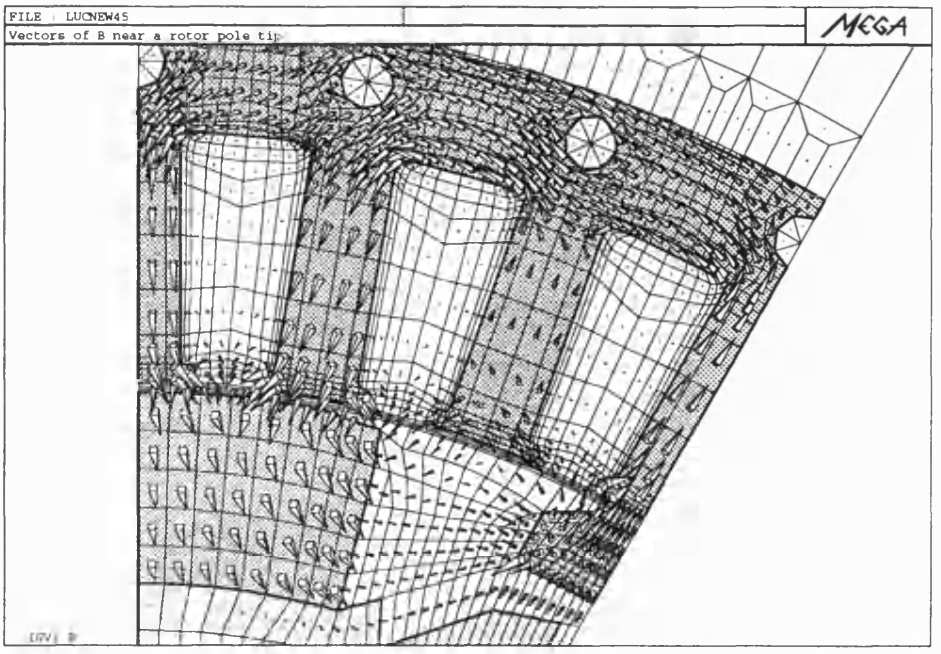

Figure 6.10: Vectors of **B** near the rotor pole tip

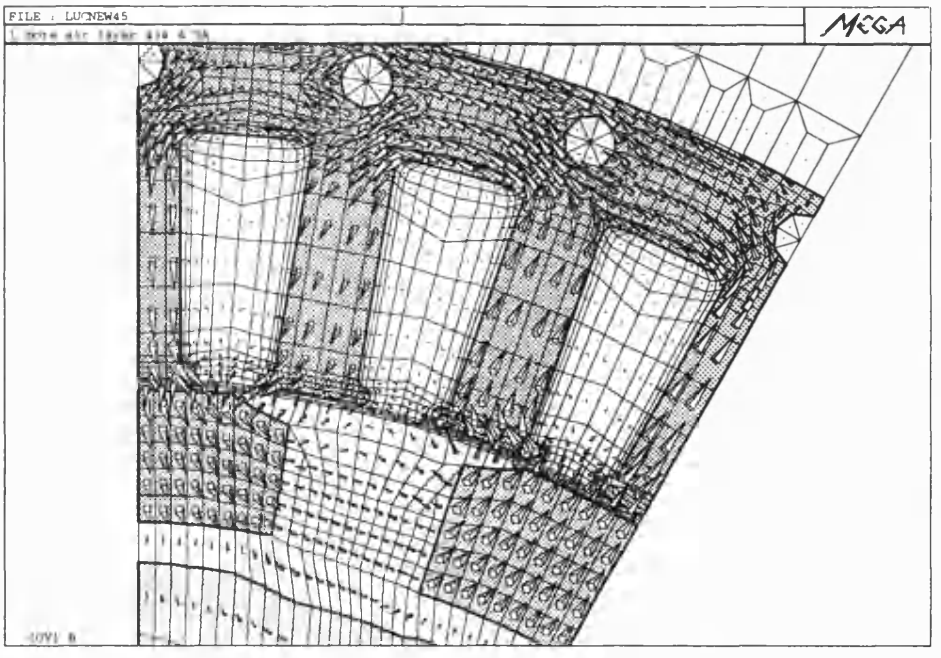

Figure 6.11: Vectors of **B** near mid-plane of stator

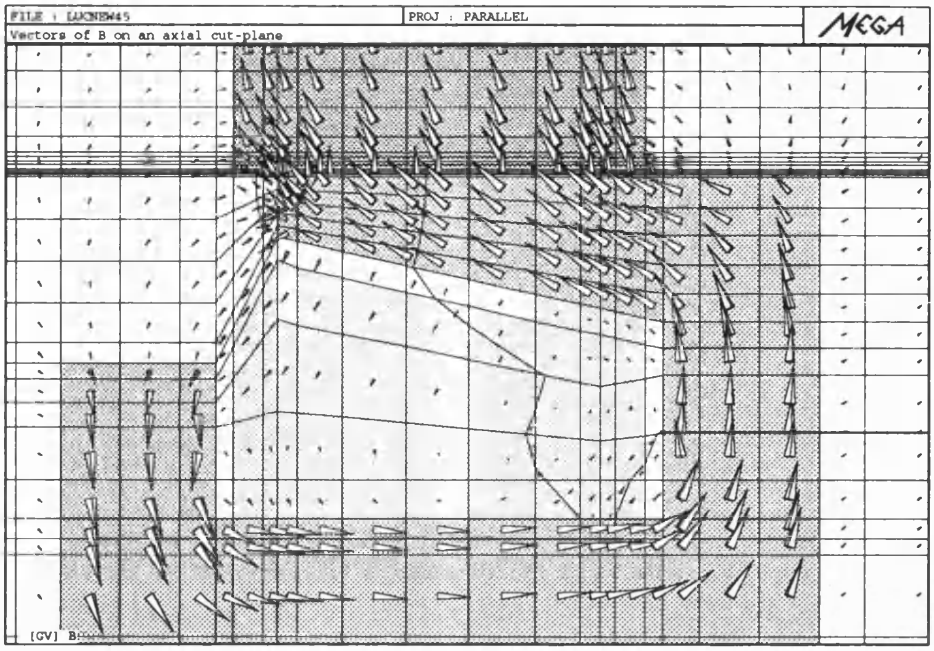

Figure 6.12: Vectors of **B** flowing in the axial direction

Table (6.3) shows this estimation at the various field current level and the same results are also plotted in Fig.(6.13). It is surprising to see that, at best, only about 61% of the main flux has reached the stator, yielding useful output. This was attained at the lowest current level, 0.5A, tested. A moderate increase in the leakage flux at a 1A field current was observed, but as the field current was raised beyond 1.5A, the percentage of main flux reaching the stator suddenly plummeted, signalling the onset of saturation. This is clearly shown by Fig.(6.14) to Fig.(6.17) which are colour contours plots of the modulus of **B** in the rotor. The same colour contour levels were used in all 4 figures and their calculation were based on the solution of the 4.5A model.

At 0.5A field current, the rotor was hardly saturated at all. Saturation began to occur locally at a field current of 1.5A, mostly around corners and the two areas di-

rectly underneath the ends of the stator. Fig.(6.18) is a similar picture as Fig.(6.15) except that the stator is also shown to illustrate this point more clearly. Beyond the 1.5A field current level, saturation spread to other parts of the rotor, resulting in a higher proportion of the newly injected flux being leaked away. At 4.5A field current most parts of the rotor were driven deep into saturation, only about 57% of the main flux managed to link the stator coils. To complete the picture, Fig.(6.19) shows a symmetry view of the 4.5A model with contours.

Field Current I_f (A)	Main rotor flux ψ_m,$\times 10^{-4}$ Wb	Stator flux ψ_s,$\times 10^{-4}$ Wb	Percentage $\frac{\psi_s}{\psi_m} \times 100\%$
0.5	0.567	0.346	61.08
1.0	1.123	0.686	61.04
1.5	1.592	0.967	60.71
2.0	1.936	1.163	60.10
2.5	2.140	1.270	59.36
3.0	2.269	1.330	58.65
3.5	2.361	1.370	58.02
4.0	2.434	1.398	57.45
4.5	2.492	1.419	56.96

Table 6.3: Showing the percentage of the main flux linking stator coils

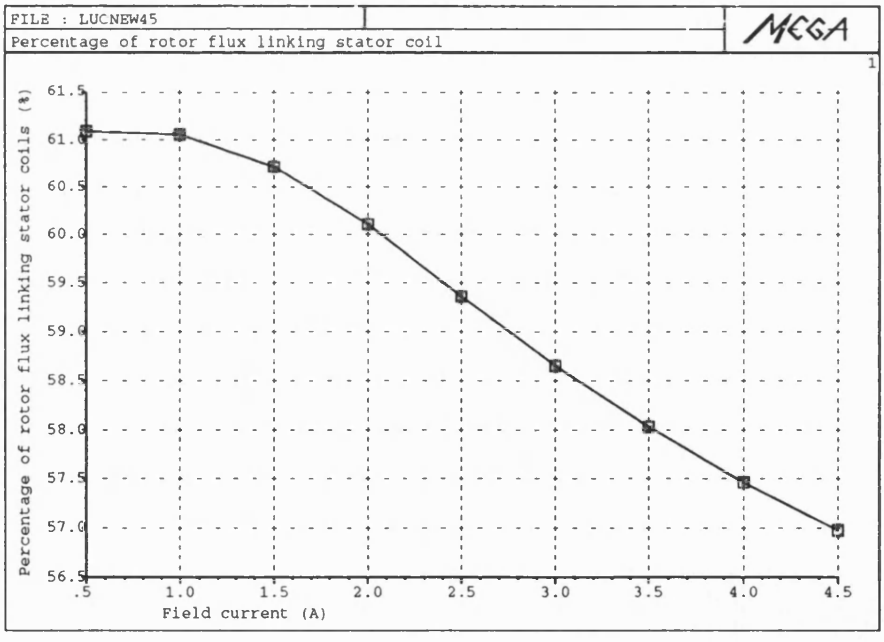

Figure 6.13: Graph showing the percentage of main flux reaching stator at different field currents

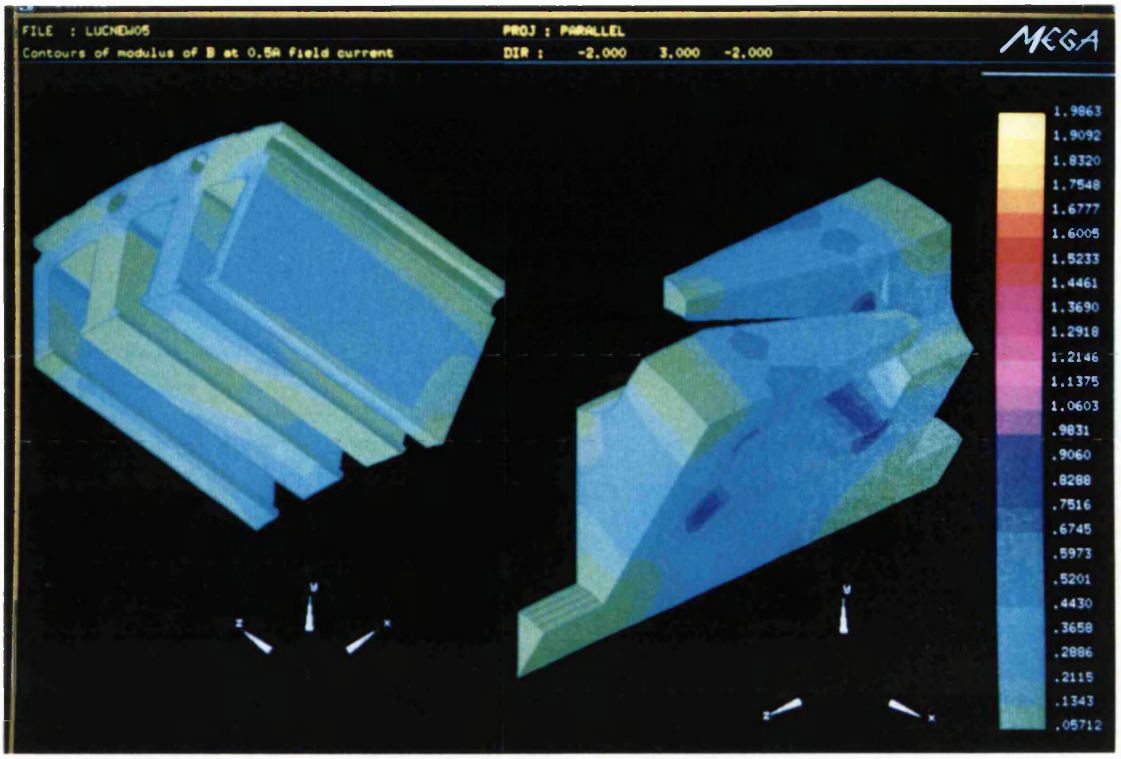

Figure 6.14: Contours of modulus of **B** at 0.5A field current

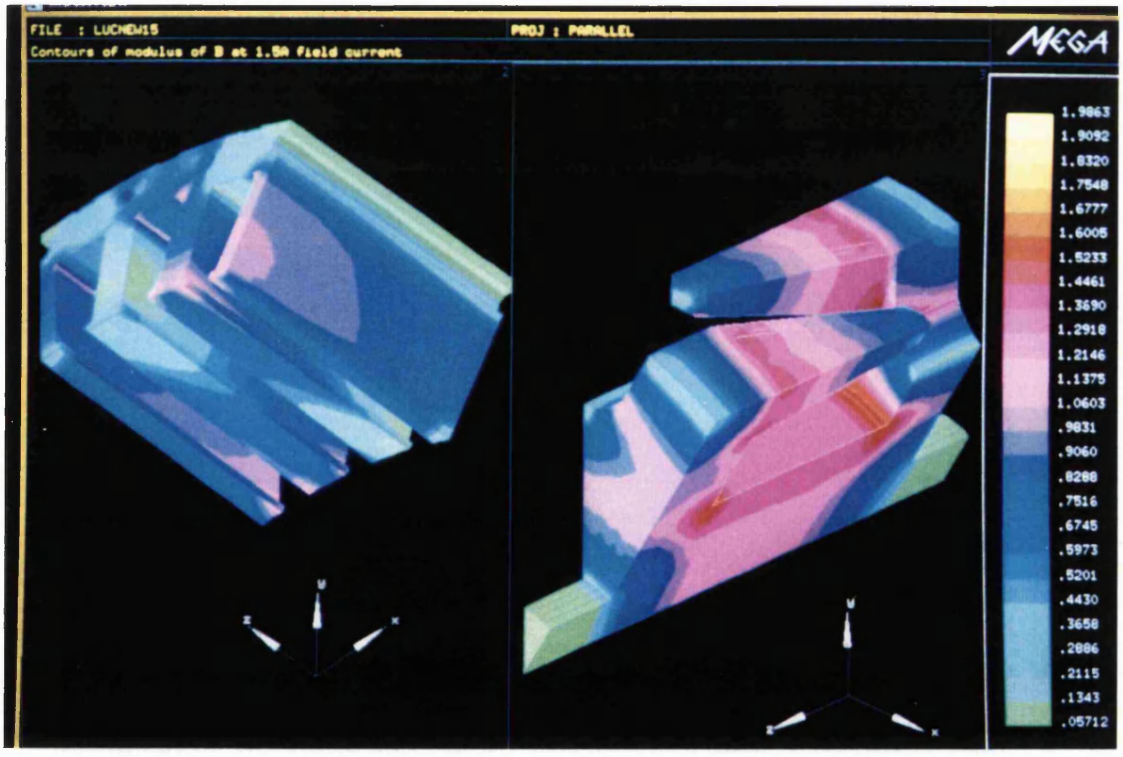

Figure 6.15: Contours of modulus of **B** at 1.5A field current

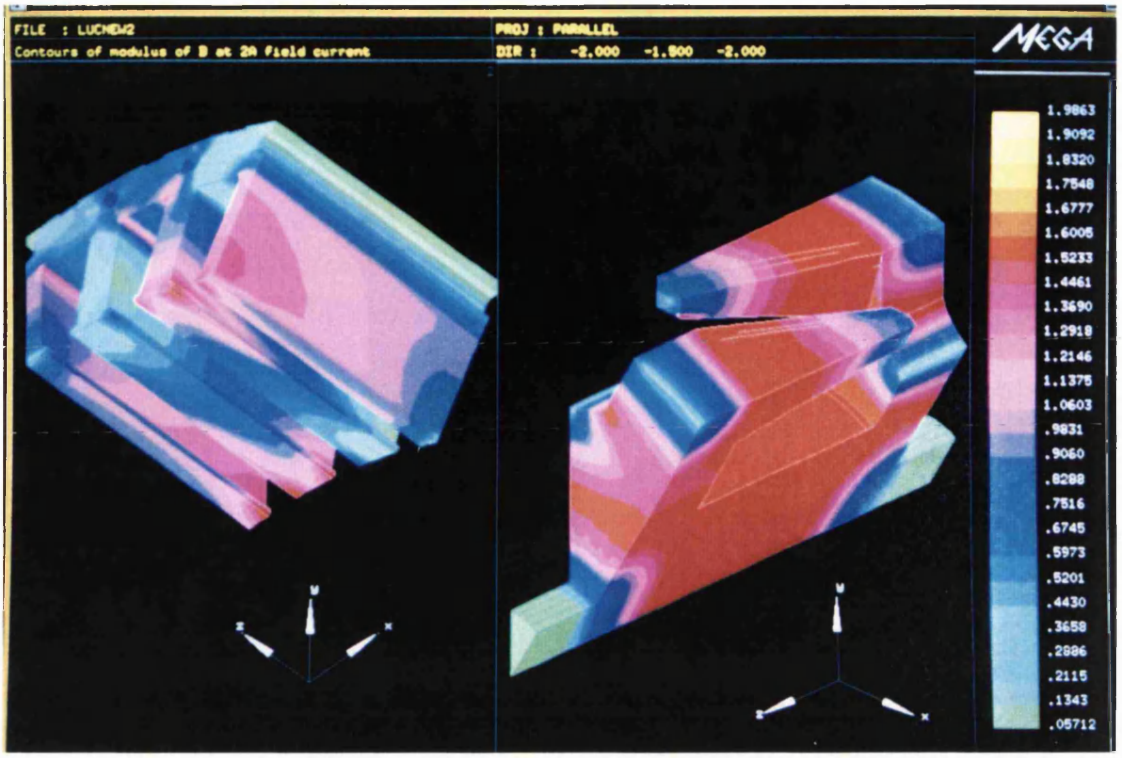

Figure 6.16: Contours of modulus of **B** at 2A field current

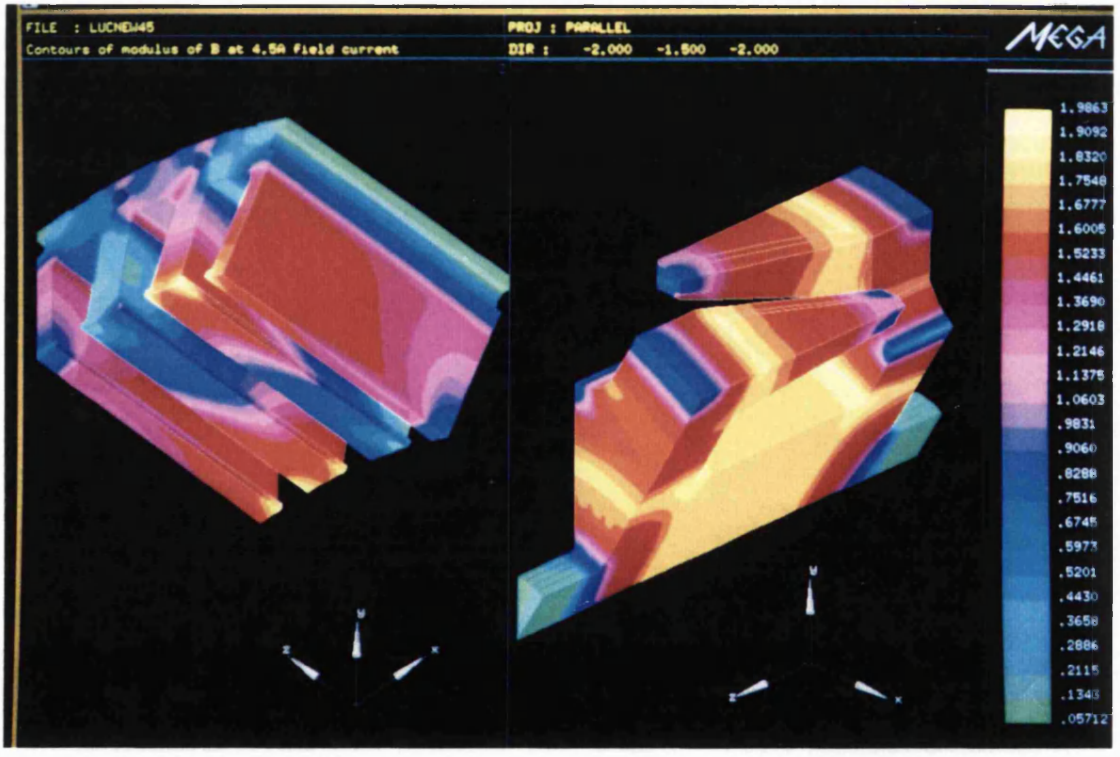

Figure 6.17: Contours of modulus of **B** at 4.5A field current

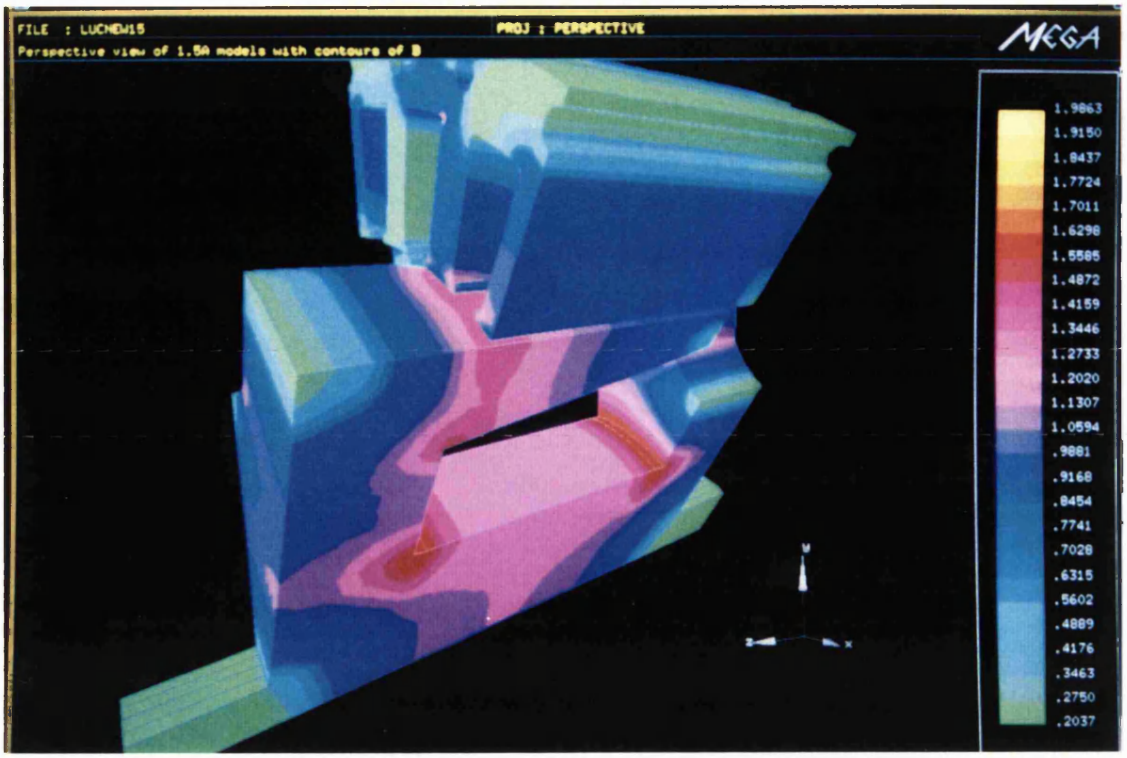

Figure 6.18: 3D contour view of 1.5A model

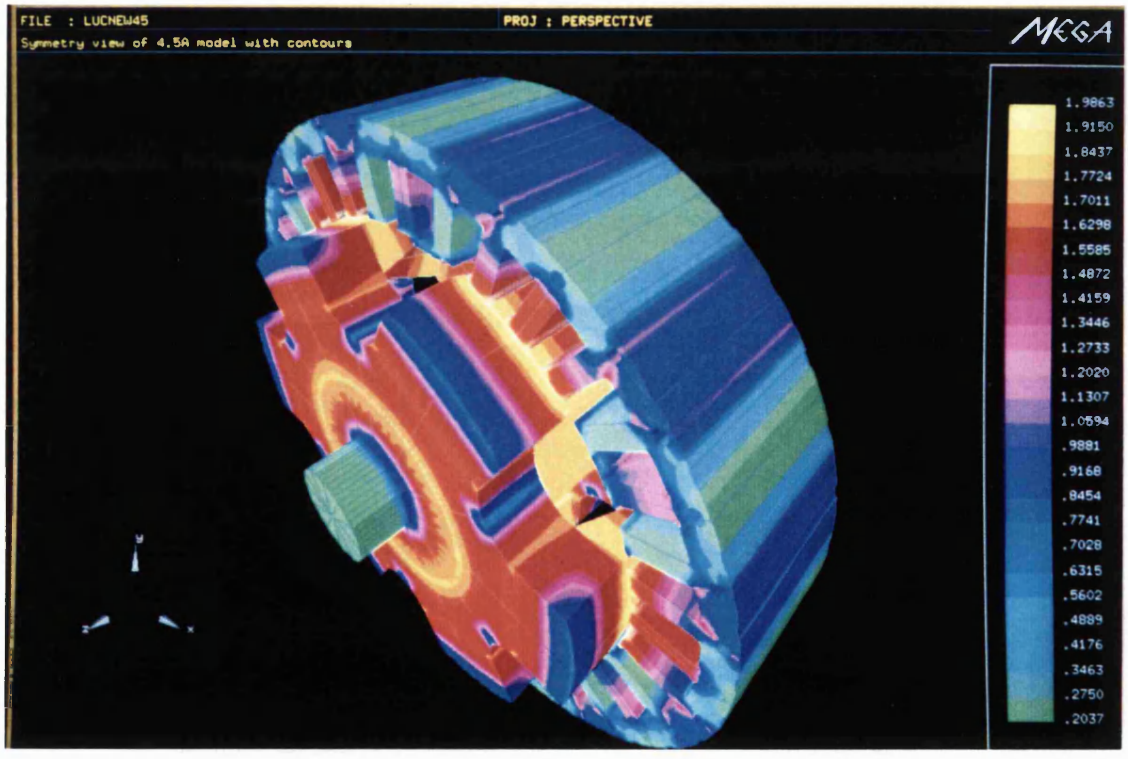

Figure 6.19: Symmetry contour view of the machine at 4.5A

6.3 Switched Reluctance Motor

There has been a considerable amount of research interest over the past two decades in Switched Reluctance Motors (SRM), most probably because of their potential use as variable speed/load drives. Such intense research activities have resulted in many interesting and stimulating papers, [28] to [29] are just some examples. Another fruitful outcome is the establishment of the SRM drive as a viable and attractive alternative to conventional D.C. and A.C. inverter drives.

The SRM has a simple but robust construction. The stator and rotor are usually constructed from laminated iron and have unequal numbers of salient poles. The rotor poles do not carry any windings. Only the stator poles have simple concentrated windings mounted on them. Typically, windings on diametrically opposite stator poles are connected in series to form a phase. A typical 3 phase SRM is shown in Fig.(6.20), it has 6 stator poles and 4 stator poles, hence it is referred to as a 6–4 SRM. Each phase windings is excited in accordance with the rotor position such that a torque will be produced which tends to align adjacent stator and rotor poles together so as attain a minimum reluctance configuration. Rotor position sensors are therefore needed to control the switching of the phases. Because the direction of the winding current is unimportant, a particularly simple unidirectional inverter can be used as the switching circuit. A schematic circuit of a simple converter circuit suitable for the 3 phase motor is shown in Fig.(6.21). Other circuit configurations are also possible. By controlling the switching angles of the phases, the desired speed/torque can be achieved.

In order to increase the output torque, the air gap of the motor is made very small

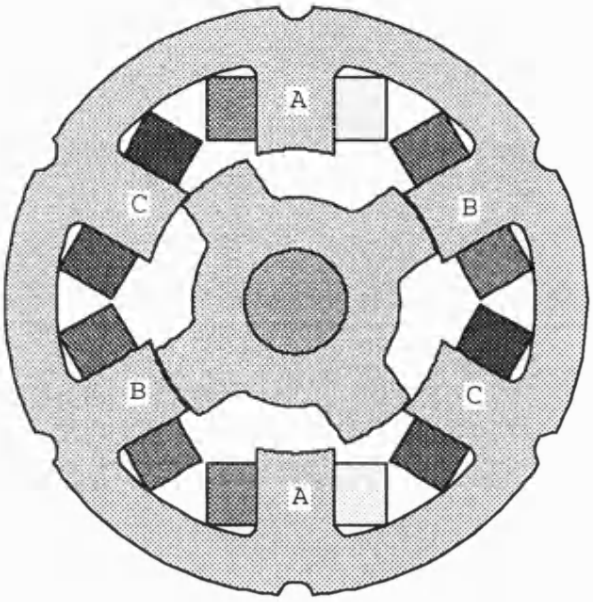

Figure 6.20: A 3 phase Switched Reluctance Motor

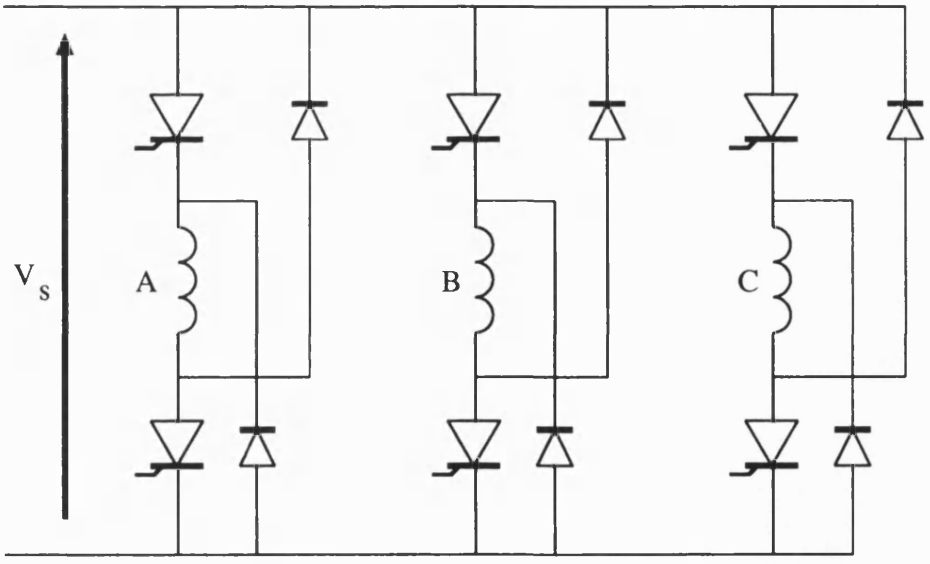

Figure 6.21: Schematic converter circuit for a 6–4 SRM

and it is customary to operate the motor under highly saturated conditions. As a result of the saturation, the effective magnetic geometry of the SRM will go through a few cycles of changes in one revolution, making it difficult to use a conventional approach to analyse the machine. The Finite Element method is ideally suited for modelling such a highly non-linear magnetic structure. Indeed, papers based on Finite Element analysis of the SRM have been published before, [30] [31] [32]. Although they were limited to two dimensional analysis, they represent a significant advance in predicting the performance of the motor.

The difficulties in modelling SRMs using Finite Elements do not lie so much in the discretization of its geometry which is simple compared to, for example, the earlier car alternator or the handling of the severe saturation when two poles overlap but in the determination of the variation of certain physical characteristics with respect to both current and rotor position. Typical examples of these are the torque characteristic and the flux/inductance characteristics which are useful in estimating the rating of circuit components required. Such studies inevitably mean that the motor has to be modelled at different rotor positions, which brings back all the problems mentioned in Chapter 1.

The Lagrange multipliers method can be used to handle this problem easily. The next few sections will demonstrated how this can be done. The more interesting case of including the model of the converter circuit into the Finite Element analysis will also be presented at the end.

6.3.1 Two Dimensional Finite Element Modelling of the SRM

The SRM used was built and extensively measured at Lucas [9]. It has 6 stator and 4 rotor poles. The cross-sectional dimensions of the stator and rotor are given in Fig.(6.22); its axial length is 0.0721m. The laminations are made of TRANSIL 315 steel and the **BH** characteristic used in the FE analysis is shown in Fig.(6.23). It has 3 phases, and each stator winding carries 18 turns.

The motor was first modelled with *MEGA* as a 2D magnetostatic problem. Only one phase winding of the motor was excited with a constant current. Fig.(6.24) shows the 2D mesh used. It is known that heavy local saturation occurs within a very small area near the poles tips at the beginning of their overlap, so failure to model this effect accurately will lead to inconsistent results [9] [33]. The mesh was therefore made reasonably fine especially around the air gap region to cater for these positions where the poles begin to overlap.

This model contains 8647 nodes and 8368 elements. An enlarged view of it near the air gap is given in Fig.(6.25). It can be seen that the model is in fact made up of two meshes touching each other in the centre of the air gap. Lagrange multipliers are again used to link them together. The advantage of adopting this approach is that different rotor positions can be solved without the need of any remeshing at all. To solve a new position, it is only required to rotate the rotor by the desired angle and the model is resubmitted for solving. In fact, an even more convenient way of dealing with this type of problem has been implemented in *MEGA* ; a special command which allows the user to specify the number of positions to be solved and the displacement between consecutive positions. At the end of each position, the solver will automatically rotate the rotor by the specified angle and repeat the

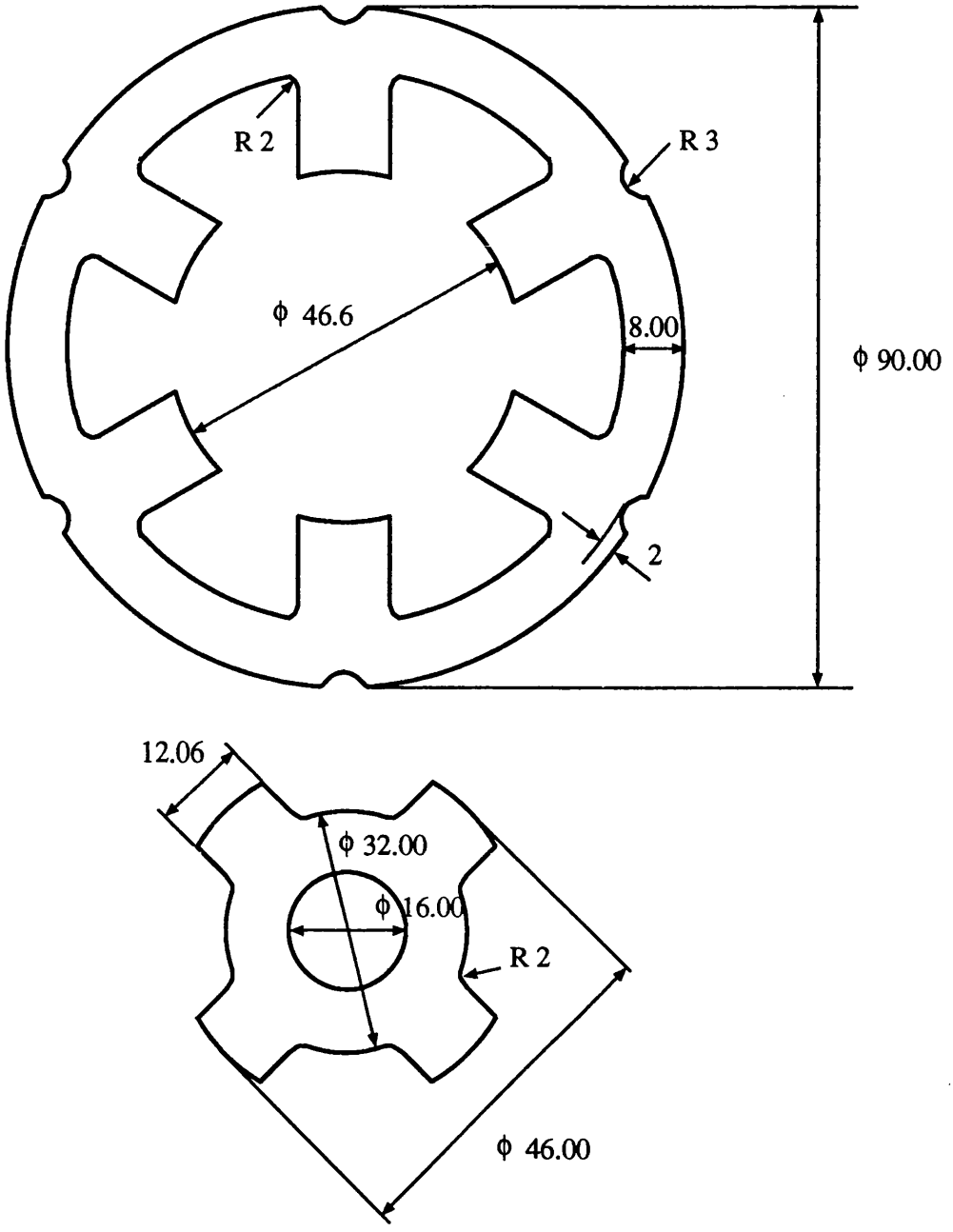

All dimensions in mm

Figure 6.22: Lamination Dimensions

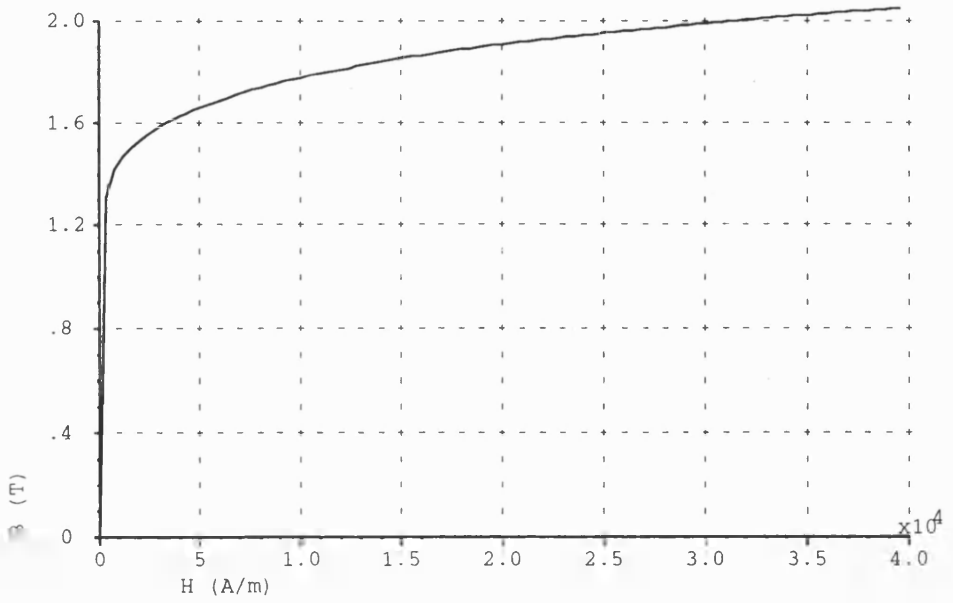

Figure 6.23: **BH** characteristic for the laminations

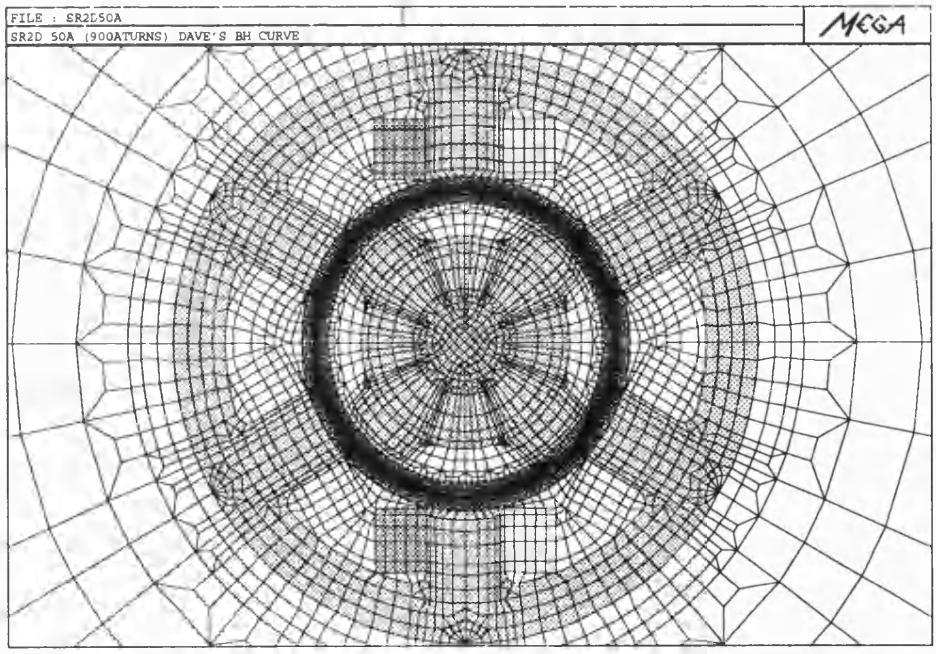

Figure 6.24: SRM mesh used in the 2D analysis

solve again. The task of solving a multiple positions problem is reduced to one simple command set-up call in the pre-processing stage. An additional advantage of this approach, as shown before, is that the non-linear solution of a new position converges very quickly as the answer of the last position can be used as the starting vector.

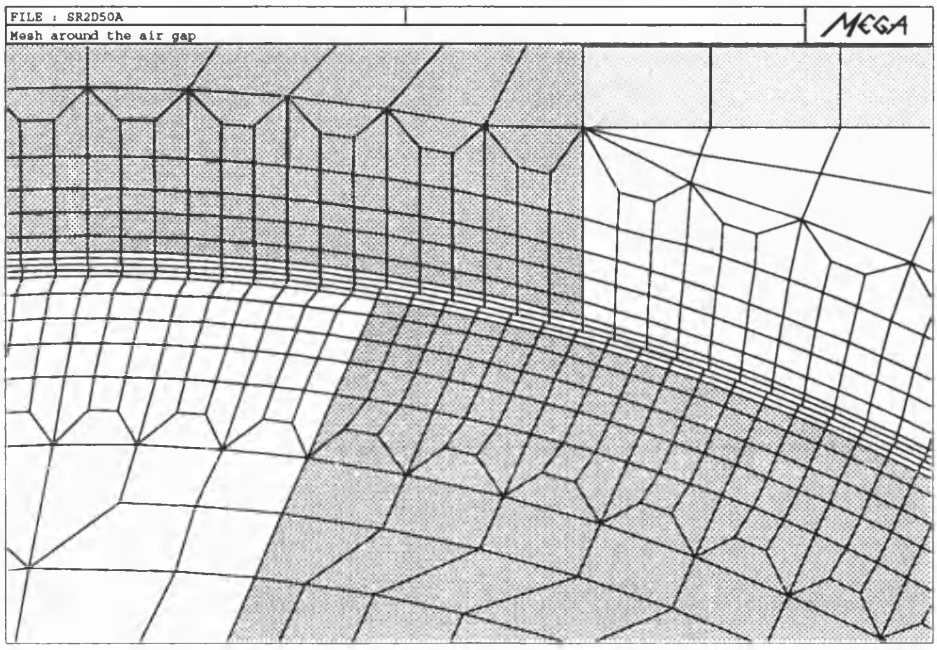

Figure 6.25: Enlarged view of the air gap region

To obtain proper profiles for the torque, inductance, co-energy, it is necessary to model the motor as the rotor moves from the unaligned to the aligned position. Unaligned position is the position in which the rotor pole is opposite the stator slot, whereas in the aligned position, the stator and rotor poles are opposite each other. In this particular case, the aligned and unaligned position are 45° apart; 46 rotor positions, each 1° apart, were solved. Fig.(6.26) compares the measured and

calculated torque at a field of 50A. The torque was calculated using the Maxwell-Stress method and also from the rate of change of co-energy. The unaligned position was arbitrary taken to be the 0° position.

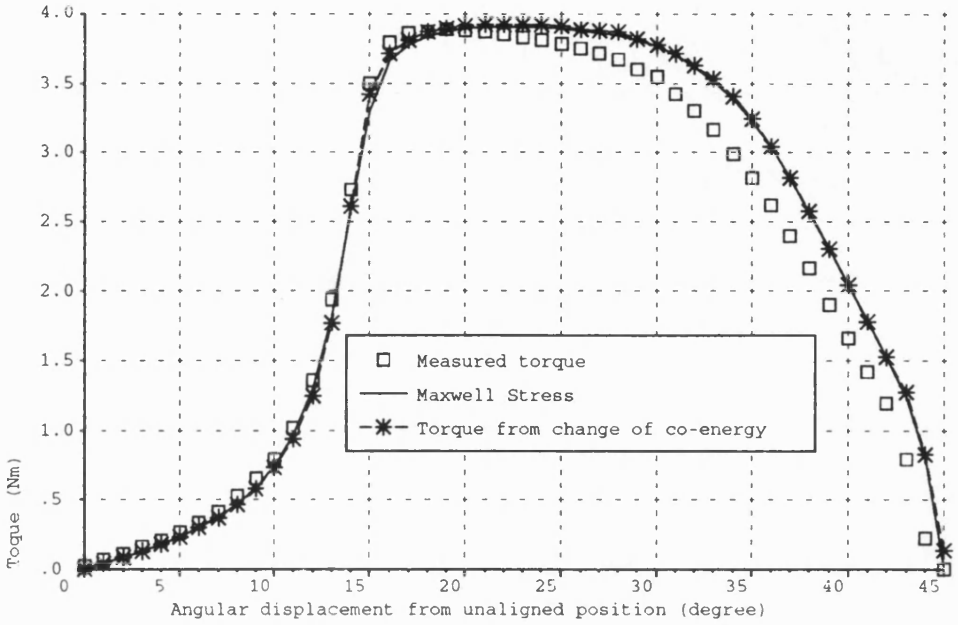

Figure 6.26: Comparison of measured and 2D calculated torque at 50A field current

It can be seen that the two calculated torques agreed with each other quite well. The consistency of these two values with respect to each other is usually an indication of whether the field in the air gap when overlap occurs is being modelled accurately. Previous results, [9] [33], have shown that the Maxwell-Stress method of torque calculation is very sensitive to the accuracy of the fields in its integration path, the air gap in the present case. The presence of distorted elements or elements which have a large aspect ratio in the air gap will lead to inconsistency in the calculated torque. This problem has been relieved somewhat by the use of the

Lagrange multipliers method. As there is no need to match the rotor and stator mesh on their interface, the mesh in and around the air gap can be made to be as well-formed as it is practically allowed. Nevertheless, sensible meshing on both sides is still an important factor to bear in mind. The agreement between the measured and calculated torques are, however, not as good especially after the two poles have overlapped substantially. These discrepancies are thought most likely to be due to a departure of the manufacturer's **BH** data from the laminations' actual characteristic, though neglecting the end effect also contributes errors.

Fig.(6.27) to Fig.(6.30) show the colour contour plots of the modulus of **B** and the contours of **A** . The existence of severe local saturation around the poles tips is clearly displayed in Fig.(6.28). This slowly gave way to the overall bulk saturation as the poles overlap more. Fig.(6.31) shows an overall comparison of the measured and calculated torques at various current levels.

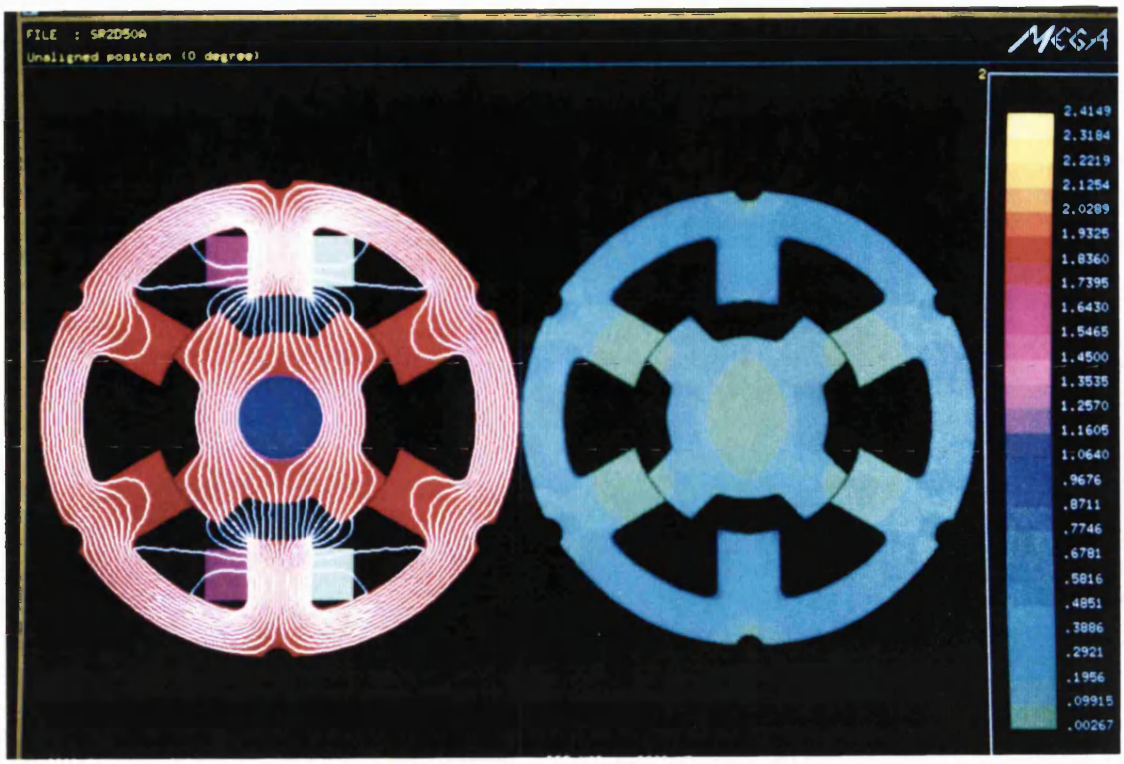

Figure 6.27: Contours of modulus of **B** and **A** at unaligned position

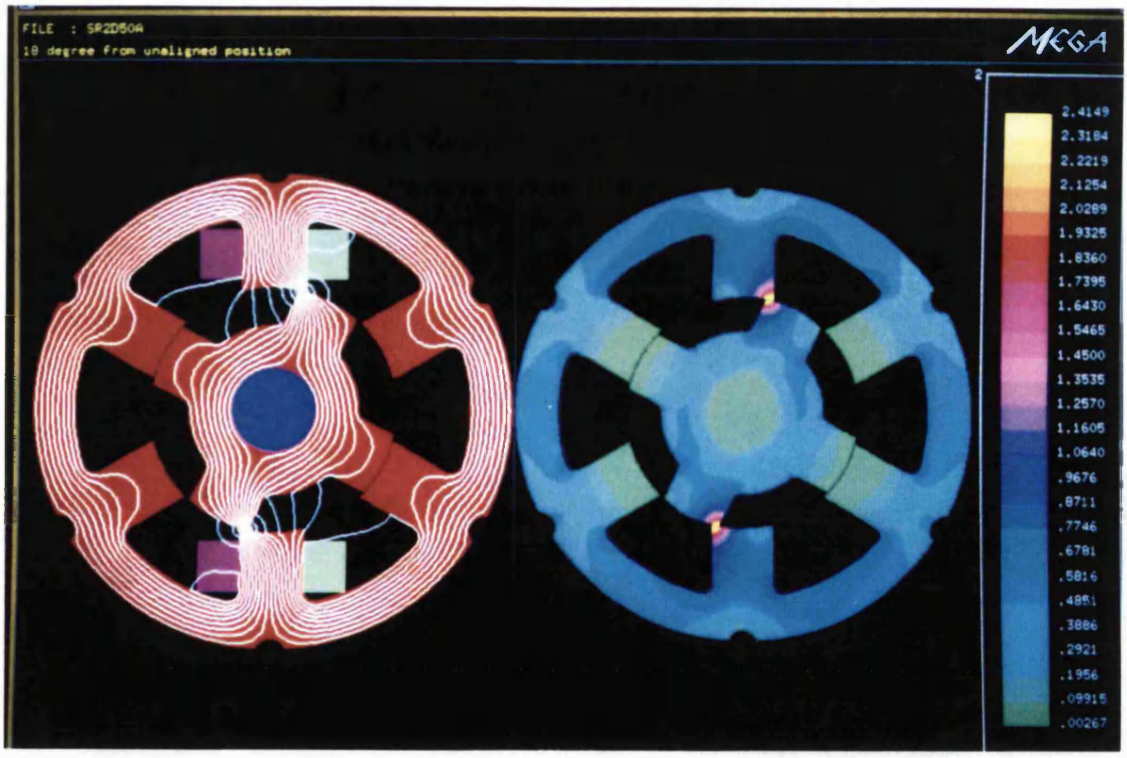

Figure 6.28: Contours of modulus of **B** and **A** 18° from unaligned position

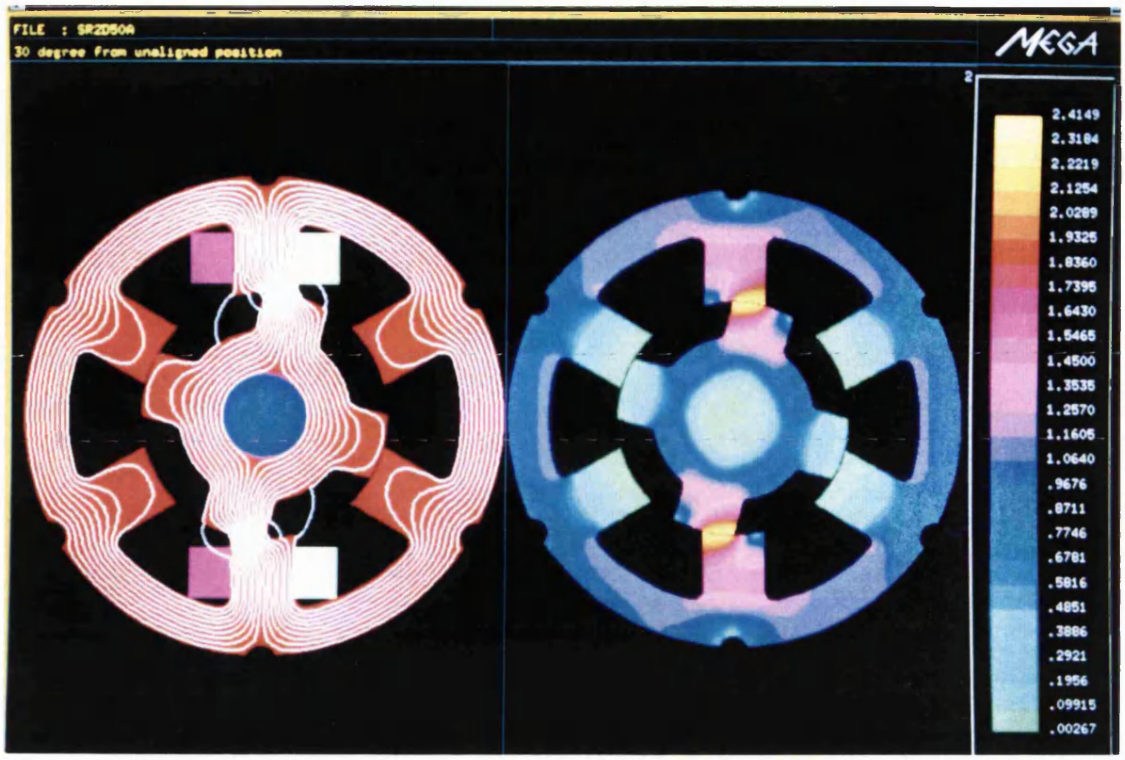

Figure 6.29: Contours of modulus of **B** and **A** 30° from unaligned position

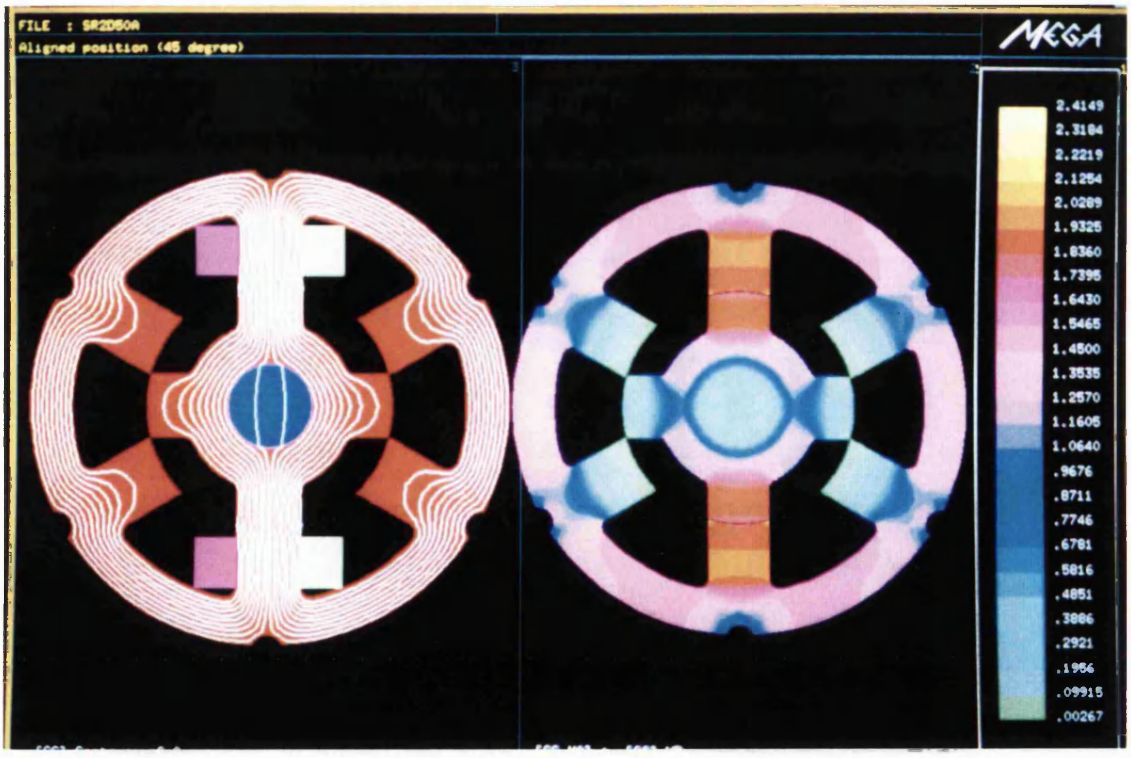

Figure 6.30: Contours of modulus of **B** and **A** at aligned position

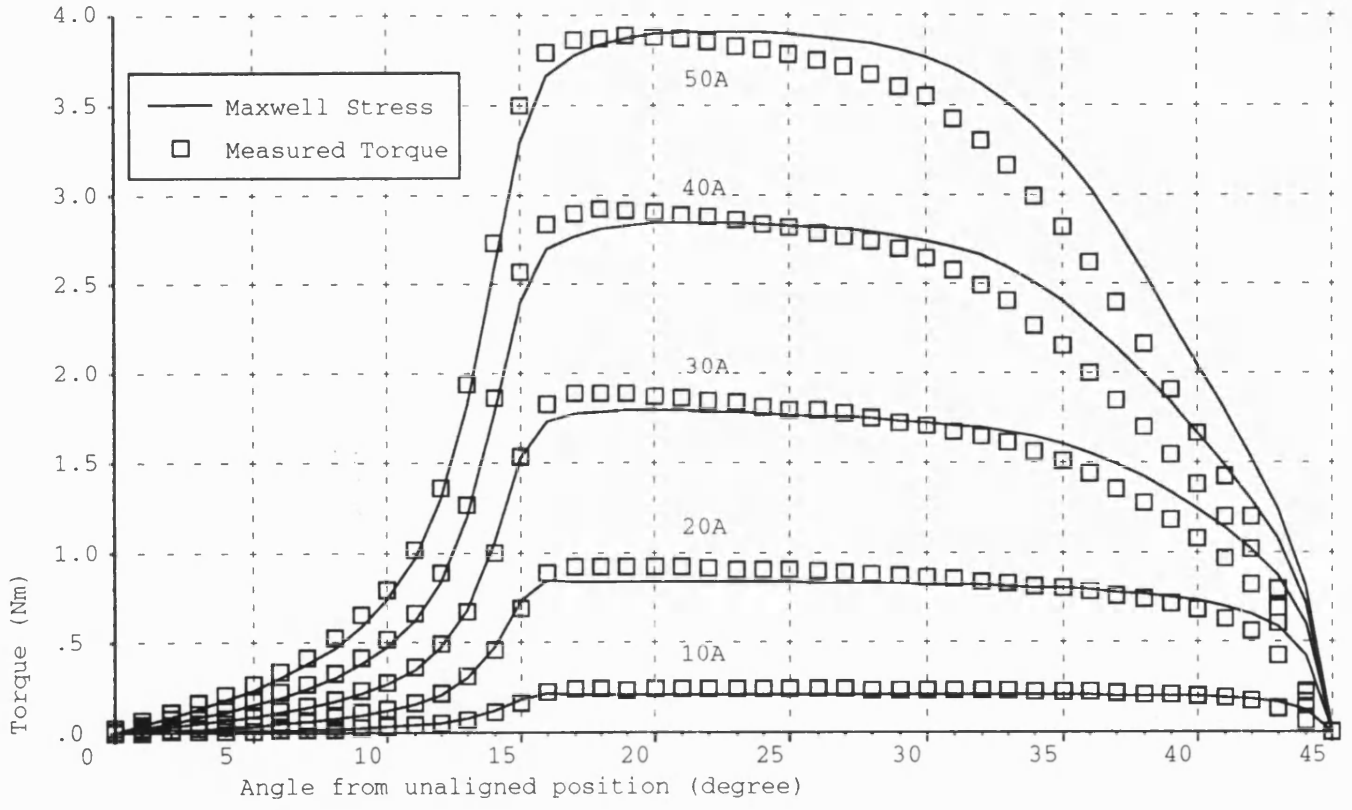

Figure 6.31: Comparison of measured and 2D calculated torque

6.3.2 Three Dimensional Finite Element Modelling of the SRM

A similar 3D Finite Element study of the SRM has also been carried out. This would provide some indication of the significance of the end effects of the SRM tested. The 3D mesh was again created by extruding a 2D base plane into levels. Half of the motor was modelled and the mesh has 58201 nodes and 51864 elements. The elements were a mixture of first order 8-noded bricks and 6-noded triangular prisms. The model consists of once again two disjointed meshes, touching each other at the centre of the air gap and linked together by Lagrange multipliers. A series of rotor positions between the unaligned position (0°) and the aligned position (45°) were solved at a few current levels. A 3D view of the model is shown in Fig.(6.32). The reduced scalar regions which enclosed the source coils are not shown so that the coils can be displayed.

Fig.(6.33) compares the torque calculated from the 3D models with the source current fixed at 50A using the Maxwell-Stress method with measurement. Also compared in the graph is the earlier 2D results. The 2D and 3D Maxwell-Stress results look fairly similar to each other overall, nevertheless the torque calculated with 3D FE is close to the measured results. The higher calculated torque obtained when the two poles are substantially overlapped still points to the use of a more optimistic **BH** curve.

Fig.(6.34) to Fig.(6.37) shows the flux density pattern of the SRM at four different rotor positions at this current level. These are similar to the corresponding 2D results shown earlier in Fig.(6.27) to Fig.(6.30). Nonetheless, variations in the field patterns towards the end of the motor's core can now be clearly seen.

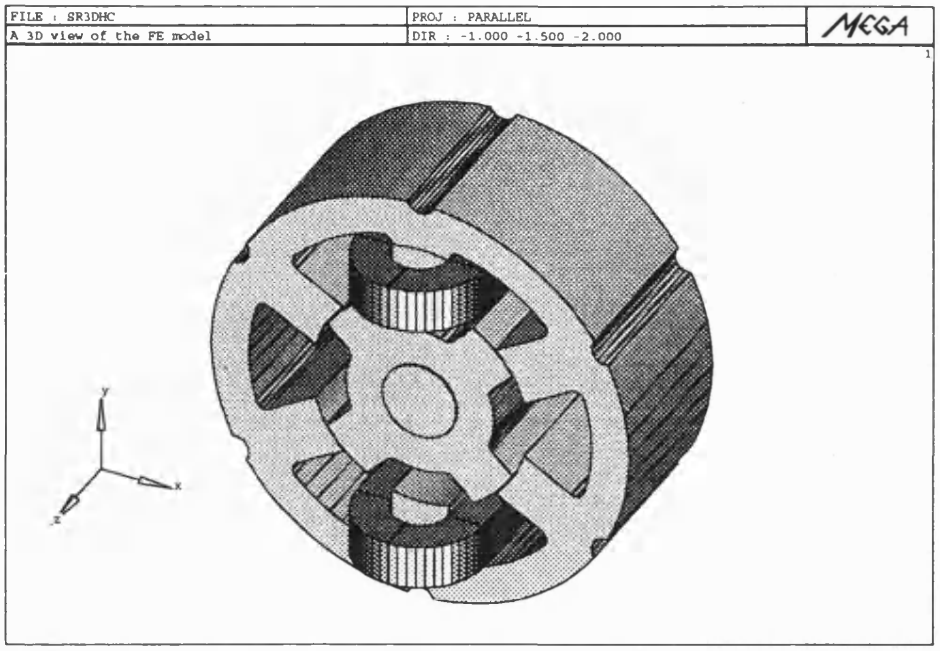

Figure 6.32: A 3D view of the SRM model

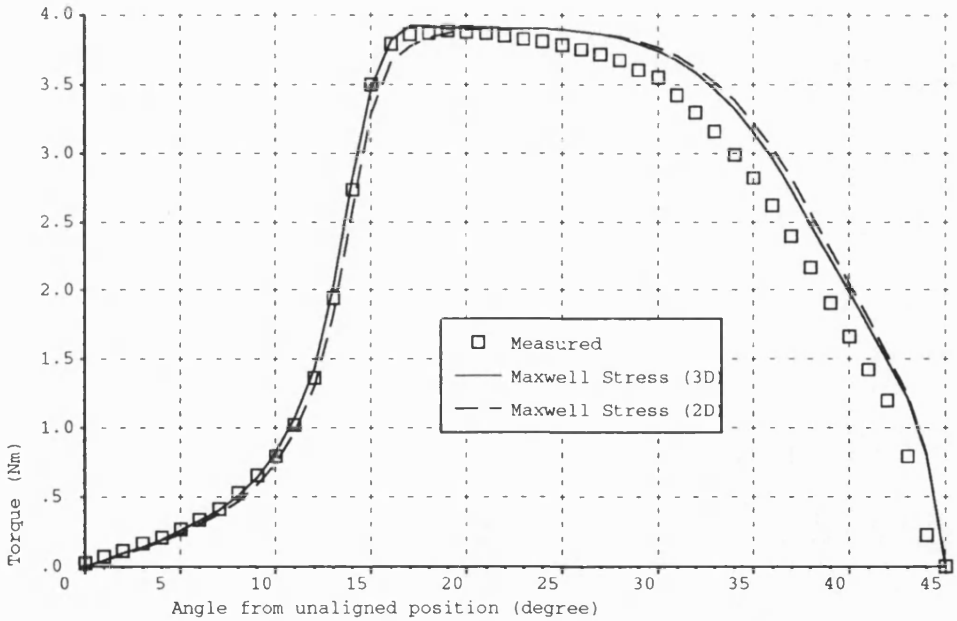

Figure 6.33: Comparison of calculated 3D and 2D torque with measurement at 50A

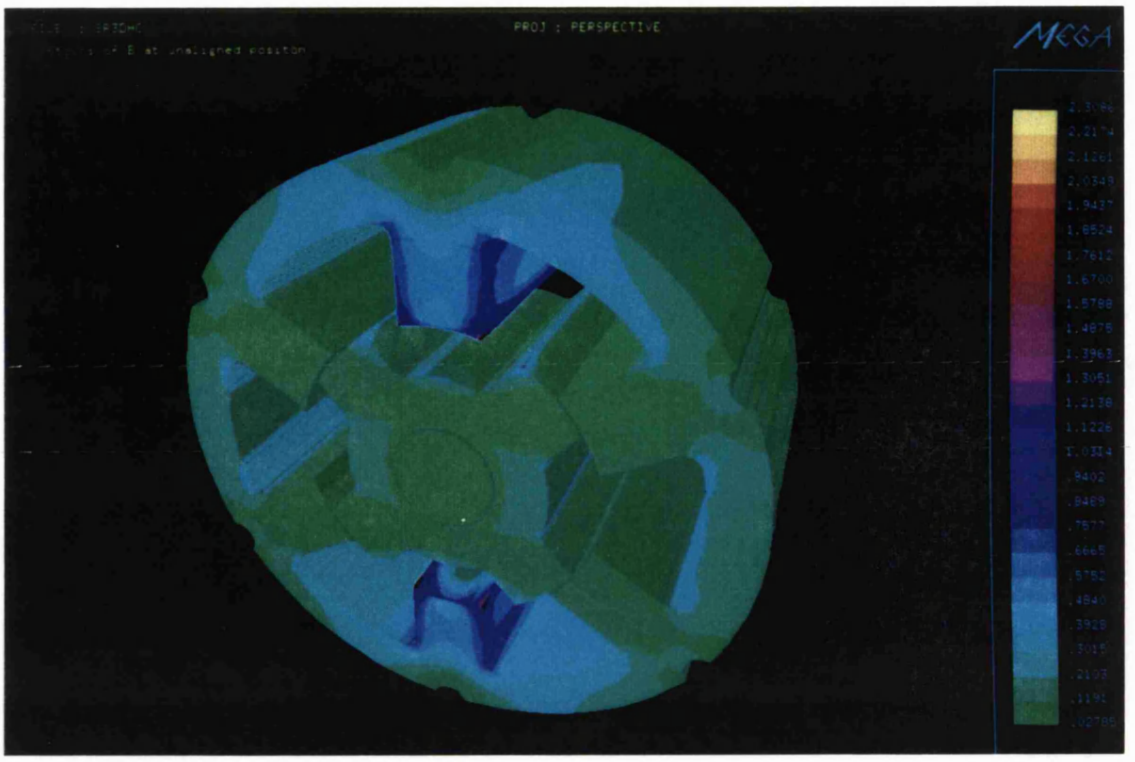

Figure 6.34: Flux density pattern of long motor at unaligned position

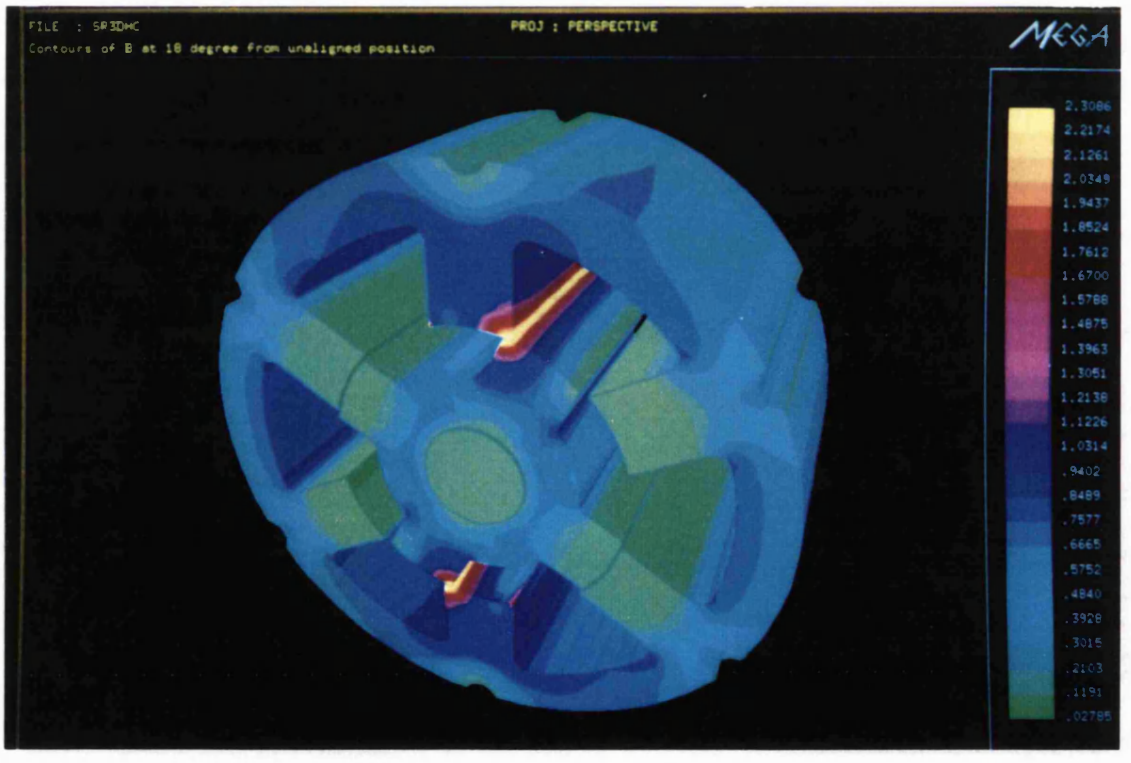

Figure 6.35: Flux density pattern of long motor at 18 degree from unaligned position

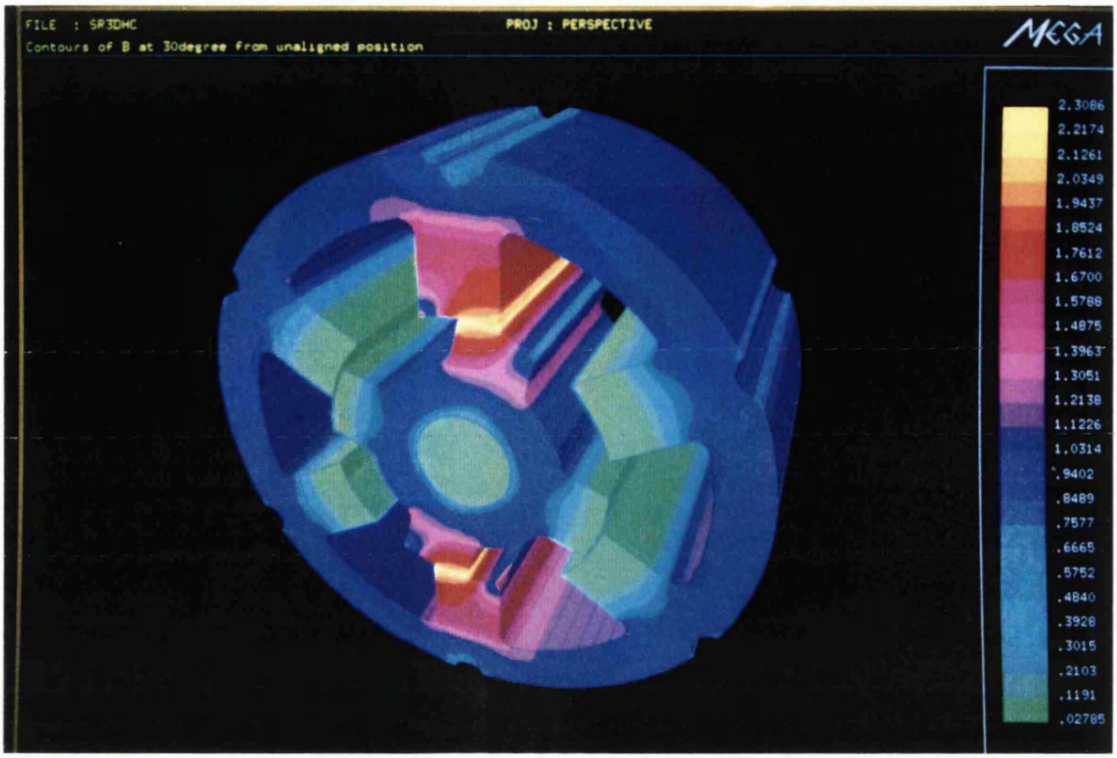

Figure 6.36: Flux density pattern of long motor at 30 degree from unaligned position

Figure 6.37: Flux density pattern of long motor at aligned position

Fig.(6.38) shows a more detailed 3D contour view of the variation of the **B** field along the axial length at the aligned position at the same current level. The band of lighter colour (higher **B**) contour about half way up the stator pole indicates clearly the position where the coil is situated. The value of the flux can be seen to stay reasonably constant throughout most of the core length. Towards the end of the core, however, the pole flux has noticeably increased, typically by as much as 16%. Correspondingly, the air gap flux has dropped by about 13% from its value at the centre plane of the core. Flux is also leaking out from the end of the core. This is particular apparent at the unaligned position as shown in Fig.(6.39). 2D Finite Elements does not model this effect. By comparing the calculated phase inductance from both 2 and 3D results, it is possible to see what effect the omission of this leakage flux has on the solution. Table (6.4) compares these calculated values with measurement. The inductances were obtained at a current level of 5A. The unaligned phase inductance results evidently highlight the problem of approximating the SRM with 2D Finite Elements.

Method	Aligned phase inductance (mH)	Unaligned phase inductance (mH)
2D FE	2.49	0.235
3D FE	2.578	0.267
Measurement	2.488	0.262

Table 6.4: Comparison of calculated and measured inductance

To illustrate this problem even more clearly, the inductances of a second SRM constructed with the same laminations but with a shorter core length [9]*was also

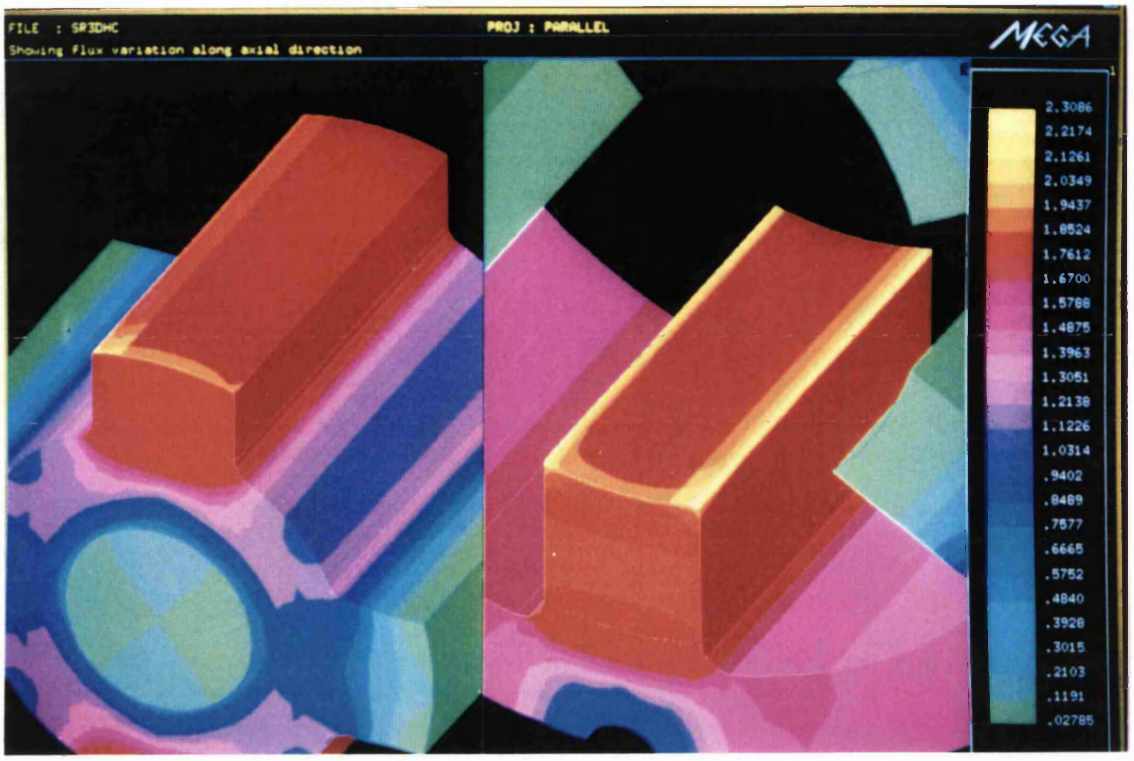

Figure 6.38: Flux density variation in axial direction

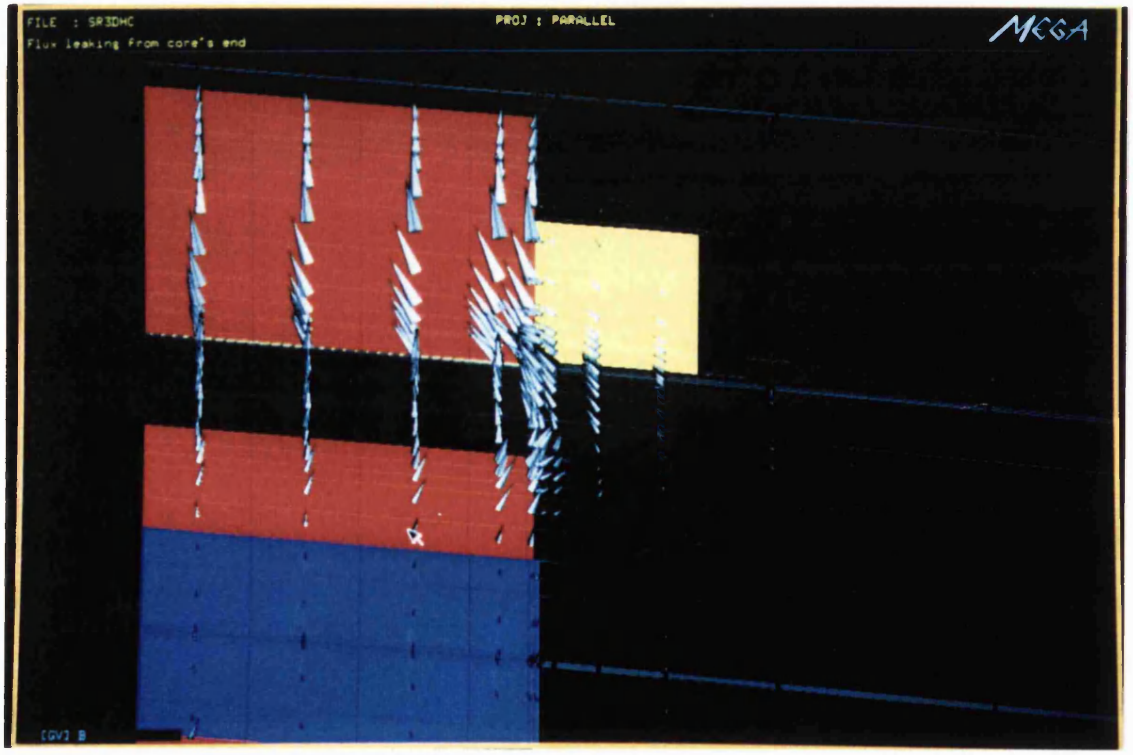

Figure 6.39: Showing core's end leakage flux at unaligned position

estimated using 3D Finite Elements. This short SRM has a core length of 0.0241m as compared to 0.0721m in the long one. Table (6.5) summarises the results. The 2D Finite Elements approach has done extremely poorly in estimating the unaligned inductance. Both inductances calculated from the 3D FE solution show a good degree of agreement with the measurement. Shortening the length of the SRM basically increases the influence of the end effects and ignoring them, as in 2D FE, will drag the model further away from reality. The torque calculation also reflects the inadequacy of the 2D model in representing the short motor. This is shown in Fig.(6.40). The tendency of the 3D results towards the measurements is now unmistakable.

Other current levels have also been solved in both motors. The torque results are shown in Fig.(6.41) and Fig.(6.42). Each graph in these two figures was obtained by solving a succession of rotor positions, 46 in steps of 1° in this case. A reduction of computation time on a position was achieved by using the solution of the previous position as the initial guess for the non-linear iterations. A 40% reduction in the number of Newton-Raphson steps required was typical.

Method	Aligned phase inductance (mH)	Unaligned phase inductance (mH)
2D FE	0.833	0.0786
3D FE	0.892	0.109
Measurement	0.875	0.108

Table 6.5: Comparison of calculated and measured inductance of the SHORT SRM

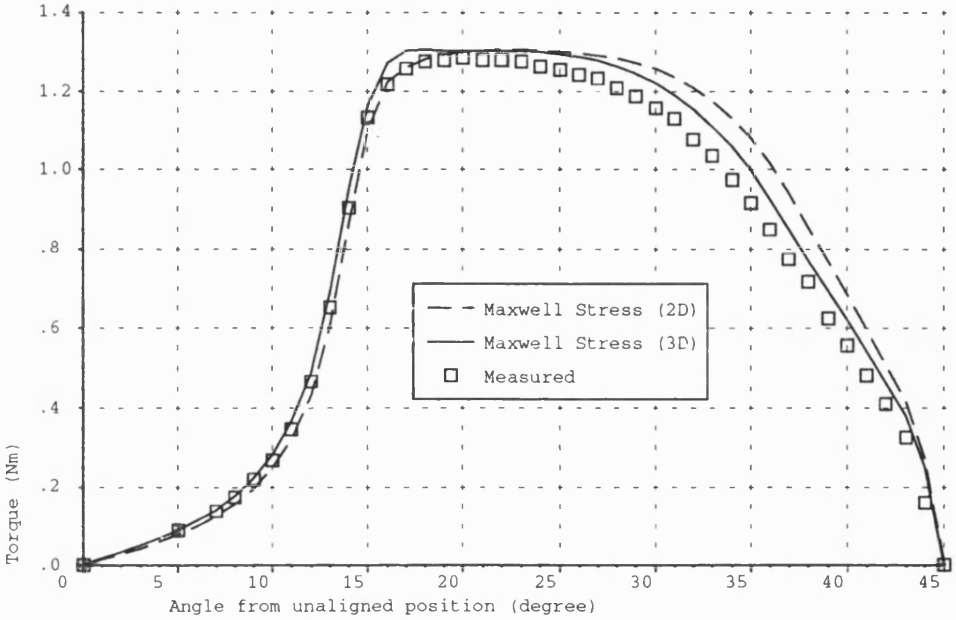

Figure 6.40: Torque of the short motor at 50A

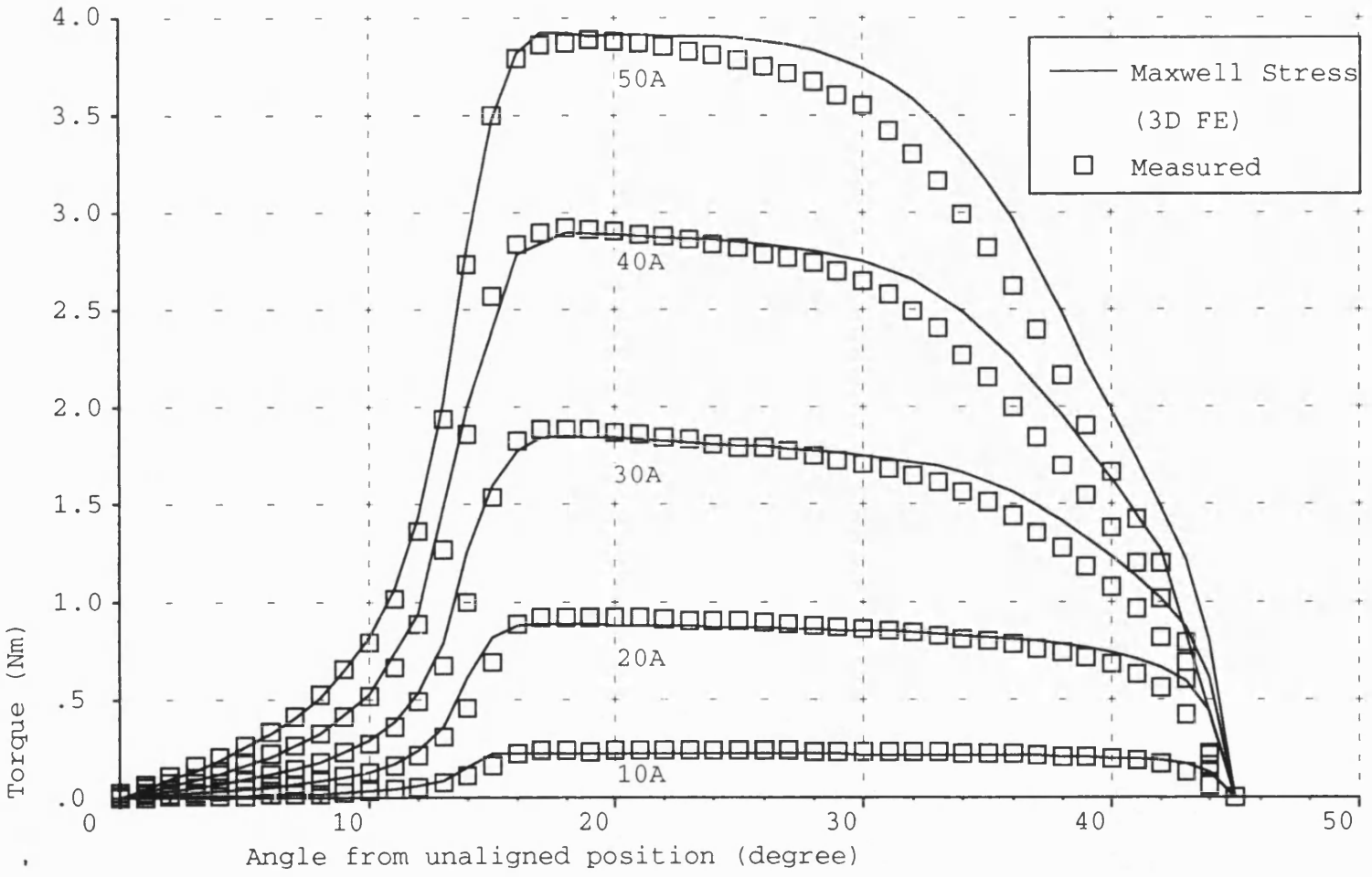

Figure 6.41: Comparison of measured and 3D FE calculated torque of the long SRM

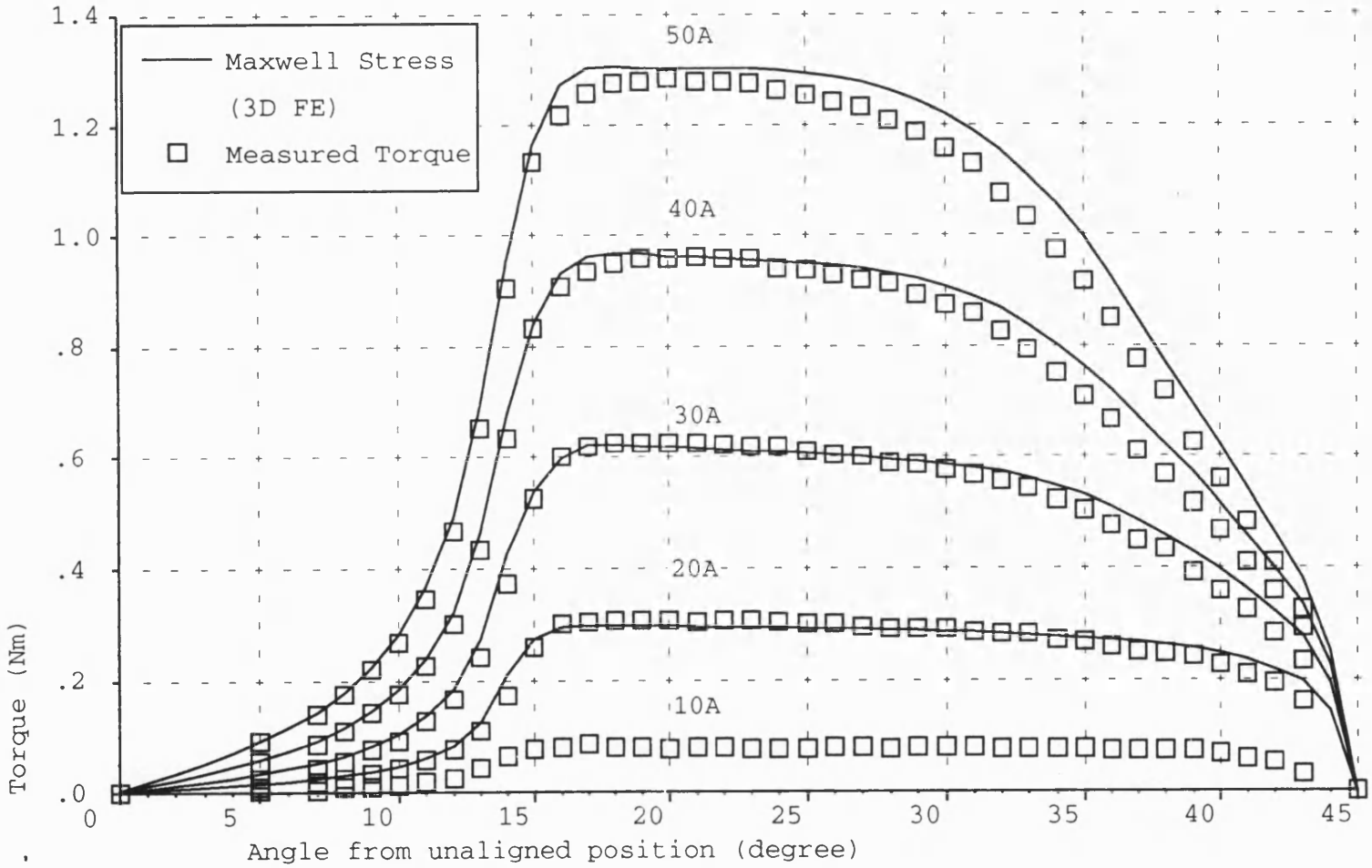

Figure 6.42: Comparison of measured and 3D FE calculated torque of the short SRM

6.3.3 External Circuit Connection

The last section has described how the Lagrange multipliers method can be used to solve a series of predefined static positions of an SRM. The next logical progression is to apply it to the case in which the SRM is rotating and is connected to an external switching circuit. The circuit shown in Fig.(6.43) was used. *MEGA* has a facility which allows a Finite Element model to be connected to an external circuitry through '*Ports*' [27]. These ports can be regarded as physical terminals which can in turn be connected to other '*circuit branches*' consisting of more fundamental circuit elements like resistors, inductors, capacitors and so on. Each circuit element is connected between two ports, an external '*circuit branch*' is formed by connecting the ports in the desired manner. The external circuit is constructed in turn by joining together these branches. Besides the three basic types of circuit elements, diodes, voltage dependent resistors and position dependent resistors are also available. The last circuit element is particular useful in simulating the positional sensor found in an SRM control circuit.

The characteristics of the circuit elements used are given in Table (6.6). The winding resistance of each phase was modelled as an external resistor to the Finite Element model. The load test was performed on the long motor at a rotational speed of 2000rpm and each phase was switched on and off at the rotor angles as specified in Table (6.7) [9]. These two angles are given relative to the unaligned position. The FE model was set up so that the rotor was at the switched on angle initially ($t = 0$). The rotationally speed of the rotor was also set to a constant 2000rpm.

The mesh was the one used earlier in the static analysis, Fig.(6.24). The model was solved with a time step of 0.1 ms and it took a DEC α 3000/400 workstation just over

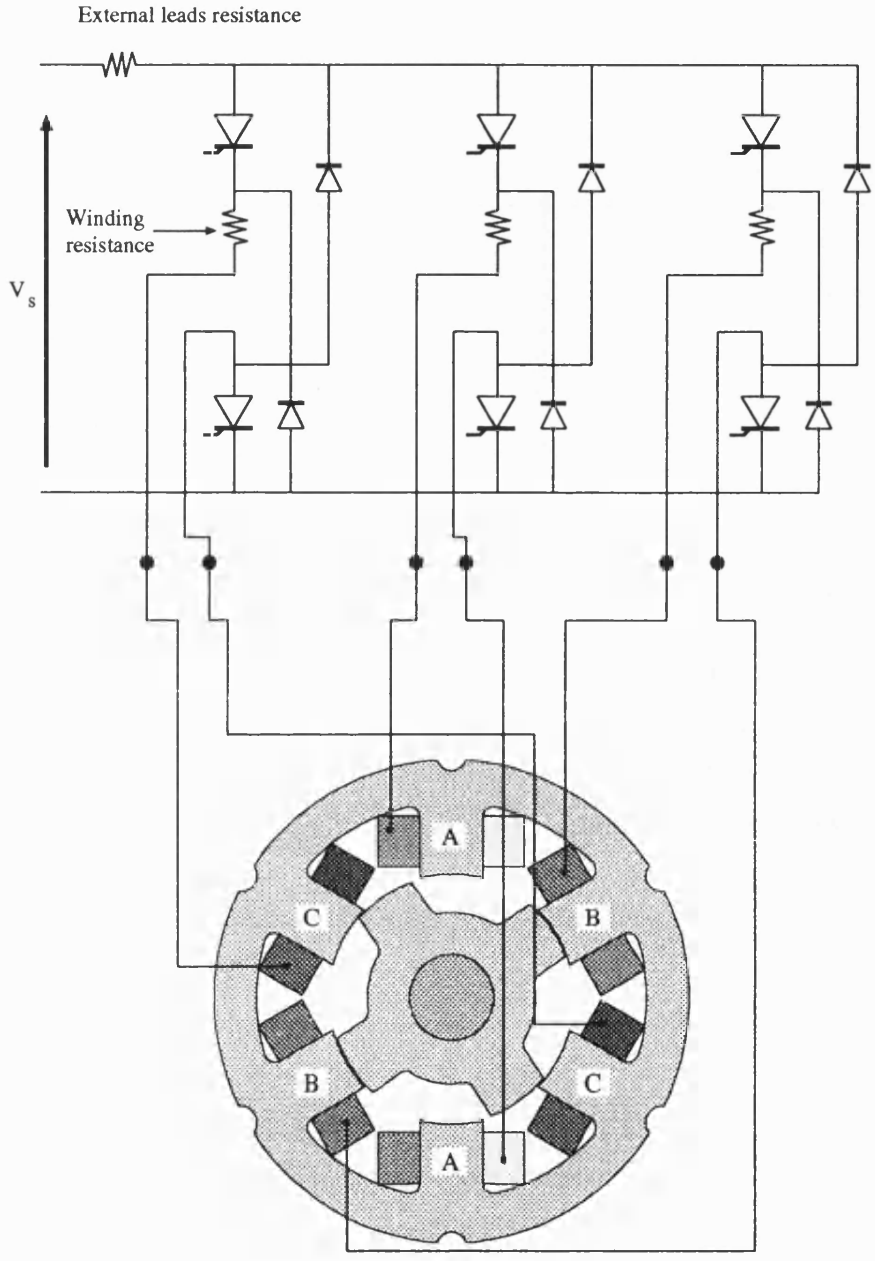

Figure 6.43: Connecting the SRM FE model to external circuit

Average DC phase resistance	$64.9m\Omega$
DC resistance of external leads	$23.86m\Omega$
Quiescent voltage drop in IGBT	$1.5V$
Forward resistance of IGBT	$15m\Omega$
Quiescent voltage drop in diode	$1.2V$
Forward resistance of diodes (estimated)	$1.875m\Omega$

Table 6.6: Characteristics of control circuit devices

Speed (rpm)	V_s (V)	Switch-on angle (degree)	Switch-off angle (degree)
2000	23.8	34.5	64.5

Table 6.7: The load test

6 hours to reach the preset 40ms end time. Table (6.8) compares some calculated and measured quantities [9]. Results agree reasonably well. The variations of the torque, the phase flux linkage and the phase current with respect to the rotor position are given in Fig.(6.44), Fig.(6.45) and Fig.(6.46) respectively. These also compare well with previously calculated results [9]. Zero degrees in the graphs corresponds to the initial switch-on position.

Method	mean torque Nm	Peak I A	I (rms) A
Measurement	2.40	86.1	39.58
2D FE	2.40	90.47	42.05

Table 6.8: Comparison of calculated and measured results

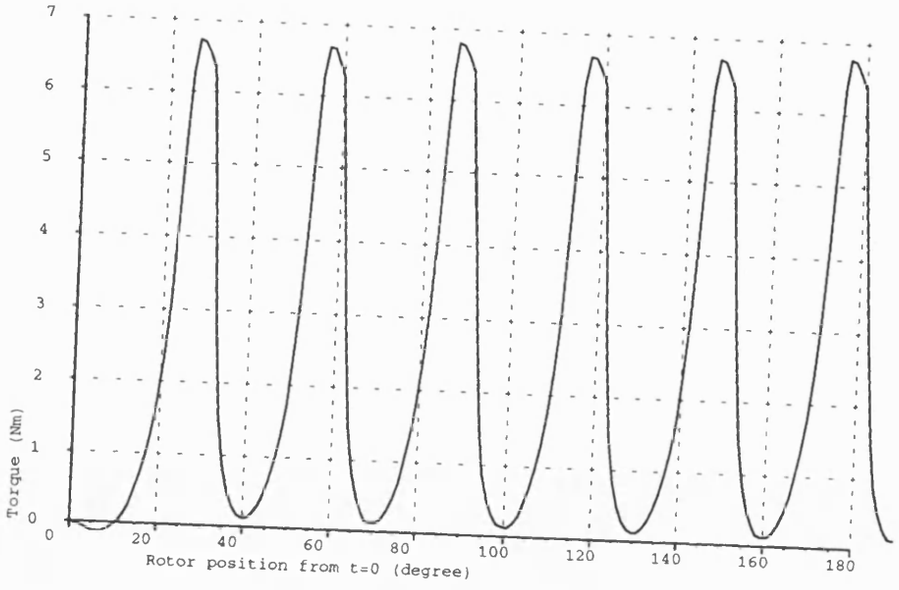

Figure 6.44: Variation of Torque with rotor position

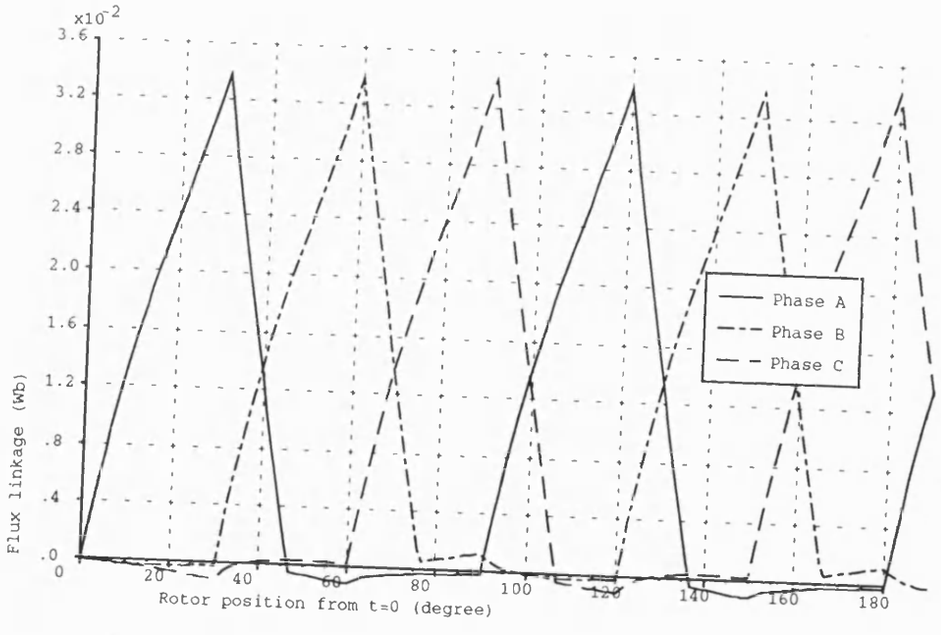

Figure 6.45: Variation of phase flux linkage with rotor position

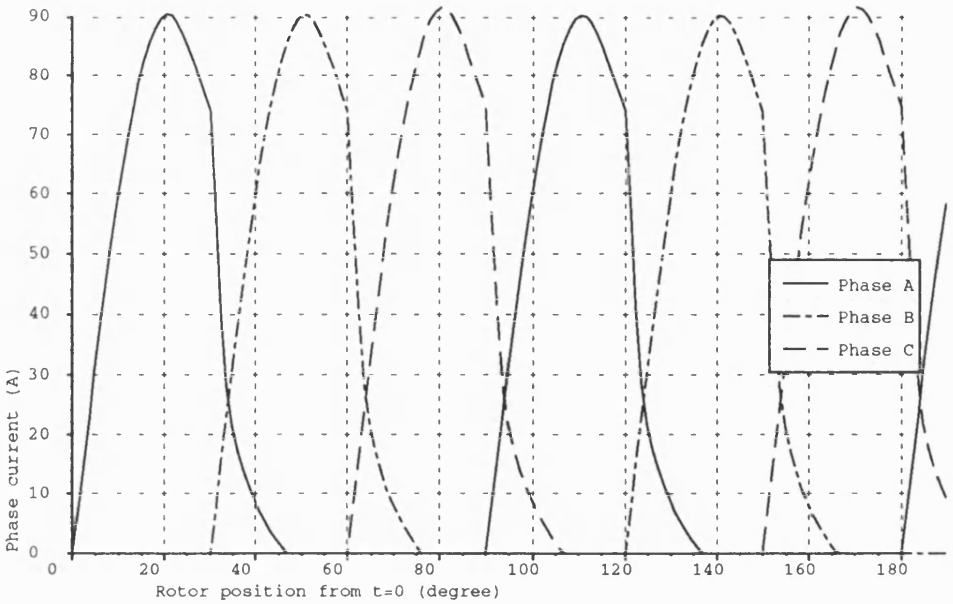

Figure 6.46: Variation of phase current with rotor position

6.4 Conclusions

This chapter has demonstrated two example applications of the Lagrange multipliers method in the Finite Element modelling of electrical machines, both of which are troublesome to model using standard meshing approach, though for slightly different reasons. The method facilitates the modelling process by allowing the rotor and the stator of the machine to be discretized into two disconnected meshes with the possibilities of each having different node densities and distribution patterns at their interface. The user benefits as a result because he or she can concentrate on devising the meshes that best describes the two individual parts without having to worry about whether their use will compromise the quality of the elements in the intermediate air created when the two are joined together.

Good quality elements, that is, those with low aspect ratio and relatively undistorted, in and around the air gap are critical to the proper modelling of the saturated fields produced when the stator and rotor of a machine overlap.

The chapter has also pointed out the inadequacy of 2D Finite Elements in modelling magnetic structures like the SRM which exhibit substantial 3D end effects. Evidence of this is shown in both the torque and inductance calculations. In the inductance calculations considered, the 2D FE answers can differ from the measurement by as much as 30% in the worse case, whereas the 3D FE answer for the same case came within 1% of the experimental result.

The difficulties of solving multiple rotor positions in machine problems has also been overcome. With the use of the Lagrange multipliers technique, the requirement of generating a new mesh for each position is eliminated. In fact, the whole process

has now been simplified to one pre-processing command call. The approach has also brought about substantial saving in file storage as there is only one mesh involved throughout, different rotor positions can be easily reconstructed from the compactly stored position information. A considerable amount of computer time can also be saved on solving a multiple-position problem by using the result of a previous position as a starting guess.

The ability of the method to handle arbitrary rotor angles has also enabled a dynamic simulation of the motor with connection to an external circuit to be carried out. Although the case considered had a constant rotational speed, real dynamic simulation of the motor with its speed governed by instantaneous torque is possible [34].

Chapter 7

Conclusions

This thesis has presented a new approach to model electromagnetic devices with moving parts. It is unconventional in that it breaks the traditional requirement that each finite element has to be 'compatible' with its adjacent neighbours. By relaxing this requirement, many of the stumbling blocks commonly encountered in the simulation of the moving parts at different positions arising from the need to remesh at each position are eliminated. As a result, such exercises can now be readily carried out.

The technique is based on the use of the classical Lagrange multipliers method in solving a constrained problem. Stationary and moving members of a model are discretized separately as disconnected meshes, touching each other at a common interface. They are then coupled together by the enforcement of an extra constraint condition, arising from a consideration of the continuity of potentials across the interface, using the Lagrange multipliers method.

Results have proved favourable. Good agreement with experimental measurements were obtained. The use of the Lagrange multipliers method, however, imposes a penalty on the solution time. Typically, it takes about 25% more time to solve the same model with a comparable normal Finite Element mesh. Nevertheless, it was felt that the convenience and the time saved in the pre-processing stage easily compensates for this disadvantage.

Practical applications of the method have also been demonstrated. A car alternator

was modelled. The flexibility of the method in dealing with such a complex 3D structure was clearly displayed. A more profitable application of the method is perhaps in the modelling of multiple rotor positions of a machine like the Switched Reluctance motor. Since the need to remesh at a new position is removed, only one mesh is required throughout, thus resulting in a substantial saving in file storage. More importantly, by using the solution of the preceding position as a starting vector for the Newton-Raphson iterations, a reduction of about 40% on the computer time taken to solve a whole series of rotor positions was achieved.

A form of dynamic rotor rotation with the Switched Reluctance motor connected to an external circuit controlling the firing of the phases and the rotor given a constant speed has also been attempted. Results agree well with previous measurements and calculations. The logical next step is to model a true dynamic movement of the motor from standstill with the acceleration, velocity and displacement of the rotor and the supply current all determined dynamically at each time step. In fact, a similar kind of dynamic movement modelled using this Lagrange multipliers approach has already been reported [34].

Appendix A

Element Shape Functions

A.1 Two Dimensional Element Shape Function

With few exceptions, the subdivision of a 2D problem into 4-noded finite elements usually results in irregular quadrilaterals being the majority type of elements. It is not difficult to realise that the calculation of element stiffness matrices,equation (2.17), and the load vectors, equation (2.18), for such elements would be awkward if performed directly in the global xy coordinates system. Even for nicely formed rectangular elements, the calculation is not so straightforward as the shape functions and the limits of integrations etc., change from element to element.

One way of dealing with this problem is to derive a transformation which maps the element onto an master element of simple shape so that operations on the element such as integration can be conveniently done on the master element. Fig.(A.1) below illustrates the idea.

Consider, for instance, the element $\hat{\Omega}$ shown in Fig.(A.2). It is a simple square defined in local coordinates ξ and η with centre located at the origin and edges of 2 units in length. The nodal shape function which attains a unit value at the node concerned and zero at all other nodes and along all sides of the element that do not contain the node can be expressed as

$$\hat{N}_i = \frac{1}{4}(1+\xi_i\xi)(1+\eta_i\eta), \qquad \text{(A.1)}$$

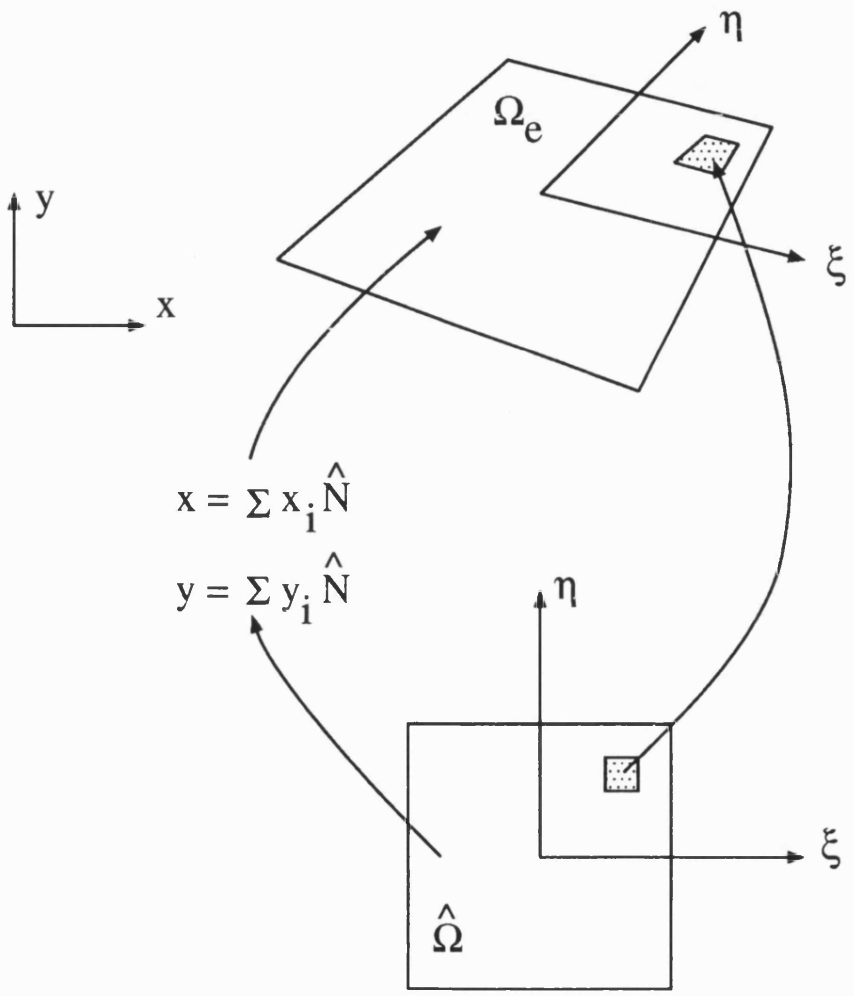

Figure A.1: Mapping of Master to 2D element

where (ξ_i, η_i) are local coordinate of node i.

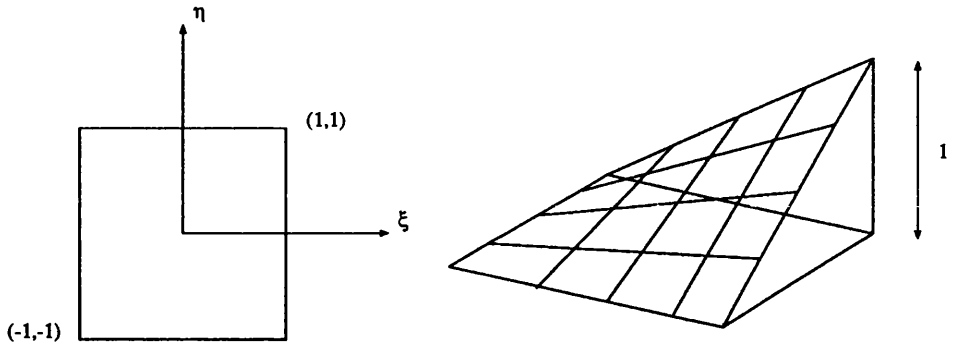

Figure A.2: A typical shape function of a 2D element

A simple way to map this master element into an arbitrary quadrilateral in the xy system is perhaps to utilise the same concept used in approximating the potential functions, that is we have :

$$\begin{aligned} x &= \sum_{i=1}^{4} x_i \hat{N}_i(\xi, \eta) \\ y &= \sum_{i=1}^{4} y_i \hat{N}_i(\xi, \eta) \end{aligned} \tag{A.2}$$

Because of this, the element is called an *isoparametric* element. The partial derivatives of N_i^e with respect to x and y can be related to the readily computed ξ and η derivatives by using the chain rule :

$$\begin{aligned} \frac{\partial \hat{N}_i}{\partial \xi} &= \frac{\partial N_i^e}{\partial x}\frac{\partial x}{\partial \xi} + \frac{\partial N_i^e}{\partial y}\frac{\partial y}{\partial \xi} \\ \frac{\partial \hat{N}_i}{\partial \eta} &= \frac{\partial N_i^e}{\partial x}\frac{\partial x}{\partial \eta} + \frac{\partial N_i^e}{\partial y}\frac{\partial y}{\partial \eta} \end{aligned} \tag{A.3}$$

This can be written in matrix form as

$$\begin{bmatrix} \frac{\partial \hat{N}_i}{\partial \xi} \\ \frac{\partial \hat{N}_i}{\partial \eta} \end{bmatrix} = \begin{bmatrix} \frac{\partial x}{\partial \xi} & \frac{\partial y}{\partial \xi} \\ \frac{\partial x}{\partial \eta} & \frac{\partial y}{\partial \eta} \end{bmatrix} \begin{bmatrix} \frac{\partial N_i^e}{\partial x} \\ \frac{\partial N_i^e}{\partial y} \end{bmatrix} = \mathcal{J} \begin{bmatrix} \frac{\partial N_i^e}{\partial x} \\ \frac{\partial N_i^e}{\partial y} \end{bmatrix}. \tag{A.4}$$

$\mathcal{J}$ is the Jacobian matrix of the transformation which can be easily calculated as

$$\begin{bmatrix} \frac{\partial x}{\partial \xi} & \frac{\partial y}{\partial \xi} \\ \frac{\partial x}{\partial \eta} & \frac{\partial y}{\partial \eta} \end{bmatrix} = \begin{bmatrix} \sum_{i=1}^{4} x_i \frac{\partial \hat{N}_i}{\partial \xi} & \sum_{i=1}^{4} y_i \frac{\partial \hat{N}_i}{\partial \xi} \\ \sum_{i=1}^{4} x_i \frac{\partial \hat{N}_i}{\partial \eta} & \sum_{i=1}^{4} y_i \frac{\partial \hat{N}_i}{\partial \eta} \end{bmatrix}. \tag{A.5}$$

To find the global derivatives, we use

$$\begin{bmatrix} \frac{\partial N_i^e}{\partial x} \\ \frac{\partial N_i^e}{\partial y} \end{bmatrix} = \mathcal{J}^{-1} \begin{bmatrix} \frac{\partial \hat{N}_i}{\partial \xi} \\ \frac{\partial \hat{N}_i}{\partial \eta} \end{bmatrix}. \tag{A.6}$$

The evaluation of the elemental stiffness matrix (2.17) and load vectors (2.18) can now be carried out over the master element as

$$K_{ij}^e = \int_{-1}^{1} \int_{-1}^{1} \nu_e \left(\frac{\partial N_i^e}{\partial x} \frac{\partial N_j^e}{\partial x} + \frac{\partial N_i^e}{\partial y} \frac{\partial N_j^e}{\partial y} \right) |\mathcal{J}| \, \mathrm{d}\xi \mathrm{d}\eta$$

and

$$f_i^e = \int_{-1}^{1} \int_{-1}^{1} N_i^e |\mathcal{J}| \, \mathrm{d}\xi \mathrm{d}\eta$$

The integration is typically calculated using Gaussian Quadrature. With this isopara-

metric approach, the element matrix can be calculated in a general and systematic way. In addition, higher order curvilinear elements can also be easily handled in an identical way.

A.2 Three Dimensional Element Shape Function

The Master element concept is readily extended to 3D. Here, the master element will be an 8-noded brick element defined in the $\xi\eta\zeta$ local coordinate system as shown in Fig.(A.3). The nodal shape function for node i now becomes

$$\hat{N}_i = \frac{1}{8}(1 + \xi_i\xi)(1 + \eta_i\eta)(1 + \zeta_i\zeta). \tag{A.7}$$

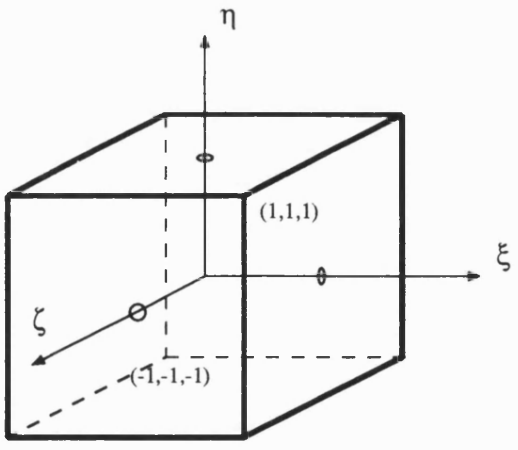

$$N_i = \frac{1}{8}(1+\xi_i\xi)(1+\eta_i\eta)(1+\zeta_i\zeta)$$

Figure A.3: 3D Master element

Similar to 2D, the global derivatives of the shape function can be found by

$$\begin{bmatrix} \frac{\partial N_i^e}{\partial x} \\ \frac{\partial N_i^e}{\partial y} \\ \frac{\partial N_i^e}{\partial z} \end{bmatrix} = \mathcal{J}^{-1} \begin{bmatrix} \frac{\partial \hat{N}_i}{\partial \xi} \\ \frac{\partial \hat{N}_i}{\partial \eta} \\ \frac{\partial \hat{N}_i}{\partial \zeta} \end{bmatrix}, \tag{A.8}$$

where J is given by

$$\begin{bmatrix} \frac{\partial x}{\partial \xi} & \frac{\partial y}{\partial \xi} & \frac{\partial z}{\partial \xi} \\ \frac{\partial x}{\partial \eta} & \frac{\partial y}{\partial \eta} & \frac{\partial z}{\partial \eta} \\ \frac{\partial x}{\partial \zeta} & \frac{\partial y}{\partial \zeta} & \frac{\partial z}{\partial \zeta} \end{bmatrix} = \begin{bmatrix} \sum_{i=1}^{8} x_i \frac{\partial \hat{N}_i}{\partial \xi} & \sum_{i=1}^{8} y_i \frac{\partial \hat{N}_i}{\partial \xi} & \sum_{i=1}^{8} z_i \frac{\partial \hat{N}_i}{\partial \xi} \\ \sum_{i=1}^{8} x_i \frac{\partial \hat{N}_i}{\partial \eta} & \sum_{i=1}^{8} y_i \frac{\partial \hat{N}_i}{\partial \eta} & \sum_{i=1}^{8} z_i \frac{\partial \hat{N}_i}{\partial \eta} \\ \sum_{i=1}^{8} x_i \frac{\partial \hat{N}_i}{\partial \zeta} & \sum_{i=1}^{8} y_i \frac{\partial \hat{N}_i}{\partial \zeta} & \sum_{i=1}^{8} z_i \frac{\partial \hat{N}_i}{\partial \zeta} \end{bmatrix}. \tag{A.9}$$

The elemental stiffness matrix is calculated from the master element by

$$K_{ij}^e = \int_{-1}^{1}\int_{-1}^{1}\int_{-1}^{1} \nu_e \left(\frac{\partial N_i^e}{\partial x}\frac{\partial N_j^e}{\partial x} + \frac{\partial N_i^e}{\partial y}\frac{\partial N_j^e}{\partial y} + \frac{\partial N_i^e}{\partial z}\frac{\partial N_j^e}{\partial z} \right) |\mathcal{J}| \, \mathrm{d}\xi \mathrm{d}\eta \mathrm{d}\zeta.$$

Appendix B

Equivalent Functional

We consider here equations of the following form :

$$Au = f; \tag{B.1}$$

in which A is a linear differential operator. When A is positive definite it can be shown that [35] the solution that satisfies the above equation also minimises the following quadratic function $Q(u)$:

$$Q(u) =< Au, u > -2 < f, u >, \tag{B.2}$$

where $< \cdot, \cdot >$ denotes the inner product. In magnetostatic problems using Magnetic Vector Potential, the governing partial differential equation is

$$\nabla \times \nu \nabla \times \mathbf{A} = \mathbf{J}. \tag{B.3}$$

The equivalent functional for equation (B.3) can be written, following equation (B.2), as

$$\Pi = \int_{\Omega} \mathbf{A} \cdot (\nabla \times \nu \nabla \times \mathbf{A}) - 2(\mathbf{A} \cdot \mathbf{J}) \, dV. \tag{B.4}$$

Using the Vector identity

$$\mathbf{G} \cdot \nabla \times \mathbf{F} = \nabla \cdot (\mathbf{F} \times \mathbf{G}) + \mathbf{F} \cdot \nabla \times \mathbf{G}$$

and the Divergence theorem, Π can be re-written in the following form :

$$\Pi = \int_{\Omega} (\nabla \times \mathbf{A}) \cdot \nu(\nabla \times \mathbf{A}) - 2(\mathbf{A} \cdot \mathbf{J})\,\mathrm{d}V + \oint_{\Gamma} (\nu \nabla \times \mathbf{A} \times \mathbf{A}) \cdot \mathrm{d}\mathbf{S}. \qquad \text{(B.5)}$$

The surface integral term can be written in a more familiar form using

$$(\mathbf{G} \times \mathbf{H}) \cdot \mathbf{F} = \mathbf{G} \cdot (\mathbf{H} \times \mathbf{F}) = \mathbf{H} \cdot (\mathbf{F} \times \mathbf{G}).$$

Hence, we have

$$\Pi = \int_{\Omega} (\nabla \times \mathbf{A}) \cdot \nu(\nabla \times \mathbf{A}) - 2(\mathbf{A} \cdot \mathbf{J})\,\mathrm{d}V - \oint_{\Gamma} \mathbf{A} \cdot (\nu \nabla \times \mathbf{A} \times n)\,\mathrm{d}S. \qquad \text{(B.6)}$$

In 2D Finite Elements using one component of $\mathbf{A}$, this equation can be simplified to

$$\Pi = \int \nu \left[\left(\frac{\partial \mathrm{A}}{\partial x} \right)^2 + \left(\frac{\partial \mathrm{A}}{\partial y} \right)^2 \right] - 2(\mathrm{AJ})\,\mathrm{dxdy} - \oint_{\Gamma} \mathrm{A} \cdot \frac{\partial \mathrm{A}}{\partial n}\,\mathrm{dl}. \qquad \text{(B.7)}$$

Under homogeneous Dirichlet and Neumann boundary conditions, the line integral vanishes and Π can be written as

$$\Pi = \frac{1}{2} \int \nu \left[\left(\frac{\partial \mathrm{A}}{\partial x} \right)^2 + \left(\frac{\partial \mathrm{A}}{\partial y} \right)^2 \right] - (\mathrm{AJ})\,\mathrm{dxdy}. \qquad \text{(B.8)}$$

This is often written as

$$\Pi = \int_{0}^{B} \int \mathrm{H}\,\mathrm{dB} - \mathrm{AJ}\,\mathrm{dxdy}. \qquad \text{(B.9)}$$

Appendix C

The Weighted Residual Method

The Weighted Residual method [13] is a method popularly used in Finite Elements for obtaining an approximation solution to the governing differential equations. The differential equations can be written in the general form

$$\mathrm{Au} = \mathrm{f}, \tag{C.1}$$

where A is the differential operator, u is the function to be found and f is the right hand side. In the finite element method, u is approximated by a linear combination of shape functions as

$$\mathrm{u} \approx \hat{\mathrm{u}} = \sum_{i=1}^{n} N_i \hat{u}_i \tag{C.2}$$

where N_i is the shape function of node i and $\hat{u}_i$ is the nodal value of $\hat{\mathrm{u}}$ at node i. There are n nodes in the problem. Substituting $\hat{\mathrm{u}}$ into equation (C.1) results in a residual

$$R = \mathrm{A}\hat{\mathrm{u}} - \mathrm{f} \tag{C.3}$$

which is generally not equal to zero. The aim now is to determine the $\hat{u}_i$'s so that the residual is forced to be zero in some average sense over the problem domain. This can be achieved by selecting a set of weighting functions w_j and then requiring the product of each of these w_j and the residual R integrated over the problem

domain be zero. That is, we have

$$\int_{\Omega} w_j(\mathrm{A}\hat{\mathrm{u}} - \mathrm{f})\,\mathrm{d}\Omega = 0 \qquad (j = 1, 2, \ldots, n) \tag{C.4}$$

This results in n equations from which the n $\hat{u}_i$ can be determined. Various forms of weighting functions can be used in practice, and each choice leads to a different weighted residual method. The following describes briefly three different choices of the weighting functions.

1. Point Collocation Method

   In this method, the residual of equation (C.3) is forced to be zero at n points within the problem domain. Therefore, we set

   $$R\,|_{\mathbf{x}_i} = 0 \qquad \text{for } i = 1 \ldots n, \tag{C.5}$$

   where $R\,|_{\mathbf{x}_i}$ means the residual R at point $\mathbf{x}_i$ within the problem domain.

2. Sub-domain Collocation Method

   The weighting function w_j here is chosen to be unity in the subregion Ω_j and zero everywhere else. This forces the residual to be zero in each of the subdomains.

3. The Galerkin Method

   Here, the weighting functions are chosen simply to be the same as the shape functions. That is,

   $$w_j = N_j \tag{C.6}$$

Bibliography

[1] A.M. Winslow. "Magnetic field calculation in an irregular triangle mesh". *Proc Internatl. Symp. on Magnet Technology, Stanford, Calif.*, pages 170–181, October 1965.

[2] P. Silvester and M.V.K. Chari. "Finite element solution of saturable magnetic field problems". *IEEE Trans. Power App. Syst.*, PAS–89(7):1642–1651, September 1970.

[3] D.Rodger and J.F.Eastham. "Finite element solution of 3D eddy current flow in magnetically linear conductors at power frequencies". *IEEE Trans. Mag.*, 18:481–485, 1982.

[4] P.J.Leonard and D.Rodger. "A finite element scheme for transient 3D eddy currents". *IEEE Trans. Mag.*, 24(1):90–93, Aug 1987.

[5] W.Renhart, H.Stogner, and K.Preis. "Calculation of 3D eddy current problems by finite element method using either an electric or a magnetic vector potential.". *IEEE Trans. Mag.*, 24(1), August 1987.

[6] T.Nakata, N.Takahashi, K.Fujiwara, and A.Ahagon. "3-D finite element method for analysing magnetic fields in electrical machines excited from voltage sources". *IEEE Trans. Mag.*, 24(6):2582–2584, November 1988.

[7] B.Davat, Z.Ren, and M.Lajoie-Mazenc. "The movement in field modeling". *IEEE Trans. Mag.*, 21(6), November 1985.

[8] K.Ho-Le. "Finite element mesh generation methods: A review and classification". *Computer Aided Design*, 20(1), January 1988.

[9] P.S.Sangha. *Transient Solution of Switched Devices Using Finite Elements.* PhD thesis, School of Electrical Engineering, University of Bath, 1992.

[10] A.A. Abdel-Razek J.L. Coulomb M. Feliachi and J.C. Sabonnadiere. "Conception of an airgap element for the dynamic analysis of the electromagnetic field in electrical machines". *IEEE Trans-Mag*, MAG 18(2):655–659., March 1982.

[11] P. Hammond. *Applied Electromagnetism.* Pergamon Press, 1971.

[12] P.P. Silvester and R.L. Ferrari. *Finite Elements for Electrical Engineers.* Cambridge University Press, 2nd edition, 1990.

[13] O.C.Zienkiewicz. *"The Finite Element Method".* McGraw-Hill Book Company Limited, 3rd edition, 1986.

[14] J.Simkin and C.W.Trowbridge. "On the use of the total scalar potential in the numerical solution of three dimensional magnetostatic problems". *IJNME*, 14:423–440, 1979.

[15] H. Akima. "A new method of interpolation and smooth curve fitting based on local procedures". *Journal of the Association for Computing Machinery*, 17(4), October 1970.

[16] M.R. Hestens and E. Stiefel. "Methods of conjugate gradients for solving linear systems". *Journal of the Research of the National Bureau of Standards*, 49(6), December 1952.

[17] A.Jennings. "Influence of the eigenvalue spectrum on the convergence rate of the conjugate gradients method". *J. Inst. Maths. Applics*, 20, 1977.

[18] J.A.Meijerink and H.A.van der Vorst. "An iterative solution method for linear systems of which the coefficient matrix is a symmetric m-matrix". *Math. Comp.*, 31, 1977.

[19] Gene H. Golub and Charles F. Van Loan. *Matrix Computations.* The John Hopkins University Press, 2nd edition, 1991.

[20] D.S.Kershaw. "The incomplete cholesky-conjugate gradient method for the iterative solution of systems of linear equations". *J. Comput. Phys.*, 26, 1978.

[21] David G. Luenberger. *Linear and Nonlinear Porgramming.* Addison-Wesley Publishing Company, 2nd edition, 1984.

[22] S.D. Conte and Carl de Boor. *Elementary Numerical Analysis. An Algorithmic Approach*, chapter 7. McGraw-Hill Book Company, 3rd edition, 1980.

[23] D.Rodger T.Karagular and P.J.Leonard. "A formulation for 3D moving eddy current problems". *IEEE Trans. Mag.*, 25(5), September 1989.

[24] B.A. Finlayson. *The Method of Weighted Residuals and Variational Principles.* Academic Press, 1972.

[25] Y.Marechal, G.Meunier, J.L.Coulomb, and H.Magnin. "A general purpose tool for restoring inter-element continuity". *IEEE Trans. Mag.*, 28(2), March 1992.

[26] Graham F. Carey and J. Tinsley Oden. *Finite Elements. A Second Course*, volume 2. Prentice-Hall, Inc., 1983.

[27] "MEGA Version 5 user manual ". *Applied Electromagnetic Research Centre, Bath University, UK.*

[28] P.J.Lawrenson, J.M.Stephenson, P.T.Blenkinsop, J.Corda, and N.N.Fulton. "Variable-speed switched reluctance motors". *IEE Proc. B*, 127(4), July 1980.

[29] R.M. Davis, W.F.Ray, and R.J. Blake. "Inverter drive for switched reluctance motor : circuits and component ratings". *IEE Proc. B*, 128(2), March 1981.

[30] G.E. Dawson A.R. Eastham and J. Mitzia. "Switched reluctance motor torque characteristics; finite element analysis and test results". *IEEE Industrial Applications Soc. annual meeting.*, 1:864–867, 1986.

[31] J.F. Lindsay, R. Arumugam, and R. Krishnan. "Finite-element analysis characterisation of a switched reluctance motor with multitooth per stator pole". *IEE Proc. B*, 133(6):347–353, November 1986.

[32] M. Moallem and C.M. Ong. "Predicting the steady-state performance of a switched reluctance machine". *IEEE Trans. Industy Appl.*, 27(6), November 1991.

[33] M.Moallem and C.M.Ong. "Predicting the torque of a switched reluctance machine from its finite element field solution". *IEEE Trans-EC*, 5(4):733–739, December 1990.

[34] P.J.Leonard, H.C.Lai, G.Hainsworth, D.Rodger, and J.F.Eastham. "Analysis of the performance of tubular pulsed induction launchers". *IEEE Trans Mag.*, 29(1):686–690, 1993.

[35] J.N. Reddy. *Applied Functional Analysis and Variational Mehtods in Engineering.* McGraw-Hill inc, 1986.

Related Publications

COUPLED ELEMENTS FOR PROBLEMS INVOLVING MOVEMENT

D Rodger, H C Lai and P J Leonard
University of Bath
Bath BA2 7AY
UK

Abstract

A new technique for use in finite element models of devices which move is proposed. Independent meshes are coupled together at a suitable interface, such as the air gap of a conventional electrical machine using Lagrange multipliers.

Introduction

Many electrical devices include parts which can move relative to the others. Examples of this include rotating electrical machines and linear actuators. A representative machine is shown in Fig. 1. This class of device can be troublesome to model using finite elements. Often a simulation of such a machine requires modelling many different rotor positions. Several different approaches are described in the literature, as follows:

Several different models can be meshed and used in turn. This is not very satisfactory, it is expensive to produce many meshes and difficult to generalise the method.

Local remeshing is also possible, the program could move the rotor, retaining the same mesh topology as long as is practical, and then re-mesh, joining 'nearest nodes' on the moving interface (Fig. 2). This can produce distorted elements and loss of accuracy.

It is possible to avoid meshing the moving interface by coupling finite element meshes together using a boundary element technique, or, of course, by modelling the entire problem using an integral technique. Unfortunately, integral techniques are not well known for high accuracy in narrow air gap situations.

The airgap can be modelled using a Fourier technique and then coupled to both rotor and stator [1]. This is applicable to some electrical machines.

In this contribution we propose a fairly general technique for solving this problem, using independent finite element meshes which are free to translate and rotate and which are coupled together using Lagrange multipliers. This allows a finite element mesh to move with respect to an adjacent mesh without any need for remeshing. At different positions, only the terms which couple the meshes together at the interface are altered. In this contribution only the problem of producing many different magnetostatic solutions or 'snapshots' of the rotor at different instants in time is addressed. The more interesting problem of treating velocity induced eddy currents in a time transient situation should be possible by extending the basic techniques outlined here. Only two dimensional representations are discussed although it is thought that it should be possible to use the method in 3D problems.

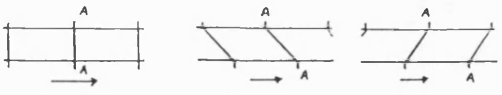

Figure 2 Local remeshing of moving problems

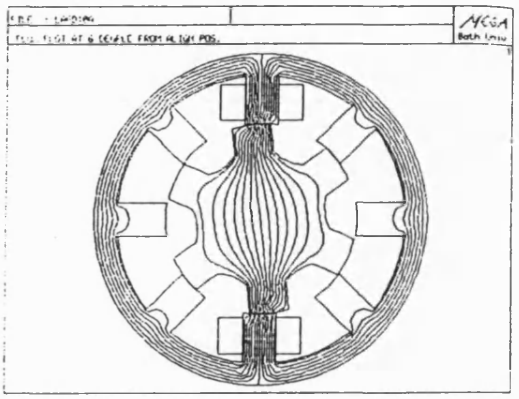

Figure 1 A switched reluctance motor [3]

Theory

Fig. 3 shows a typical problem. The outer region s represents a stationary member such as a machine stator. Region r is a machine rotor. The circular surface Γ_1 extends round the airgap of the machine.

In 2D fields are often modelled using one component of A, the magnetic vector potential. A can be determined by solving:

$$\text{curl}\left(\frac{1}{\mu}\,\text{curl}\,\bar{A}\right) = \bar{J} \qquad (1)$$

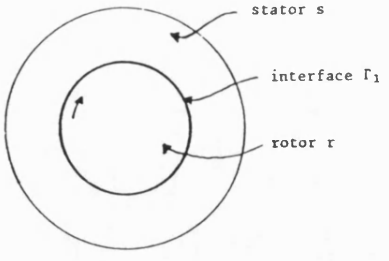

Figure 3 A typical problem. Γ_1 is the interface between two regions.

0018-9464/90/0300-0548$01.00 © 1990 IEEE

As is well known, eqn (1) can be solved approximately using finite elements by finding the stationary point of a functional π:

$$\pi = \frac{1}{2}\int \text{curl } \bar{A} \cdot \frac{1}{\mu}\text{curl } \bar{A}\, d\Omega - \int \bar{J} \cdot \bar{A}\, d\Omega \qquad (2)$$

In our simple 2D situation, using only the z component of A, this simplifies to:

$$\pi = \frac{1}{2}\int\left[\frac{1}{\mu}\left[\frac{\partial A_z}{\partial x}\right]^2 + \frac{1}{\mu}\left[\frac{\partial A_z}{\partial y}\right]^2\right] d\Omega - \int J_z A_z d\Omega \qquad (3)$$

In eqns 2 and 3, J is assumed to be prescribed.

Performing the variation of eqn 3 and using Green's theorem:

$$\delta\pi = -\int \delta A\left[\frac{\partial}{\partial x}\left[\frac{1}{\mu}\frac{\partial A}{\partial x}\right] + \frac{\partial}{\partial y}\left[\frac{1}{\mu}\frac{\partial A}{\partial y}\right] + J\right] d\Omega + \int \delta A\left[\frac{1}{\mu}\frac{\partial A}{\partial n}\right] d\Gamma \qquad (4)$$

In the above, the z subscripts from A and J have been dropped. The surface terms in eqn 4 cancel on adjacent elements throughout the interior of a region to yield continuity of H x n. On the boundary, these terms can be used to prescribe any value of H x n including the value zero, the 'natural' boundary condition.

Returning to the problem of Fig. 3, a functional such as that of eqn 3 can be specified for each region:

$$\pi = \pi_r + \pi_s \qquad (5)$$

The variables on surface Γ_1 have to be linked together in such a way that continuity of B.n and H x n is satisfied.

In Fig. 4 the k^{th} rotor variable A_{rk} can be coupled to the variables in an adjacent stator element s by applying a constraint:

$$A_{rk} = \sum_{i=1}^{4} A_{si}\, N_{si}(k) \qquad (6)$$

$N_{si}(k)$ is the usual shape function evaluated at point k. Any N_{si} which is not on the interface Γ_1 will result in a zero contribution to eqn 6, but we find that it is easier to include them all than to decide which are zero.

All similar constraints on surface Γ_1 can be written as:

$$A_r - f\left[A_s\right] = 0 \qquad (7)$$

This condition may be enforced by introducing a new set of variables which exist only on Γ_1, Lagrange multipliers.

A constrained variational principle may be obtained:

$$\pi = \pi_r + \pi_s + \int_{\Gamma_1} \lambda\left[A_r - f\left[A_s\right]\right] d\Gamma \qquad (8)$$

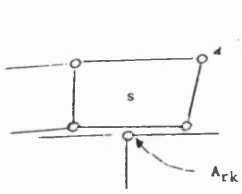

Figure 4 Coupling at rotor node k

$\delta\pi$ is now:

$$-\int_{\Omega_r}(\text{rotor area terms})\, d\Omega + \int_{\Gamma_1}\delta A_r\left[\frac{1}{\mu_r}\frac{\partial A_r}{\partial n}\right] d\Gamma$$

$$-\int_{\Omega_s}(\text{stator area terms})\, d\Omega - \int_{\Gamma_1}\delta A_s\left[\frac{1}{\mu_s}\frac{\partial A_s}{\partial n}\right] d\Gamma$$

$$+\int_{\Gamma_1}\lambda\left[\delta A_r - f\left[\delta A_s\right]\right] d\Gamma + \int_{\Gamma_1}\delta\lambda\left[A_r - f\left[A_s\right]\right] d\Gamma \qquad (9)$$

This is required to be zero for all variations of λ, A_r and A_s. The 'area terms' in eqn 9 are identical to those of eqn 4. The normal has been arbitrarily defined as being positive out of the rotor into the stator. The first three line integral terms define λ as being equal to:

$$\frac{1}{\mu_r}\frac{\partial A_r}{\partial n} \quad \text{or} \quad -\frac{1}{\mu_s}\frac{\partial A_s}{\partial n}$$

Hence, H x n is continuous from rotor to stator in an average sense. Continuity of B.n is assured by the continuity of the constrained variables on the interface.

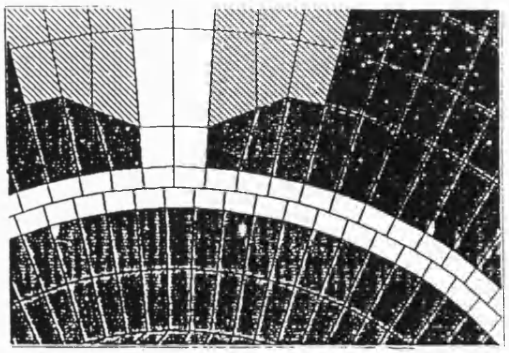

Figure 5 Illustrating how the nodes need not be coincident on the Lagrange interface

Results

Switched reluctance motors (SRM) give a torque which varies considerably with rotor position, hence the performance of such a machine can only be evaluated using finite elements by solving for many different rotor positions. The new scheme was used to model an SRM which has been previously evaluated in some detail using conventional finite elements [3]. Fig. 1 shows the machine for the position in which a rotor and stator pole are 6 degrees away from alignment. Fig. 5 shows the airgap region (for a different machine) and illustrates how the interface nodes need not be coincident. Fig. 6 shows the flux linkage for one stator pole when the rotor is in several different positions. Good agreement with the previous results were obtained, considering that the B-H characteristics were inaccurately taken from a small diagram from reference [3].

Conclusions

We have found in various trials that comparable results from this scheme and conventional meshes are obtained for similar discretisations.

It is worth remarking that Lagrange type functionals are stationary on saddle points and are not minima or maxima; this should play havoc with attempts to find upper and lower bounds.

The preconditioned conjugate gradient scheme which we use to solve equations needed more iterations to find a solution to the coupled problems. The worst case so far found in any problem is 50% higher. The reason for this could be the saddle point or the zeros on the diagonal of the Lagrange variables making the incomplete triangularisation of the matrix used in the solution less accurate, or perhaps a combination of both effects.

This coupled scheme still seems useful, a moving problem need only be meshed once, the program can then take care of any rotations or shifts of mesh.

This method of coupling disconnected meshes is also useful in cases where no movement is involved but where it is convenient to join an area of fine discretisation to another where the mesh can be more coarse. This is very common in non destructive testing and magnetic recording problems.

Irregular meshes and even different numbers of nodes and elements on both sides of the Lagrange surface are possible. If motion is being modelled, the only restriction on the Lagrange surface is that it will allow the required region to move. For instance, it should be circular and concentric with the rotor in a rotary machine or situated along the airgap, parallel to the direction of motion, in the case of a linear actuator.

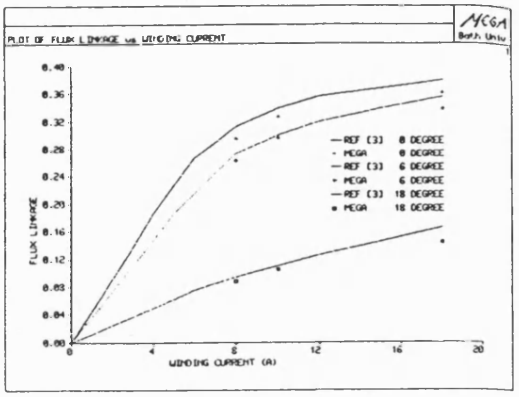

Figure 6 Pole flux linkage versus current at different positions - a comparison of results with those of reference [3].

References

[1] A.A. Abdel-Razek, J.L. Coulomb, M. Feliachi and J.C. Sabonnadiere, "Conception of an airgap element for the dynamic analysis of the electromagnetic field in electrical machines," IEEE Trans Mag Vol. MAG 18, No. 2, March 1982, pp. 655-659.

[2] O.C. Zienkiewicz, "The finite element method, 3rd edition", McGraw-Hill, 1977.

[3] G.E. Dawson, A.R. Eastham and J. Mizia, "Switched reluctance motor torque characteristics: Finite element analysis and test results", Conf. record of the 1986 IEEE Industrial Applications Soc. annual meeting, IAS 86, Vol. 1, pp. 864-867.

Coupling meshes in 3D problems involving movements

H.C.Lai, D.Rodger and P.J.Leonard
University of Bath,
Claverton Down,
BATH BA2 7AY, UK

Abstract — **This paper presents a new technique for use in Finite Element models for coupling independent three dimensional meshes together. The coupling is done at an interface using Lagrange Multipliers which can be identified as the normal component of B on the interface. This technique is particularly well suited to the analysis of devices with moving parts where the modelling of the moving parts at different positions is required.**

I. INTRODUCTION

In the analysis of electrical devices with moving parts, for example, a switched reluctance motor, it is often required to model the device with its moving parts at several different positions relative to the stationary parts. This is necessary in order that characteristics of interest such as torque, flux linkages etc., which vary with position can be evaluated.

Typically, to carry out this kind of analysis, several meshes have to be created, one for each position, and then each solved in turn. This involves extensive pre-processing and is laborious and time consuming even in two dimensional cases. Several schemes [1], [2], [3], have been proposed to alleviate this problem in the two dimensional cases.

The difficulties escalates enormously when one trys to perform a similar kind of analysis on three dimensional models. A previous paper [1] has highlighted these difficulties and proposed a coupling technique for solving the problem in two dimension.

The technique involves the use of Lagrange Multipliers to couple independent meshes at a suitable interface. In the case of a rotary machine, for instance, a circular surface that spans round the full air gap of the machine would be a suitable choice. Stationary and moving members of a model are meshed up as independent meshes which are free to move relative to each other. In order to model the device at different positions, it is only required to place the moving member at the appropriate location. The terms which couple the meshes together are re-calculated. The meshes need not be altered.

The present paper shows how the idea can be extended to three dimensional problems.

Manuscript received July 7, 1991

II. THEORY

In 3D, the magnetic field in non-conducting region, for example, air, can be modelled by the magnetic scalar potential ψ, and we solve for

$$\nabla\cdot\mu\nabla\psi = 0 \tag{1}$$

Equation (1) can be solved approximately by finding the stationary point of a functional Π :

$$\Pi = \frac{1}{2}\int_{\Omega} \nabla\psi\cdot\mu\nabla\psi \, d\Omega \tag{2}$$

Performing a variation on the functional and using Green's theorem, we have

$$\delta\Pi = -\int_{\Omega} \delta\psi\left[\frac{\partial}{\partial x}\left(\mu\frac{\partial\psi}{\partial x}\right)+\frac{\partial}{\partial y}\left(\mu\frac{\partial\psi}{\partial y}\right)+\frac{\partial}{\partial z}\left(\mu\frac{\partial\psi}{\partial z}\right)\right] d\Omega + \int_{\Gamma}\delta\psi\left(\mu\frac{\partial\psi}{\partial n}\right) d\Gamma \tag{3}$$

The $\frac{\partial\psi}{\partial n}$ term in the above equation is the prescribed $B\cdot\hat{n}$ on the boundary.

Consider a typical case shown in Figure 1 which consists of a stationary stator region S and a rotating rotor region R. The interface Γ_L extends round the full air gap of the machine

0018-9464/92$03.00 © 1992 IEEE

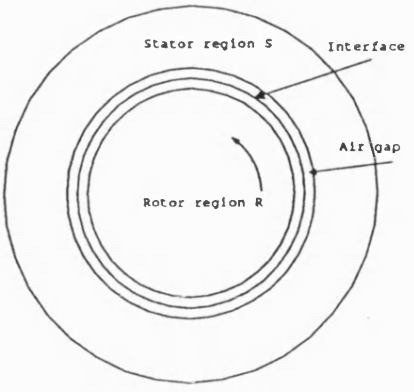

Figure 1. A typical problem with a stationary and moving region.

Functionals of the form of (2) can be specified for the rotor and stator region and the functional of the the whole system can then be written as

$$\Pi = \Pi_R + \Pi_S \tag{4}$$

To couple the variables on the interface Γ_L , we introduce an additional constraint into the original system

$$\psi_r - \psi_s = 0 \quad \text{on } \Gamma_L \tag{5}$$

where ψ_r and ψ_s are variables on Γ_L .

This additional constraint may then be incorporated into the original problem by forming a new functional

$$\Pi' = \Pi + \int_{\Gamma_L} \lambda(\psi_r - \psi_s)\,d\Gamma \tag{6}$$

where λ is a set of new variables, the Lagrange Multiplier, which exist only on the interface Γ_L

Similar to the scalar potential, ψ, λ can be approximated by

$$\lambda = \sum_{i=1}^{m} \lambda_i N_i \tag{7}$$

and the surface integral in (6) can be carried out in the usual element by element manner on Γ_L .

It should be noted that the additional of this extra set of constraints introduces zeros on the diagonal of the Lagrange variables of the matrix.

Performing a variation on the new functional, we have

$$\delta\Pi' = \delta\Pi + \int_{\Gamma_L} \delta\psi_r \mu \frac{\partial \psi_r}{\partial n}\,d\Gamma + \int_{\Gamma_L} \delta\psi_s \mu \frac{\partial \psi_s}{\partial n}\,d\Gamma + \int_{\Gamma_L} \delta\lambda(\psi_r - \psi_s)\,d\Gamma + \int_{\Gamma_L} \delta\psi_r \lambda\,d\Gamma - \int_{\Gamma_L} \delta\psi_s \lambda\,d\Gamma \tag{8}$$

$$\delta\Pi' = \delta\Pi + \int_{\Gamma_L} \delta\lambda(\psi_r - \psi_s)\,d\Gamma + \int_{\Gamma_L} \delta\psi_r \left(\lambda + \mu \frac{\partial \psi_r}{\partial n}\right) d\Gamma - \int_{\Gamma_L} \delta\psi_s \left(\lambda - \mu \frac{\partial \psi_s}{\partial n}\right) d\Gamma \tag{9}$$

This is required to be zero for all variations of λ, ψ_r and ψ_s. The first surface term in the above equation simply reiterates the constraint of (6). The second and third identify λ as being equal to

$$-\mu \frac{\partial \psi_r}{\partial n} \quad \text{or} \mu \frac{\partial \psi_s}{\partial n} \tag{10}$$

That is, $\mathbf{B} \cdot \hat{\mathbf{n}}$ on the interface Γ_L

III. RESULTS

The new scheme has been implemented in three dimension and was used to model an switched reluctance motor which has been modelled previously using conventional Finite Elements [4].

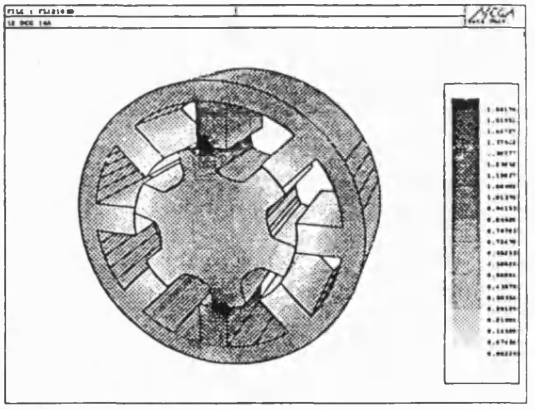

Figure 2. Contours of magnitude of B with rotor 12 degree from aligned position.

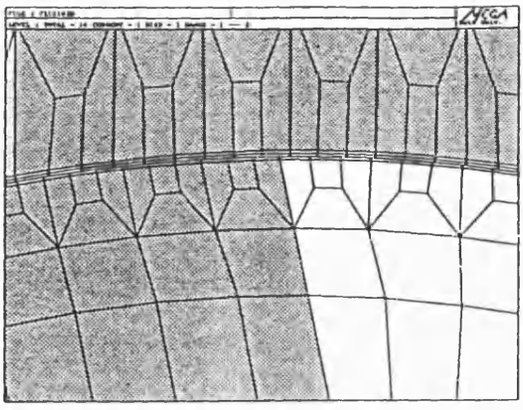

Figure 3. Showing how nodes at the interface need not be matched.

Figure 2 shows a computer generated three dimensional view of the model with the rotor 12 degree away from the aligned position. The figure also shows a contour plot of the magnitude of **B**. Figure 3 illustrates how the nodes of the stator and rotor region need not be joined at the interface.

Figure 4 below shows how the flux linkage for one stator pole obtained with the new schemes compares with earlier 2D results. The higher flux linkage exhibited in the three dimensional results are caused by the end turns of the coil giving rise to higher flux densities at the end of the poles.

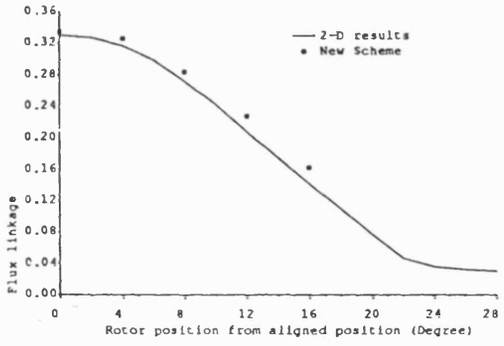

Figure 4. Graph showing pole flux linkage against rotor position.

IV. CONCLUSIONS

The technique reduces significantly the amount of work required to model devices with moving parts. In fact, it is only necessary to mesh up the problem once.

Although it was found that more iterations was required to obtain a solution to the couple problem when using an ICCG technique, we think that the time saved and the convenience introduced in the pre-processing phase easily compensates for this disadvantage.

The new technique applies equally well to problem with translational motion such as linear motor modelling and also in cases where it is convenient to join an area of fine discretisation to another area of relatively coarse discretisation.

REFERENCES

[1] D. Rodger, H.C. Lai, and P.J. Leonard. Coupled elements for problems involving movement. *IEEE Trans-Mag*, MAG 26(2):548–550, March 1990.

[2] A.A. Abdel-Razek, J.L. Coulomb, M. Feliachi, and J.C. Sabonnadiere. Conception of an airgap element for the dynamic analysis of the electromagnetic field in electrical machines. *IEEE Trans-Mag*, MAG 18(2):655–659., March 1982.

[3] S. Ratnajeevan and H. Hoole. Rotor motion in the dynamic finite element analysis of rotating electrical machinery. *IEEE Trans-Mag*, MAG 21(6):2292–2295., November 1985.

[4] G.E. Dawson, A.R. Eastham, and J. Mitzia. Switched reluctance motor torque characteristics; finite element an alysis and test results. *IEEE Industrial Applications Soc. annual meeting.*, 1:861–867, 1986.

A FINITE ELEMENT METHOD FOR PROBLEMS WITH MOVING PARTS

H C Lai, D Rodger and P J Leonard

University of Bath UK

International Conference on
Computation in Electromagnetics
November 1991
IEE Conference Publication Number 350

ABSTRACT

A new method for coupling independent three dimensional meshes together is described. The coupling is performed at their interface using Lagrange Multipliers. The densities and distributions of the nodes at the interface do not need to be the same. Applications of the method to a switched reluctance motor is given.

INTRODUCTION

The Finite Element Method [1] has emerged during the past two decades as a powerful and versatile analysis tool for solving a wide range of magnetic field problems. One of the many applications of the Finite Element Method is in the analysis of electrical device with moving parts. Examples of this class of devices include linear and rotational machines.

Unlike devices with only static parts, the knowledge of how certain device characteristics, such as torque or inductance, vary with positions is essential in the analysis and optimisation process. This can be obtained using finite elements. Many positions of the device, however, have to be modelled and solved. The difficulty in carrying out this kind of study is that the movement of the parts gradually distort the elements in the air gap until eventually the distortion is so big that the whole air gap region has to be remeshed. This involves extensive pre-processing and is time consuming even in two dimensional case. Moreover, the presence of many distorted elements will cause a loss of accuracy in the solution and will produce inconsistant results [2] [3]. Several schemes have been put forward to tackle this problem in two dimensional cases [4], [5],[6].

This paper describes a new method which couples independent three dimensional meshes at their interface. The coupling is done by using Lagrange Multipliers which can be identified as the normal of the magnetic flux density at the interface. This technique allows stationary and moving members of a model to be meshed up independently and then coupled together at a later stage. As the meshes are free to move independent to each other, a new postion can be solved simply by placing the moving members at the desired position and then recalculating the coupling terms. The need to remesh at different positions is eliminated.

Another convenient feature is that the densities and distributions of the nodes of adjacent meshes need not be the same on the interface, thus making it possible to use as well-formed a mesh as possible around the interface.

THEORY

Figure (1) shows a typical case of this kind of problem. It consists of a stationary stator region S and a rotating rotor region R. The interface Γ_L extends round the full air gap of the machine.

In three dimensional finite elements, the magnetic field in regions containing no currents can be represented by the magnetic scalar potential ψ,

$$H = -\nabla\psi \tag{1}$$

And we must solve for

$$\nabla\cdot\mu\nabla\psi = 0 \tag{2}$$

Equation (2) can be solved approximately by finding the stationary point of the functional Π :

$$\Pi = \frac{1}{2}\int_{\Omega} \nabla\psi\cdot\mu\nabla\psi \, d\Omega \tag{3}$$

In our case, we can specified functionals of the form of (3) for the rotor and stator region separately. The functional of the the whole system can then be written as

$$\Pi = \Pi_R + \Pi_S \tag{4}$$

The variables on the interface Γ_L have now to be linked together. To do this we introduce an additional constraint into the system.

$$\psi_r - \psi_s = 0 \quad \text{on}\Gamma_L \tag{5}$$

where ψ_r and ψ_s are variables on Γ_L .

This additional constraint may then be incorporated into the original problem using Lagrange Multipliers. A new functional, Π', can be formed such that

$$\Pi' = \Pi + \int_{\Gamma_L} \lambda(\psi_r - \psi_s)\, d\Gamma \tag{6}$$

where λ is a new function, the Lagrange Multiplier, which exits only on the interface, Γ_L .

λ can be approximated in a similar way to the scalar potential, ψ, by

$$\lambda = \sum_{i=1}^{m} \lambda_i N_i \tag{7}$$

The surface integral in (6) can be carried out in the usual element by element manner on Γ_L . The final matrix formed will now possess zeros on the diagonal of the Lagrange rows.

We now proceed to show that the Lagrange variables can be identified as the B normal on the interface.

Performing a variation on the functional (3) and using Green's theorem, we have

$$\delta\Pi = -\int_{\Omega} \delta\psi \left[\frac{\partial}{\partial x}\left(\mu\frac{\partial\psi}{\partial x}\right) + \frac{\partial}{\partial y}\left(\mu\frac{\partial\psi}{\partial y}\right) + \frac{\partial}{\partial z}\left(\mu\frac{\partial\psi}{\partial z}\right)\right] d\Omega + \int_{\Gamma} \delta\psi \left(\mu\frac{\partial\psi}{\partial n}\right) d\Gamma \quad (8)$$

The $\frac{\partial\psi}{\partial n}$ term above is the prescribed $\mathbf{B}\cdot\hat{\mathbf{n}}$ on the boundary.

Performing a variation on the new functional Π', we have

$$\delta\Pi' = \delta\Pi + \int_{\Gamma_L} \delta\lambda(\psi_r - \psi_s)\,d\Gamma + \int_{\Gamma_L} \delta\psi_r\lambda\,d\Gamma - \int_{\Gamma_L} \delta\psi_s\lambda\,d\Gamma \quad (9)$$

where $\delta\Pi$ is the variation of the original functional. $\delta\Pi'$ can be written as

$$\delta\Pi' = -\int_{\Omega_R} (\text{rotor terms})\,d\Omega - \int_{\Omega_S} (\text{stator terms})\,d\Omega + \int_{\Gamma_L} \delta\psi_r\left(\lambda + \mu\frac{\partial\psi_r}{\partial n}\right) d\Gamma - \int_{\Gamma_L} \delta\psi_s\left(\lambda - \mu\frac{\partial\psi_s}{\partial n}\right) + d\Gamma \int_{\Gamma_L} \delta\lambda(\psi_r - \psi_s)\,d\Gamma \quad (10)$$

This is required to be zero for all variations of λ, ψ_r and ψ_s. The last surface term in the above equation simply restates our extra constraint (10). The first two surface integrals state the following relations,

$$\lambda = \mu\frac{\partial\psi_r}{\partial n} \quad (11)$$

$$\lambda = -\mu\frac{\partial\psi_s}{\partial n} \quad (12)$$

This identifies λ as the $\mathbf{B}\cdot\hat{\mathbf{n}}$ on the interface Γ_L

RESULTS

The Switched Reluctance Motor (SRM) has a double salient structure with a very small air gap and is usually operates under highly saturated conditions. The complicated magnetic structure, together with the highly saturated operating condition makes finite elements a suitable tool to be used in the analysis of the motor.

The new scheme has been implemented and incorporated into the finite element package *MEGA*. It has been used to model a switched reluctance motor [7] three dimensionally. The nonlinear characteristic of the motor material has been taken into account. The variation of the torque with rotor positions has been evaluated.

Figure 2 shows a three dimensional view of the motor modelled with the rotor 10 degrees away from the aligned position. The figure also shows a contour plot of the magnitude of B. Areas with high flux density can readily be identified from the view.

Figure 3 illustrates how the nodes of the stator and rotor region need not be matched at the interface. This enables the use of uniform meshes around the interface.

Figure 4 shows how the the torque of the motor varies with the rotor position. The torque is obtained by the method of Maxwell Stress.

CONCLUSIONS

A new technique for coupling meshes together has been implemented and was applied sucessfully to evaluate the variation of the torque with position of an SRM. The amount of work required to model the motor at different rotor positions was reduced considerably. In fact, the problem was only meshed up once.

However, it was found that more iterations was required to obtain a solution to the coupled problem when using an ICCG technique. Yet, we still think the time saved and the convenience introduced in the pre-processing phase easily compensate for this disadvantage.

The method can also be applied readily to couple meshes with different discretisation density together. This opens up the possibility of meshing up different parts of a problem separately with the appropiate mesh density and then using this technique to couple them together.

References

[1] O.C Zienkiewicz. *The Finite Element Mehtod.* McGraw-Hill Book Company Limited, 3rd edition, 1986.

[2] A.R.Eastham J.Mizia, K.Adamiak and G.E.Dawson. Finite element force calculation: Comparison of methods for electric machines. *IEEE Trans-Mag*, MAG 24(1):447–450, January 1988.

[3] M.Moallem and C.M.Ong. Predicting the torque of a switched reluctance machine from its finite element field solution. *IEEE Trans-EC*, 5(4):733–739, December 1990.

[4] H.C. Lai D. Rodger and P.J. Leonard. Coupled elements for problems involving movement. *IEEE Trans-Mag*, MAG 26(2):548–550, March 1990.

[5] M. Feliachi A.A. Abdel-Razek, J.L. Coulomb and J.C. Sabonnadiere. Conception of an airgap element for the dynamic analysis of the electromagnetic field in electrical machines. *IEEE Trans-Mag*, MAG 18(2):655–659., March 1982.

[6] S. Ratnajeevan and H. Hoole. Rotor motion in the dynamic finite element analysis of rotating electrical machinery. *IEEE Trans-Mag*, MAG 21(6):2292–2295., November 1985.

[7] A.R. Eastham G.E. Dawson and J. Mitzia. Switched reluctance motor torque characteristics; finite element an alysis and test results. *IEEE Industrial Applications Soc. annual meeting.*, 1:864–867, 1986.

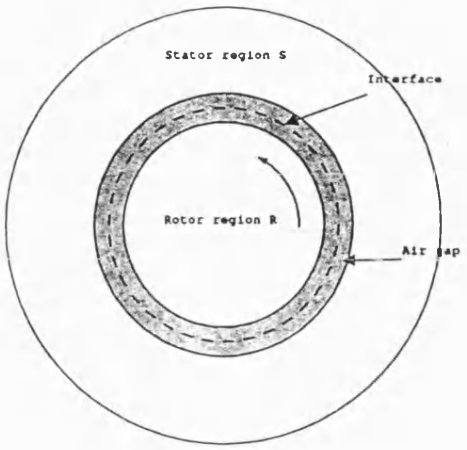

Figure 1. A typical problem with moving parts.

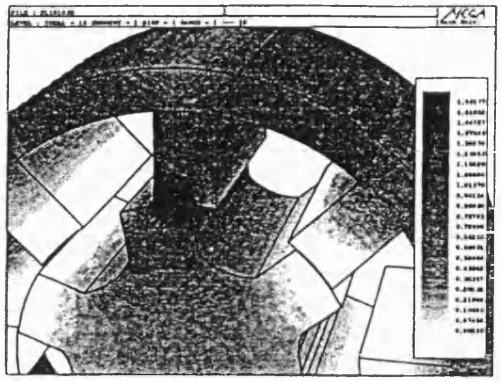

Figure 2. Contours plot of magnitude of B with rotor 10 degrees from aligned position.

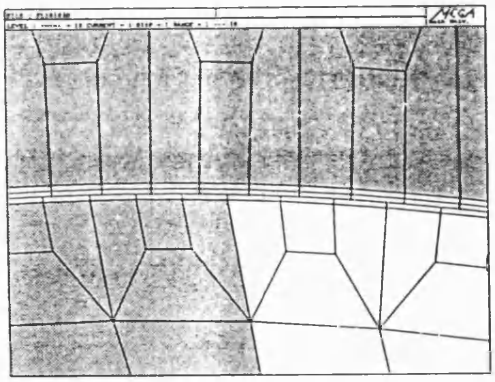

Figure 3. Illustrates that nodes at the interface do not need to be matched.

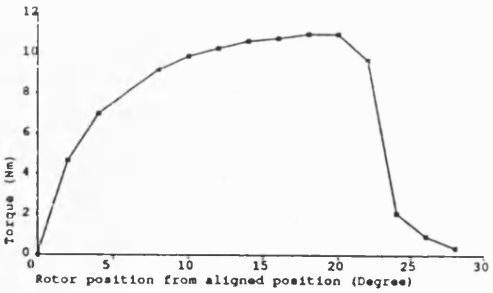

Figure 4. Graph of Torque against rotor position

Analysis of the Performance of Tubular Pulsed Coil Induction Launchers

P.J.Leonard H.C.Lai G.Hainsworth D.Rodger and J.F.Eastham
University of Bath,
Claverton Down,
BATH BA2 7AY, UK

Abstract — **This paper presents a scheme for modelling coil guns using finite elements. The relative motion between the coils and the projectile is modelled by using two distinct meshes which are coupled using Lagrange multipliers which depend on the relative position of the two meshes. This scheme allows the inner mesh to slide during the transient simulation without the need to remesh the problem. Results are presented for a simple experiment involving a single coil and aluminium projectile.**

I. INTRODUCTION

In the past, transient models of coil guns have typically been based on a mutually coupled circuit approach [1] [2]. The projectile is modelled as a set of concentric conducting rings, each having a self inductance and a mutual inductance with respect to the other rings and source coils. In this scheme the motional effects are taken care of by the change in mutual inductance between the coils and the projectile, these values and their derivatives with respect to position must be calculated at each position during the time step simulation.

The scheme presented in this paper is based on a finite element model for the distributed field. Finite elements have previously been used for modelling devices with stationary parts or devices in which the moving part has a regular cross section in the direction of motion. In the later case we can use the Minkowski transformation to calculate the induced current in the moving conductor [3]. This approach can typically be used for rail guns, where we can choose the projectile as the frame of reference and let the rails move backwards. With coil guns, neither the projectile or the coils have a constant cross section in the direction of motion so a new scheme must be used.

A. Sliding Meshes

The method presented here splits the problem into two regions, an inside cylinder containing the projectile and the outside region containing the coil. The two regions touch at a given radius but have no nodes in common.

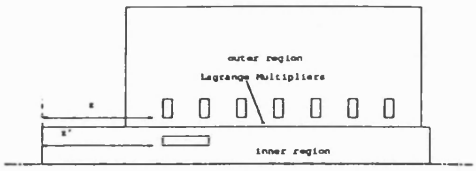

Fig. 1. Showing the two regions

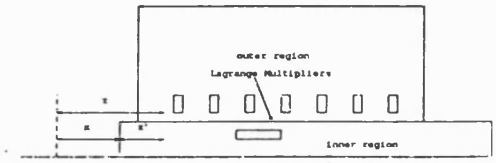

Fig. 2. Showing the two regions after some movement

The field is represented by an unknown potential, for example a 2D axisymmetric model used in this paper solves for the circumferential component of the magnetic vector potential **A**. The field is given by,

$$\begin{aligned} \mathbf{B} &= \nabla \times \mathbf{A} \\ \mathbf{J} &= \mathbf{J}_{source} - \sigma \frac{\partial \mathbf{A}}{\partial t} \end{aligned} \quad (1)$$

Because the two meshes are not connected we need to enforce the continuity of normal flux tangential e.m.f. The coupling is done by adding a set of equations which "tie" together the unknowns on the interface for a given position [4].

0018-9464/93$03.00 © 1993 IEEE

Let us denote the unknown potential on the outer interface as $A(z)$ and on the inner interface $\acute{A}(\acute{z})$. Note that z and $\acute{z}$ are distances measured in two different frames of reference. If the relative displacement between the two meshes is x, then z is the same point as $\acute{z} + x$. At any given point on the interface $\acute{z} = z - x$. Now we can relate the potentials,

$$A(z) = \acute{A}(z - x) \tag{2}$$

One approach of coupling the potentials is to add new rows that represent the above equation at a set of points along the interface. However, in our experience better results are obtained by "weakly" enforcing $A = A'$, using a set of weighting functions, N_j, associated with the Lagrange multipliers,

$$\int N_j(z) \left[A(z) - \acute{A}(z - x)\right] \mathrm{d}\, z = 0 \tag{3}$$

The extra unknowns (Lagrange multipliers) appear as new columns in the original equations as source terms which are symmetric with the additional rows. They supply the necessary sources to enforce the continuity conditions imposed by the extra rows.

This technique allows stationary and moving members of a model to be meshed up independently and then coupled together at a later stage. As the meshes are free to move independent to each other, a new position can be solved simply by placing the moving members at the desired position and then recalculating the coupling terms. The need to remesh at different positions is eliminated.

An additional feature of this scheme is that the densities and distributions of the nodes of adjacent meshes need not be the same on the interface.

B. Time stepping

At any given position the Finite Element method yields a system of equations of the form,

$$[\mathrm{K}]\mathbf{A} + [\mathrm{C}]\dot{\mathbf{A}} = \mathbf{f} \tag{4}$$

The matrices [K] and [C] are usually called the stiffness and damping matrices which correspond to the magnetostatic solution and the "damping" due to eddy currents.. The unknown vector A is the collection of the unknown nodal potentials. The r.h.s. f is due to known current, in this case the coils.

The mechanical system is modelled by a single unknown position x. The force on the projectile, F, can be calculated from the electromagnetic solution and the acceleration can be found. Integrating the acceleration gives the velocity and position. The position is then fed back into the electromagnetic model to recalculate the matrix entries for the Lagrange multiplier terms for the new position.

The time stepping procedure is based on backward difference method for the electromagnetic system and forward difference for the mechanical system. It is summarised as follows,

1. Initialise the electromagnetic unknowns $\mathbf{A} = \mathbf{A}_0$ for time $t = 0$. Initialise position, x_0, velocity, v_0. Set $n = 0$ and the time step Δt

2. Assemble electromagnetic system of equations for this position, x_n, $[\mathrm{K_n}]$.

3. Calculate electromagnetic solution, using backward differences

$$\begin{aligned} \alpha_n &= ([\mathrm{C}] + \Delta t[\mathrm{K_n}])^{-1} \{\mathbf{f}_n - [\mathrm{K_n}]\mathbf{A}_n\} \\ \mathbf{A}_{n+1} &= \mathbf{A}_n + \alpha_n \Delta t \end{aligned} \tag{5}$$

   note that α_n is the approximate rate of change the electromagnetic unknowns,

4. Calculate the force from the electromagnetic solution and hence the acceleration a. Use forward difference to calculate the velocity and new position,

$$\begin{aligned} v_{n+1} &= v_n + a\Delta t \\ x_{n+1} &= x_n + v_{n+1}\Delta t \end{aligned} \tag{6}$$

5. set $n = n + 1$, Repeat from 2.

This scheme assumes that the displacement during each time step is fairly small so [K] is reasonably constant during the time step. This can always be satisfied by reducing Δt.

II. RESULTS

The model has been verified using a single coil and an aluminium cylinder. The dimensions of the model are given in TABLE 1.

TABLE I
EXPERIMENTAL DATA

Coil	
Inner radius	$0.02857m$
Outer radius	$0.03427m$
Length	$0.03688m$
Turns	60
Cylinder	
Inner radius	$0.02205m$
Outer radius	$0.02485m$
Length	$0.06352m$
Conductivity	$3.0 \times 10^7 Sm^{-1}$

The coil was driven using a resonant discharge from a capacitor which produced the current waveform shown in Fig. 3

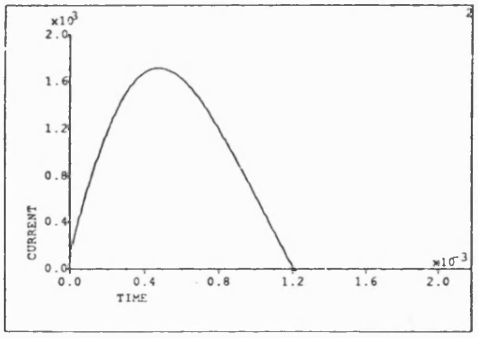

Fig. 3. Current waveform in coil

The predicted flux is shown in Figs. 4,5 and 6, just after the switch on, after $1ms$ and after $2ms$.

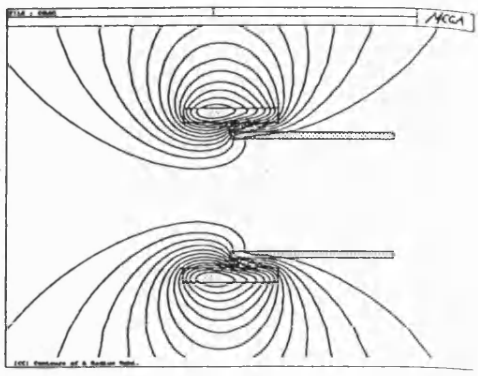

Fig. 4. Flux plot just after switch on

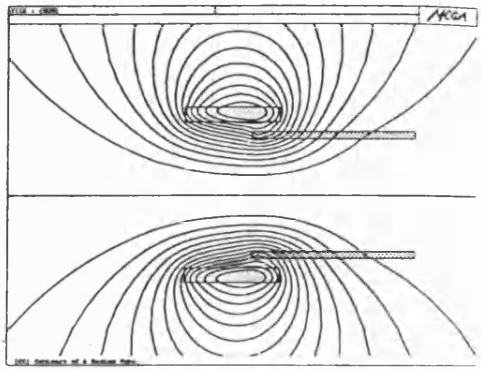

Fig. 5. Flux plot at $1ms$

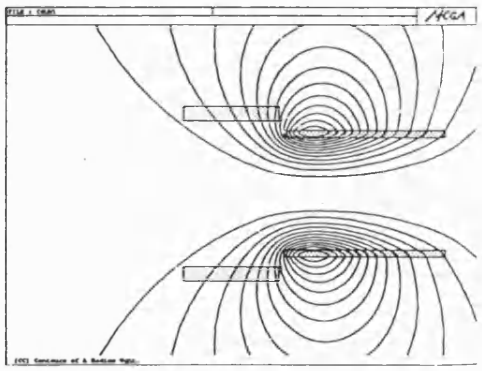

Fig. 6. Flux plot at $2ms$

The measurement of velocity of the projectile proved to be quite difficult. The first attempt measured the position of the projectile fairly crudely using optical sensors and a trailing metal tape with holes. However the tape was not completely rigid explaining the rather jerky experimental results shown in Fig. 7, the experimental velocity is very sensitive to the errors in position measurement.

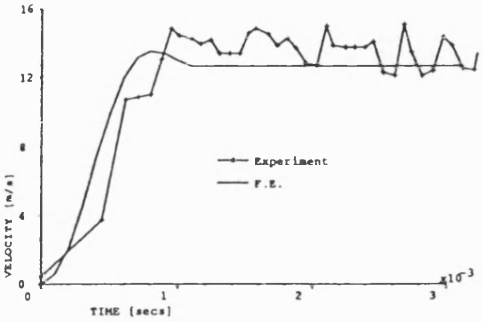

Fig. 7. Experimental and predicted velocity (using tape)

An attempt was made to directly measure the thrust on the projectile by mounting the gun on a force table and measuring the reaction force. This method was a complete failure, the measurements were dominated by the resonant modes of the structure.

Finally the experiment was repeated using an optical sensor to detect black strips on the projectile. This improved the measurements but with only one sensor limited the observation to a the length of the projectile. The current waveform used in this firing is shown in Fig. 9. Whilst the derived velocity is shown in Fig. 8

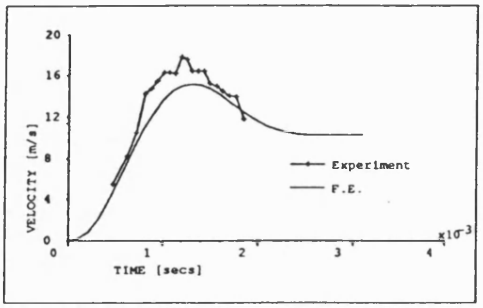

Fig. 8. Experimental and predicted velocity (using stripes)

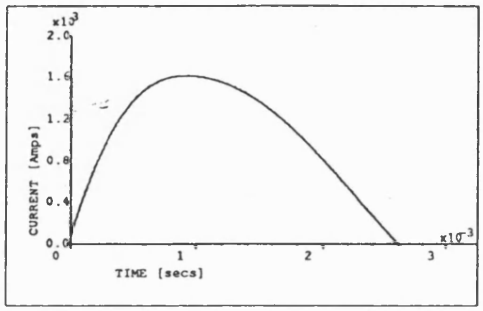

Fig. 9. Current waveform in coil (striped run)

It is interesting to see the small negative acceleration as the cylinder leaves the field due to the coil.

III. CONCLUSION

The new method has been verified for a simple 2D case. The initial results are very promising. For axisymmetric problems a mutual inductance model would probably be more appropriate [2], however the technique is easily generalised to 3D which would allow any features which are not axisymmetric to be modelled. The use of Finite Elements also allows the same mesh to be used for a thermal model driven by the eddy current heating in the projectile. This could in turn be coupled to the electromagnetic model by having a temperature dependent conductivity.

For longer guns the outer mesh containing the coils could be "recycled", the mesh would be long enough to model the active coils at any given time. The mesh could be pushed forward, re-assigning the elements to the coils being energised.

REFERENCES

[1] S.Williamson and P.J.Leonard. "Analysis of air-cored tubular induction motors". *IEE Proc A.*, 133(4), July 1986.

[2] M.M.Widner. "WARP-10 a numerical simulation model for the cylindrical reconnection launcher ". *IEEE Trans. Mag.*, 27(1):634–638, January 1991.

[3] D.Rodger and P.J.Leonard. "Alternative schemes for em modelling of rail guns at speed using finite elements". *Proc of the 3'rd European Symposium on EML Technology (London, England)*, April 1991.

[4] D. Rodger, H.C. Lai, and P.J. Leonard. "Coupled elements for problems involving movement". *IEEE Trans-Mag*, MAG 26(2):548–550, March 1990.